Optimization of microstructure and properties of high strength spring steel

고강도 스프링강의 미세조직 및 물성 최적화

Ph.D. thesis

January, 2011

Sangwoo Choi

Optimization of microstructure and properties of high strength spring steel

Proefschrift

door

Sangwoo CHOI

Master of Science in Materials Science and Engineering
Korea Advanced Institute of Science and Technology, Korea
born at Gwangju, KOREA

Dit proefschrift is goedgekeurd door de promotor:
Prof. dr. ir. S. van der Zwaag

Dit proefschrift is goedgekeurd door de promotor:

Rector Magnificus, voorzitter
Prof. dr. ir. S. van der Zwaag, TU Delft, promotor
Prof. dr. ir. J. Sietsma, TU Delft
Prof. dr. R. Boom, TU Delft
Prof. dr. E.H. Brueck, TU Delft
Prof. dr. Y. Houbaert, Ghent University, Belgium
Prof. dr. ir. R. Benedictus, TU Delft
Dr. P.E.J. Rivera Díaz del Castillo, University of Cambridge, United Kingdom

Cover designed by Inkyung You

To my parents and wife, daughters

Contents

1
Introduction

1.1 Review of spring steel evolution (and justification of the research in an economic context)

Over the past three decades, considerable efforts have been made in the development of high performance spring steels to meet weight and cost saving needs in the automobile industry. Weight reduction is important so as to reduce the amount of fuel consumption, which can be achieved in part by improving the design strength of suspension coil springs. However, the increment in strength should not degrade other spring properties such as formability and fatigue. In an effort to improve the properties of spring steels, POSCO is continuously developing new alloys for spring steels possessing high tensile strength, good sag resistance, and good formability. Based on the present industrial situation, new suspension spring steels having 2350 MPa grade tensile strength must be developed. Microstructures consisting of both bainitic and martensitic phases may be expected to raise the strength to the desired levels. Two aspects are essential for achieving the target mechanical properties: (1) the control of the alloy composition by incorporating new cost-effective alloying elements, and (2) finding appropriate heat treatment routes to optimize desired multiphase structures.

1.2 Metallurgical background of spring steel

1.2.1 Effect of chemical composition on the tempering property

In order to combine high strength and high sag resistance in spring steels, alloying elements such as Si, Cr, V, and Nb are added, causing complex microstructural transitions.   To understand the behavior of mechanical properties during tempering of spring steel, the tempering of plain carbon steel is usually studied as the first step.   In this section, the effects of Si, V and Nb on the tempering behavior are described.

1.2.1.1   *Microstructural change of plain carbon steel during tempering*

For carbon steels having more than 0.2 %C, the microstructural changes during tempering have been investigated in detail.   Generally, the microstructural change of martensitic steels during tempering occurs in four temperature regimes [1-3]:   Between 100 and 250 ^{o}C, carbon migrates towards the dislocations and laths boundaries, inducing the formation of transition carbides.   Jack et al. reported that during tempering of Fe-0.7% C steel, ε - carbide formed at the intergranular boundary having coherency with the matrix at around 150 ^{o}C and showed that these carbides form at dislocations in the matrix induced by martensite.[4]

Between 200 and 300 ^{o}C, retained austenite transforms to bainite, ferrite and carbides. However, the direct observation of retained austenite in the microstructure has always been rather difficult, particularly if it is present in low concentrations.   In martensitic plain carbon steels below 0.5 %C, the retained austenite is often 2%, rising to around 6% at 0.8 %C and over 30% at 1.25 %C.   The little available evidence suggests that in the range of 200 ~ 300 ^{o}C, retained austenite decomposes to ferrite and cementite, but no detailed comparison between the decomposed phase and lower bainite has yet been made.

Between 250 and 350 ^{o}C the phases formed at lower temperatures transform to ferrite and cementite.   Speich reported that at around 400 ^{o}C, by the mechanism of Oswald ripening, rodlike carbides transforms to sphere-type cementite.[5]   In high carbon martensite, the cementite is easily formed at the boundary between ε - carbide and matrix, and transitional carbides are gradually dissolved while cementite particles form.   Nucleation of carbides also occurs at twin boundaries.   Another site for the nucleation of cementite is the grain boundary regions, both the interlath boundaries of the martensite and the original austenite grain boundaries.   The cementite can form as very thin films which are difficult to detect but which gradually spheroidize to give rise to well defined particles of Fe$_3$C in the grain boundary regions.   There is some evidence to show that these grain boundary cementite films can adversely affect ductility.   However, they can be modified by addition of alloying elements.[3]

At temperatures higher than 350 ^{o}C, cementite undergoes a coarsening process and essentially loses its crystallographic morphology, becoming spheroidized.   The coarsening commences at around 350 ^{o}C, while spheroidization takes place increasingly up to 700 ^{o}C. At the higher end of this range of temperature, the martensite lath boundaries are replaced by more equi-axed ferrite grain boundaries by a process which is best described as recrystallization.   The final result is an equi-axed array of ferrite grains with coarse spheroidized particles of Fe$_3$C.   Due to a high density of cementite precipitates, the ferrite boundary is pinned and grain growth is suppressed.   The size of spheroidized cementite and ferrite grains increases with temperature.   The final process is the continued coarsening of the Fe$_3$C particles and gradual ferrite grain growth.

As the microstructural changes of steel strongly affect the mechanical properties, the

tempering temperature is of first order importance.   The trends displayed by the Fe-C system are shown in Fig. 1.1.[3]   For the 0.2 %C steel, the transition carbide did not exist and then the hardness did not change.   The hardness changes during tempering are also very dependent on carbon content levels, as shown in Fig. 1.1 for steels up to 0.4 %C.   Above this concentration, an increase in hardness was observed in the temperature range 50 ~ 150 ^{o}C, as ε - carbide precipitation strengthens the martensite.   However, the general trend is an overall softening, as the tempering temperature increased.   The diagram indicates the main physical processes contributing to the change in mechanical properties.
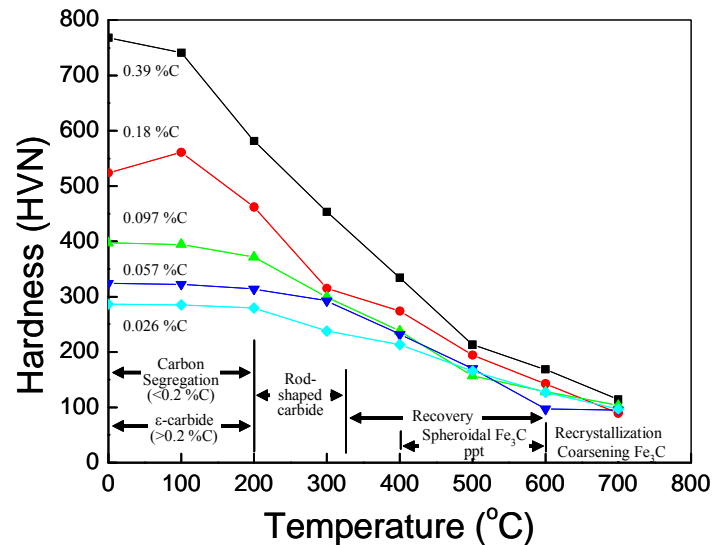
FIGURE 1.1.   Hardness of iron-carbon martensite tempered at 100 ~ 700 ^{o}C for 1 hr.

1.2.1.2   Effect of Si in Spring steel

Si delays the softening process during tempering;   It delays the formation of cementite at tempering in the 250 ~ 350 ^{o}C range.   Alten and Payson investigated the effect of Si in 0.6 %C steel tempering.[6]   Gordine et al. reported that for Si-Cr steel having 0.3 - 1.5 %Si, the effects of Si on tempering were similar to those in carbon steel.[7]   In 0.3% Si steel, sag resistance was independent of the amount of Cr and the tempering kinetics did not change up to 0.7%, when Cr became a strong carbide former.   In the case of 1.5% Si addition, ε - carbide was stabilized and recrystallization was suppressed while independent to the amount of Cr.   Fig. 1.2 shows the weight fraction ratio of Si / (Fe + Cr) of the extracted carbide after tempering at 500 ^{o}C.   It indicates that most of Si in carbide was removed and all the carbide was pure Fe_3C cementite.

As to the mechanisms explaining the effect of Si, initially it has been suggested that Si delays the transition of ε - carbide to cementite by postulating the existence of Si in the carbide.   A second mechanism suggests suppressing the growth of cementite by the formation of Si layer around the cementite.[8]   Altstetter et al. reported that Si did not influence the formation of ε - carbide in the range of 100 ~ 250 ^{o}C tempering but affects the transition to cementite.[9]   It was reported that for 0.3 %Si steel, tempering in the range of 250 ~ 350 ^{o}C consists of 2 steps due to stabilizing action of alloying elements on the ε - carbide.   In other words, during the first step in the range of 250 ~ 350 ^{o}C of tempering, low

carbon martensite was transformed into the cementite and ferrite, and ε - carbide was continuously dissolved or conversed to form the cementite.   However, it was noted that Si delays the first step and influences the next step.

   In contrast to this proposed mechanism, Owen et al. reported that Si increases the temperature at which ε - carbide is dissolved.[10]   They suggested that the kinetics at temperatures higher than 300 °C was controlled by the diffusion of Si along the boundary of ferrite and cementite instead of C.   Leak et al. reported that the bulk diffusion of carbon in ferrite did change up to 3.0% Si.[11]   The addition of Si increases the strengthening of spring steels via a solid solution mechanism, e.g. SAE9260 steel (1.8 ~ 2.2 %Si).[12,13]   Moreover, Si influences the distribution and shape of precipitates during tempering.   In SAE9260 steel decarburization occurs due to Si additions.   The solution to this problem has been to decrease the amount of Si and by adding Cr (SAE9254), improving decarburization and hardenability.
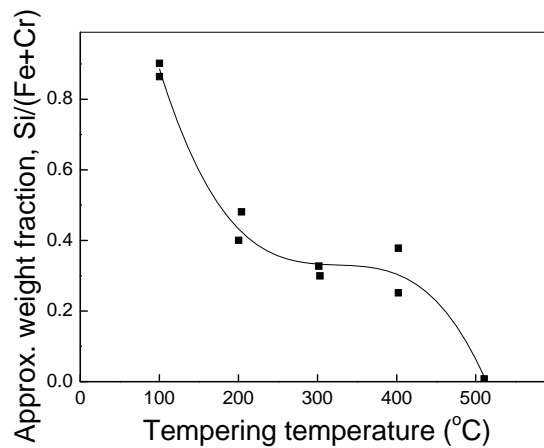
FIGURE 1.2.   Approximate Si/(Fe+Cr) weight fraction ratio in the extracted carbides with the tempering temperature.

1.2.1.3   Effect of V and Nb in spring steel

   In general, the strengthening methods for spring steel are precipitation hardening, solid solution strengthening and grain refinement.   The solid solution strengthening is carried out by adding Si, the precipitation strengthening is fostered by adding the carbide formers such as V and Nb, which induce the precipitation of M_3C, M_2C and MC_x type particles.   VC and NbC serve the purpose of grain refinement, their precipitation in the form of fine particles takes place during hot rolling and cooling.

1.2.2   Sag resistance

   Sag resistance, together with fatigue is considered as a key property of spring steel. Kawakami et al. evaluated the effect of alloying elements on the sag resistance of Si-Cr, Si-Cr-Mo and Si-Cr-V steels by using the Bauschinger torsion test.[14]   To evaluate the sag resistance of springs, real springs were used.   This method took a long time to evaluate the sag resistance.   Furr et al. suggested the Bauschinger torsion instead of testing the real

product.[15]   The sag resistance was evaluated as the area within the hysteresis loop measured by Bauschinger torsion testing (Fig. 1.3).   Si-Cr spring steel having 1.5% Si displays a good sag resistance, but it decreases by increasing the amount of Cr.   It was reported that the sag resistance of Si-Cr-Mo and Si-Cr-V steels were similar to that of Si-Cr steel and the sag resistance was then improved by the addition of V and Nb.
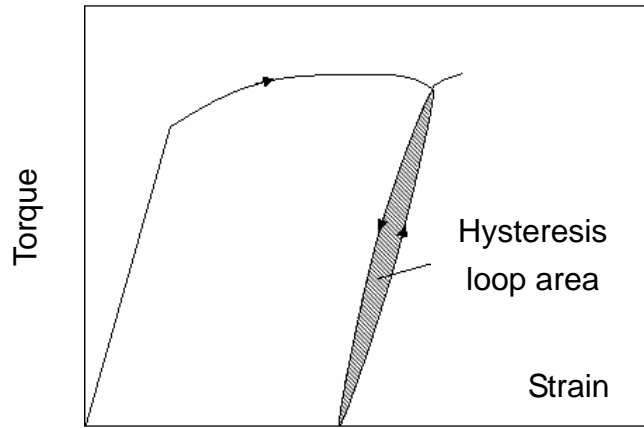
FIGURE 1.3.   Schematic diagram of bauschinger torsion test.

In general, dislocations accumulate or entangle at the grain boundary, and at the precipitate/matrix boundary when steel is deformed, and as a result micro residual back stresses (MRBS) are produced.   This phenomenon takes place during final manufacturing procedure of the spring.   The factors influencing the results of the Bauschinger effect are the grain size, distribution of precipitates, chemical composition, level of presetting, and strain rate.   The area of the hysteresis loop increases with the refinement of grain sizes. Increasing the amount of Si, V and Nb in spring steel, increases the sag resistance.[16-18]

1.2.3   Fatigue
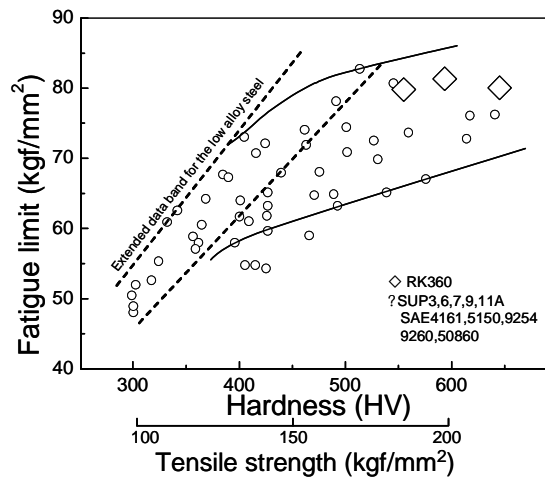
FIGURE 1.4.   Fatigue limit influenced by the tensile strength and hardness[19].

In the past, alloying elements were used to increase the strength and to improve the fatigue limit of spring steels.[19,20]   However, Fig. 1.4 shows that the fatigue limit increases proportionally with increments of hardness up to 400 Hv, from which a plateau is approached. Fatigue strength is largely influenced by the external surface due to decarburization, surface defect, and nonmetallic inclusions.   Moreover, there is a relation between the fatigue limit and prior austenite grain size (PAGS), as shown in Fig. 1.5.[21]   Fig. 1.6 shows the relation between the fatigue limit and the amount of retained austenite.   The results show that within an optimum range of PAGS and the amount of retained austenite, a higher fatigue limit can be reached.
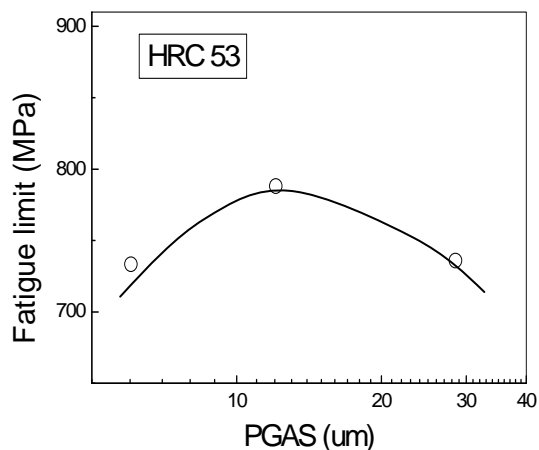
FIGURE 1.5.   Fatigue limit on the prior austenite grain size of spring steel[21].
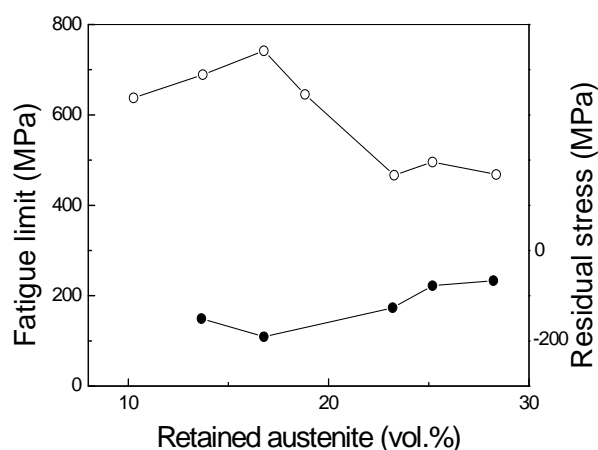
FIGURE 1.6.   Fatigue limit on the amount of retained austenite[21].

1.3   Development of suspension spring steel

In the past, plain carbon steel was often used for suspension coil spring.   Recently the plain carbon steel was replaced by SAE9254 having the desired strength 1000 MPa, was developed by adding the Cr and Si.   By further adding V and Ni, 1200 MPa strength steels was developed.[17]   Two technologies have been necessary to develop for high strength spring steel: 1) Alloying elements which increases the strength (YS, TS), and 2) manufacturing processes such as shot peeing and presetting, which improve fatigue, but also improve strength up to 100 ~ 150 MPa in accordance with the conditions of the shot peeing and presetting.   Until now, currently developed suspension spring steels have achieved the 2200 MPa level.   Two commercial strength grades have been put on the market recently : 1800 and 2000 MPa grades.   Table. 1.1 shows the chemical compositions of such grades.[17]

TABLE 1.1.   Chemical compositions of commercial spring steels.

Grade (MPa)	Compositions (wt.%)							
	C	Si	Mn	Cr	Ni	Cu	V	Ti
1800	0.55	1.5	0.7	0.7	-	-	-	-
2000	0.48	2.1	0.65	0.7	0.3	0.25	0.08	0.02

1.3.1   1800MPa grade steel : SAE9254

The 1800MPa grade steel has been used widely in the automotive industry and its chemical composition is based on Si and Cr additions.   Most coil springs for automotive applications are quenched and tempered medium carbon high-strength steels.   The microstructure consists of tempered martensite and precipitates.   By lowering the tempering temperature the strength increases while the reduction of area, i.e. the ratio between the fracture area and the initial sample cross-sectional area, decreases.   As a result the spring formability decreases and the toughness is lowered, causing early failure of springs.

In general, Si retards the conversion of carbide to cementite during tempering.   It is also known that Si refines the carbides and improves the sag resistance significantly.   For spring steels, the research in alloying additions has been focused on increasing the strength while maintaining good ductility, toughness and fatigue properties.   The conventional heat treatment does not exploit the maximum potential of existing steel grades.   For a fixed composition, in order to increase the strength the tempering temperature should be decreased, but with a potential the ductility will be reduced.   However, the loss in ductility is additionally dependent on impurity element concentration.
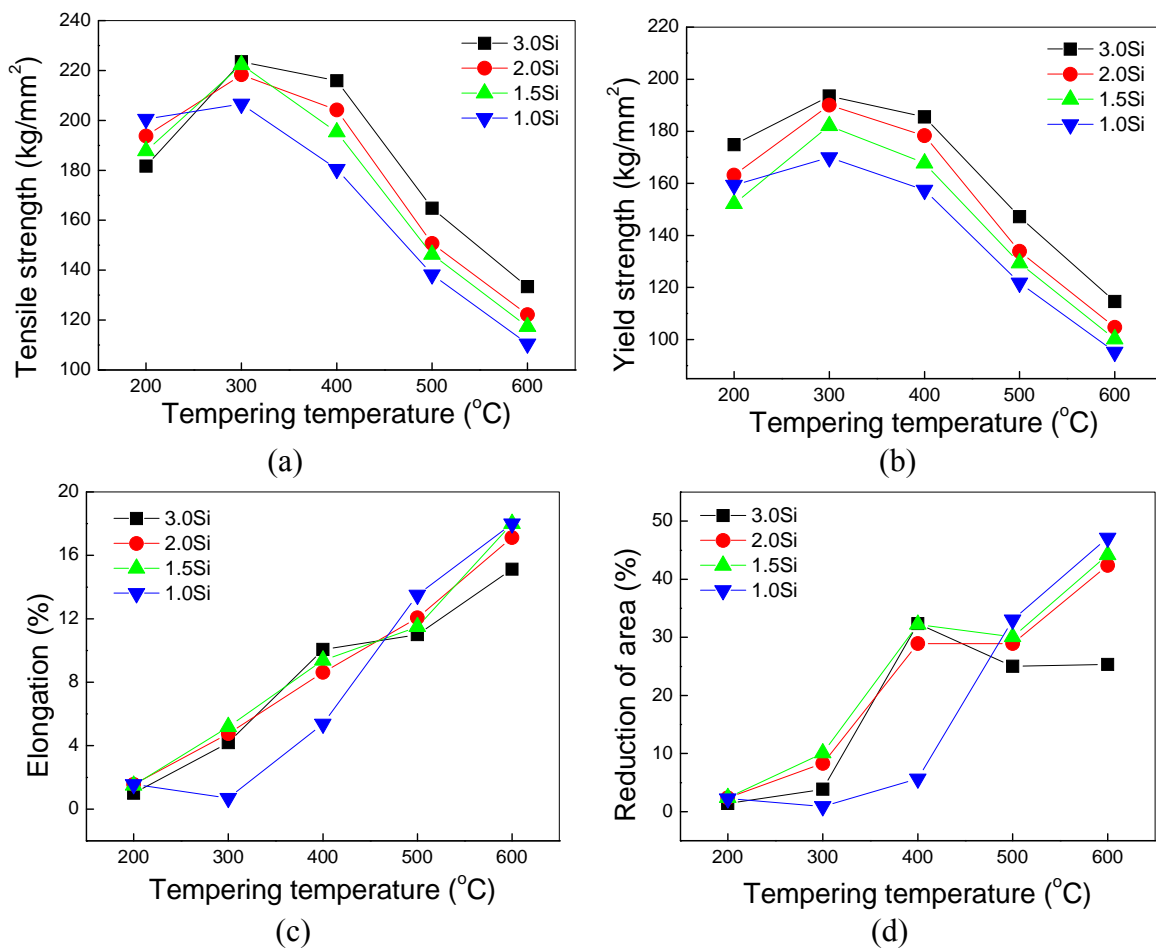
FIGURE 1.7.   Mechanical properties of SAE9254 in proportion to the tempering temperature[17].   (a) Tensile strength (b) Yield strength (c) Elongation (d) Reduction of area.

Fig. 1.7 shows the mechanical properties of SAE9254 for various Si levels. The specimens were heated at 950 °C for 30 min and subsequently quenched in oil.   Then, the alloy was tempered in the range of 200 ~ 600 °C for 30 min and quenched in oil.   The yield strength and tensile strength showed a peak value while the strength gradually decreased with further increase with tempering temperature.   The increase in strength (YS, TS) depended on the Si level.   The elongation and the reduction of area increase with the tempering temperature, but in the case of 3.0 % Si decreased at tempering temperature higher than 450 °C.   The change of mechanical property on the contents of carbon is shown in Fig. 1.8.   The yield and tensile strength show a maximum around tempering temperature of 300 °C and decrease with the carbon contents.   The elongation and the reduction of area were increased with the tempering temperature.   The yield strength and tensile strength decrease depending on the carbon content at 200 °C and 300 °C of tempering temperature.   The reduction of area decreases in proportion to the carbon contents and displays a low value up to 0.55 %C at tempering temperatures lower than 300 °C.
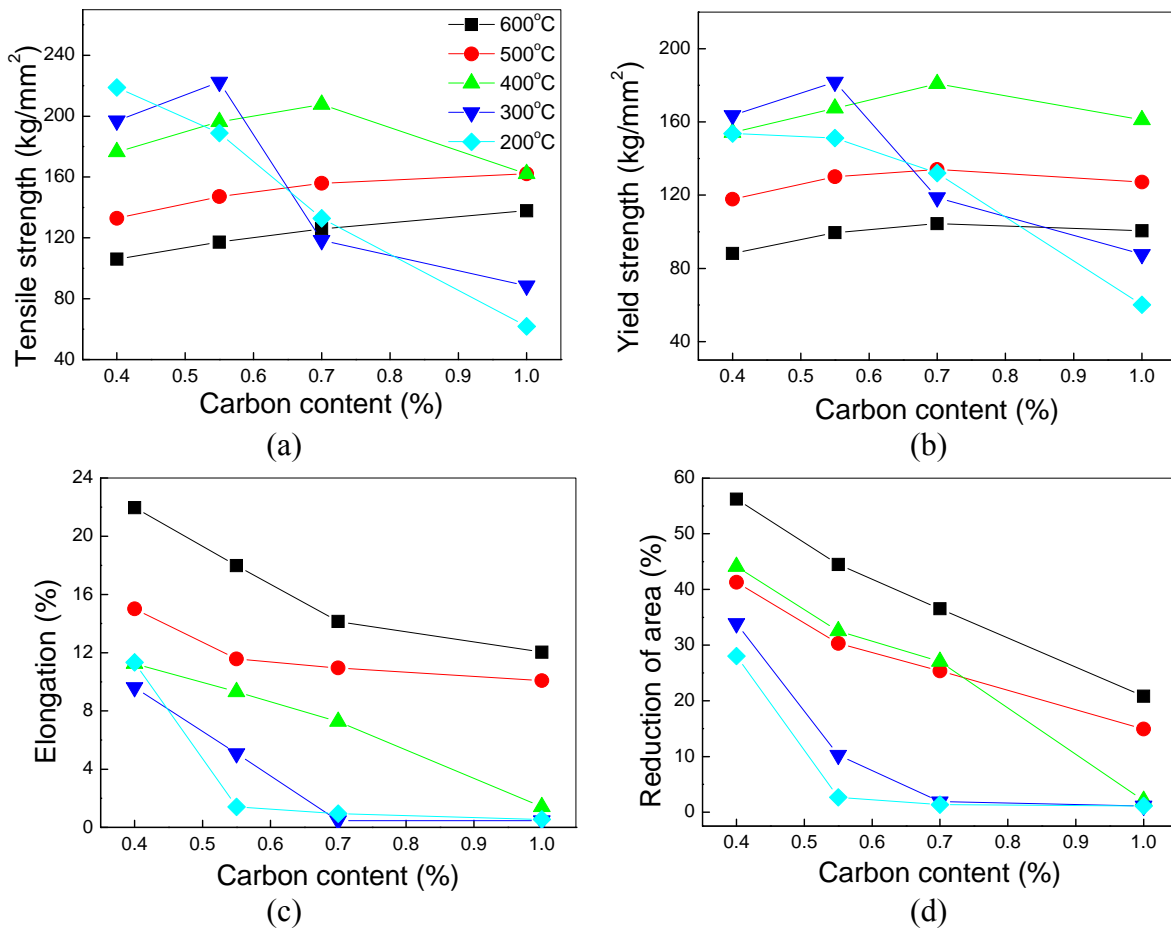
FIGURE 1.8.   Mechanical properties of SAE9254 in proportion to the contents of carbon.[17] (a) Tensile strength   (b) Yield strength   (c) Elongation   (d) Reduction of area (symbol : ■ - 600 °C, ● - 500 °C, ▲ - 400 °C, ▼ - 300 °C, ◆ - 200 °C).

The effects of C and Si on the mechanical property of SAE9254 were reviewed previously. It is stressed that the reduction of area is mainly affected by the carbon content.   Based on these results, the chemical composition and the condition of heat treatment of SAE9254 were

modified.   Table 1.2 shows the mechanical properties of SAE9254 at various tempering temperatures.   The samples were heated at 980 ^{o}C and tempered in the range of 360 ~ 450 ^{o}C.

TABLE 1.2.   Mechanical properties of SAE9254 at various tempering temperatures

Tempering (^{o}C)	UTS(MPa)	RA(%)	El(%)
360	2009	28	5.7
390	1901	32	7.8
420	1832	36	9.8
450	1626	40	10.9
480	1538	41	11.6

1.3.2   Steel grades higher than 2000MPa

In a recent effort to enhance the spring steel performance even further, new alloy grades have been developed whose mechanical properties, especially the tensile strength, are superior to that of the well known SAE9254, 1800 MPa grade.[17]   Kawakami et al. [14] and Furr [15] studied the effects of Si, Cr, Mo, C and V on sag resistance and found that Cr was detrimental to sag resistance, whereas Si, Mo, C and V improved it.   Borik et al. reported that additions of Si and Mo had beneficial effect on sag resistance according to the results from stress relaxation tests.[22]   Tata et al., using static and dynamic tests on prototype springs, showed that Si improved sag resistance with its content up to 2.2%.[23]

TABLE 1.3.   Mechanical properties of 2000 MPa grade spring steel

Tempering (^{o}C)	UTS (MPa)	Reduction of area (%)	Elongation (%)
380	2019	40.2	8.4
400	1949	41.0	9.5
420	1798	42.9	10.6
440	1713	44.4	11.6

Table 1.3. shows the mechanical properties of 2000 MPa grade as a function of tempering temperature.   The specimen was heated at 980 ^{o}C for 3 min and subsequently quenched in oil.   The optimum combination of properties was achieved by tempering at 400 ^{o}C.   The resulting microstructure was tempered martensitic structure with precipitates.[16]   Fig. 1.8 shows the precipitates such as AlN, TiC, VC present in the martensitic matrix.

1.4   Processing of suspension spring

1.4.1   Manufacturing process of wire rods

In this section, the manufacturing process of wire rod is briefly introduced.   Wire rods for high strength spring applications not requiring surface grinding are made by increasing steel cleanliness through nonmetallic inclusion morphology control, and by P and S content reduction in the steelmaking process.   Moreover, steel quality is improved by homogenization in the bloom continuous casting process, by assuring desired surface and internal quality in the billet conditioning process and by preventing surface flaws and

decarburization in the rolling process.
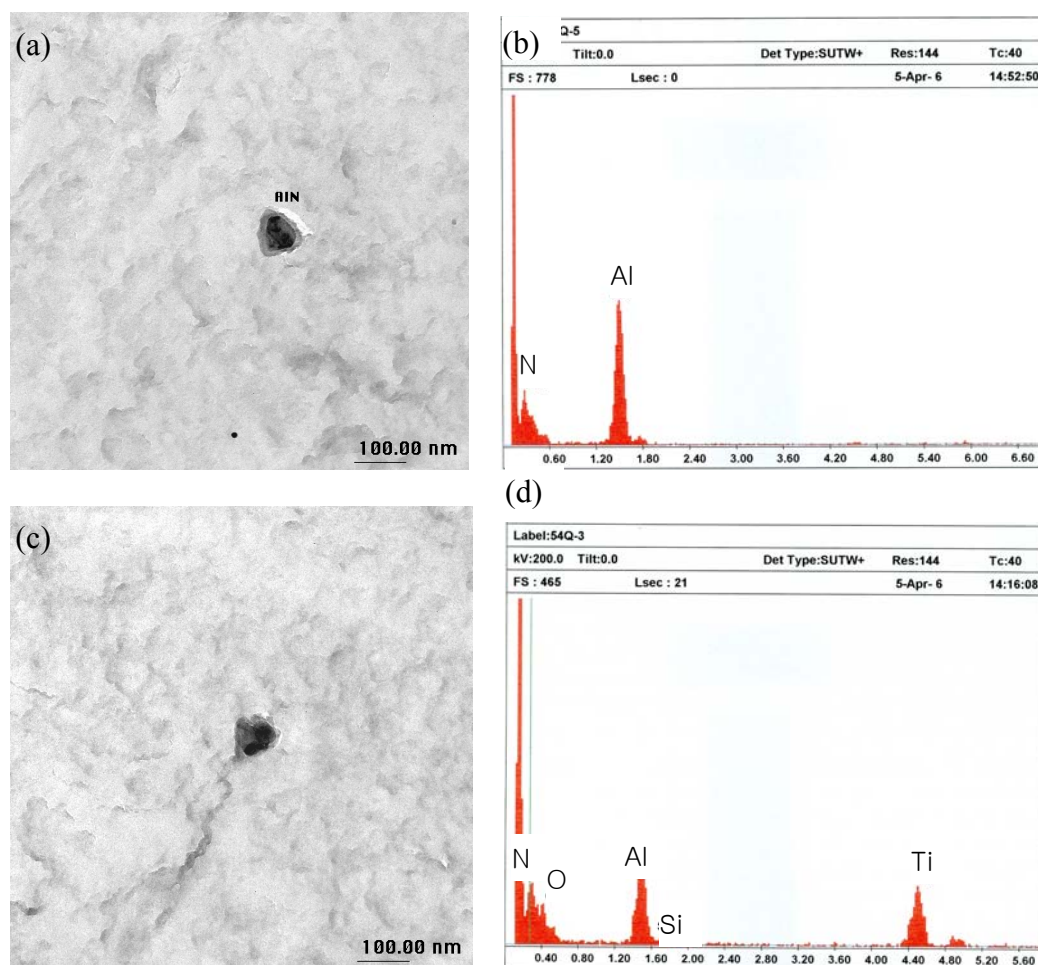
FIGURE 1.8.   TEM image and EDAX analysis of extraction replicas of 2000 MPa grade spring steel: AlN (a) Image and (b) EDAX, and unidentified precipitate (c) Image and (d) EDAX

A typical manufacturing process for alloy steel wire rods for suspension springs is shown in Fig. 1.9.   Various methods are adopted for the ladle refining of rod steel for suspension springs.   The RH vacuum degasser is employed by POSCO for economic degassing and flotation and separation of nonmetallic inclusions.   Especially if high strength is required, such a method is also effective for controlling the composition of nonmetallic inclusions, rendering them harmless without significantly reducing the oxygen content of the steel.

This type of spring steel was formerly fabricated by the ingot casting process.   The recent establishment of techniques for decreasing the amount of nonmetallic inclusions (prevention of reoxidation, flotation and separation of nonmetallic inclusions) and for preventing segregation (low-superheat casting, electromagnetic stirring, etc) in the continuous casting process has made it possible to produce blooms of quality equal to that of the bottom to middle of ingots.   As a result, spring steel wire rods with a minimum fluctuation in properties and with a high reliability are now produced from continuously cast blooms. Besides the reduction of nonmetallic inclusions in the steelmaking stages, ultrasonic

inspection for nonmetallic inclusions in billets is made in both the cross-section (center and subsurface) and longitudinal section.   Billets are also inspected for surface defects by magnetic particle testing.   Surface defects thus detected are removed by grinding.
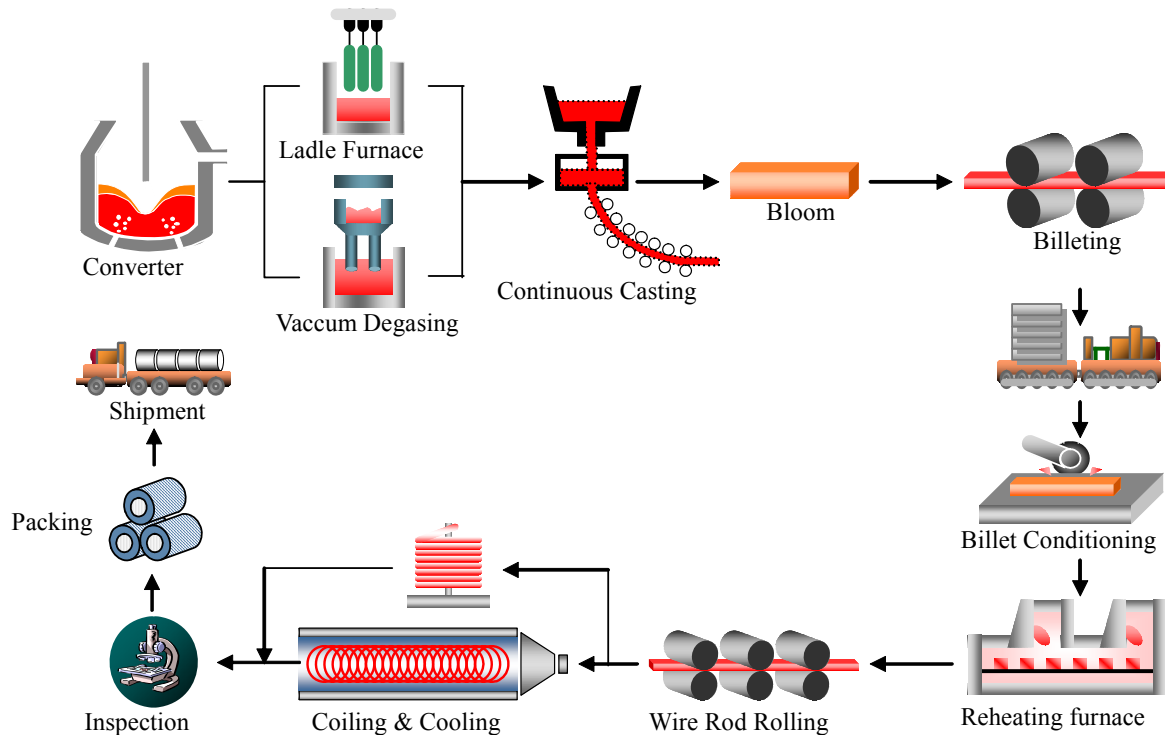
FIGURE 1.9.   Schematic diagram of manufacturing process of the wire rods

Billets are reheated in a furnace and the heating temperature and residence time are controlled to prevent decarburization.   Billets are rolled at a single-strand, non-twist mill consisting entirely of vertical-horizontal roll stands which ensure a minimum of surface defects and are inspected for surface defects using a hot eddy-current detector. Decarburization is also prevented by controlling the cooling rate of coiled rods.   Generally, this type of spring steel does not always have good drawability in the as-rolled condition. Wire rods are softened or surface lubricated before they are shipped.   Softening of small diameter wire rod is accomplished by in-line softening treatment as well as by low temperature annealing.   Wire rods are packaged so as to prevent surface defects and rust during transportation.

1.4.2 *Manufacturing process of suspension coil spring*

A schematic representation of the manufacturing process of suspension coil springs is shown in Fig. 1.10.   The process begins at the bar preparation stage, where large reels of steel are peeled into bars on a peeling machine.   The main benefit of the peeling operation is that all potentially harmful defects, such as decarburization, seams and abrasion marks are eliminated by the removal of the surface layer of the steel.   In addition, the peeling operation allows a variable diameter bar to be produced.   Such operation not only reduces the spring weight by limiting the placement a full diameter section to most stressed sections.

W/R	peeling	Inspect	Heating	Hot form (Spring)	Oil Q.

Spring	Surface treat.	Presetting	Tempering
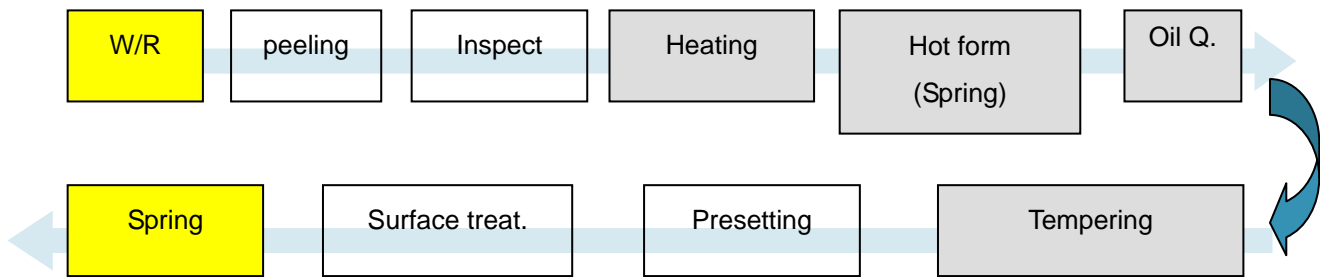
FIGURE 1.10.   Schematic diagram of the manufacturing process of hot-formed suspension spring (*Oil Q.: Oil Quenching)

In order to achieve the proper temperature profiles and heating rates for various grades of microalloyed spring steels, the heat treatment operation process must be performed in specialized furnaces.   The furnace operation must be carefully set-up and closely monitored so that the finished springs display the desired metallurgical properties.   Spring makers have invested a great amount of time and money to conduct in-depth research on the heat treatment of microalloyed spring steel grades.   Based on the results of this work, precise heat treatment parameters have been established for the different steel grades.   Shot peening is another critical step in the manufacturing process that significantly affects the ultimate life of the spring.   Spring makers have developed the shot peening operation for high-stress springs in order to achieve higher levels of compressive residual stress in the finished parts.

In addition to higher operating stresses, there are certain increased risks associated with the more aggressively designed coil springs.   Because the micro-alloyed spring steels are generally produced at higher hardness levels, the coil springs made from this material are more susceptible to notch-type failures, such as those created by corrosion pitting.   For this reason, it is very important that the high-stress coil springs be protected from corrosion. Most high-stress coil spring designs will specify a dual-coat paint system, with an electrocoat base (e-coat) for corrosion protection.   In addition to a tough, plastic powder top coat that protects from stone chipping.   Once the integrity of the paint's barrier is compromised, corrosion will begin, and before long, a corrosion pit begins to form.   The amount of time needed for a spring to break due to the corrosion pit depends on the rate of growth of the pit. That, in turn, is influenced by the severity of the environment in which the spring operates. Obviously, a corrosion pit grows more quickly in the winter climate regions (where salt is used on the road in the winter), than it does in the southern areas.

1.5   Need for developing a new suspension spring steel

In recent years, there has been an increasing demands for light weight suspension springs reflecting a trend for light weight automobiles.   As an attempt to satisfy such demands, it is desired to design springs with an increased tensile stress specification.   However, if presently available spring steels are used under a high stress conditions, problems related to durability and sagging will exist; consequently, the length of the springs will be lowered and accordingly, the height of the vehicle will be decreased leading to serious safety problems.

The strengthening of the spring steel would be improved by 1) controlling the alloy

elements and 2) changing the processing conditions of the spring manufacturing.   Fig. 1.11 shows the basic trends strengthening the spring steel by using alloy elements.[16]   As shown in Fig. 1.11, the fatigue properties can be improved by the decrease of the crack sensitivity and the sag resistance is improved by the high strengthening and dislocation pinning.   The formation of precipitate dispersions improving the sag resistance takes place during tempering shown in Fig. 1.12.   In general, V precipitate forms at temperatures exceeding 500 $^{\circ}$C and then it is important to form the V precipitates within the temperature range 300 ~ 500 $^{\circ}$C.[18] Cr is good for the decarburization and hardenability, but harmful for sag resistance due to the promotion of cementite precipitation.   When Mo is added, Cr promotes the precipitation of M_2C early and might be added at levels in excess of 0.8%.
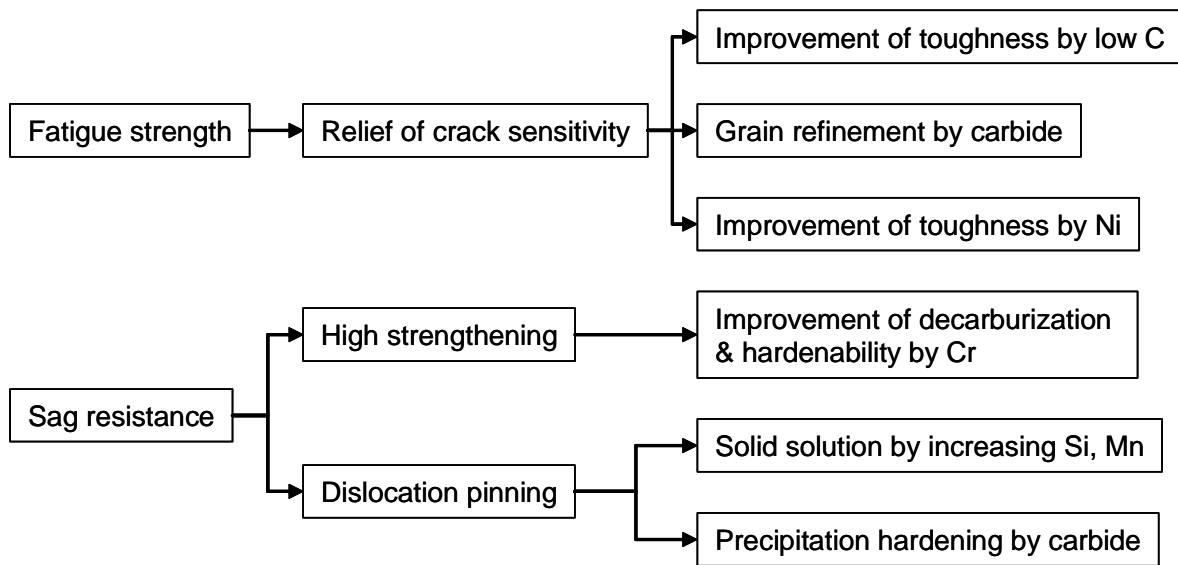
FIGURE 1.11.   Methods for strengthening of spring steel by adding the alloy elements
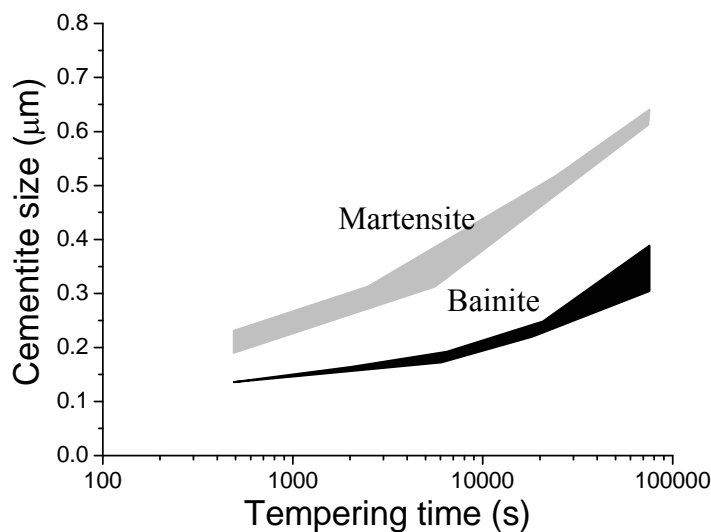
FIGURE 1.12.   Size of cementite precipitated in martensite and bainite during tempering

In recent studies, the effect of B on strengthening of high carbon spring steel was reported to increase the strength without significantly diminishing the reduction of area and keeping the other spring properties.   Table 1.4 shows the mechanical properties resulting from B additions in 2000MPa grades tempered at 400 ^{o}C.   Based on the B effects on tempering, it can be used to increase the strength of spring.

TABLE 1.4.   Mechanical properties of boron added steel on the tempering temperature[16]

B (ppm)	TS (MPa)	RA(%)	El. (%)
-	1950	41	9.5
20	2107	39	7.5
50	2126	27	7.6
100	2097	35	8.4

Another method for spring steel strengthening is the use of multiphase mixtures such as martensite and bainite.   The precipitation kinetics taking place in martensite and bainite quantitatively and qualitatively differs.   ε-carbide precipitates first and is then converted to the stable phase cementite during tempering.   The lower the transformation temperature, the larger the amount of ε-carbide remains untransformed.   By decreasing the transformation temperature, the supersaturated carbon in bainite lath needs more time to diffuse to austenite accelerating the formation of ε-carbide.   The size of cementite in martensite and bainite during tempering displays different trends.   As shown in Fig. 1.12, for medium carbon steel the carbides in tempered martensite nucleate and grow at the lath boundaries whereas those formed in bainite appear.[18]   It should be noted that the carbide in bainite is more stable that that in tempered martensite.

In the case of thick coil spring or a thick torsion bar having a diameter of at least 20 mm, it is difficult to harden the material at the centre of the cross-section.   Such portion tends to be composed of bainite or ferrite/pearlite regions which possess a lower hardness than martensite, and showing an inferior sag-registance.   Thus, it is desired to provide a steel for springs, which, even in a form of a thick coil spring and/or a thick torsion bar, is capable of forming a martensite structure extending to its centre by the heat treatment.

1.6   Aim of the research

Although spring steels have reached excellent combinations of properties a further development based on a microstructural design is needed.   It is essential for achieving the target mechanical properties by controlling the alloy composition and finding appropriate heat treatments routes to optimize the desired multiphase structures.   To this aim we developed a new method to desire the phase transformation during cooling from the austenitic state.   This model takes into account the austenite – ferrite, austenite - pearlite reactions and their interaction.   The purpose of Chapter 2 is to describe a method for quantitatively relating the dilatation curves to the phase transformation kinetics during the cooling of spring steels.   If the volume fractions of phases can be quantitatively related to the dilatation data, the dilatometric technique may be efficiently applicable to the investigation of the phase

transformation kinetics.   The model for estimating the phase transformation information from the dilatation curve is proposed in Chapter 2.

A significant step in thermo-mechanical processing of steels is reaustenitization.   Since reaustenitization usually affects the grain size distribution and alloying element concentration homogeneity, the prior austenite microstructure has a great impact on the kinetics of further phase transformations, and in turn on the mechanical properties of components in subsequent cooling processes, such as quenching, normalizing and annealing.   Since dilatometric analysis is a technique very often employed to study the phase transformation kinetics during heating, the relative change in length which occurs during austenite formation has been studied as a function of temperature.   This lever-rule technique is not capable of describing concurrent phase transformations.   The experimental observations of reaustenitization kinetics and morphology developments are difficult because austenite formed during heating is subsequently destroyed due to the transformation during cooling.   The purpose of Chapter 3 is to describe the new method to track microstructure evolution during heating.

In order to improve fatigue strength and sag resistance, new spring steel with high strength and reduction of area needs to be developed.   For spring steels, the emphasis in materials research has been focused on increasing the strength while maintaining good ductility, toughness and fatigue properties.   The purpose of Chapter 4 is to design the spring steel with the tensile strength 2350 MPa and reduction of area more than 25 % for the desired strength 1400 MPa grade spring.   The aim of Chapter 5 is to analyze the microstructure change with conditions of austenitization and tempering.   In order to improve the optimum level of tensile strength the strengthening mechanisms are studied by using TEM and SEM.

Chapter 6 describes some of the interrelated chemical and microstructural causes associated with the decrease in reduction of area and embrittlement phenomena in carbon and low alloy steels and relates these causes to characteristic cleavage, or intergranular fracture surfaces. Embrittlement implies a processed microstructural condition that creates lower toughness than expected for steel.   For example, a generally valid rule for coupling mechanical properties and toughness states that the lower the hardness and strength, the higher are the ductility and toughness of a microstructure.   However, embrittlement phenomena are exceptions to this rule, and tempered martensite embrittlement, for example, lowers ductility and toughness as, hardness decreases within a certain range of tempering temperatures.   Embrittlement fracture is thus one of the largest factors obstructing the further strengthening of steels.   Therefore, it is the aim of the Chapter 6 to probe the decrease in reduction of area and embrittlement phenomena with respect to the microstructural evolution during heat treatment.   The aim of Chapter 7 is to describe the new route of tempering treatment in order to improve the tensile strength and reduction of area.   This method is called as step tempering which accelerates the fine precipitates with suppressing the decrease of reduction of area.   In order to improve the mechanical properties, the new tempering treatment was developed and consisted of two step tempering processes.   Conventional tempering is under one temperature, but step tempering is stepwise process under two temperatures.   The step tempering process was applied to improve the mechanical properties of the proposed steels.   The microstructure and mechanical property was investigated with changing the conditions of step tempering.

In addition, in order to improve the fatigue life of spring, it is necessary to suppress the surface decarburization.   Decarburization induces the formation of ferrite and reduces the fatigue life.   Surface decarburization in the process of spring steel production often leads to

deteriorated mechanical behavior of the finished components in service.   The metallurgical processes are complex and influenced by many factors, such as temperature, atmosphere, α/γ transformation, morphology of the surface, alloy composition and many more.   To understand the mutual interaction between oxidation and decarburization, computer simulation can be very helpful and assist in interpretation of complex and sometimes counter-intuitive results.   Simulation is often cheaper and faster than experimental investigation, and in many cases, can provide not only trends but also quantitative information on the material behavior under laboratory as well as industrial condition.   The objective of Chapter 8 is to depict a predictive model of the decarburization-oxidation process during reheating and cooling for high silicon spring steel in ambient atmosphere and to identify the influence of thermal cycles on the decarburization behavior.   Furthermore, the accuracy of the simulation result was confirmed experimentally.

Finally, a summary of the thesis is presented.

2
Modeling transformation kinetics from the dilatation curves during cooling

The purpose of this chapter is to describe a method for quantitatively relating the dilatation curves to the phase transformation kinetics during the cooling of spring steels. If the volume fractions of phases can be quantitatively related to the dilatation data, the dilatometric technique may be efficiently applied to the investigation of the phase transformation kinetics. In the present work, a model for extracting such information from the dilatation curve for steels is presented. The volume fraction of the phases was calculated from the dilatation curve by using the linear thermal expansion coefficients, the lattice parameters and the phase compositions under the thermodynamic condition. The proposed model is based on the carbon enrichment of the austenite and the difference in unit volume of phases during the phase transformation. The model is applied to the determination of the phase transformation kinetics from the dilatation curves and verified by comparing the model results to the experimental results of the steels.

2.1 Combining thermochemical databases with dilatation cooling kinetics

Since the crystal structure and lattice dimensions of low alloyed and engineering steels changes with temperature due to phase transformations, these steels display a significant volume change at relevant temperatures during heating and cooling. The variation in the unit volume is revealed as a departure from the behavior of the thermal expansion or

contraction at the temperature at which the transformation occurs. This behavior can be detected via the length change of a sample, and a dilatometer is commonly used to record the length change during cooling as it allows accurate measurements as well as a wide range of cooling rates relevant to industrial steel making processes. In interpreting the dilatation curve, it is assumed that the length change observed is proportional to the volume fraction of the transformation.

In general, the so-called lever rule, i.e., the fraction material transformed is proportional to the thermal expansion corrected length change during the phase transformation, is used to obtain information on the phase transformations from the dilatation curve with temperature. The lever rule can be, however, only applicable in the case of the dilatation experiment which involves a single and non-partitioning phase transformation.[24,25] In the case of the hypoeutectoid steels, this method is not directly applicable for two reasons. Firstly, the carbon redistributes between the proeutectoid ferrite and the remaining austenite during cooling, which increases the unit volume of the remaining austenite. Secondly, the formation of pearlite has a distinctly different volume change compared with that of proeutectoid ferrite. This invalidates a simple interpretation of the dilatometric data in the investigation of the phase transformation kinetics. The dilatometric technique can be efficiently applied to the investigation of the phase transformation kinetics if the relation between the volume fractions of phases, the temperature, the compositions of phases and their dilatation is taken into account, explicitly.

Many investigations have reported procedures to extract correct information from the dilatation curves of hypoeutectoid steels. Takahasi *et al.* [24] and Onink *et al.* [25] analyzed the dilatation data during an isothermal transformation. Qiu *et al.* [26] and Garcia de Andres *et al.* [27] provided a model that could calculate the dilatation during the heating of steels. Kop *et al.* [28] presented a model for the cooling for the hypoeutectoid steels. Zhao *et al.* [29] analyzed the dilatation curve by using the density function of the phases.

In the present work, a new model for extracting the information on the proeutectoid ferrite and the pearlite transformation from the dilatation curve for the hypoeutectoid steels is presented. The volume fraction of phases during the phase transformation is calculated using the dilatation data, coefficients of thermal contraction, lattice parameters of phases and the chemical compositions of phases under (para-)equilibrium [30,31] conditions. This model is essentially based on the carbon enrichment of the austenite and the difference in unit volume of the phases. In addition, a self-calibration technique to obtain more exactly the lattice parameter variation of the phases with temperature from the dilatation curve is proposed. The presented technique not only helps to correct the experimental uncertainties, but also enables the model to be used in situations where accurate property data are not available.

The model was verified by comparing its results to experimental observations which involved the proeutectoid ferrite and the pearlite transformed from austenite.   The model was successfully applied to extract the proeutectoid ferrite and the pearlite transformation kinetics from the dilatation curves for hypoeutectoid steels.

2.1.1   *Physical and mathematical model*

It is assumed that the expansion/contraction of a sample for the analysis of the dilatation

curve is isotropic and plastic deformation to accommodate local strains due to the transformation does not occur. For small volume changes the relative length change (ε) of a sample is related to the relative volume change as follows.[24,27,28]

$$\varepsilon = \frac{\Delta L}{L_o} = \frac{L - L_o}{L_o} = \frac{V - V_o}{3 \cdot V_o} = \frac{\Delta V}{3 \cdot V_o} \tag{1}$$

where L is the length of a sample at any temperature and L_o is the initial length at room temperature having the initial content of alloy elements. ΔV and V_o are the unit volume change and the initial unit volume, respectively.

2.1.1.1 Length of a sample during cooling

Samples of a hypoeutectoid steel cooled from the austenite region will necessarily cross the austenite/ferrite two-phase region. During cooling below A$_3$ temperature, initially the austenite transforms into proeutectoid ferrite. Upon further cooling to below the A1 temperature the austenite decomposes into proeutectoid ferrite and pearlite. Taking into account the fact that the diffusion coefficients for substitutional alloying elements are several orders of magnitude smaller than those for carbon, the redistribution of substitutional soluble elements between phases during the phase transformation can be neglected.[28,29] Hence, the length of a sample at any temperature is assumed to be dependent on the temperature and the carbon contents only. The total length of the sample in the austenite region at the temperature, T_1, can be expressed as

$$L(T_1) = L_\gamma(T_1, C_o) \tag{2}$$

where L_γ is the length of the austenite at temperature, T_1, having an initial carbon content C_o. It is noted that the length of a sample in the austenite region is changed only by variation in temperature.

The transformation of proeutectoid ferrite and pearlite from austenite is assumed to take place in two separate temperature regions, as is expected from the phase diagram. The dilatation curve of a sample is thus analyzed in two steps. When the proeutectoid ferrite initially forms from the austenite, there is no pearlite. The length of the sample consists of contributions from the contributions of the austenite and the proeutectoid ferrite. The transformation of proeutectoid ferrite from the austenite is assumed to be governed by the diffusion of solute carbon in the austenite. During the phase transformation the remaining austenite will enrich in carbon, C_γ. It is generally accepted that the carbon enrichment in the remaining austenite starts at the transformation interface during the phase transformation. This may lead to a carbon concentration profile across the austenite grain. However, Zhao *et al.* [29] reported that for analyzing the relative length change of a sample due to the phase transformation, it is permitted to use the average concentration of carbon in the austenite instead of calculating the carbon concentration profile across the grain. Both the formation of proeutectoid ferrite and the carbon enrichment of austenite cause an expansion of the sample. The total length of a sample at a transforming temperature, T_2 during the proeutectoid ferrite formation is a function of length changes due to the austenite and the proeutectoid ferrite.

$$L(T_2) = f_\gamma(T_2)L_\gamma(T_2, C_\gamma) + (1 - f_\gamma(T_2))L_\alpha(T_2, C_\alpha) \tag{3}$$

where $f_\gamma(T_2)$ is the volume fraction of the remaining austenite and $(1 - f_\gamma(T_2))$ is the volume fraction of the proeutectoid ferrite transformed from the austenite.

In the second part of the transformation only pearlite is assumed to form.   This means that the volume fraction of the proeutectoid ferrite is constant.   As no further carbon enrichment in the austenite occurs, the volume fraction of the remaining austenite is therefore only temperature dependent.   The remaining austenite decomposes continuously into pearlite, a mixture of eutectoid ferrite and eutectoid cementite of concentrations $C_{p\alpha}$ and $C_{p\theta}$, respectively.   The total length of the sample during the pearlite transformation at a transforming temperature, T_3, consists of the concentrations of the remaining austenite, the proeutectoid ferrite and the pearlite.

$$L(T_3) = (1 - f_\gamma(T_3))L_\alpha(T_3, C_\alpha) + (f_\gamma(T_3) - f_p(T_3))L_\gamma(T_3, C_\gamma) + f_p(T_3)L_p(T_3, C_\gamma) \tag{4}$$

where $f_\gamma(T_3)$ is the volume fraction of the austenite which remains after the completion of proeutectoid ferrite transformation, $(1-f_\gamma(T_3))$ is the volume fraction of the proeutectoid ferrite, and $f_p(T_3)$ is the volume fraction of the pearlite.   The volume fraction of proeutectoid ferrite found from the analysis of the high-temperature part of the dilatation curve determines both the carbon content of the austenite during the pearlite transformation and the ratio of the cementite and the ferrite in the pearlite. $L_p(T_3, C_\gamma)$ is the effective length of the pearlite and consists of the lengths of the eutectoid ferrite and the eutectoid cementite:

$$L_p(T_3, C_\gamma) = f_{p\alpha}(T_3)L_{p\alpha}(T_3, C_{p\alpha}) + (1 - f_{p\alpha}(T_3))L_{p\theta}(T_3, C_{p\theta}), \tag{5}$$

where $f_{p\alpha}$ is the fraction of eutectoid ferrite and $(1 - f_{p\alpha})$ is the fraction of eutectoid cementite in the transformed pearlite. $L_{p\alpha}$ and $L_{p\theta}$ are the length contributions of the eutectoid ferrite and the eutectoid cementite, respectively.   In order to take into account the undercooling effects during cooling process, in this model the pearlite transformation is assumed to start when the average carbon content of the austenite reaches the A_{cm} line, which is extrapolated to temperatures below the A_1 temperature on the phase diagram [32,33].   The A_{cm} line is the temperature-composition line which gives the chemical composition of austenite in equilibrium with cementite.   The austenite then decomposes into ferrite and cementite at a mass ratio of $f_{p\alpha}$ which is determined by using the phase diagram and carbon conservation during the decomposition.

2.1.1.2   *Relative length change due to the proeutectoid ferrite transformation*

For a given temperature the length change due to the transformation of the proeutectoid ferrite is expressed by subtracting Eq. (2) from Eq. (3),

$$L(T_2) - L(T_1) = (f_\gamma(T_2)L_\gamma(T_2, C_\gamma) + (1 - f_\gamma(T_2))L_\alpha(T_2, C_\alpha)) - L_\gamma(T_1, C_o) \tag{6}$$

Eq. (6) can be rearranged as follows.

$$L(T_2) - L(T_1) = f_\gamma(T_2)\left((L_\gamma(T_2,C_o) - L_\gamma(T_1,C_o)) + (L_\gamma(T_2,C_\gamma) - L_\gamma(T_2,C_o))\right)$$
$$+ (1 - f_\gamma(T_2))(L_\alpha(T_2,C_\alpha) - L_\gamma(T_1,C_o)) \tag{7}$$

Eq. (7) shows that the length change of a sample consists of three terms: the length change of the austenite due to the variation in temperature, $f_\gamma(T_2)((L_\gamma(T_2,C_o) - L_\gamma(T_1,C_o))$, the length change due to the carbon enrichment in the austenite, $f_\gamma(T_2)((L_\gamma(T_2,C_\gamma) - L_\gamma(T_2,C_o))$ and the length change due to the proeutectoid ferrite transformation, $(1 - f_\gamma(T_2))((L_\alpha(T_2,C_\alpha) - L_\gamma(T_1,C_o))$. The carbon content of proeutectoid ferrite is calculated under the equilibrium [30,31] condition by using the Thermo-Calc program. The average carbon content of the austenite (C_γ) is calculated by the carbon conservation relation.

$$C_\gamma = \frac{C_o - f_\alpha C_\alpha}{1 - f_\alpha} = \frac{C_o - (1 - f_\gamma)C_\alpha}{f_\gamma} \tag{8}$$

where C_o is the initial carbon content of the austenite, f_α is the volume fraction of the proeutectoid ferrite and C_α is the carbon content of the proeutectoid ferrite. Since the relative length change (ε) of a sample is related to the relative volume change by Eq. (1), Eq. (7) can be rearranged as follows,

$$\varepsilon(T_2) - \varepsilon(T_1)$$
$$= f_\gamma(T_2)\left(\frac{V_\gamma(T_2,C_o) - V_\gamma(T_1,C_o)}{3V_\gamma(T_1,C_o)}(1 + \varepsilon_\gamma(T_1,C_o)) + \frac{V_\gamma(T_2,C_\gamma) - V_\gamma(T_2,C_o)}{3V_\gamma(T_2,C_o)}(1 + \varepsilon_\gamma(T_2,C_o))\right) \tag{9}$$
$$+ (1 - f_\gamma(T_2))\left(\frac{V_\alpha(T_2,C_\alpha) - V_\gamma(T_1,C_o)}{3V_\gamma(T_1,C_o)}(1 + \varepsilon_\gamma(T_1,C_o))\right)$$

where $\varepsilon(T_2)$ and $\varepsilon(T_1)$ are the relative length changes of a sample measured from the dilatation curve at temperatures T_2 and T_1, and V_i is the unit volume of the phase ($i = \gamma, \alpha$). $\varepsilon_\gamma(T_2,C_o)$ and $\varepsilon_\gamma(T_1,C_o)$ are the relative length changes of the austenite at temperatures, T_2 and T_1, which has the initial contents of carbon (C_o).

To calculate the volume fractions of the existing phases, the relative length changes and the compositions and the unit volume for the phases are needed. The relative length changes and the chemical compositions are easily determined from the dilatation curve and Thermo-Calc program. The unit volume of phases is calculated from the lattice parameters. Therefore, Eq. (9) can be used for all dilatation curves where austenite decomposes into a mixture of the carbon-enriched remaining austenite and the proeutectoid ferrite.

2.1.1.3   Relative length change due to the pearlite transformation

For a given temperature the length change of a sample due to the pearlite transformation is expressed by subtracting Eq. (2) from Eq. (4),

$$L(T_3) - L(T_1)$$
$$= \left((1 - f_\gamma(T_3))L_\alpha(T_3,C_\alpha) + (f_\gamma(T_3) - f_p(T_3))L_\gamma(T_3,C_\gamma) + f_p(T_3)L_p(T_3,C_\gamma)\right) - L_\gamma(T_1,C_o) \tag{10}$$

Similar to the proeutectoid ferrite transformation, we can rearrange Eq. (10) as follows,

$$
\begin{aligned}
&\varepsilon(T_3) - \varepsilon(T_1) \\
&= \left(1 - f_\gamma(T_3)\right) \frac{V_\alpha(T_3, C_\alpha) - V_\gamma(T_1, C_o)}{3V_\gamma(T_1, C_o)} \left(1 + \varepsilon_\gamma(T_1, C_o)\right) \\
&+ \left(f_\gamma(T_3) - f_p(T_3)\right) \left(\frac{V_\gamma(T_3, C_o) - V_\gamma(T_1, C_o)}{3V_\gamma(T_1, C_o)} \left(1 + \varepsilon_\gamma(T_1, C_o)\right) + \frac{V_\gamma(T_3, C_\gamma) - V_\gamma(T_3, C_o)}{3V_\gamma(T_3, C_o)} \left(1 + \varepsilon_\gamma(T_3, C_o)\right) \right) \quad (11) \\
&+ f_p(T_3) \left(f_{p\alpha}(T_3) \frac{V_{p\alpha}(T_3, C_{p\alpha}) - V_\gamma(T_1, C_o)}{3V_\gamma(T_1, C_o)} + \left(1 - f_{p\alpha}(T_3)\right) \frac{V_{p\theta}(T_3, C_{p\theta}) - V_\gamma(T_1, C_o)}{3V_\gamma(T_1, C_o)} \right) \left(1 + \varepsilon_\gamma(T_1, C_o)\right)
\end{aligned}
$$

In using Eq. (11), the volume fraction of the existing phases at a given temperature during the pearlite transformation is calculated from the unit volume, the composition of the phases and the relative length change of a sample. The key for the calculation is the determination of the unit volume of the phases. In the next section, the method calculating the unit volume of the phases during the phase transformation is introduced.

2.1.2   Algorithm

In this section, the algorithm for calculating the phase transformation kinetics from dilatation data is described (see Fig. 2.1).   The dilatation data and chemical composition of the steel are used as input parameters.   The linear thermal expansion coefficients are calculated from the temperature dependent length over the temperature regime during which no transformation takes place and the region of phase transformation was determined as the region in which dilatation described from the linearly extrapolated volume from the non-transformation region.

The carbon content in ferrite is calculated by Thermo-Calc program and that in austenite calculated by the carbon conservation relation.   Once the proeutectoid transformation is completed, the remaining austenite transforms to pearlite.   The final phases are consisted of ferrite and pearlite.   The carbon contents in ferrite and pearlite are calculated by Thermo-Calc program.   Fig. 2.2 shows that the carbon content in austenite increases during transformation and the pearlite forms from austenite when the average carbon content in austenite meets the Acm line.   After the phase transformation is completed, the lattice parameter of ferrite is calculated by self calibration method.   Based on the calculated lattice parameter of ferrite, the fraction of transformed phases is recalculated.   Finally, the output data consists of the phase fraction and the carbon content in these phases.

2.2   Unit volume and lattice parameter of phases

The lattice structures of austenite and ferrite are face centered cubic (FCC) and body centered cubic (BCC) respectively; cementite has an orthorhombic crystal structure.   The unit volume of austenite and ferrite are equal to $(a_\gamma)^3/4$ and $(a_\alpha)^3/2$, respectively, where a_γ and a_α are their lattice parameters.   The unit volume of the cementite is given by $(a_\theta)\cdot(b_\theta)\cdot(c_\theta)/12$, where a_θ, b_θ, c_θ are its lattice parameters.   The factors of *1/4*, *1/2* and *1/12* are the result of the number of atoms per unit cell.   Many researchers [27-29] reported that if no phase

transformations would occur, the lattice parameter of austenite varies linearly with temperature in the range of 300 ~ 1200°C.   Based on the work of Garcia de Andres *et al.*[27], the
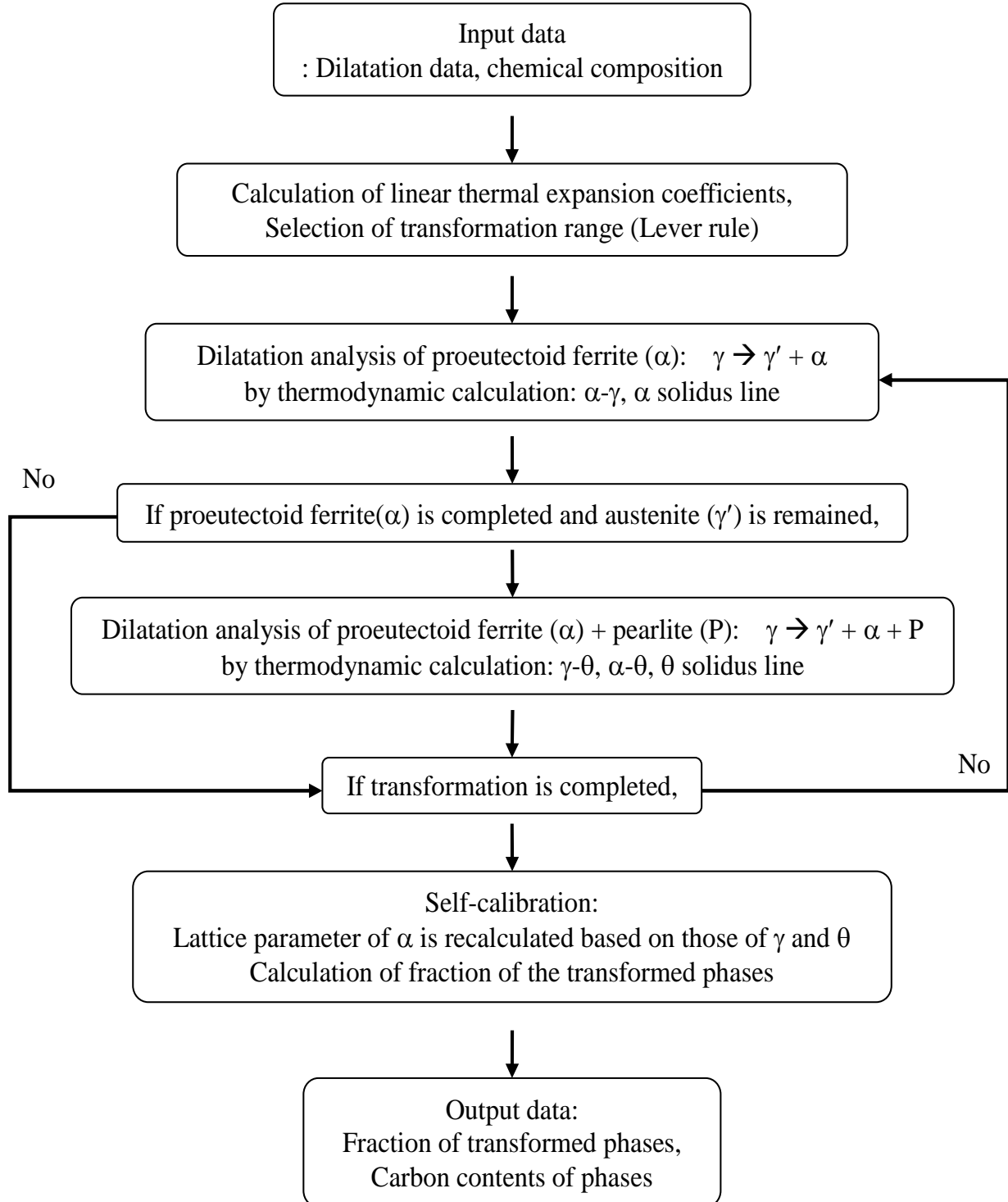
FIGURE 2.1.   Flow diagram of calculating the transformation kinetics from the dilatation data
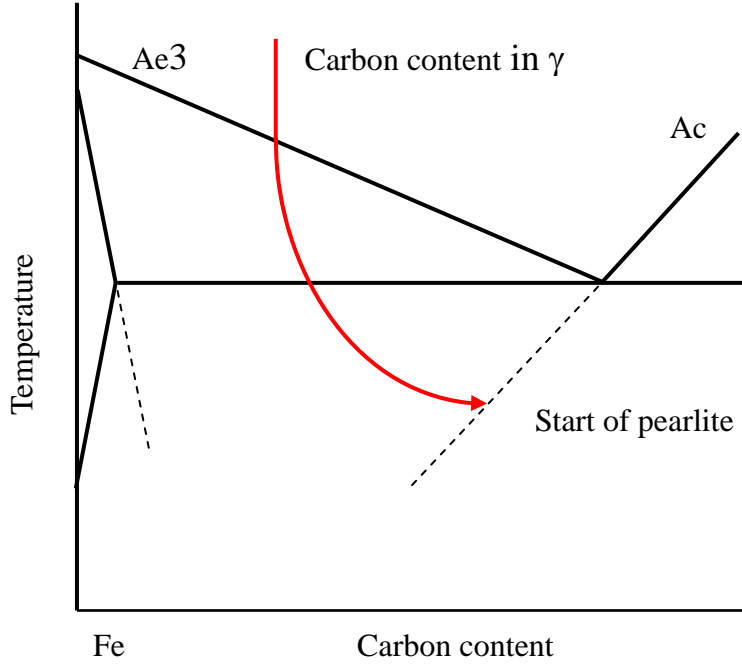
FIGURE 2.2. Transition of the transformation from ferrite + austenite to ferrite + pearlite, or bainite on the phase diagram.[32]

temperature dependent lattice parameter of austenite can be expressed as,

$$a_\gamma = a_{\gamma o}\left(1 + \beta_\gamma(T - 300)\right) \tag{12}$$

where $a_{\gamma o}$ is the lattice parameter of austenite at room temperature, β_γ is the linear thermal contraction coefficient of austenite, and T is the temperature in K. The dependence of the lattice parameter of austenite on substitutional alloying elements was as reported by Ridley *et al.* [34] and Dyson and Holmes [35],

$$a_{\gamma 0} = 3.573 + 0.033[C] + 0.00095[Mn] - 0.0002[Ni] + 0.0006[Cr] + 0.0031[Mo] + 0.0018[V] \tag{13}$$

where [i] is the wt % concentration of i = C, Mn, Ni, Cr, Mo and V, and $a_{\gamma o}$ is expressed in Å. The linear thermal contraction coefficient of the austenite is generally assumed to be almost constant, although small differences exist between the thermal contraction coefficients have been reported by different authors [27-29,36]. In the present work the linear thermal contraction coefficient of the austenite is calculated directly from each dilatation curve to compensate for experimental errors. The linear thermal contraction coefficient of the austenite is calculated from the slope ($k = (\partial \varepsilon_\gamma / \partial T)$) of the relative length change (ε_γ) in the austenite region of the dilatation curve, by using the equation:

$$\beta_\gamma = \frac{A^{1/3} - 1}{T_1' - A^{1/3}T_1}, \qquad\qquad \text{in the austenite region} \tag{14}$$

$$A = 1 + \frac{3k(T_1' - T_1)}{1 + \varepsilon_\gamma(T_1)} = 1 + 3\left(\frac{\partial \varepsilon_\gamma}{\partial T}\right)\frac{(T_1' - T_1)}{1 + \varepsilon_\gamma(T_1)} \tag{15}$$

where T_1' and T_1 are two temperatures in the austenite region. For the ferrite and the cementite in binary Fe-C alloys, the lattice parameters are calculated following the work of Kop $et\ al.$ [28].

$$a_\alpha = 2.8863\big(1 + 17.5 \times 10^{-6}(T - 800)\big), \qquad\qquad 800 < T < 1200\ K \qquad (16)$$

$$a_\theta = 4.5234\big(1 + \beta_\theta(T - 300)\big), \qquad\qquad 300 < T < 1000\ K \qquad (17)$$

$$b_\theta = 5.0883\big(1 + \beta_\theta(T - 300)\big), \qquad\qquad 300 < T < 1000\ K \qquad (18)$$

$$c_\theta = 6.7426\big(1 + \beta_\theta(T - 300)\big), \qquad\qquad 300 < T < 1000\ K \qquad (19)$$

$$\beta_\theta = 5.311 \times 10^{-6} - 1.942 \times 10^{-9}T + 9.655 \times 10^{-12}T^2 \qquad\qquad\qquad (20)$$

where β_θ is the linear thermal contraction coefficient of the cementite. a_α at room temperature was taken to be the lattice parameter of pure iron; however, this is affected by the alloying elements in the ferrite.

The lattice parameter of ferrite is affected by the concentration of alloying elements due to their solubility in ferrite. The inclusion of all alloy elements in the lattice parameter of ferrite is determined from the analysis of the dilatation curve. Under the condition of the complete transformation, the lattice parameter is adjusted with calibration factors (slope and ordinate to origin) and taken to be the value that best matches the model and the dilatation experiments.

$$a_\alpha' = (V_\alpha')^{1/3} = S * T + Y \qquad\qquad (21)$$

where

$$S = \frac{\partial V_\alpha'(T_1, C_\alpha)}{\partial T} = \frac{3V_\alpha'(T_1, C_\alpha)}{1 + \varepsilon_\gamma(T_4, C_0)} \cdot \frac{\partial \varepsilon(T_1)}{\partial T},$$

$$Y = V_\alpha'(T_1, C_\alpha) = V_\gamma(T_4, C_0) + \frac{3V_\gamma(T_4, C_0)}{f_\alpha^0(T_1)}\left[\frac{\varepsilon(T_1) - \varepsilon(T_4)}{1 + \varepsilon(T_4)} - f_\theta^0(T_1)\frac{V_\theta(T_1, C_\theta) - V_\gamma(T_4, C_0)}{3V_\gamma(T_4, C_0)}\right]$$

In fact, the lattice parameter of the ferrite constructed was used only for the analysis of the dilatation curve during the phase transformation. This self-calibration method determining the practical values of the lattice parameter of the austenite and the ferrite has the great advantages to correct for the experimental dilatation uncertainties and the approximate parameters.

2.3   Experiments

2.3.1   Experiments for the dilatation analysis during cooling

In order to validate the proposed method, dilatation experiments with Fe-C-Mn-Si steels (Table 2.1) have been performed. The dilatation of a sample with the temperature was measured using a Bähr 805 dilatometer. The sample was a hollow cylinder machined to 10.0 mm length. The outer and inner diameters of the sample were 3.0 and 1.5 mm, respectively. K-type thermocouples were spot welded onto the sample, which was lighty clamped between

quartz push rods.   The length change of the sample was recorded by a Linear Variable Displacement Transducer.   The sample was heated up to 850, 900 and 950 ^{o}C, held at this temperature for 5min and then cooled down at a rate of 1°C/sec.   Two plain carbon steel grades were used, whose compositions are listed in Table 2.1.

TABLE 2.1. Chemical composition of the hypoeutectoid steels. (wt.%)

	C	Mn	Si	Cr
0.26 %C steel	0.26	0.45	0.21	0.018
0.46 %C steel	0.46	0.73	0.22	

2.3.2   Microstructural investigations

   Samples for the metallographic examinations were prepared using standard polishing techniques and were etched using 2 % Nital.   Determination of the fractions of the existing phases was conducted using Quantitative Image Analysis software.

2.4   Results and Discussion

   Fig. 2.6 shows the dilatation curve represented as $\Delta L/L_o$ vs. temperature, for the 0.26 %C and 0.46 %C steels given in Table 2.1.   The steels were heated to the austenitizing temperatures 950, 900 and 850 ^{o}C at a rate of 1 ^{o}C/sec , held at these temperatures for 5min, and then cooled down to room temperature at a rate of 1 ^{o}C/sec.   The results calculated by the proposed model for the dilatation curves of Fig. 2.6 are shown in Fig. 2.7.   As stated above, the volume fractions of the proeutectoid ferrite and the remaining austenite were calculated simultaneously with the carbon enrichment in the remaining austenite by using Eqs. (8) and (9).   The volume fraction of pearlite was then readily found from Eq. (11).   The volume fraction of proeutectoid ferrite found from the analysis of the high-temperature part of the dilatation curve determines both the carbon content of the austenite at the onset and during the pearlite transformation and the ratio of the cementite and the ferrite in the pearlite.   At the end, the volume fraction of the existing phases during the overall phase transformation sequence was calculated in an iterative process using the Newton-Raphson method.

   For the 0.26 %C steel, the volume fraction of the phases and the carbon content in the austenite calculated by the proposed model are presented in Fig. 2.7 (a), (b) and (c).   Fig. 2.7 (a) shows that during cooling from the austenitizing temperature, 950 ^{o}C, the transformation of proeutectoid ferrite began at 783 ^{o}C accompanied by the enrichment of carbon in the remaining austenite.   The pearlite transformation started at 691 ^{o}C when the average carbon content of the remaining austenite was 0.653 %C.   The calculated volume fraction of the proeutectoid ferrite was 62.2 %.   The volume fractions of the proeutectoid ferrite were measured to be 66.0 %.

   Fig. 2.7 (b) and (c) illustrate the calculated results for the dilatation curves (Fig. 2.6 (b) and (c)) of the 0.26 %C steels cooled from the different austenitizing temperatures, 900°C and 850 ^{o}C.   The volume fractions of the proeutectoid ferrite calculated from Fig. 2.6 (b) and (c) were 61.6 % and 63.3 %, respectively.   The volume fractions of the proeutectoid ferrite were measured to be 62.5 % and 63.4 %, respectively.   Measurements of the volume fractions of phases were accomplished using quantitative image analysis software.   It was confirmed (Fig. 2.8) that all austenite was transformed to the proeutectoid ferrite and the pearlite during

continuous cooling. The calculated fractions of proeutectoid ferrite and pearlite coincided with the measured fractions.
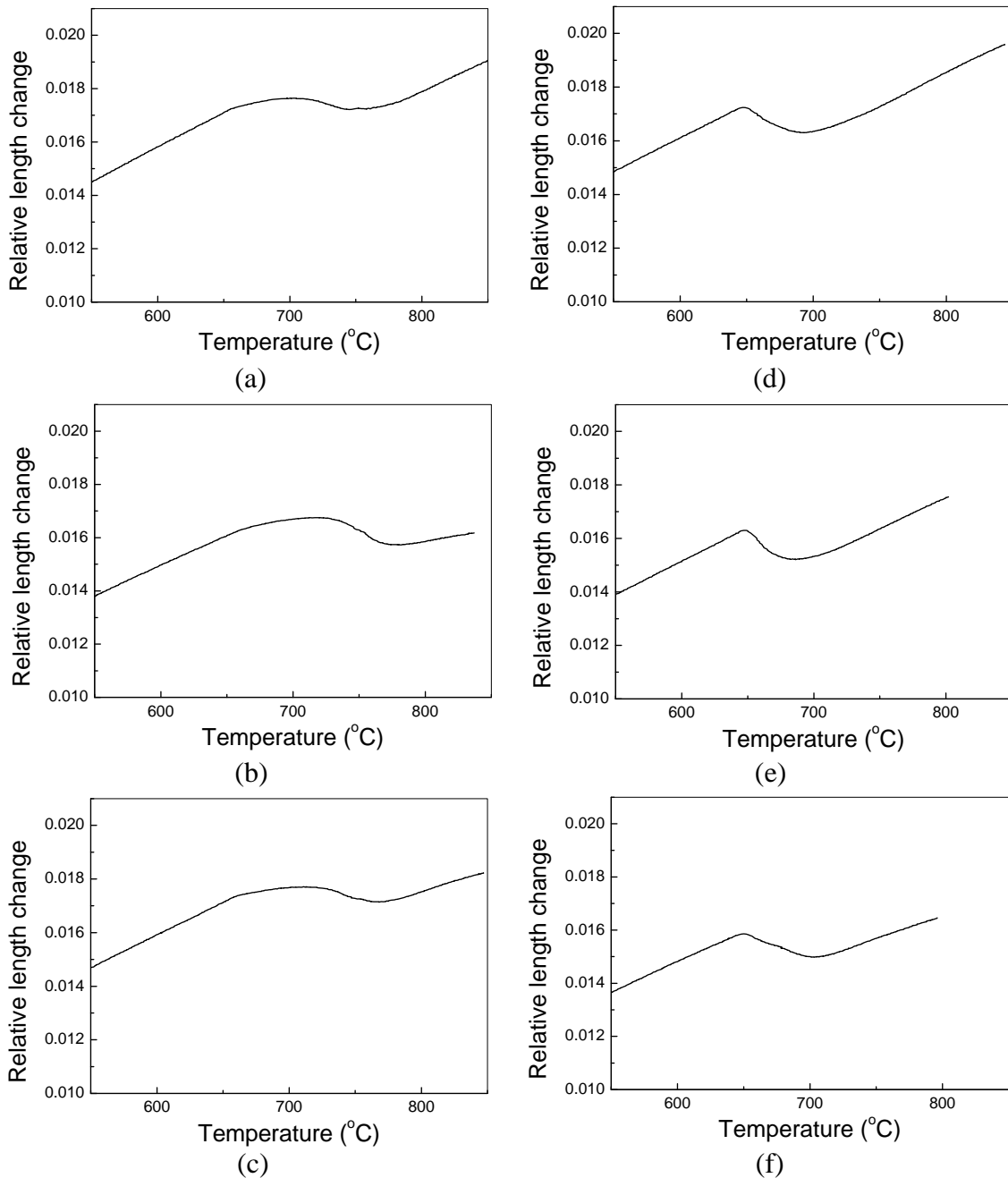
FIGURE 2.6.   Relative length changes of the 0.26 %C and 0.46 %C steels cooled at a rate of 1°C/sec from the different austenitizing temperatures, 950, 900, 850 °C.   0.26 %C steel ; austenitizing temperature (a) 950 °C, (b) 900 °C, (c) 850 °C, 0.46 %C steel ; austenitizing temperature (d) 950 °C, (e) 900 °C, (f) 850 °C

For the dilatation curves of the 0.46 %C steel, the volume fraction of the phases and the carbon content in the austenite calculated by the proposed model are illustrated in Fig. 2.7 (d), (e) and (f).   Fig. 2.7 (d) shows that during cooling from the austenitizing temperature, 950 °C, the proeutectoid ferrite transformation began at 737 °C accompanied by the enrichment of carbon in the remaining austenite.   When the average carbon contents of the remaining

austenite reached at 0.608%, the pearlite transformation started at 674 $^{\circ}$C. The calculated volume fraction of the proeutectoid ferrite was 25.0%. The volume fraction of the proeutectoid ferrite was 23.5 %. The calculated results for the dilatation curves cooled from the different austenitizing temperatures, 900 $^{\circ}$C and 850 $^{\circ}$C were shown in Fig. 2.7 (e) and (f). The volume fractions of the proeutectoid ferrite calculated from Fig. 2.6 (e) and (f) were 24.1 % and 27.6 %. The volume fractions of the proeutectoid ferrite were measured to be 24.4 % and 30.4 %, respectively. The calculated results for the 0.46 %C steels were in good agreement with the metallographic examinations.

FIGURE 2.7.   Volume fractions of phases and carbon concentration of remaining austenite of the 0.26 %C and 0.46 %C steels calculated from Fig. 2.6.   0.26 %C steel ; austenitizing temperature (a) 950 $^{\circ}$C, (b) 900 $^{\circ}$C, (c) 850 $^{\circ}$C, 0.46 %C steel ; austenitizing temperature (d) 950 $^{\circ}$C, (e) 900 $^{\circ}$C, (f) 850 $^{\circ}$C
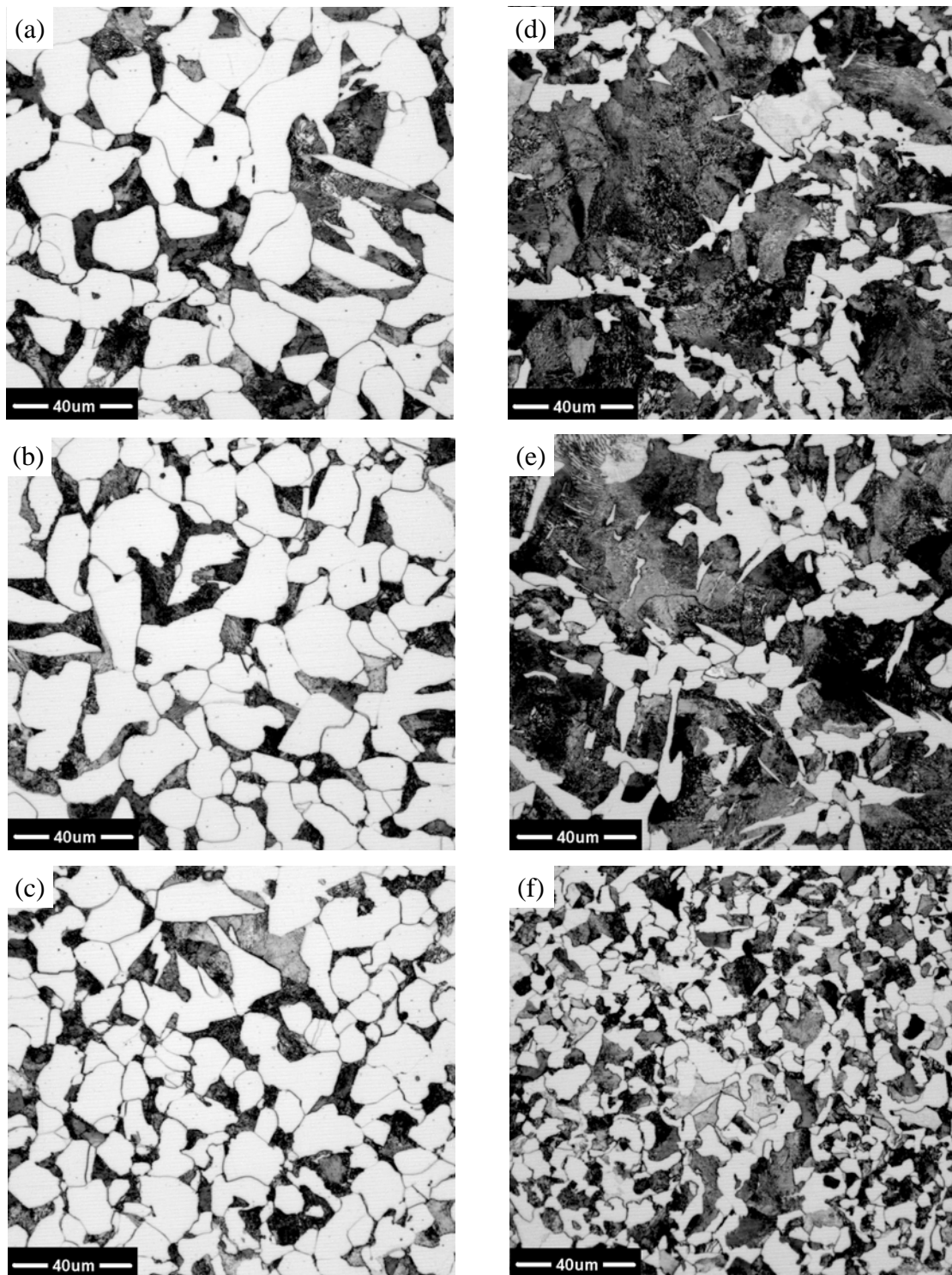
FIGURE 2.8. Microstructures of the 0.26 %C and 0.46 %C steels cooled at a rate of 1 ^{o}C/sec. 0.26 %C steel : austenitizing temperature (a) 950 ^{o}C, (b) 900 ^{o}C, (c) 850 ^{o}C. 0.46 %C steel : austenitizing temperature (d) 950 ^{o}C, (e) 900 ^{o}C, (f) 850 ^{o}C

For the dilatation curves of the 0.46 %C steel, the volume fraction of the phases and the carbon content in the austenite calculated by the proposed model are illustrated in Fig. 2.7 (d), (e) and (f). Fig. 2.7 (d) shows that during cooling from the austenitizing temperature, 950 ^{o}C, the proeutectoid ferrite transformation began at 737 ^{o}C accompanied by the enrichment of

carbon in the remaining austenite.   When the average carbon contents of the remaining austenite reached at 0.608%, the pearlite transformation started at 674 $^{\circ}$C. The calculated volume fraction of the proeutectoid ferrite was 25.0%. The volume fraction of the proeutectoid ferrite was 23.5 %.   The calculated results for the dilatation curves cooled from the different austenitizing temperatures, 900 $^{\circ}$C and 850 $^{\circ}$C were shown in Fig. 2.7 (e) and (f). The volume fractions of the proeutectoid ferrite calculated from Fig. 2.6 (e) and (f) were 24.1 % and 27.6 %.   The volume fractions of the proeutectoid ferrite were measured to be 24.4 % and 30.4 %, respectively.   The calculated results for the 0.46 %C steels were in good agreement with the metallographic examinations.
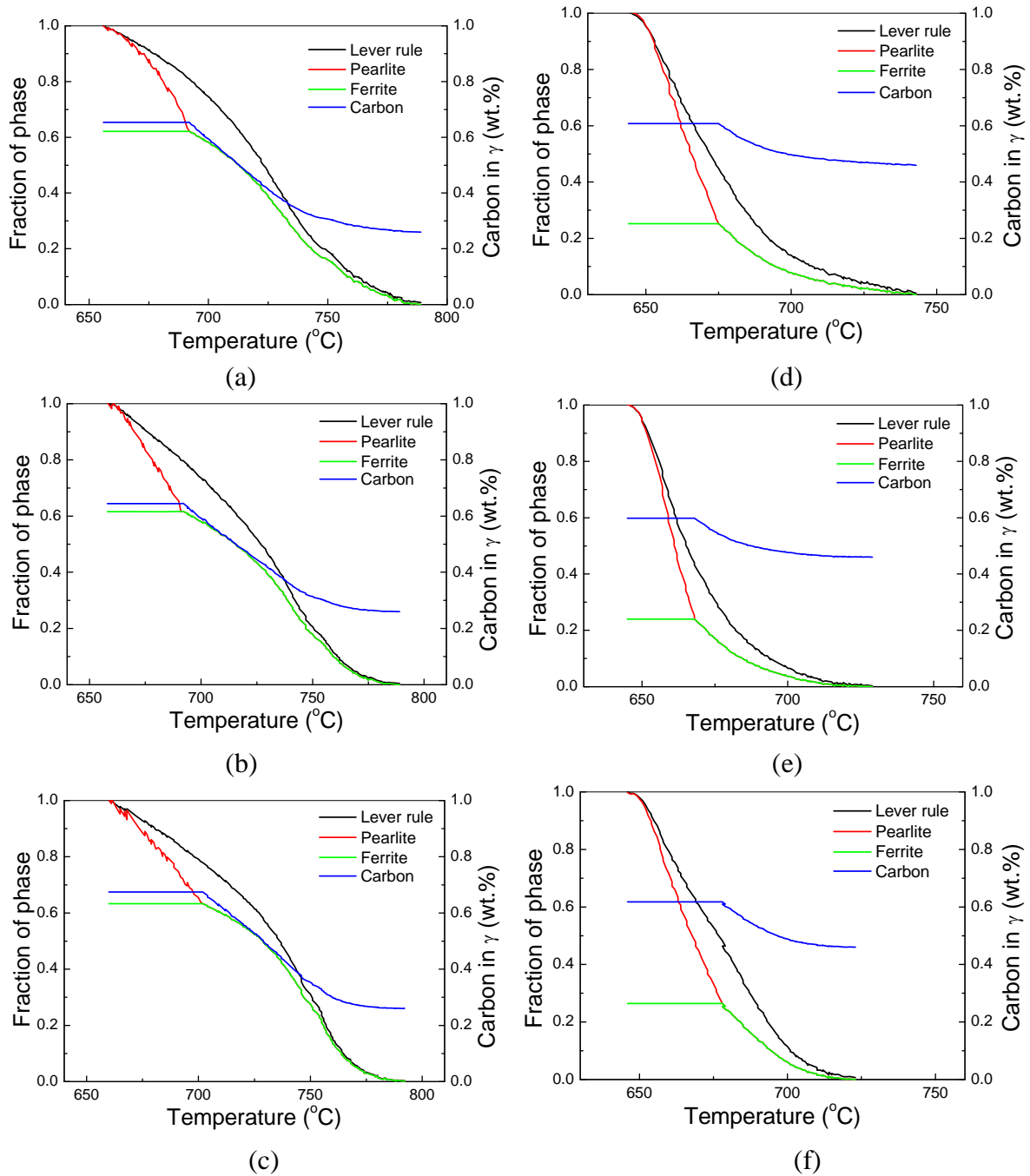
In addition, the dilatation curves were analyzed with the lever rule method. In Fig. 2.7, the volume fractions of the phases calculated from the lever rule were compared with the results calculated from the proposed model.   In interpreting the phase transformation kinetics from the dilatation curve, the lever rule could investigate only the transformed/untransformed austenite and not determine the transformation kinetics of the proeutectoid ferrite and the pearlite.   It can be seen that the proposed model extracted successfully the information on the phase transformation kinetics from the dilatation curves.   The good coincidence between the calculated fractions and the measured results verifies the usefulness of the proposed model.

2.5   Conclusion

Since the relative length changes detected by dilatometer are related to the degree of transformation, dilatometric analysis is a useful technique to obtain the experimental data concerning the phase transformation kinetics in steels.   This paper described a detailed method for quantitatively relating the dilatation curves to the phase transformation kinetics during continuous cooling of the hypoeutectoid steels.   The dilatation curves during the ferrite/pearlite transformation have been analyzed by using the linear thermal contraction coefficients, the lattice parameters of phases and the compositions of phases under thermodynamic equilibrium.   The proposed model was essentially based on the carbon enrichment of the austenite and the difference in unit volume of the phases.   The self consistent model has been applied to the determination of the phase transformation kinetics from the dilatation curves and verified by comparing the model results to experimental results of hypoeutectoid steels.   Excellent agreements between the calculation and the experiments results are observed.

3
Modeling transformation kinetics from the dilatation curves during heating

A significant step in thermo-mechanical processing of steels is reaustenitization. The investigation of the rate of austenite formation under rapid heating conditions is of great interest from a productivity standpoint. Currently, there is a tremendous international effort concerned with the development of quantitative models for reaustenitization, occurring during diverse processes such as welding, hot rolling and heat treatment of steels.[37-40] Since reaustenitization usually affects the grain size, grain size distribution and alloying element concentration homogeneity, the prior austenite microstructure has a great impact on the kinetics of further phase transformations, and in turn on the mechanical properties of components in subsequent cooling processes, such as quenching, normalizing and annealing.

Notwithstanding the efforts to describe reaustenitization[27,41-52], the accuracy of the resulting methods is very limited. The work presented here is part of a systematic attempt to remedy this situation. Since dilatometric analysis is a technique very often employed to study phase transformation kinetics in steels, the relative change in length which occurs during austenite formation has been studied as a function of temperature. Both kinetics and/or dilatometric analyses have been used to validate the model proposed for austenite formation in steels.

There are many cases in which the applicability of the lever rule is very limited. For example, proeutectoid ferrite and pearlite can transform into austenite on heating in sequential stages, but the lever-rule can not tell the difference between these two separate transformations, as the lever rule is not capable of describing concurrent phase

transformations.   The experimental observation of reaustenitization kinetics and morphology developments is difficult because austenite formed during heating is subsequently destroyed due to the transformation during cooling.   Computer modeling provides an alternative approach to track microstructure evolution during heat treatment.

3.1   Physical and mathematical model

3.1.1   Classical model

A typical initial condition of hypoeutectoid carbon steel consists of two distinctive microstructures, pearlite and ferrite.   As already recognized by Hultgren in 1928 [49], the growth of austenite (γ) from ferrite/cementite(α/θ) aggregates requires the simultaneous movement of two moving boundaries: the θ/γ as well as the γ/α interface.   Austenite nuclei in pearlite grow when carbon atoms are transported through the austenite by diffusion from the austenite/cementite boundary to the ferrite/austenite boundary and from the ferrite/cementite boundary through the ferrite, resulting in a transformation of the ferrite to austenite.

The austenitization transformation of the hypoeutectoid steel proceeds via two processes: pearlite transforms into austenite (p $\rightarrow$ γ) and proeutectoid ferrite transforms into austenite (α $\rightarrow$ γ).[53-61]   It is well known that pearlite transformation occurs very quickly due to the existence of short diffusion distances for the carbon in pearlite colonies.   During the pearlite transformation, nucleation of austenite grains takes place just above the eutectoid temperature and generally at the interfaces between pearlite colonies.   At this stage, austenite takes the eutectoid carbon composition.   The transformation of proeutectoid ferrite into austenite occurs at higher temperatures and is only completed above the (α+ γ)/γ line in the phase diagram (Ac$_1$).

3.1.1.1   Mathematical model

(a)   (b)   (c)   (d)
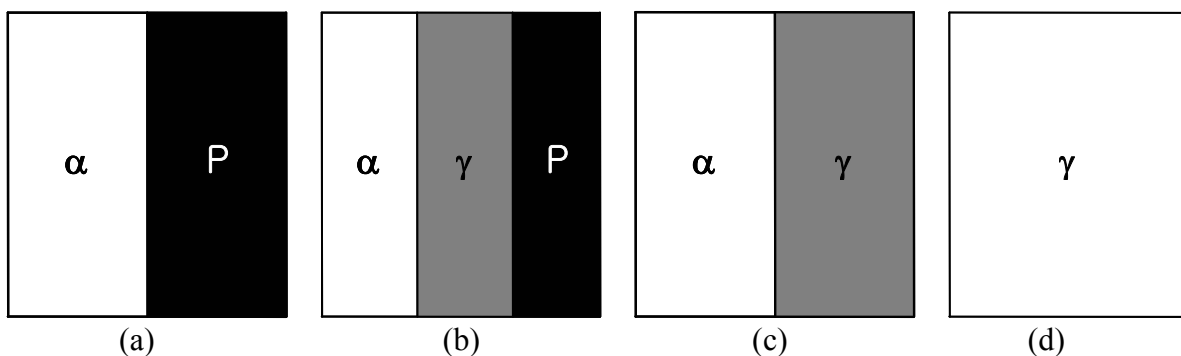
FIGURE 3.1.   Schematic illustration of the formation of austenite from ferrite-cementite mixtures by classical model : (a) Ferrite-pearlite mixtures just before austenitization, (b) 1-step formation of austenite from pearlite by eutectoid reaction (carbon concentration in austenite assumed to be equal to eutectoid composition) (c) 2-step formation of austenite from ferrite after complete dissolution of pearlite (d) Complete formation of austenite.

For small volume changes the relative length change (ε) of a sample is related to the

relative volume change.[33]   It is assumed that the expansion/contraction of a sample is isotropic and transformation plasticity does not affect net length changes.   In the present model it is assumed that unless completion of the first stage was achieved, austenitization did not proceed to the second stage ($\alpha \rightarrow \gamma$).   In other words, the two processes in austenitization were taken as occurring sequentially, in order to simulate the overall austenitization process (see Fig. 3.1).

Considering the fact that the diffusion coefficients for substitutional alloying elements are several orders of magnitude smaller than that of carbon, the redistribution of substitutional elements between phases is neglected.   Hence, dilatation is assumed to be dependent on the temperature and the carbon concentration in each phase, only.   The total length of a sample in the ferrite-pearlite state region at a given temperature (T_1) before austenitization can be expressed as

$$\begin{aligned}
L(T_1) &= f_{\alpha 0}(T_1)L_\alpha(T_1,C_\alpha) + f_{p0}(T_1)\left(f_\alpha^{p0}(T_1)L_\alpha(T_1,C_\alpha) + f_\theta^{p0}(T_1)L_\theta(T_1,C_\theta)\right) \\
&= f_{\alpha 0}(T_1)L_\alpha(T_1,C_\alpha) + f_{\theta 0}(T_1)L_\theta(T_1,C_\theta)
\end{aligned} \tag{1}$$

where L_α and L_θ are the length of the ferrite and the cementite at a given temperature (T_1) having respectively the initial concentration of carbon C_α and C_θ, $f_{\alpha 0}(T_1)$ and $f_{p0}(T_1)$ are the initial volume fractions of proeutectoid ferrite and pearlite, respectively. $f_\alpha^{p0}(T_1)$, $f_\theta^{p0}(T_1)$ is the initial volume fraction of the pearlitic ferrite and the pearlitic cementite.   In other words, total fraction of initial ferrite and initial cementite are $f_{\alpha 0}(T_1)$ and $f_{\theta 0}(T_1)$, respectively.

During the phase transformation, the ferrite-pearlite mixture will gradually transform into the austenite, in which the maximum solubility of carbon in ferrite, C_α and the solubility of carbon in cementite, C_θ is limited, and the newly formed austenite will have eutectoid composition C_e, as the classical model stated above.   The total length of a sample at a given transforming temperature (T_2) during the pearlite $\rightarrow$ austenite transformation is a function of the length changes of each of those phases:

$$\begin{aligned}
L(T_2) &= f_{\alpha 0}(T_2)L_\alpha(T_2,C_\alpha) + f_p(T_2)f_\alpha^p(T_2)L_\alpha(T_2,C_\alpha) + f_p(T_2)f_\theta^p(T_2)L_\theta(T_2,C_\theta) + f_\gamma L_\gamma(T_2,C_e) \\
&= f_{\alpha 0}(T_2)L_\alpha(T_2,C_\alpha) + \left(f_{p0}(T_2)f_\alpha^{p0}(T_2) - f_\gamma^\alpha(T_2)\right)L_\alpha(T_2,C_\alpha) \\
&\quad + \left(f_{p0}(T_2)f_\theta^{p0}(T_2) - f_\gamma^\theta(T_2)\right)L_\theta(T_2,C_\theta) + \left(f_\gamma^\alpha(T_2) + f_\gamma^\theta(T_2)\right)L_\gamma(T_2,C_e) \\
&= f_{\alpha 0}(T_2)L_\alpha(T_2,C_\alpha) + f_{p0}(T_2)f_\alpha^{p0}(T_2)L_\alpha(T_2,C_\alpha) + f_{p0}(T_2)f_\theta^{p0}(T_2)L_\theta(T_2,C_\theta) \\
&\quad + f_\gamma^\alpha(T_2)\left(L_\gamma(T_2,C_e) - L_\alpha(T_2,C_\alpha)\right) + f_\gamma^\theta(T_2)\left(L_\gamma(T_2,C_e) - L_\theta(T_2,C_\theta)\right)
\end{aligned} \tag{2}$$

where $f_\gamma(T_2)$ is the volume fraction of the transformed austenite, equal to ($f_\gamma^\alpha(T_2) + f_\gamma^\theta(T_2)$) and $f_\gamma^\alpha(T_2)$, $f_\gamma^\theta(T_2)$ are the volume fraction of the austenite transformed from the pearlitic ferrite and the pearlitic cementite respectively. $f_{\alpha 0}(T_2)$ is the initial volume fraction of the proeutectoid ferrite and $f_p(T_2)f_\alpha^p(T_2)$ is the volume fraction of the remaining pearlitic ferrite, $f_p(T_2)f_\theta^p(T_2)$ is the volume fraction of the remaining pearlitic cementite. $L_\gamma(T_2,C_e)$ is the length of the transformed austenite having the average carbon content, C_γ.   In the classical model, it is assumed that the average carbon content of austenite is eutectoid carbon content, C_e. $L_\alpha(T_2,C_\alpha)$ is the length of the ferrite which has the carbon content C_α and $L_\theta(T_2,C_\alpha)$ is the lengths of the cementite which has the carbon content C_θ, expected from the phase

diagram.   The overall mass conservation of carbon requires:

$$C_0 = f_{\alpha 0}(T_2)C_\alpha + f_p(T_2)f_\alpha^p(T_2)C_\alpha + f_p(T_2)f_\theta^p(T_2)C_\theta + f_\gamma C_e \tag{3}$$

The second step is the transformation of proeutectoid ferrite into austenite. This transformation occurs at higher temperatures and is only completed above the $(\alpha + \gamma)/\gamma$ line in the phase diagram.

$$L(T_3) = f_\alpha(T_3)L_\alpha(T_3, C_\alpha) + \left(f_\gamma^{p0}(T_3) + f_\gamma(T_3)\right)L_\gamma(T_3, C_\gamma) \tag{4}$$

where $f_\alpha(T_3)$ is the volume fraction of remaining ferrite (proeutectoid ferrite) and $f_\gamma^{p0}(T_3)$ is the previous volume fraction of austenite formed from pearlite reaction, $f_\gamma(T_3)$ is the volume fraction of the austenite formed from remaining ferrite after complete dissolution of pearlite. $L_\alpha(T_3, C_\alpha)$ is the ferrite length with a carbon content C_α (expected from the phase diagram). $L_\gamma(T_3, C_\gamma)$ is the length of the transformed austenite with the carbon content C_γ.   The carbon concentration in the austenite decreases as the transformation progresses and finally equals the initial carbon concentration of the steel.   The remaining ferrite will gradually transform into austenite, while the maximum solubility of carbon in the ferrite C_α, is limited.   The overall mass conservation of carbon is as follows.

$$C_0 = f_\alpha(T_3)C_\alpha + \left(f_\gamma^{p0}(T_3) + f_\gamma(T_3)\right)C_\gamma \tag{5}$$

Finally, once reaustenitization is completed, the total length of a sample at a temperature (T_4) is only a function of length changes in austenite:

$$L(T_4) = L_\gamma(T_4, C_\gamma) = L_\gamma(T_4, C_0) \tag{6}$$

3.1.1.2   Relative length change due to the reaustenitization transformation from ferrite + cementite

For a given temperature, the length change due to the reaustenitization of pearlitic structure $(\alpha + \theta)$ is expressed by subtracting Eq. (6) from Eq. (2),

$$
\begin{aligned}
L(T_2) - L(T_4) &= f_{\alpha 0}(T_2)L_\alpha(T_2, C_\alpha) + f_p(T_2)f_\alpha^p(T_2)L_\alpha(T_2, C_\alpha) + f_p(T_2)f_\theta^p(T_2)L_\theta(T_2, C_\theta) \\
&\quad + f_\gamma L_\gamma(T_2, C_e) - L_\gamma(T_4, C_0) \\
&= f_{\alpha 0}(T_2)\left(L_\alpha(T_2, C_\alpha) - L_\gamma(T_4, C_0)\right) + f_{p0}(T_2)f_\alpha^{p0}(T_2)\left(L_\alpha(T_2, C_\alpha) - L_\gamma(T_4, C_0)\right) \\
&\quad + f_{p0}(T_2)f_\theta^{p0}(T_2)\left(L_\theta(T_2, C_\theta) - L_\gamma(T_4, C_0)\right) \\
&\quad + f_\gamma^\alpha(T_2)\left(\left(L_\gamma(T_2, C_e) - L_\gamma(T_2, C_0)\right) + \left(L_\gamma(T_2, C_0) - L_\gamma(T_4, C_0)\right) - L_\alpha(T_2, C_\alpha)\right) \\
&\quad + f_\gamma^\theta(T_2)\left(\left(L_\gamma(T_2, C_e) - L_\gamma(T_2, C_0)\right) + \left(L_\gamma(T_2, C_0) - L_\gamma(T_4, C_0)\right) - L_\theta(T_2, C_\theta)\right)
\end{aligned}
\tag{7}
$$

The carbon contents of ferrite, cementite and austenite are calculated by employing the TQ-interface of Thermo-Calc S/W.   Since the relative length change (ε) of a sample is related to the relative volume change [33], Eq. (7) can be rearranged as follows:

$$\frac{\varepsilon(T_2)-\varepsilon(T_4)}{1+\varepsilon_\gamma(T_4,C_0)} = f_{\alpha 0}(T_2)\left(\frac{V_\alpha(T_2,C_\alpha)-V_\gamma(T_4,C_0)}{3V_\gamma(T_4,C_0)}\right)$$

$$+f_{p0}(T_2)f_\alpha^{p0}(T_2)\left(\frac{V_\alpha(T_2,C_\alpha)-V_\gamma(T_4,C_0)}{3V_\gamma(T_4,C_0)}\right)$$

$$+f_{p0}(T_2)f_\theta^{p0}(T_2)\left(\frac{V_\theta(T_2,C_\theta)-V_\gamma(T_4,C_0)}{3V_\gamma(T_4,C_0)}\right)$$

$$+f_\gamma^\alpha(T_2)\left[\left(\frac{V_\gamma(T_2,C_e)-V_\gamma(T_2,C_0)}{3V_\gamma(T_2,C_0)}\right)\left(\frac{1+\varepsilon_\gamma(T_2,C_0)}{1+\varepsilon_\gamma(T_4,C_0)}\right)+\left(\frac{V_\gamma(T_2,C_0)-V_\gamma(T_4,C_0)}{3V_\gamma(T_4,C_0)}\right)\right.$$

$$\left.-\left(\frac{V_\alpha(T_2,C_\alpha)-V_\gamma(T_4,C_0)}{3V_\gamma(T_4,C_0)}\right)-1\right]$$

$$+f_\gamma^\theta(T_2)\left[\left(\frac{V_\gamma(T_2,C_e)-V_\gamma(T_2,C_0)}{3V_\gamma(T_2,C_0)}\right)\left(\frac{1+\varepsilon_\gamma(T_2,C_0)}{1+\varepsilon_\gamma(T_4,C_0)}\right)+\left(\frac{V_\gamma(T_2,C_0)-V_\gamma(T_4,C_0)}{3V_\gamma(T_4,C_0)}\right)\right.$$

$$\left.-\left(\frac{V_\theta(T_2,C_\theta)-V_\gamma(T_4,C_0)}{3V_\gamma(T_4,C_0)}\right)-1\right] \tag{8}$$

where $\varepsilon(T_2)$ and $\varepsilon(T_4)$ are the relative length changes of a sample measured from the dilatation curve at temperatures T_2 and T_4, and V_i is the unit volume of the phase (i). $\varepsilon_\gamma(T_2,C_0)$ and $\varepsilon_\gamma(T_4,C_0)$ are the relative length changes of the austenite at a temperature T_2, T_4, which has the initial content of carbon (C_0). To calculate the volume fractions of existing phases, the relative length changes and the compositions, and the unit volume for the phases are needed. The relative length changes and the chemical compositions are easily determined from the dilatation curve and Thermo-Calc package. The unit volume of phases is generally calculated from the lattice parameters. Therefore, Eq. (8) can be used for all dilatation curves where austenite is transformed from the pearlitic microstructure. Using this method, the following equation can be derived for the reaustenitization from the ferrite.

3.1.1.3 Relative length change due to the reaustenitization transformation from ferrite

For a given temperature, the length change due to the reaustenitization of the ferrite is expressed by subtracting Eq. (6) from Eq. (4),

$$L(T_3)-L(T_4) = f_\alpha(T_3)L_\alpha(T_3,C_\alpha)+\left(f_\gamma^{p0}(T_3)+f_\gamma(T_3)\right)L_\gamma(T_3,C_\gamma)-L_\gamma(T_4,C_0)$$

$$= \left(1-f_\gamma^{p0}(T_3)-f_\gamma(T_3)\right)\left(L_\alpha(T_3,C_\alpha)-L_\gamma(T_4,C_0)\right) \tag{9}$$

$$+\left(f_\gamma^{p0}(T_3)+f_\gamma(T_3)\right)\left(\left(L_\gamma(T_3,C_\gamma)-L_\gamma(T_3,C_0)\right)+\left(L_\gamma(T_3,C_0)-L_\gamma(T_4,C_0)\right)\right)$$

Similar to the reaustenitization transformation of the pearlite, we can rearrange Eq. (9) as follows:

$$
\frac{\varepsilon(T_3) - \varepsilon(T_4)}{1 + \varepsilon_\gamma(T_4, C_0)}
$$

$$
= \left(1 - f_\gamma^{p0}(T_3) - f_\gamma(T_3)\right)\left(\frac{V_\alpha(T_3, C_\alpha) - V_\gamma(T_4, C_0)}{3V_\gamma(T_4, C_0)}\right) + \tag{10}
$$

$$
\left(f_\gamma^{p0}(T_3) + f_\gamma(T_3)\right)\left(\left(\frac{V_\gamma(T_3, C_\gamma) - V_\gamma(T_3, C_0)}{3V_\gamma(T_3, C_0)}\right)\left(\frac{1 + \varepsilon_\gamma(T_3, C_0)}{1 + \varepsilon_\gamma(T_4, C_0)}\right) + \left(\frac{V_\gamma(T_3, C_0) - V_\gamma(T_4, C_0)}{3V_\gamma(T_4, C_0)}\right)\right)
$$

By using Eq. (10), the volume fraction of the existing phases at a given temperature during the pearlite transformation is calculated from the unit volume, the composition of the phases and the relative length change of a sample. The key for the calculation is the determination of the unit volume of the phases. In the next section, the method calculating the unit volume of the phases during the phase transformation is introduced.

3.1.1.4   Algorithm

The algorithm for calculating the phase transformation kinetics from dilatation data is shown Fig. 3.2. The dilatation data and chemical composition are used as input parameters. In addition, the initial fraction of phases is required to analyze the transformation kinetics during heating. First, the linear thermal expansion coefficients are calculated and the region of phase transformation is determined on the basis of deviation from linear extrapolation. In eutectoid transformation during heating, ferrite and cementite transform to austenite and its carbon concentration in austenite equals the eutectoid composition. The carbon concentration in ferrite is calculated by Themo-Calc program. Then, the remaining ferrite transforms to austenite and the carbon concentration in austenite equals gradually the initial carbon concentration of steel.(Fig. 3.3) In case of hypereutectoid steel, the ferrite is remained after the eutectoid transformation and the carbon concentration in austenite decreases gradually up to the initial carbon concentration of steel during heating. The carbon concentration in austenite is calculated by the carbon conservation relation.

3.1.2   New model

According to the classical model, austenite initially forms on the basis of pearlite reaction. This model can not explain that as the heating rate increases, cementite dissolves up to higher temperature. In order to study the kinetics of austenite formation, the simplifying assumption was adopted stating that austenite (γ) nucleates at the Fe$_3$C/α lamellar interfaces, creating two new interfaces, Fe$_3$C/γ and γ/α, as shown in Fig. 3.4. Austenite growth then takes place by the simultaneous movement of these two interfaces into Fe$_3$C and α, respectively. Here, we are concerned with the dilatometric change during reaustenitization from mixtures of cementite and ferrite.

3.1.2.1   Mathematical model

As mentioned above, the total sample length in the ferrite-pearlite state region at a given temperature (T_1) before austenitization can be expressed as
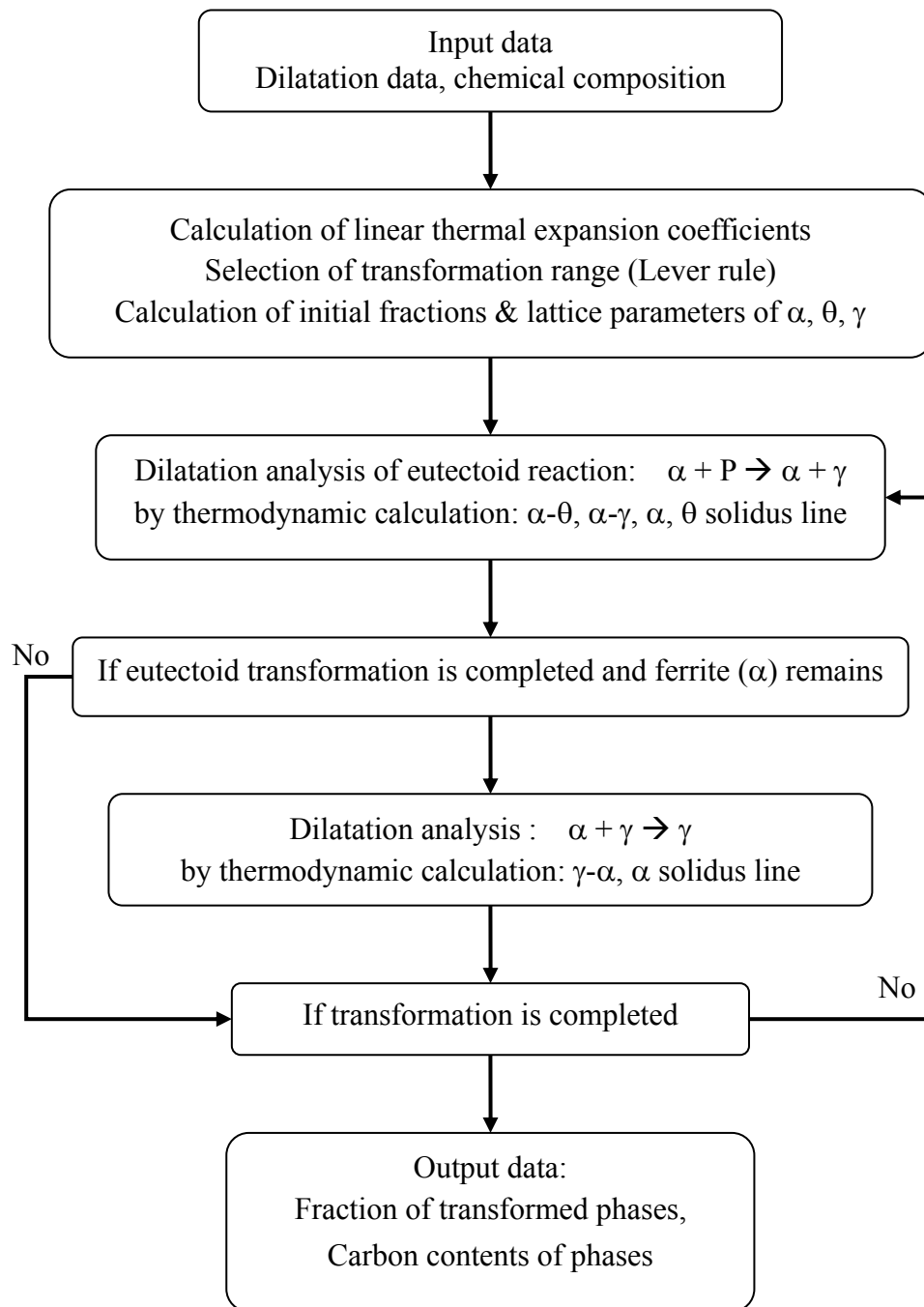
FIGURE 3.2.   Flow diagram of calculating the transformation kinetics from the dilatation data.
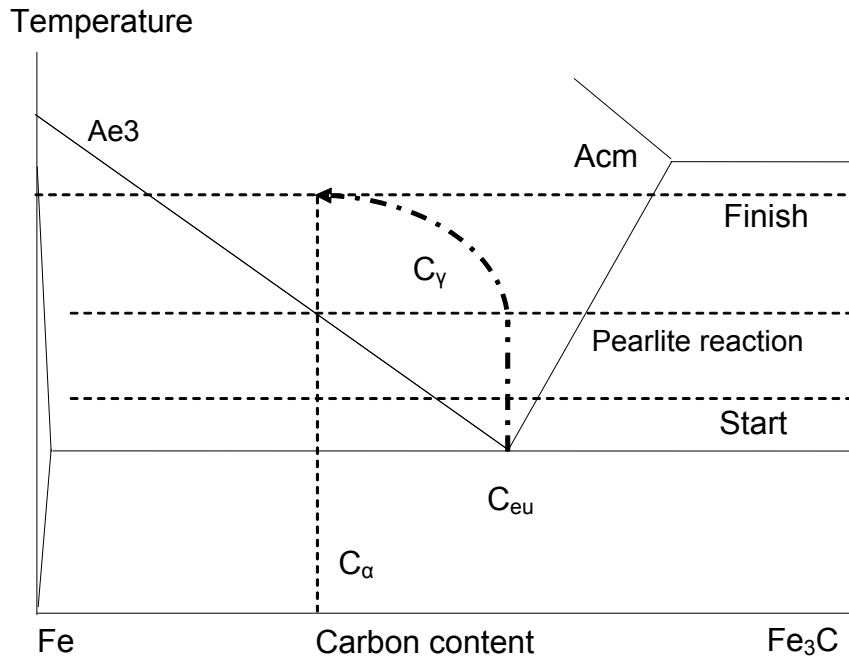
FIGURE 3.3.   Transition of the transformation from ferrite + cementite to austenite on the phase diagram.
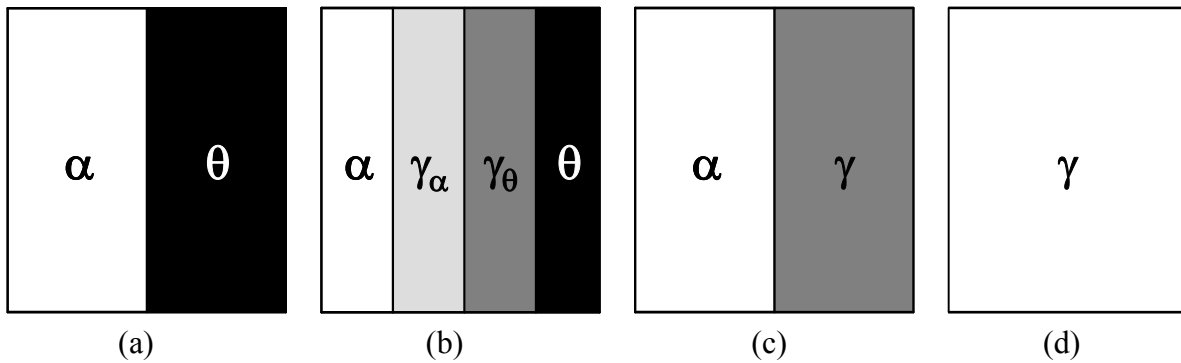
FIGURE 3.4.   Schematic illustration of the formation of austenite from ferrite-cementite mixtures by new model: (a) Ferrite-cementite mixtures just before austenitization, (b) 1-step formation of austenite from ferrite-cementite mixtures (γ_α formed under ferrite-austenite local equilibrium and γ_θ formed under cementite-austenite local equilibrium), (c) 2-step formation of austenite from ferrite after complete dissolution of cementite, (d) Complete formation of austenite.

$$L(T_1) = f_{\alpha 0} L_\alpha(T_1, C_\alpha) + f_{\theta 0} L_\theta(T_1, C_\theta) \tag{11}$$

where L_α and L_θ are the length of the ferrite and the cementite at a given temperature (T_1) having respectively the initial concentration of carbon C_α and C_θ. $f_{\alpha 0}$ and $f_{\theta 0}$ are the initial volume fractions of ferrite and cementite, respectively.

Ferrite-cementite mixture will gradually transform into austenite during heating to a given

temperature above A_1 temperature. The total length of a sample at a given transforming temperature (T_2) during ferrite + cementite $\rightarrow$ austenite transformation is a function of the length changes of each of these phases:

$$L(T_2) = \left(f_{\alpha 0} - f_{\gamma \alpha}(T_2)\right)L_\alpha(T_2, C_\alpha) + f_{\gamma \alpha}(T_2)L_\gamma(T_2, C_{\gamma \alpha})$$
$$+ \left(1 - f_{\alpha 0} - f_{\gamma \theta}(T_2)\right)L_\theta(T_2, C_\theta) + f_{\gamma \theta}(T_2)L_\gamma(T_2, C_{\gamma \theta}) \tag{12}$$

where $f_{\gamma \alpha}(T_2)$ is the volume fraction of austenite transformed from ferrite region and $f_{\gamma \theta}(T_2)$ is volume fraction of austenite transformed from cementite region. $L_\gamma(T_2, C_{\gamma \alpha})$ is the length of austenite formed from ferrite region, having the local equilibrium carbon content $C_{\gamma \alpha}$. $L_\gamma(T_2, C_{\gamma \theta})$ is the length of austenite formed from cementite region, having the local equilibrium carbon content $C_{\gamma \theta}$. $L_\alpha(T_2, C_\alpha)$ is the length of the ferrite which has the carbon content C_α and $L_\theta(T_2, C_\theta)$ is the lengths of the cementite which has the carbon content C_θ expected from the phase diagram. The overall mass conservation of carbon requires:

$$C_0 = \left(f_{\alpha 0} - f_{\gamma \alpha}(T_2)\right)C_\alpha + f_{\gamma \alpha}(T_2)C_{\gamma \alpha} + \left(1 - f_{\alpha 0} - f_{\gamma \theta}(T_2)\right)C_\theta + f_{\gamma \theta}(T_2)C_{\gamma \theta} \tag{13}$$

The second step is the transformation of the remaining ferrite into austenite after complete dissolution of cementite. It is the same process as in the classical model. Upon completion of the first stage, this high-carbon austenite formed from ferrite-cementite mixture grows at the expense of ferrite, a process comprising the second stage of austenitization.

$$L(T_3) = f_\alpha(T_3)L_\alpha(T_3, C_\alpha) + \left(f_\gamma^{p0}(T_3) + f_\gamma(T_3)\right)L_\gamma(T_3, C_\gamma) \tag{14}$$

where $f_\alpha(T_3)$ is the volume fraction of remaining ferrite (proeutectoid ferrite) and $f_\gamma^{p0}(T_3)$ is the previous volume fraction of austenite formed from pearlite reaction, $f_\gamma(T_3)$ is the volume fraction of the austenite formed from remaining ferrite after complete dissolution of pearlite. $L_\alpha(T_3, C_\alpha)$ is the length with a carbon content C_α (expected from the phase diagram). $L_\gamma(T_3, C_\gamma)$ is the length of the transformed austenite with the carbon content C_γ. The carbon concentration in the austenite decreases as the transformation progresses and finally equals the initial carbon concentration of the steel. The remaining ferrite will gradually transform into the austenite, in which the maximum solubility of carbon in the ferrite C_α, is limited. The overall mass conservation of carbon is as follows.

$$C_0 = f_\alpha(T_3)C_\alpha + \left(f_\gamma^{p0}(T_3) + f_\gamma(T_3)\right)C_\gamma \tag{15}$$

Finally, once reaustenitization is completed, the total length of a sample at a temperature (T_4) is only a function of length changes in austenite:

$$L(T_4) = L_\gamma(T_4, C_\gamma) = L_\gamma(T_4, C_0) \tag{16}$$

3.1.2.2 Relative length change due to the reaustenitization transformation from ferrite + cementite

For a given temperature, the length change due to the reaustenitization of ferrite-cementite structure ($\alpha + \theta$) is expressed by subtracting Eq. (16) from Eq. (12),

$$L(T_2) - L(T_4) = \left(f_0 - f_{\gamma\alpha}(T_2)\right)\left(L_\alpha(T_2, C_\alpha) - L_\gamma(T_4)\right) + f_{\gamma\alpha}(T_2)\left(L_\gamma(T_2, C_{\gamma\alpha}) - L_\gamma(T_4)\right)$$
$$+ \left(1 - f_0 - f_{\gamma\theta}(T_2)\right)\left(L_\theta(T_2, C_\theta) - L_\gamma(T_4)\right) + f_{\gamma\theta}(T_2)\left(L_\gamma(T_2, C_{\gamma\theta}) - L_\gamma(T_4)\right) \tag{17}$$

The carbon contents of ferrite, cementite and austenite are calculated by employing the TQ-interface of Thermo-Calc program. Since the relative length change (ε) of a sample is related to the relative volume change, Eq. (17) can be rearranged as follows:

$$\varepsilon(T_2) - \varepsilon(T_4) = \left(f_0 - f_{\gamma\alpha}(T_2)\right)\left(\frac{V_\alpha(T_1, C_\alpha) - V_\gamma(T_4)}{3V_\gamma(T_4)}\right)\left(\varepsilon(T_4, C_0) + 1\right)$$
$$+ f_{\gamma\alpha}(T_2)\left(\frac{V_\gamma(T_2, C_{\gamma\alpha}) - V_\gamma(T_4)}{3V_\gamma(T_4)}\right)\left(\varepsilon(T_4, C_0) + 1\right)$$
$$+ \left(1 - f_0 - f_{\gamma\theta}(T_2)\right)\left(\frac{V_\theta(T_1, C_\theta) - V_\gamma(T_4)}{3V_\gamma(T_4)}\right)\left(\varepsilon(T_4, C_0) + 1\right) \tag{18}$$
$$+ f_{\gamma\theta}(T_2)\left(\frac{V_\gamma(T_2, C_{\gamma\theta}) - V_\gamma(T_4)}{3V_\gamma(T_4)}\right)\left(\varepsilon(T_4, C_0) + 1\right)$$

where $\varepsilon(T_2)$ and $\varepsilon(T_4)$ are the relative length changes of a sample measured from the dilatation curve at temperatures T_2 and T_4, and V_i, where $i = \gamma, \theta, \alpha$, is the unit volume of i. $\varepsilon_\gamma(T_4, C_0)$ are the relative length changes of the austenite at a temperature T_4 which has the initial content of carbon (C_0). To calculate the volume fractions of existing phases, the relative length changes and the compositions, and the unit volume for the phases are needed. The relative length changes and the chemical compositions are easily determined from the dilatation curve and Thermo-Calc program. The unit volume of phases is generally calculated from the lattice parameters. Therefore, Eq. (8) can be used for all dilatation curves where austenite is transformed from the ferrite-cementite microstructure. Using this method, the following equation can be derived for the reaustenitization from the ferrite. As this process is equal to the classical model, a detailed description is omitted here.

3.1.2.3   Algorithm

The algorithm for calculating the phase transformation kinetics from dilatation data is shown in Fig. 3.5. The dilatation data and chemical composition are used as input parameters. In addition, the initial fraction of phases is required to analyze the transformation kinetics during heating. First, the linear thermal expansion coefficients are calculated and the region of phase transformation is determined on the basis of deviation from linear extrapolation. Ferrite and cementite transform to austenite and its carbon concentration in austenite is calculated under local equilibrium of each phase boundary. The carbon concentration in ferrite is calculated from Themo-Calc program. Then, the remaining ferrite transforms to austenite and the carbon concentration in austenite equals gradually the initial carbon concentration of steel.(Fig. 3.6) The carbon concentration in austenite is calculated by employing the carbon conservation relation.
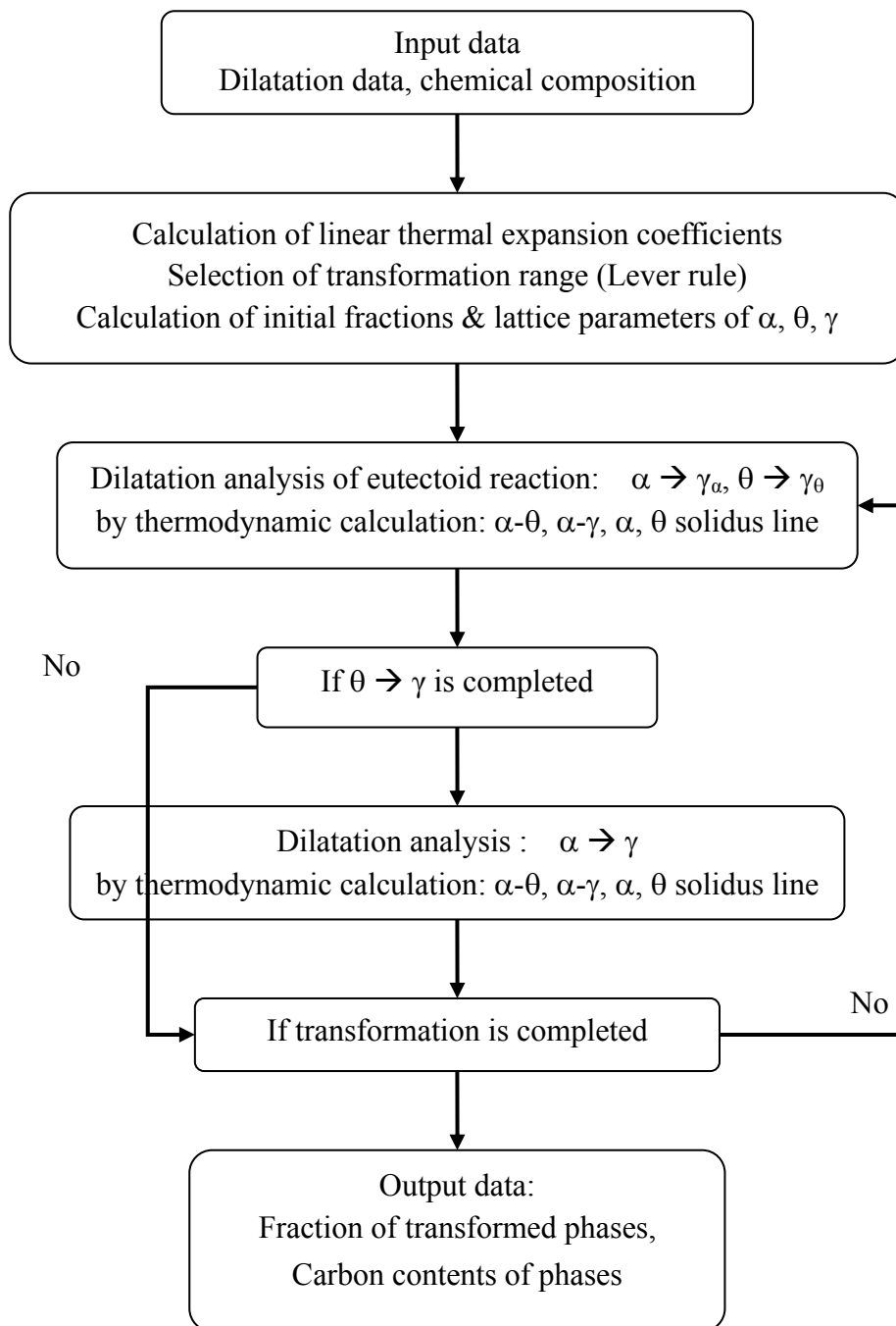
FIGURE 3.5. Flow diagram of calculating the transformation kinetics from the dilatation data by new model.
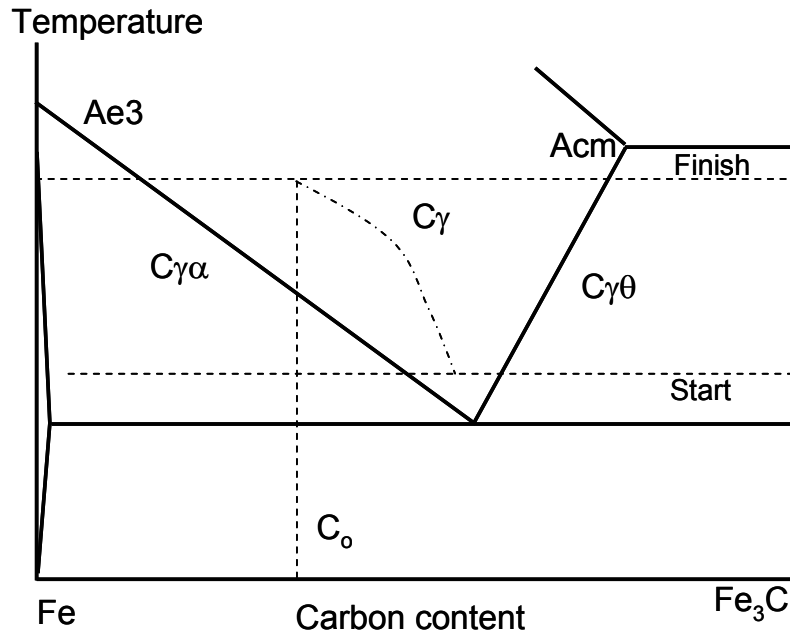
FIGURE 3.6.   Transition of the transformation from ferrite + cementite to austenite on the phase diagram by new model.

3.2   Unit volume and lattice parameter of phases

The crystal structures of austenite and ferrite are face centered cubic (FCC) and body centered cubic (BCC) respectively; cementite has an orthorhombic crystal structure.   The unit volume of austenite and ferrite are equal to $(a_\gamma)^3/4$ and $(a_\alpha)^3/2$, respectively, where a_γ and a_α are their lattice parameters.   The unit volume of cementite is given by $(a_\theta) \cdot (b_\theta) \cdot (c_\theta)/12$, where a_θ, b_θ, c_θ are its lattice parameters.   The lattice parameters of the phases are computed following the approach shown in Chapter 2.

3.3   Experiments

In order to validate the model, dilatation experiments on plain carbon steels (Table 3.1) have been performed.   A Bähr-Gerätebau GmbH dilatometer and a Dilatronic III, Theta Inc. was employed.   Hollow cylindrical specimens of 10.0 mm length and outer and inner diameter 3.0 and 1.5 mm, respectively were produced.   K-type thermocouples were spot welded to the sample, which was lightly clamped between quartz push rods.   The length change of the sample was recorded by a Linear Variable Displacement Transducer.   The sample was heated up to 1000 $^{\circ}$C at a rate of 1 $^{\circ}$C/sec.

TABLE 3.1. Chemical composition of the plain carbon steels. (wt.%)

	C	Si	Mn	Cr	Cu	Nb	B
S1	0.11	0.3	1.5		0.01	0.03	
S2	0.2	0.19	0.73	0.15			0.0022

Samples for the metallographic examinations were prepared using standard polishing techniques and were etched using 2 % Nital.   The determination of the fractions of the existing phases was conducted using Quantitative Image Analysis software.

3.4   Results and discussion

The steels employed in the heat treatment process are usually in the normalized condition, i.e. their starting microstructure consists of a mixture of lamellar pearlite and proeutectoid ferrite.   In order to validate the models presented here, the kinetics of austenite formation was studied and compared to the classical and new models.   The classical model assumes that at the first stage of austenitization, pearlite colonies dissolve forming austenite of eutectoid composition, and subsequently this carbon enriched austenite grows at the expense of ferrite.   In the new model, it is assumed that ferrite and cementite dissolve first and form the respective austenites under local equilibrium at the ferrite-austenite and cementite-austenite boundaries.   The second stage in the new model is equal to the classical model.
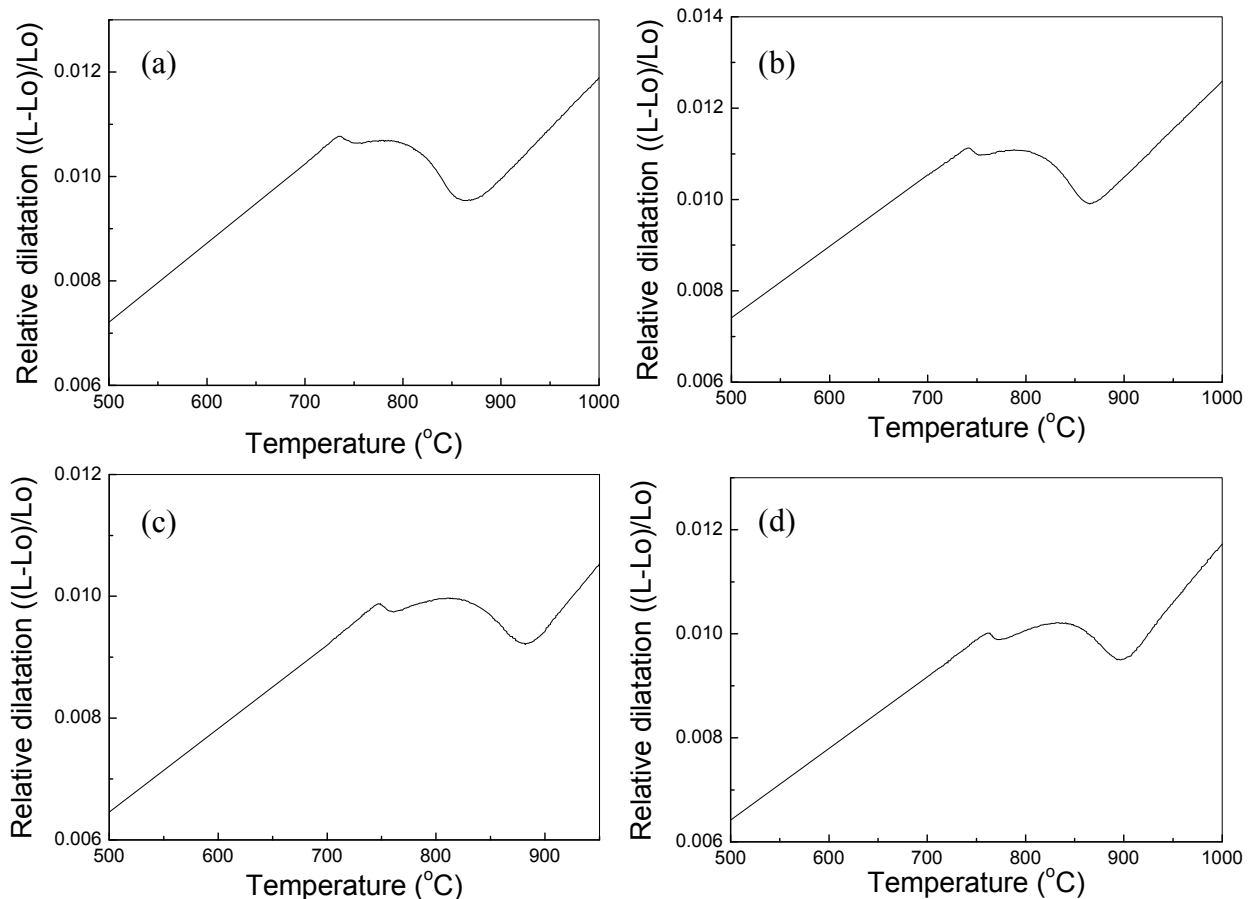

FIGURE 3.7.   Relative length changes of S1 steel heated to 1000 ^{o}C.   Heating rate : (a) 0.05, (b) 0.5, (c) 5, (d) 10 ^{o}C/s.

Fig. 3.7 shows the dilatation curves represented as $\Delta L/L_o$ vs. temperature, for S1 (Table 3.1). The steels were heated to 1000 ^{o}C at rates of 0.05, 0.5, 5 and 10 ^{o}C/s.   The relative dilatation

and volume fraction calculated by the new and classical models for the dilatation curves of Fig. 3.7 are shown in Fig. 3.8.   As classical model stated above, the carbon concentration of austenite is eutectoid composition until the pearlite (cementite) dissolves completely.   After completion of the pearlite reaction for heating, the remaining ferrite transforms to austenite and the carbon concentration in austenite decreases gradually to the initial carbon concentration.   The higher the heating rate, the higher the temperature for the austenite formation, but the temperature range for the cementite dissolution remains nearly constant. The finishing temperature of cementite dissolution shifts from 746 $^{\circ}$C to 768 $^{\circ}$C.   It has been reported that at higher heating rates, the cementite dissolution temperature increases.[54]
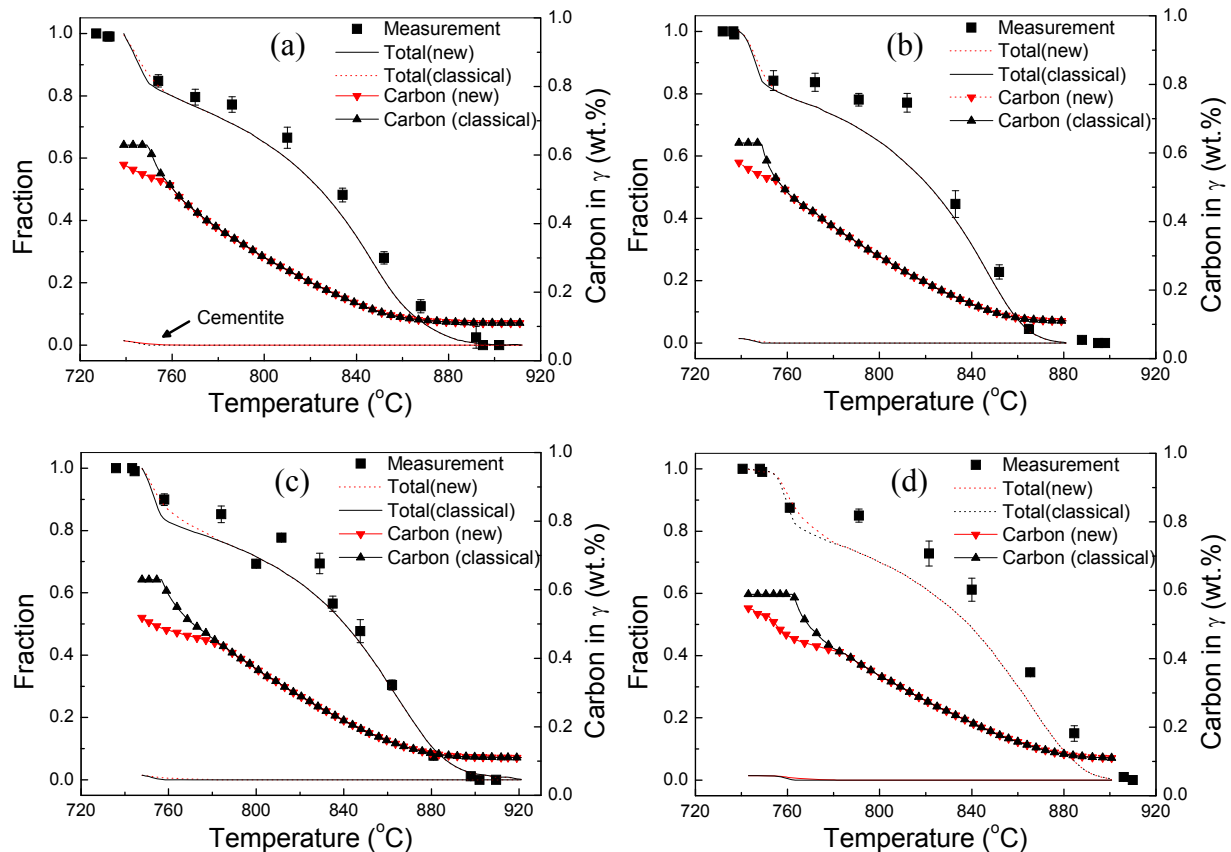
FIGURE 3.8.   Volume fractions of phases and carbon concentration of remaining austenite of S1 steel calculated from Fig. 3.7.   Heating rate : (a) 0.05, (b) 0.5, (c) 5, (d) 10 $^{\circ}$C/s.

In the proposed model, the volume fractions of austenite, ferrite and cementite are similar to those of the classical model.   However, the volume fraction of austenite from the new model becomes lower as heating rate increases.   The finishing temperature of cementite dissolution shifts 750 $^{\circ}$C to 842 $^{\circ}$C.   In other words, the temperature range for cementite dissolution extends widely above A3 temperature (831 $^{\circ}$C).   At the first stage of austenitization, average carbon concentration of austenite is less than the eutectoid composition and decreases as heating rate increases, resulting in the dissolution of cementite at higher temperatures (Fig. 3.9).   Such shift cannot be explained by the classical model (pearlite reaction): the kinetics of austenitization during heating is controlled not only by the pearlite reaction (pearlite $\rightarrow$ austenite), but also by the concurrent ferrite-austenite and cementite-austenite boundary reactions.

FIGURE 3.9.   Comparison of fraction of cementite between new model and classical model. Heating rate : (a) 0.05 $^\circ$C/s and (b) 10 $^\circ$C/s.

For S2 steel, the volume fraction of phases and the carbon content in the austenite calculated by the proposed model and the classical model are shown in Fig. 3.10.   Fig. 3.10 (a) is relative dilatation data measured during heating.   Fig. 3.10 (b) is the calculation results for dilatation curve.   Good agreement between the predictions by the proposed model and the experiment data is observed.   Fig. 3.11 shows the optical micrographs quenched at 730, 760, 790 and 820 $^\circ$C during heating.
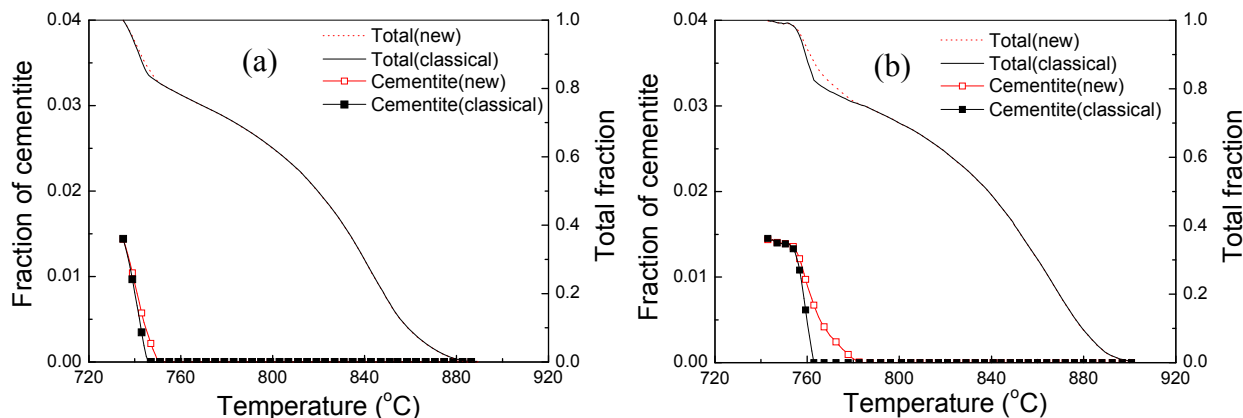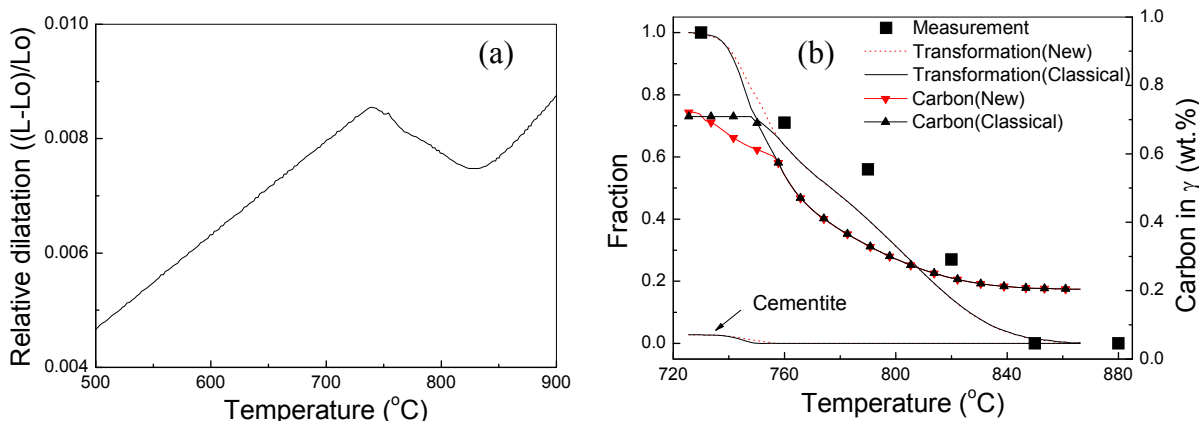

FIGURE 3.10.   Transformation kinetics of S2 steel calculated by new model and classical model, heated at a rate of 1 $^\circ$C/sec.   (a) relative dilatation and (b) transformation kinetics.

Fig. 3.12 shows the schematic diagram of austenitization kinetics of the classical model and the proposed model.   In the classical model, austenite forms by dissolving pearlite and carbon concentration of austenite is eutectoid composition.   As shown in Fig. 3.12 (b), the boundary of pearlitic ferrite and pearlitic cementite to austenite move equally to hold the eutectoid composition.   It indicates that when austenite transforms from pearlite, pearlitic ferrite and pearlitic cementite are dissolved as a constant rate to form austenite having eutectoid composition.   Fig. 3.12 (d) shows the austenitization behavior of pearlite computed by the proposed model.   In the proposed model, when austenite forms from pearlite, it is not necessary for the transformed austenite to have the eutectoid composition.   It is well known that as heating rate increases, pearlitic cementite dissolves slower than pearlitic ferrite.   In other words, pearlitic ferrite dissolves completely but some of pearlitic cementite was retained depending on the heating condition.   The classical model can not explain the slow

dissolution of cementite during heating.   It indicates that the boundary of pearlitic ferrite to austenite moves faster than that of pearlitic cementite as shown in Fig. 3.12 (d).
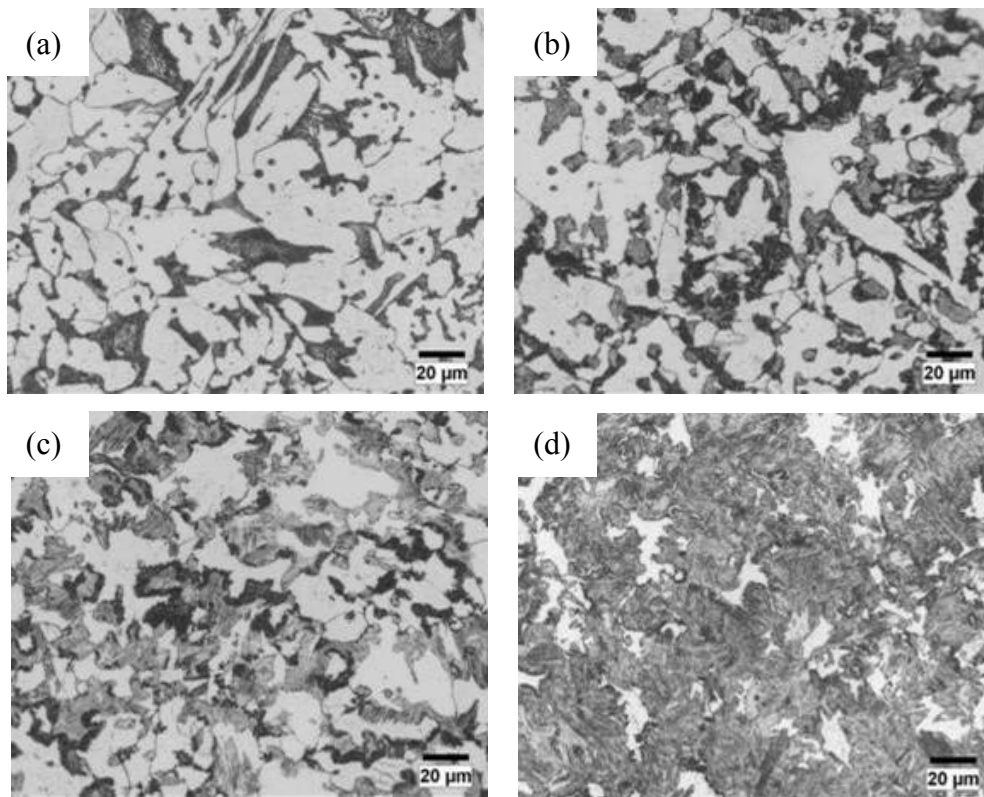
FIGURE 3.11.   Microstructures of S2 steels heated at a rate of 1 ^{o}C/sec.   (a) 730 ^{o}C, (b) 760 ^{o}C, (c) 790 ^{o}C, (d) 820 ^{o}C.
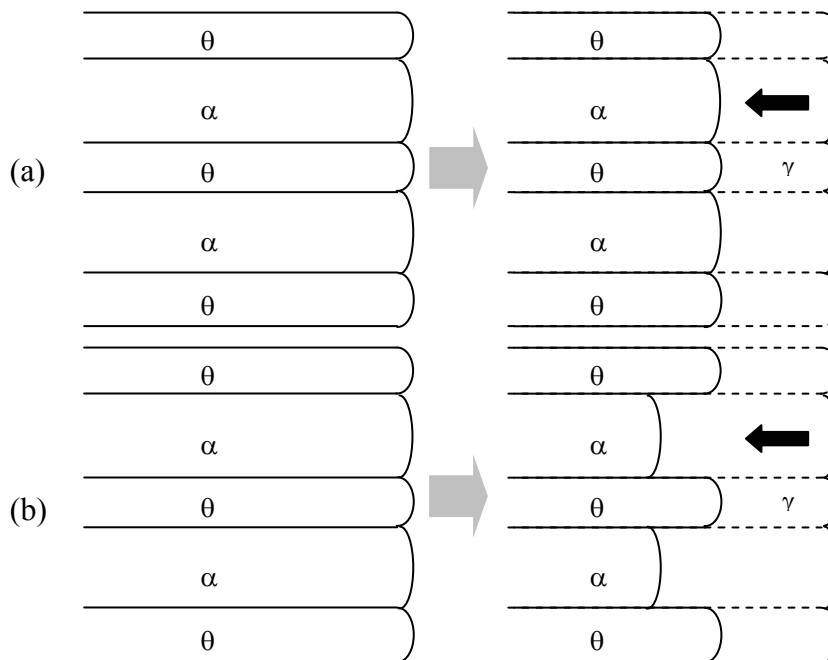
FIGURE 3.12.   Schematic diagram of austenitization of the classical model and the new model.   (a) austenitization kinetics from pearlite of the classical model and (b) austenitization kinetics from pearlite of the new model.

3.5   Conclusion

The conclusion is that it possible to derive the formation it possible to derive the formation of the reaction products during reaustenitization with good accuracy due to the new model and that it gives a slight but significant difference in the pearlite dissolution kinetics.

4

Development of new spring steels with optimized strength/ductility combinations

4.1   Design concept of new alloys

Today, most springs for automotive applications are made of quenched and tempered, medium carbon high strength steels.[62-67]   In order to improve fatigue strength and sag resistance, spring steel with increased tensile strength and reduction of area should be developed.   For spring steels, the emphasis in materials research has been focused on increasing the strength while maintaining good ductility (reduction of area, elongation) and fatigue properties.   The aim of this study is to develop a spring steel with a tensile strength 2350 MPa and reduction of area more than 25 %.

Two aspects are fundamental for achieving this target: (1) the control of the chemical composition, by incorporating new cost-effective alloying elements, and (2) finding proper conditions of heat treatment.   In order to increase the strength, alloying elements such as C, Si, Cr and V are added to steels.[68-72]   The strengthening is based on solution hardening and precipitation hardening.   The addition of such elements as C, Si and Cr is effective in increasing strength as described at Chapter 1.   Fine V carbonitrides precipitated in martensitic structures are finely dispersed and control austenitic grain growth to increase toughness.

C, Cr and Mo increase the softening resistance of steel during tempering, and these alloy elements are also effective in improving sag resistance.   Carbon is reduced for increasing corrosion fatigue life.   Si remains at a relatively high level for sag resistance but

decarburization and stability of ferrite will be increased during heating. The content of Si should be optimized. Ni is added to retard pitting corrosion [73], and V and B are added for grain refinement and strengthening of the prior-austenite grain boundary. It was reported that B increase the strength regardless of relatively high carbon spring steels. Boron can be used to increase the strength of spring without increasing the cost significantly.

It is well known that the addition of certain substitutional alloying elements modifies the tempering characteristics of martensite. The addition of Si has attracted much interest in the past, as it leads to tempering resistance.[62-66] The tempering resistance was attributed to the stabilization of the ε-carbide by Si enrichment. It is clear that certain elements, notably Si, can stabilize the ε-carbide at higher temperature. The evidence suggests that both the nucleation and the growth of ε-carbide are slowed down and that Si enters into the ε-carbide structure. It is also clear that the transformation of ε-carbide to cementite is delayed considerably.[74]

It refines the carbides and improves the sag resistance significantly. Si also retards the precipitation of cementite from austenite.[75-83] These general statements about the retardation of precipitation are only valid when the cementite is forced by circumstances to inherit the silicon concentration of the matrix from which it precipitates. Si has a negligible solubility in cementite, which can form rapidly if diffusion permits the Si to partition into the parent phase during growth. This is only possible when transformation occurs at elevated temperatures. Owen [10] proposed that silicon rejected from cementite acts as a growth barrier and causes the inhibition of cementite precipitation.

The mechanism for the possible enhancement of ε-carbide is not understood, but it could be the case that ε-carbide is more tolerant to silicon than cementite or that it becomes prominent simply because cementite has been suppressed. The ε-carbide [84], like cementite [85], has been shown to inherit the silicon concentration of the steel during precipitation at relatively low temperatures; the redistribution of silicon during the transition of ε-carbide to cementite has also been reported.[86]

When steel containing V is tempered at a temperature of 450 ^{o}C or above, secondary precipitation hardening occurs and increases the softening resistance of the steel during tempering. This is also effective in improving sag resistance, making V carbide that is effective in increasing steel strength. Nb is also effective in reducing the austenitic grain size [87], and it is added to high strength spring steel to act in the same manner as V.

Another method to increase the strength of spring steel is to decrease the tempering temperature. The conventional heat treatment does not exploit the maximum potential of existing steel grades. For a fixed chemical composition the increase in strength requires the decrease of tempering temperature. But the ductility drops with decreasing tempering temperature in an unacceptable manner, when fixing the total tempering time.

Systematic investigations into optimizing the mechanical properties of martensitic steels by focusing on austenite grain refinement are rare.[88] It is known that refinement of austenite grain size can improve the toughness of martensitic steels because it refines the microstructural units of martensite, i.e. the packet or block size.[89,90] In case of medium carbon spring steels, effects of microalloying elements have been studied in combination with thermomechanical treatments [88,90-93] and superior combinations of mechanical properties

were achieved.   In these studies the aim was to stabilize the structure of austenite produced by deformation prior to quenching with a fine dispersion of V or Nb carbonitrides. Carbonitride of microalloying elements such as V and Nb can refine the austenite grain size during heat treatment.

The loss in ductility is also dependent on impurity element concentration.   It is known that, for steels adjusted to the same hardness, the steel tempered at a higher temperature tends to show a higher fatigue limit.   The fatigue properties can be improved by the decrease of the crack sensitivity and the sag resistance is improved by the high strengthening and dislocation pinning.

This study is conducted to obtain high strength and reduction of area either by changing the tempering conditions or by adding chemical compositions.   Hence, in order to develop a new high strength steel with a tensile strength larger than 2350 MPa and RA larger than 25%, several steels were designed based on the high C-Si composition and small amounts of B, Mo and Nb or combinations were added and changed to find the optimum composition with target properties.

4.2   Experimental methods

4.2.1   Materials and processing conditions

Table 4.1 shows the chemical compositions of the material designed for the present work. Steels S1 ~ S5 each contain 0.55 wt. % carbon.   Steel S1 is a reference steel and steel S2 ~ S5 contain B, Mo and Nb respectively.

TABLE 4.1.   Chemical compositions of experimental steels.   (wt. %)

	C	Si	Mn	Cr	V	Ti	Ni	B	Cu	Mo	Nb
S1	0.55	2.2	0.7	0.9	0.1	0.03	0.2	-	0.15	-	-
S2	0.55	2.2	0.7	0.9	0.1	0.03	0.2	0.005	0.15	-	-
S3	0.55	2.2	0.7	0.9	0.1	0.03	0.2	0.005	0.15	0.2	-
S4	0.55	2.2	0.7	0.9	0.1	0.03	0.2	0.005	0.15	-	0.03
S5	0.55	2.2	0.7	0.9	0.1	0.03	0.2	0.005	0.15	0.2	0.03

Steels S1 ~ S5, described in Table 4.1 were vacuum melted as 50 kg ingots, heated at 1250 ^{o}C for 6 hr in a nitrogen atmosphere, hot rolled to 50 mm thickness plate and air cooled, in order to erase the casting structure.   These plates were then heated to 1100 ^{o}C for 2 hr in a nitrogen atmosphere, hot rolled to 15 mm plate thickness and cooled slowly in air, for homogenizing the microstructure.   From these plates, cylindrical specimens for heat treatment were machined as tensile test specimen.   The axis of tensile specimens was in the original rolling direction.   All steels were found to become fully austenite at temperatures of 830, 880, 930, 980 ^{o}C for 3 min.   They were subsequently quenched in oil at temperature of 50 ^{o}C.   Quenched specimens were tempered at temperature of 350, 400, 450 ^{o}C for 30 minutes using a salt bath.   For each condition three to five samples were tested.   Such a number of test samples gives a typical uncertainty of less than 40 MPa in tensile strength and an uncertainty in reduction of area of about 5 % for low ductility condition and 1.5 % for ductile samples.   Fig. 4.1 shows the overall sequence of experiments.

4.2.2   Mechanical tests

Tensile tests were conducted on samples with a gauge length of 25 mm, diameter 6.25 mm at a strain rate of 0.2 min^{-1}.   The Vickers hardness of the specimens was measured with a load of 10 kg applied for 10 seconds.   The surface hardness for each case was measured five times.

4.2.3   Metallographic tests

Specimens for optical microscopy observation were hot mounted in bakelite molding powder, ground with Si carbide paper down 1200 grit and then polished with 6 and 1 μm diamond pastes.   The specimens were then etched with 2 vol. % natal (nitric acid in methanol).   The optical microstructures were observed using an Olympus microscope.   The etched specimens were gold-coated in a vacuum atmosphere.   Microstructures were measured using JEOL JSM-7000F field emission scanning electron microscope.   Philips transmission electron microscopes operated at 200 kV.   Two types of specimens were examined as thin foils and carbon extraction replicas.   Thin foils were sliced from bulk specimens as 3 mm diameter discs approximately 250 μm in thickness using a Si carbide blade and cooling lubricant.   After slicing, the specimens were ground with Si carbide paper to around 50 μm thickness.   Electropolishing was done using a twin jet electropolisher. The solutions for electropolishing were 5 vol. % perchloric acid, 20 vol. % glycerol and 75 vol. % methanol.   The electropolishing was done with the solution at 20 ^{o}C, the electrical potential being set at 50 V.

Melted in vacuum furnace (50 kg ingot)

↓

Heated at 1250 ^{o}C for 6 hr

↓

Hot rolled to 50 mm thick plate and air cooled

↓

Heated at 1100 ^{o}C for 2 hr

↓

Hot rolled to 15 mm thick plate and air cooled

↓

Machined to tensile specimens

↓

Austenitized at 830 ~ 980 ^{o}C for 3 min, then oil quenched at 50 ^{o}C

↓

Tempered at 350 ~ 450 ^{o}C for 30 min, then oil cooled (20 ^{o}C)

Tensile test   Microstructure observation
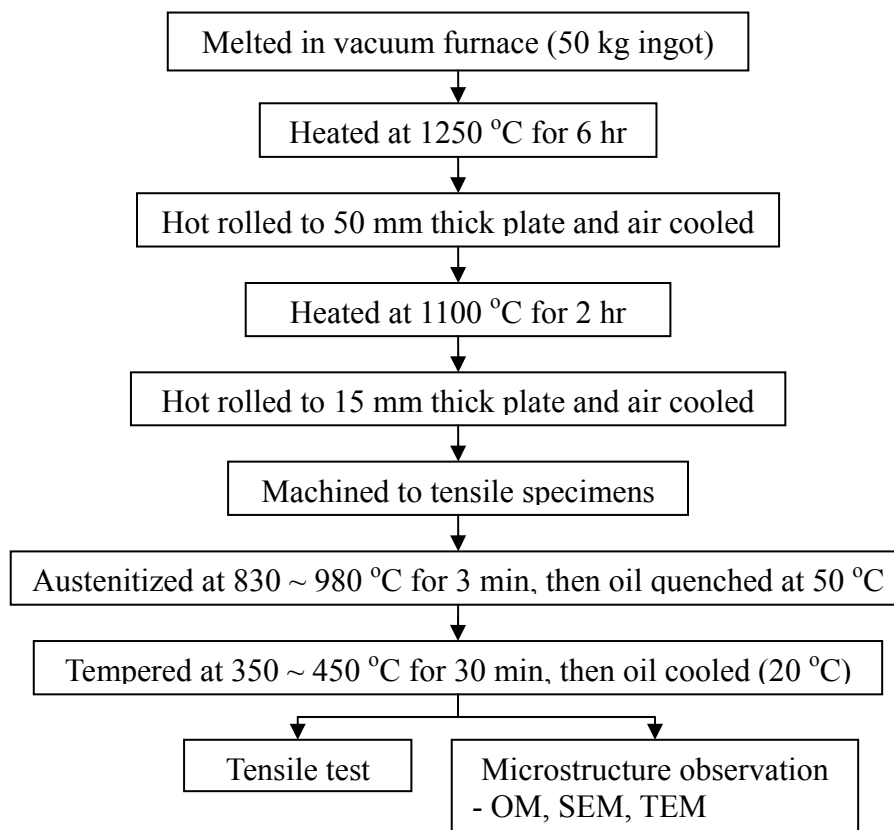   - OM, SEM, TEM

FIGURE 4.1.   Experimental conditions of S1 ~ S5 steels.

4.3 Results and Discussion

4.3.1 Mechanical properties

Tensile tests were carried out as a function of austenitization temperature and tempering temperature. The tensile strength (ultimate tensile strength) and the reduction of area of the experimental steels (S1 ~ S5) are illustrated in Fig. 4.2. These steels were austenitized at 930 and 980 ^{o}C and subsequently tempered at 350, 400 and 450 ^{o}C. The tempering time was always fixed at 30 minutes. Tensile strength decreased with increasing tempering temperatures, but reduction of area of all steels except S5 steel increased as tempering temperature rose. Both the tensile strength and the reduction of area decreased as the austenitization temperature increased from 930 ^{o}C to 980 ^{o}C. Fig. 4.2 (a) and (b) show that when austenitized at 930 ^{o}C, tensile strength was reduced and reduction of area increased a little with increasing the tempering temperature. S5 steel showed a slightly higher strength but an unacceptable RA value for higher tempering temperatures.
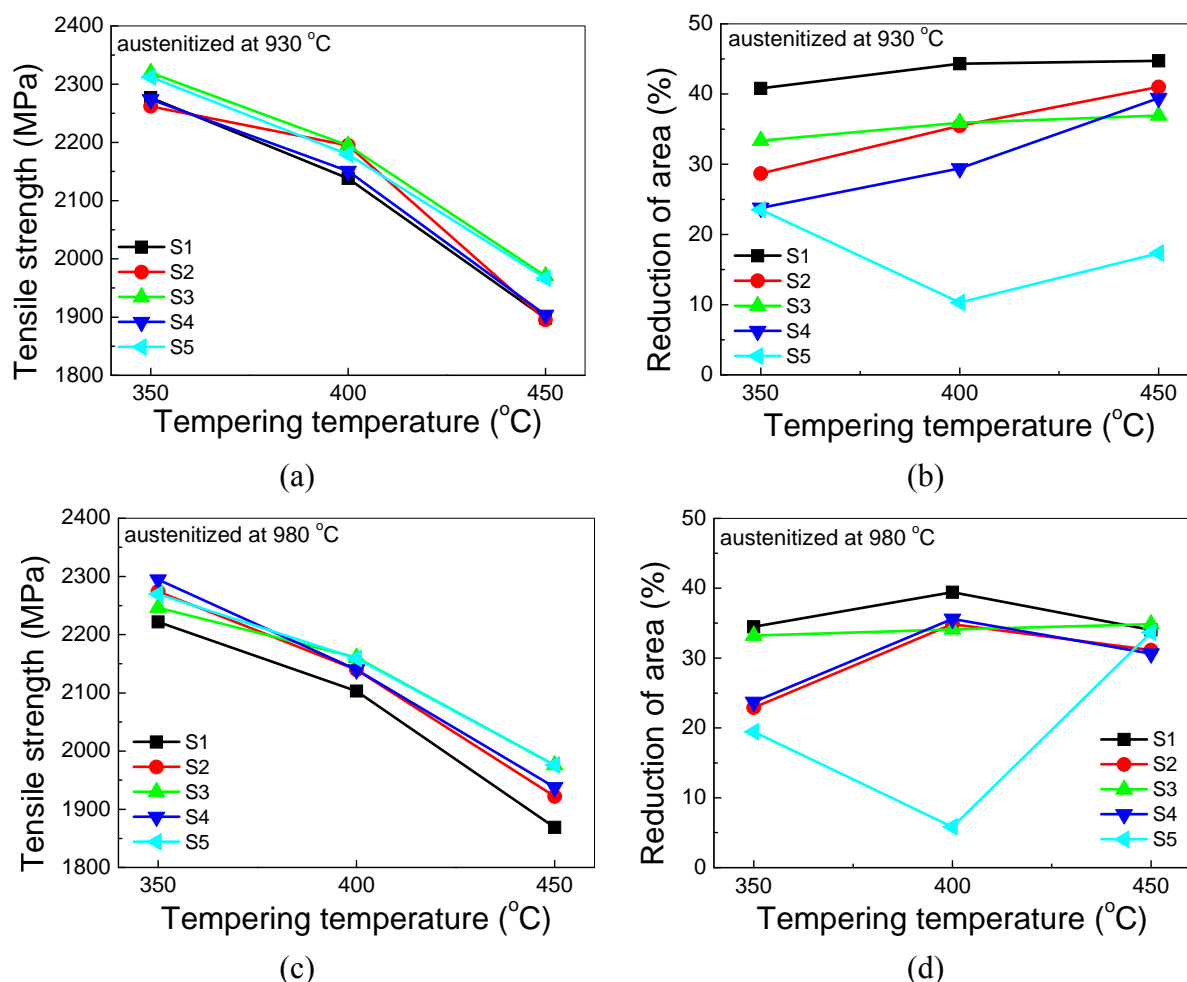

FIGURE 4.2. Tensile property and reduction of area of S1 ~ S5 steels, austenitized at 930 & 980 ^{o}C. (a) tensile properties and (b) reduction of area austenitized at 930 ^{o}C, and (c) tensile properties and (d) reduction of area austenitized at 980 ^{o}C.

Fig. 4.2 (c) and (d) show that when austenitized at 980 ^{o}C, relative to the 930 ^{o}C treatment strength was reduced and reduction of area increased a little with increasing tempering temperature.   S1 steel had the lowest strength and the highest reduction of area and S5 steel showed the reduction of area less than 20 % below similar to the result austenitized at 930 ^{o}C.

For an austenitization temperature of 930 ^{o}C, the reduction of area increased up to around 50 % with increasing tempering temperature, but tensile strength decreased continuously. Fig. 4.2 (a) and (b) show that in case of austenitization temperature 930 ^{o}C and tempering temperature 350 ^{o}C, tensile strength and reduction of area of S1 steel were 2277 MPa and 40.8 %, and these of S3 steel were 2319 MPa and 33.3% respectively.   As shown in Fig. 4.2 (c) and (d), only S3 steels had the desired values of tensile strength and reduction of area at an austenitization temperature 980 ^{o}C.   Tensile strength and reduction of area of S3 steel were 2250 MPa and 33.2 %.   S5 steel had low values of reduction of area regardless of austenitization temperature.
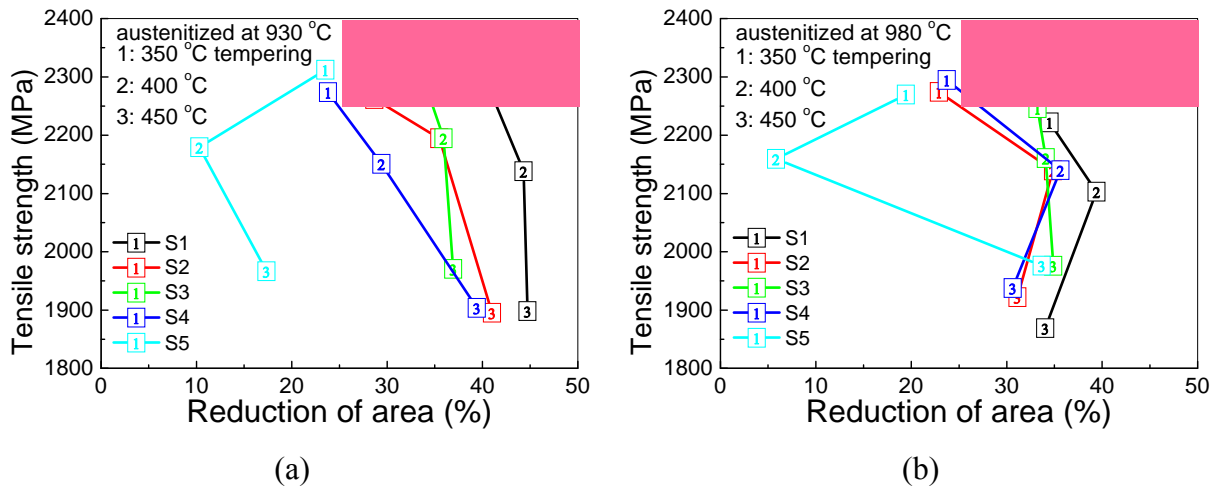

(a)   (b)

FIGURE 4.3.   Tensile properties and reduction of areas of S1 ~ S5 steel.   (a) austenitization temperature 930 ^{o}C and (b) austenitization temperature 930 ^{o}C.

Fig. 4.3 shows the relationship between tensile strength and reduction of area as function of tempering temperature and austenitization temperature.   The target zone of mechanical properties is the box area having tensile strength more than 2250 MPa and a reduction of area more than 25 %.   For the reduction of area, S1 steel had the highest value and S5 steel had the lowest value in all steels.   The steels having a reduction of area more than 25 % are S1, S2, S3 steels austenitized at 930 ^{o}C and S1, S3 steels austenitized at 980 ^{o}C in the range of tempering temperature from 350 ^{o}C to 450 ^{o}C.   Among the S1 ~ S3 steels meeting the desired value of reduction of area, the steels having tensile strength more than 2250 MPa are S1, S3 steels austenitized at 930 ^{o}C and S3 steel austenitized at 980 ^{o}C.   It indicates that only S1 and S3 steels are potential candidates for high strength spring steel.

For S1 and S3 steels, the quenching and tempering treatments were varied in the range of austenitization temperatures of 830 ~ 980 ^{o}C and tempering temperatures of 350 ~ 450 ^{o}C to investigate the possibility of the higher tensile properties and reduction of area.   For S1 steel, when austenitized at 830 ^{o}C, tensile strength was less than 2000 MPa regardless of tempering temperatures and reduction of area was less than 25% below the tempering temperature of

400 °C as shown in Fig. 4.4 (a) and (b).   In the case of tempering temperature 450 °C, tensile strength of S1 steel was abruptly decreased to 1162 MPa but reduction of area recovered from 10 % to 36%.   S1 steel austenitized at 830 °C had the lowest tensile strength and reduction of area relative to that austenitized at other temperatures.
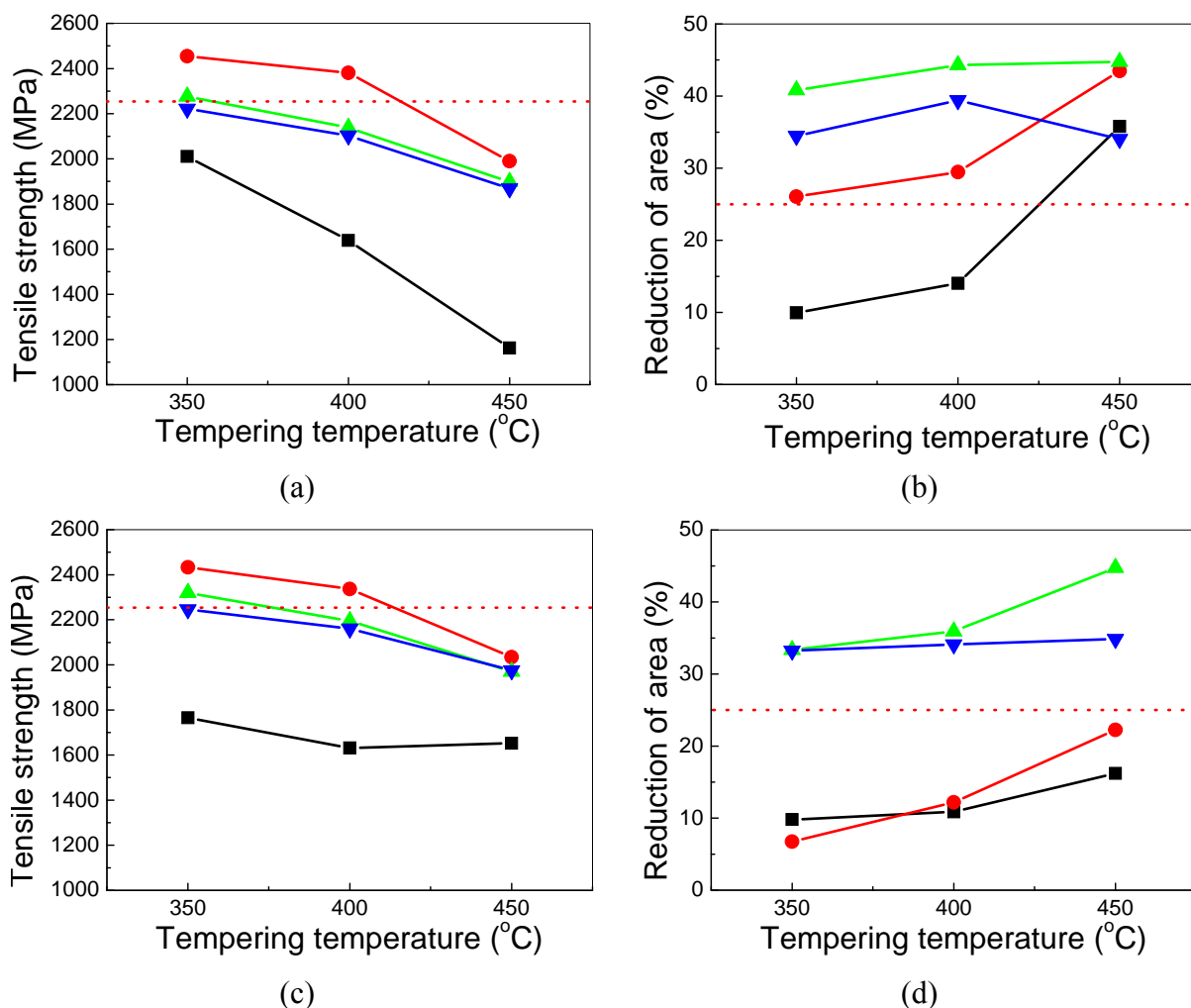

FIGURE 4.4.   Tensile properties and reduction of areas of S1 and S3 steels with increasing the tempering temperature.   (a) tensile properties and (b) reduction of area of S1 steel, and: (c) tensile properties and (d) reduction of area of S3 steel.   (Austenitization temperature: ■ - 830 °C, ● - 880 °C, ▲ - 930 °C, ▼ - 980 °C).

In increasing the austenitization temperature from 830 °C to 880 °C, tensile strength and reduction of area increased on the whole in the range of tempering temperature 350 ~ 450 °C. When austenitized at 930 °C, tensile strength of S1 steel decreased from 1898 MPa to 2277 MPa and reduction of area increased from 40.8 % to 44.7 % with increasing tempering temperature from 350 °C to 450 °C.   To get tensile properties, tempering treatment should be done at around 350 °C.   The candidate conditions of heat treatment for S1 steel are tempering treatment at 350, 400 °C after austenitizing at 880 °C and tempering treatment at 350 °C after austenitizing at 930 °C.

Fig. 4.4 (c) and (d) show that when austenitized at 830 ^{o}C, tensile strength of S3 steel decreased from 1765 MPa to 1652 MPa and reduction of area increased from 9.8 % to 16.2 % with increasing tempering temperature from 350 ^{o}C to 450 ^{o}C.   These properties were below the target property similar to those of S1 steel.   S3 steel austenitized at 830 ^{o}C had the lowest tensile strength and reduction of area in the range of all austenitization temperatures.   In increasing the austenitization temperature from 830 ^{o}C to 880 ^{o}C, tensile strength increased on the whole but reduction of area is similar.   At austenitization temperature of 880 ^{o}C, tensile strength decreased from 2433 MPa to 2034 MPa and reduction of area increased from 6.7 % to 22.2 % with increasing tempering temperature from 350 ^{o}C to 450 ^{o}C.   However, reduction of area of S3 steel is not satisfactory compared with the desired value of 25 % and less than S1 steel.   The difference of S1 and S3 steels is the addition of B and Mo and reduction of area of S3 steel may be related to the addition of these alloying elements.
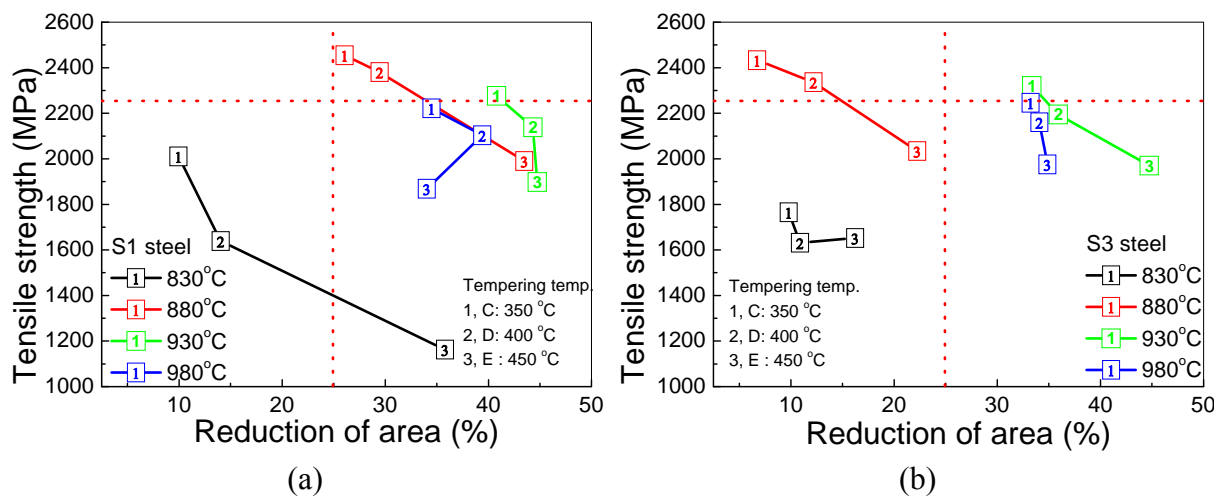

FIGURE 4.5.   Tensile properties and reduction of areas of S1 and S3 steels.   (a) S1 steel and (b) S3 steel.

At an austenitization temperature of 930 ^{o}C, tensile properties were 2319 MPa at tempering temperatures of 350 ^{o}C.   Reduction of area was more than 33 % above tempering temperature of 350 ^{o}C.   Tensile properties were less than 2250 MPa above tempering temperatures of 400 ^{o}C.   The tendency of mechanical properties of S3 steel is similar those of S1 steel.   To get the desired tensile properties, tempering treatment should be done at around 350 ^{o}C.   When increasing the austenitization temperature from 930 ^{o}C to 980 ^{o}C, tensile properties decreased from 1975 MPa to 2246 MPa and reduction of area increased from 33.2 % to 34.8 % with increasing tempering temperature from 350 ^{o}C to 450 ^{o}C. Finally, the condition of austenitization at 930 ^{o}C and tempering at 350 ^{o}C is an optimum condition to get the target properties (tensile strength $\geq$ 2250 MPa and reduction of area $\geq$ 25 %), as shown in Fig. 4.5.

4.3.2   *Microstructure of as-rolled state*

This chapter describes the microstructural changes of S1 ~ S5 steels in as-rolled state, oil-quenched state and tempered state.   Fig. 4.6 shows the optical micrographs of as-rolled
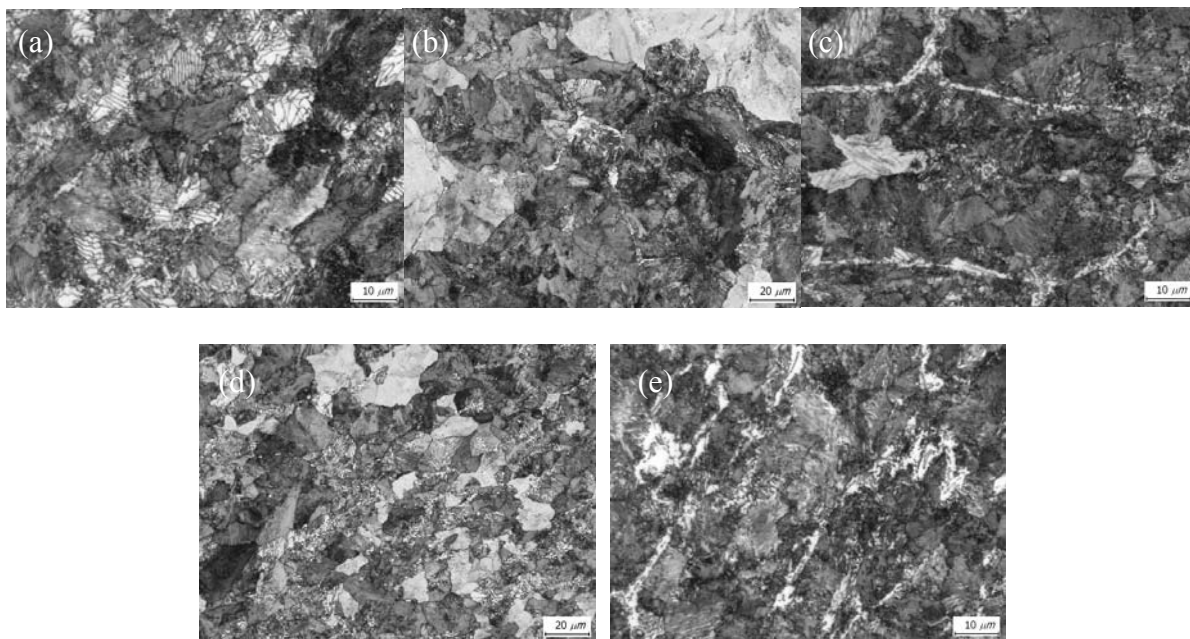
FIGURE 4.6.   Optical micrographs of as-rolled specimen of S1 ~ S5 steels.   (a) S1, (b) S2, (c) S3, (d) S4 and (e) S5 steel.
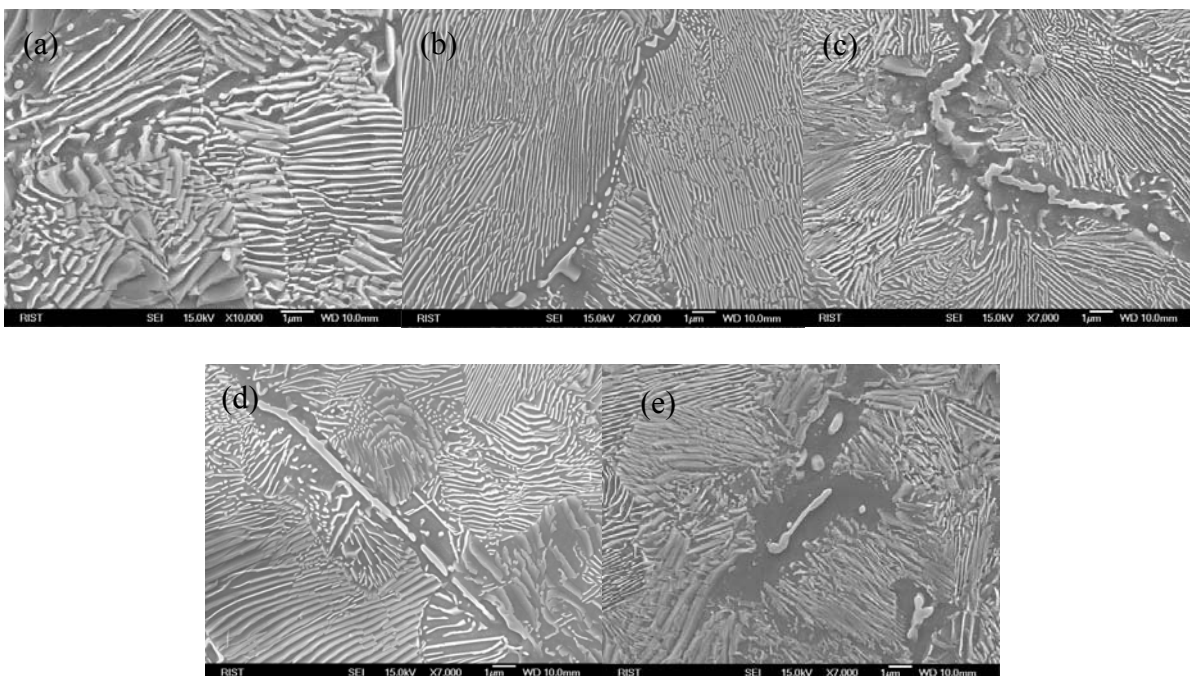

FIGURE 4.7.   SEM micrographs of as-rolled specimens of S1 ~ S5 steels.   (a) S1, (b) S2, (c) S3, (d) S4 and (e) S5 steel.

microstructures of S1 ~ S5 steels.   It is necessary to analyze the microstructure of as-rolled specimens to find a correlation of tempered microstructure and mechanical property.   The microstructure of S1 steel was mainly pearlitic as shown in Fig. 4.6 (a).   Fig. 4.6 (b) ~ (e) show that the microstructure of S2 ~ S5 steels consisted of mainly pearlite and ferrite at grain boundary.   The ferrite at grain boundary should be investigated in detail and it will be necessary to analyze the effect of this ferrite structure on the tempered structure and mechanical property.   Except for the ferrite structure, the microstructure of all steels was pearlitic and comparable.

By using SEM micrography, the microstructure of all steels was investigated in more detail and especially the grain boundary structure was explored.   Fig. 4.7 shows the SEM micrographs of as-rolled specimens of all steels.   As described above, the microstructure of S1 steel was mainly of the pearlite structure and the ferrite did not exist at the grain boundary. Fig. 4.7 (b) ~ (e) illustrate that the microstructure of S2 ~ S5 steels consisted of a mainly pearlite and ferrite structure, as well as carbide at grain boundary.   The carbide was formed along grain boundary and ferrite existed near the carbide.   It is assumed that carbide was firstly formed at austenite grain boundary and subsequently ferrite formed at interface of carbides along austenite grain boundary.

4.3.3   Microstructure of oil quenching and tempering state

The microstructures of oil quenched specimens of S1 ~ S5 steels after austenitizing at 930 ^{o}C are shown in Fig. 4.8.   Microstructure of S1 steel was a conventional martensitic structure. In the case of S2 ~ S5 steels, microstructures were also conventional martensitic structures but carbides existed at austenite grain boundary in Fig. 4.8 (b) ~ (e).   It means that the carbide of as-rolled specimen existed along grain boundary may be incompletely dissolved during austenitization.   This incomplete dissolution may be due to the short time of austenitization holding of 180 second.   Fig. 4.9 shows that microstructure of tempered specimens of S1 ~ S5 steel conventional the tempered martensitic structures.   The carbide along grain boundary was retained in the tempering treatment as shown in Fig. 4.9 (b) ~ (e).   After tempering for 30 min, the oil-quenched structure was changed to tempered martensite but the carbide existing in the oil-quenched state would be retained or grow a little along grain boundary. As a result, the carbide along grain boundary originates from the as-rolled state.   Hence, the tempered microstructure and carbide along grain boundary should be studied to improve the mechanical property.

4.3.4   Microstructure of S1 and S3 steels as a function of austenitization temperature and tempering temperature

Based on the mechanical properties of all steels studied, the S1 and S3 steels were selected as the candidate steels for high strength spring steel.   The reason for selecting both S1 and S3 steels is that tensile properties and the reduction of area of S1 and S3 steels were above the target values.   This chapter describes the microstructural changes of S1 and S3 steel with increasing austenitization temperature and tempering temperature.

Fig. 4.10 shows SEM micrographs of oil quenched specimens of S1 steel.   The as-rolled specimens were austenitized in the range of temperature 830 ^{o}C ~ 980 ^{o}C and subsequently oil
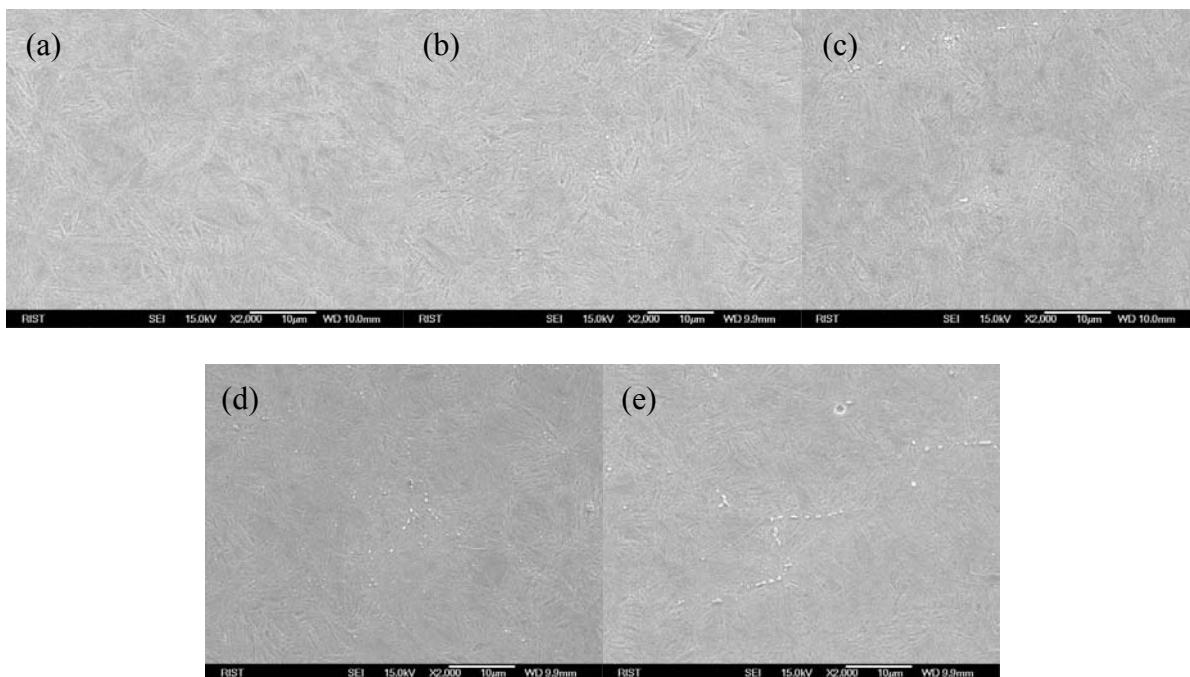
FIGURE 4.8.   SEM micrographs of oil-quenched specimens of S1 ~ S5 steels, austenitized at 930 ^{o}C.   (a) S1, (b) S2, (c) S3, (d) S4 and (e) S5 steel.
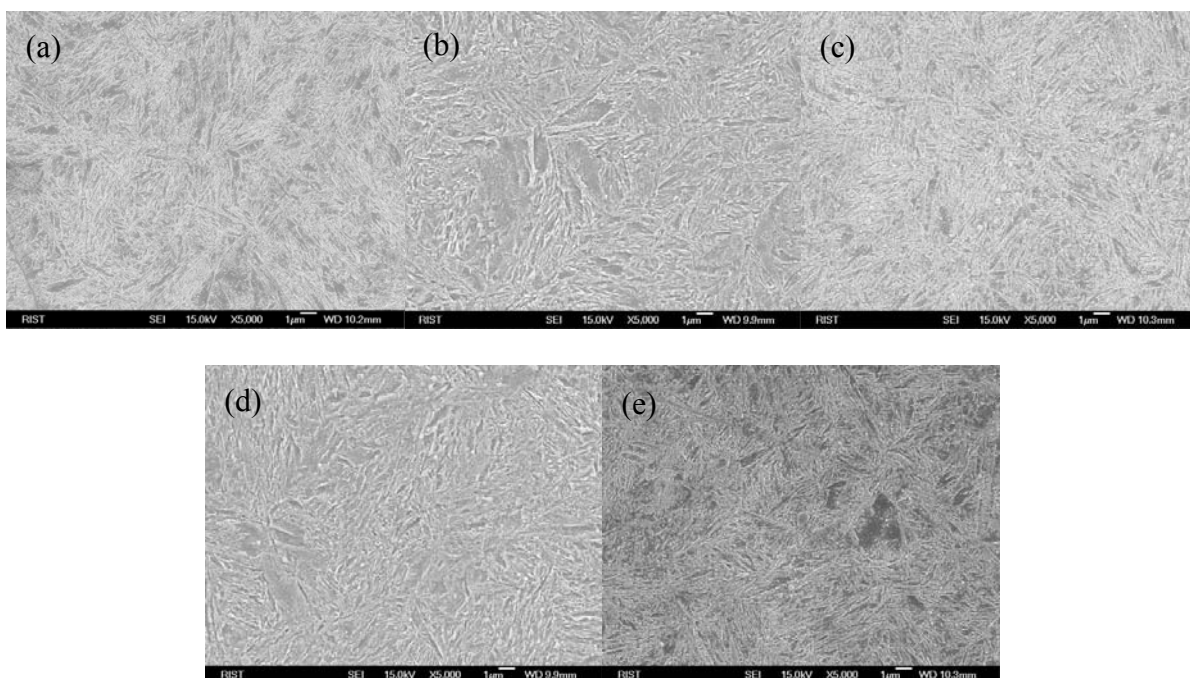

FIGURE 4.9.   SEM micrographs of tempered specimens of S1 ~ S5 steels tempered at 400 ^{o}C (austenitization temperature: 930 ^{o}C).   (a) S1, (b) S2, (c) S3, (d) S4 and (e) S5 steel.

quenched.   At the austenitization temperature of 830 ^{o}C, the microstructure consisted of mainly martensite and as a second phase, coarse carbide particles.   This microstructure is quite different from the microstructure of specimen austenitized at 880 ^{o}C ~ 980 ^{o}C.   It is estimated that at an austenitization temperature of 830 ^{o}C, the microstructure might be incompletely austenitized, and cementite and ferrite might be retained after austenitization for 180 second.   As shown in Fig. 4.10 (b) ~ (d), the microstructure of specimens austenitized at 880 ^{o}C ~ 980 ^{o}C was mainly martensitic and a part of coarse carbide network remained during austenitization, and second phases were not observed.   As the austenitization temperature increased, the second phase was completely dissolved and the coarse carbide was reduced abruptly.

FIGURE 4.10.   SEM micrographs of oil-quenched specimens of S1 steel with the austenitization temperature.   Austenitization temperature: (a) 830 ^{o}C, (b) 880 ^{o}C, (c) 930 ^{o}C and (d) 980 ^{o}C.

Fig. 4.11 shows the SEM micrographs of oil quenched specimens of S3 steel.   The as-rolled specimens were austenitized in the range of temperature 830 ^{o}C ~ 980 ^{o}C and subsequently oil quenched.   At the austenitization temperature of 830 ^{o}C, the microstructure consisted of mainly martensite and a second phase, coarse carbide particles, as shown in Fig. 4. 11 (a).   The microstructure of S3 steel austenitized at 830 ^{o}C is similar to that of S1 steel. This microstructure is again quite different to the microstructure of specimen austenitized at

880 $^{\circ}$C ~ 980 $^{\circ}$C.   It is estimated that at austenitization temperature of 830 $^{\circ}$C, the microstructure may be incompletely austenitized, and cementite and ferrite may be retained after austenitization for 180 second.   As shown in Fig. 4.11 (b) ~ (d), the microstructure of specimens austenitized at 880 $^{\circ}$C ~ 980 $^{\circ}$C was mainly martensitic structure and a part of coarse carbide retained during austenitization, and second phases did not exist.

As the austenitization temperature increased from 830 $^{\circ}$C to 980 $^{\circ}$C, the second phase was completely dissolved and the coarse carbide was reduced abruptly.   However, another carbide different to the coarse carbide was retained along prior austenite grain boundary. The carbides existed along prior austenite grain boundary were very stable and remained in the range of austenitization temperature from 830 $^{\circ}$C to 980 $^{\circ}$C.   Fig. 4.11 shows that the principal difference between S1 and S3 steel was the existence of carbide along the prior austenite grain boundary.
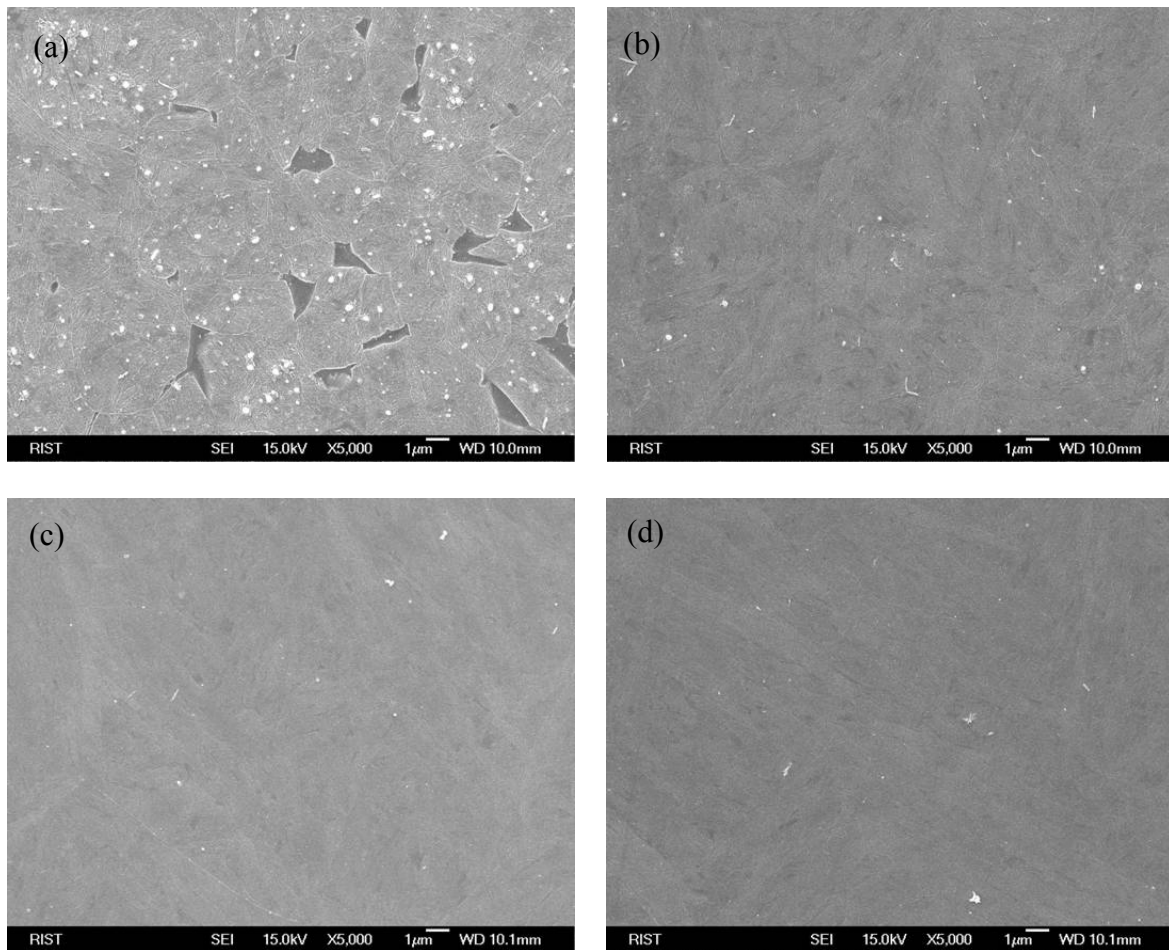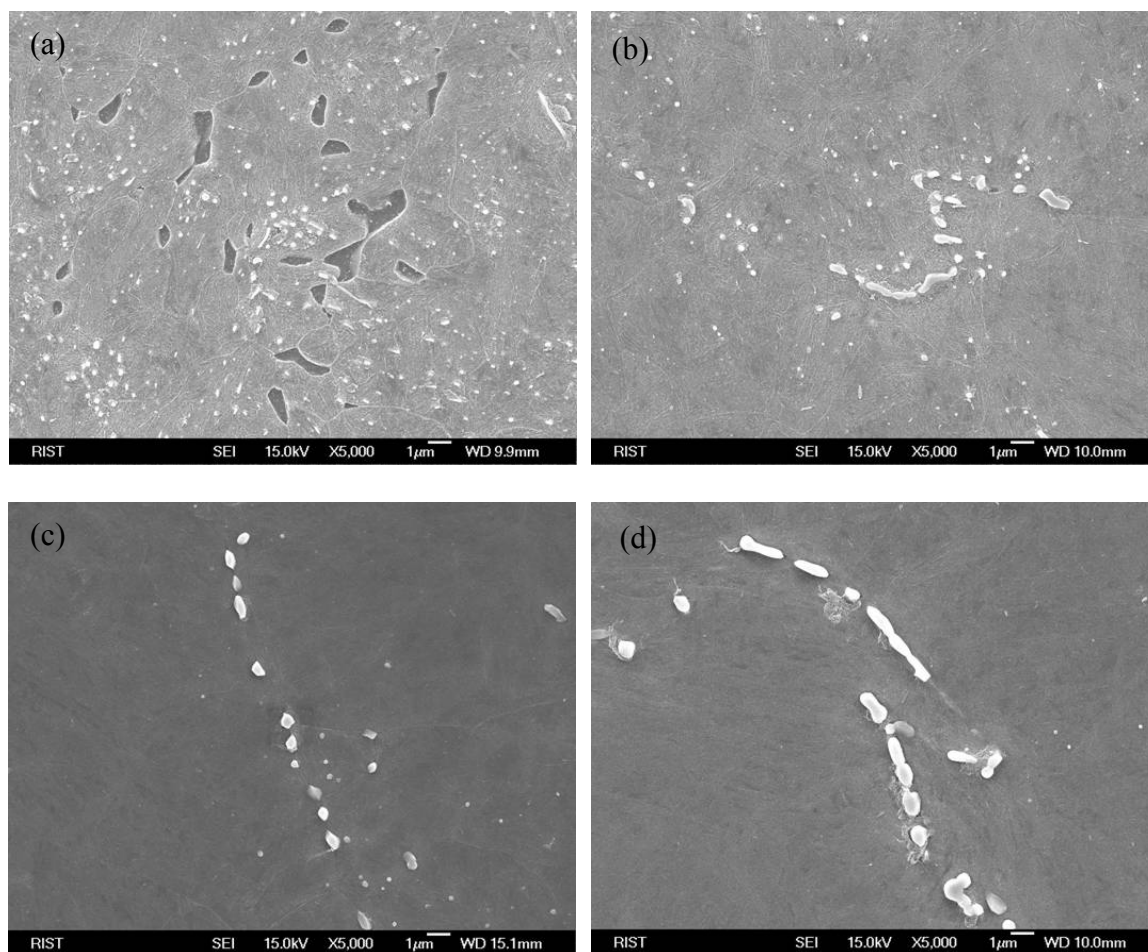

FIGURE 4.11.   SEM micrographs of oil-quenched specimens of S3 steel with austenitization temperature.   Austenitization temperature: (a) 830 $^{\circ}$C, (b) 880 $^{\circ}$C, (c) 930 $^{\circ}$C, (d) 980 $^{\circ}$C.

Fig. 4.12 (a) ~ (c) show the SEM micrographs of tempered specimens of S1 steel austenitized at 880 $^{\circ}$C.   The specimens were etched by nital acid.   The microstructure consisted of tempered martensite and spheroidal carbide regardless of tempering temperatures. It is suggested that spheroidal carbide was retained due to incomplete dissolution during
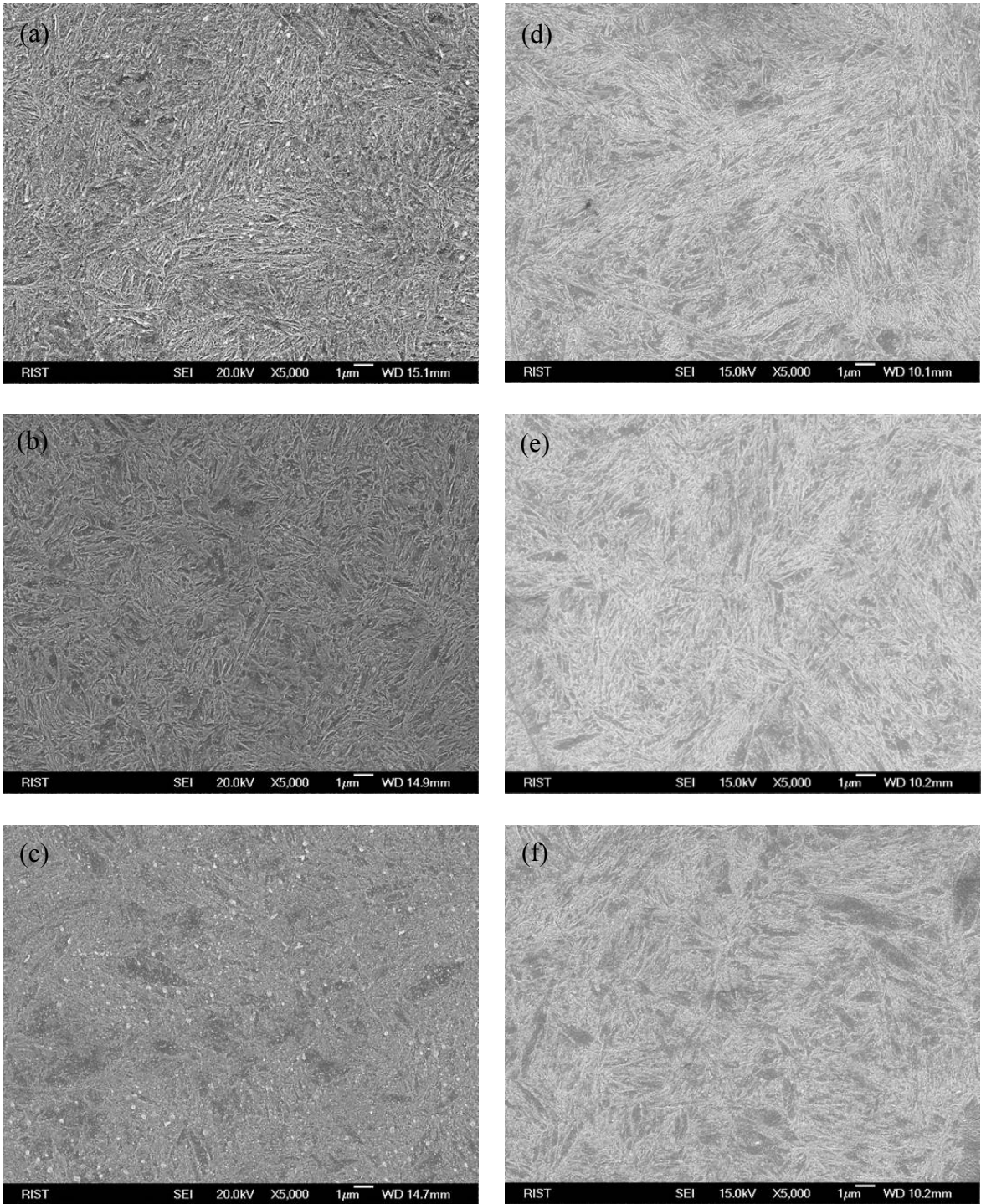
FIGURE 4.12.   SEM micrographs of tempered specimens of S1 steel tempered at (a) 350 ^{o}C, (b) 400 ^{o}C, (c) 450 ^{o}C austenitized at 880 ^{o}C, and at (d) 350 ^{o}C, (e) 400 ^{o}C, (f) 450 ^{o}C austenitized at 930 ^{o}C.

FIGURE 4.13.   SEM micrographs of tempered specimens of S3 steel tempered at (a) 350 $^{\circ}$C, (b) 400 $^{\circ}$C, (c) 450 $^{\circ}$C austenitized at 880 $^{\circ}$C, and at (d) 350 $^{\circ}$C, (e) 400 $^{\circ}$C, (f) 450 $^{\circ}$C austenitized at 930 $^{\circ}$C.

austenitization and might be grown during tempering.   Fig. 4.12 (d) ~ (f) show that when austenitized at 930 ^{o}C, the microstructure of S1 steel consisted of tempered martensite and spheroidal carbide, similar to the microstructure austenitized at 880 ^{o}C.   The spheroidal carbide dimensions decreased with increasing austenitization temperature.

Fig. 4.13 shows the SEM micrographs of tempered microstructures of S3 steel austenitized at 880 and 930 ^{o}C respectively.   The microstructure consists of tempered martensite and spheroidal carbide, longish carbide along austenite grain boundary.   Fig. 4.13 (d) ~ (f) show that when austenitized at 930 ^{o}C, the microstructure of S3 steel consists of tempered martensite and spheroidal carbide, similar to the microstructure austenitized at 880 ^{o}C.   The spheroidal carbide size decreased with increasing the austenitization temperature.   The spheroidal carbide was retained due to incomplete dissolution during austenitization and may have grown during tempering.

The carbide existing along the prior austenite grain boundary after austenitization was retained as always after tempering.   It may be assumed that the reason for decreasing the reduction of area of S3 steel is caused by the existence of carbide along prior austenite grain boundary.   Then, S1 steel had a microstructure consisting of tempered martensite and spheroidal carbide and S3 steel had a microstructure of tempered martensite, spheroidal carbide in the matrix and carbide along the prior austenite grain boundary.

4.4   Conclusion

In the present investigation, the tensile strength and the reduction of area of the 5 steel grades have been studied in order to develop a high strength spring steel without the loss of ductility.   The chemical composition was based on the high C- Si steel and additions of Mo, B and Nb.   With increasing austenitization and tempering temperatures, tensile strength was reduced but reduction of area was increased.   The S1 and S3 steel among the S1 ~ S5 steel grades best met the target properties of tensile strength and reduction of area.   It should be noted that the addition of Mo and B elements was effective in strengthening without the loss of reduction of area.   Microstructures were examined to explain the characteristics of mechanical properties with austenitization and tempering temperature.

The most relevant difference between microstructures of S1 and S3 steels was the existence of carbides along prior austenite grain boundary.   The drop of reduction of area of S3 steel was related the existence of these carbides at prior austenite grain boundary.   The reason of deceasing the tensile strength and reduction of area may be caused by the incomplete austenitization and the existence of carbide along prior austenite grain boundary.   In order to improve the strength and the reduction of area of the proposed steel, it is necessary to analyze in detail the cause of strengthening and softening during quenching and tempering treatment. The detailed study of the S3 embrittlement is done in Chapter 6.

5
Microstructural studies to determine strengthening and softening mechanism

5.1 Introduction

The mechanical properties of quenched and tempered steels are closely related to the change of microstructure during heat treatments. The strength increases when changing from a mixture of ferrite and pearlite to martensite, but the ductility decrease rapidly. The microstructure after heat treatment is complicated and consists of several phases and a large number of precipitates. The steel materials for hot formed springs are always quenched and tempered. In order to achieve higher strength of steels with holding adequate ductility, the tempered martensitic structure is generally used. It is due that a martensite is the hardest microstructure that can be produced in any carbon steel during rapid quenching.

The high hardness, strength and fatigue resistance are the prime reasons for imposing the quenching heat treatments that produce martensite.[2]   Martensite is quite hard but it is also very brittle. The brittleness of martensitic microstructure is due to a number of factors that may include the lattice distortion caused by carbon atoms trapped in the octahedral sites of the martensite, impurity atom segregation at austenite grain boundaries, carbide formation during quenching and residual stresses produced during quenching.

The formation of martensite can be achieved only if the transformation of austenite to mixture of ferrite and cementite is avoided. If the austenitization and / or quenching are incomplete, the full quenched martensite cannot be attained and the microstructure contains

martensite and other phases (ferrite, cementite, austenite).   The incomplete quenched microstructure shows lower hardness, compared with the full martensite.   Even if the same tensile strength is obtained by tempering, the elongation, reduction of area, impact value, ductility, toughness and tensile strength, and fatigue strength become lower, compared with the full martensite starting structure.[12]   Therefore, in order to obtain the desired properties of spring steels fully, complete austenitization and full quench are required.

The hardness of a quenched martensite depends mainly on the carbon content and is relatively little affected by alloying elements.[94]   Alloying elements cause very slight solid solution strengthening, but can slightly increase the hardness by depressing the Ms, causing less autotempering, and thus allowing the carbon content to exert its full hardening effect in the martensite.   Because the quenched martensite is brittle, a tempering treatment is required. Alloying elements are selected to provide both adequate hardenability and the required level of tempering resistance.

5.1.1   Microstructural change during tempering

In general, the relationship of strength and toughness is of major concern in the heat treatment and application of quench and tempered spring steels.   Tempering is the heat treatment of hardened steels that has reduction of brittleness or increased toughness as its major objective.   Ultimately it is the balance of hardness (strength) and toughness required in service that determines the conditions of tempering for a given application.   Tensile strength decreases continuously with increasing the tempering temperature, and elongation and reduction of area increase.   Depending on the amount of tempering, hardness in a given tempered martensite may vary from close to the maximum shown for the quenched martensite to the minimum associated with the spheroidized carbide structure.[2]

Thus, when martensite is tempered, there are many factors to influence the microstructure responsible for the mechanical property changes.   An important series of papers on tempering carbon steels was published by Cohen and his colleagues in the 1950s.[2,12,95-98]

Martensite formed in medium and high carbon steels (0.3 – 1.5 wt.% C) is not stable at room temperature because interstitial carbon atoms can diffuse in the tetragonal martensite lattice at this temperature.   This instability increases between room temperature and 250 ^{o}C. The carbon atom segregation to dislocations and various boundaries may occur during quenching and/or holding at room temperature and carbon atom clustering in as quenched martensite may precede carbide formation that occurs in the first stage of tempering.[2]   The transition carbide that forms in the first stage of tempering was first identified as having a hexagonal structure and designated ε – carbide by Jack.[99]   The ε – carbide ($Fe_{2.4}C$) have carbon contents substantially higher than that of the cementite (Fe_3C) that forms at higher temperatures.   This carbide precipitates as narrow laths or needles on cube planes of the matrix with a well defined orientation relationship.[74]

Austenite retained during quenching is decomposed, usually in the tempering range 230 – 300 ^{o}C.   The transformation of retained austenite during tempering occurs only after the transition carbide is well established.   The retained austenite transforms to mixtures of ferrite and cementite.   The little available evidence suggests that retained austenite decomposes to bainitic ferrite and cementite.[99]

Cementite and ferrite first appears from martensite in the third stage of tempering.   During the third stage of tempering the tetragonality of the matrix disappears and it is then, essentially, ferrite, not supersaturated with respect to carbon.   The most likely sites for the nucleation of cementite are the ε – carbide interfaces with the matrix and the ε – carbide particles gradually disappear as Fe_3C particles grow.[74]   The twins occurring in the higher carbon martensites are also sites for the nucleation and growth of cementite.   A third site for the nucleation of cementite is the interlath boundaries of the martensite and the original austenite grain boundaries.   The cementite can form as very thin films which are difficult to detect. Subsequent changes in the morphology of the cementite particles occur by an Ostwald ripening process, where the smaller particles dissolve in the matrix supplying carbon for the selective growth of the larger particles.

It is useful to define a fourth stage of tempering in which the cementite particles undergo a coarsening process.[2,74]   The final microstructure is an equi-axed array of ferrite grains with coarse spheroidized particle of Fe_3C.   The particles which preferentially grow and spheroidize are located mainly at interlath boundaries and prior austenite boundaries, although some particles remain in the matrix.   The boundary sites are preferred because of greater ease of diffusion in these regions.   A wide range of mechanical properties is obtained by tempering alloy steels between 200 ^{o}C and 700 ^{o}C.   To obtain high strength levels in tempered steels, it is useful to temper at low temperature when the martensite is still heavily dislocated and the main strengthening dispersion is cementite or ε – carbide.[74]   The carbon content has a large influence on the strength.   The toughness decreases, however, with increasing strength.

5.1.2   Strengthening mechanism of tempered martensite of alloy steels

It is generally known that the major portion of the strength of martensite is due to some combination of solid solution strengthening and precipitation strengthening.[2,74,100] However, this conclusion can only apply to plate martensites because in lath martensites the solid solution strengthening is replaced by dislocation density strengthening.[100]   The amount of strengthening due to precipitation depends on the degree of autotempering in any particular case and in generally is quite difficult to determine experimentally.   The interstitial solute, carbon, plays a key role in these mechanisms and little additional strength is obtained from substitutional solutes.   A small increment in strength without loss to ductility may be achieved by reduction of the prior austenite grain size.   Thus, major strengthening mechanisms of tempered martensite are summarized.   The strength cannot be attributed to just one of these mechanisms, but is always the result of combinations of these mechanisms.

5.1.2.1   Solid solution strengthening

This mechanism is the most interesting because of the way in which it is achieved.   It has been shown that solid solution strengthening from substitutional solutes in martensite is quite small, and that essentially all of this type of strengthening comes from interstitial carbon atoms.[100]   It should be realized, however, that substitutional alloying elements indirectly affect the strength of steels by altering the hardenability, the Ms temperature, and the amount of retained austenite.

Because we are able to transform from the high temperature phase to the low temperature phase by a diffusionless martensitic transformation, we can force carbon concentrations into solid solutions of the low temperature phase that are much higher than the values given by the equilibrium solvus line.   Cohen explained the important role that carbon atoms trapped in the octahedral interstitial sites play in the strengthening of martensite.[97]   It is based on the displacement of the iron atoms due to carbons in the body centered tetragonal lattice of martensite.   This distortion of the iron lattice makes the movement of dislocations very difficult and is considered to be a major cause of the high strength of martensite.

The interstitial solid solution of carbon which results in the tetragonality of martensite is a prime candidate for the role of major strengthening factor.[74]   The work of Winchell and Cohen enabled the determination of the yield stress as a function of carbon content under conditions when the carbon were unable to diffuse to form atmospheres and precipitates.[98] While alloying elements are used for various reasons, the most important is the achievement of higher strength in required shape and sizes.   Hardenability is, therefore, of the greatest importance, and one must aim for the appropriate concentration of alloying element needed to fully harden the section of steel under consideration.   The most economical way of increasing the hardenability of a plain carbon steel is to increase the Mn content.   Cr and Mo are also very effective, and are amongst the cheaper alloying additions per unit of increased hardenability.   Boron has a particularly large effect when added to a fully deoxidized low carbon steel.   The effect of alloying elements on hardness changes produced by tempering martensitic carbon and low alloy steels has been summarized in the investigation by Grange, Hribal and Porter.[101]

The strong carbide formers, as discussed relative to secondary hardening, do not have a large effect until high temperatures are reached.   However, Ni has a very small and constant effect on tempered hardness at all temperatures, and since it is not a carbide forming element, its influence is considered to be due to a weak solid solution strengthening effect.   Si has a substantial retarding effect on softening around 316 ^{o}C, an effect attributed to its inhibition of the transformation of the low temperature transition carbide to the more stable cementite.[102]   Mn at low tempering temperatures has little effect on softening, but at higher temperatures it has a strong effect, perhaps because of the incorporation of Mn into the carbides at higher temperatures and the attendant resistance to cementite coarsening that is associated with Mn diffusion.[103]

5.1.2.2   Dislocation strengthening

The dislocation density in plate martensite is relatively low.   However, in lath martensite the dislocation density is found to increase to extremely high values as the carbon content increases.[100]   Most of the carbon is not in solution and this carbon segregates to dislocations and lath boundaries during quenching and is extremely effective at causing the effective dislocation density to increase.   It is also to be expected that carbon atoms are segregated to the high dislocation population in martensite, bearing in mind the strong interactions found in ferrite.   Consequently, in these lath martensites a large portion of the strength is due to the high dislocation density, and only a small portion can be attributed to solid solution hardening.

5.1.2.3   Grain refining

Austenitic grain size has also been observed to affect the strength of martensite in carbon steel.   When the austenite grain size is reduced, significant increases in strength occur.   The relationship between austenite grain size and martensite structure is a result of the unique structure of martensite.   The martensite laths are arranged in packets whose size is directly related to austenite grain size.   Since the first formed martensite plates grow clear across the individual grains it is possible to reduce the martensite plate size by decreasing the prior austenite grain size.   As expected, the reduced martensite plate size does increase the strength and fortunately it is done so without loss in ductility.   Similar strengthening without loss in ductility is obtained by reducing prior austenite grain size in lath type martensites.[100]   Thus either martensite lath packet size or austenite grain size may be used to correlate with mechanical properties.   Yield strength increases with decreasing martensite lath packet size in Fe-0.2%C alloy steel.[2]   While many of these boundaries are really low angle subboundaries, they do present obstacles to dislocation movement and must, therefore, be considered to make some contribution to the overall strength.[74]

5.1.2.4   Precipitation strengthening

Since the martensite phase is highly supersaturated with carbon, there will be a strong tendency for the carbon atoms to segregate to interfaces or crystal defects and to precipitate from solutions as a carbide.   The end result of tempering is a fine dispersion of carbides in an α-iron matrix which often bears little structural similarity to the original as-quenched martensite.[2]   However, this phenomenon leads to precipitation of iron carbide on the dislocations which is responsible for the increase in strength shown by martensite aged at room temperature or just above.   Also martensites with relatively high Ms temperatures will form cementite dispersion during the quench (autotempering) which will also make some contribution to the observed strength.

Certain alloying elements also help to retard the rate of softening during tempering.   The most effective elements are strong carbide formers such as Cr, Mo and V.   Without these elements, plain carbon steels soften rapidly with increasing tempering temperature.   This softening is generally due to the rapid coarsening of cementite with increasing tempering temperature, a process dependent on the diffusion of carbon and iron.   However, the carbide forming elements not only retard softening but also form fine alloy carbides that produce a hardness increase at higher tempering temperatures.   This strength increase is referred to as secondary hardening.   In steels containing sufficient carbide-forming elements alloy carbides are formed above 500 $^{\mathrm{o}}$C where substitutional diffusion becomes significant.   These carbides replace the less stable cementite which dissolves as a finer alloy carbide dispersion forms.

Especially, Vanadium is widely used as a strong carbide former and, in steel with as little as 0.1 % V, the face centered cubic vanadium carbide VC is formed.   It is often not of stoichiometric composition, being frequently nearer V_4C_3, but with other elements in solid solution within the carbide.[74]   An orientation relationship between V_4C_3 and the ferrite matrix has been reported.[95,96] V_4C_3 forms as platelets lying on $\{100\}_\alpha$ planes.   Above 500 $^{\mathrm{o}}$C, V_4C_3 precipitates as very fine particles, of length less than 20–30 $^{\circ}$A.   Shingo and Bhadeshia reported that V_4C_3 is the stable phase in the Fe-C-V system.[106]

5.1.3   Changes of strength and reduction of area for the proposed steels

The tensile properties of S1 and S3 steels exceeded the desired values.   When tempered at 350 ^{o}C after austenitized at 880 ^{o}C, tensile strengths of S1 reached their highest value of 2454 MPa and a reduction of area of 26 %, i.e. more than desired value of 25 %.   With increasing tempering temperature, tensile strength decreases and reduction of area increases typically. As austenitization temperature decreases from 980 ^{o}C to 880 ^{o}C, tensile strength increases but reduction of area decreases rapidly.   Both tensile strength and reduction of area decrease rapidly at austenitization temperature of 830 ^{o}C.   For S3 steel, tensile strength is 2319 MPa and reduction of area is 34 % when tempered at 350 ^{o}C after austenitized at 930 ^{o}C.   Tensile strength decreases continuously and reduction of area increases with a tempering temperature increased.   However, when austenitized at 830 and 880 ^{o}C, reduction of area is less than 25 % in range of tempering temperature of 350 ~ 450 ^{o}C.   As austenitization temperature decreases from 980 ^{o}C to 880 ^{o}C, tensile strength increases and reduction of area holds above 25 %, but drops up to 10 % at austenitization temperature 880 ^{o}C.   Tensile strength and reduction of area decrease rapidly at austenitization temperature of 830 ^{o}C.

As described above, tensile strength and reduction of area of S1 and S3 steels varies with austenitization and tempering conditions.   Microstructural changes and carbides are of great importance in obtaining reliable mechanical properties in S1 and S3 steels.   Especially, they play a very important role in controlling the microstructure and obtaining the required strength.   A great deal of experimental work has been carried out to analyze the strengthening mechanism.

5.2   Experimental methods

5.2.1   Optical and SEM metallography

Specimens for optical microscopy observation were hot mounted in bakelite molding powder, ground with silicon carbide paper down 1200 grit and then polished with 6 and 1 μm diamond pastes.   The specimens wee then etched with 2 vol. % natal (nitric acid in methanol).   The optical microstructures were observed using an Olympus microscope.   The etched specimens were gold-coated in vacuum atmosphere.   SEM was performed using JEOL JSM-7000F field emission scanning electron microscope.

5.2.2   TEM metallography

TEM was performed using Philips transmission electron microscopes operated at 200 kV. Two types of specimens were examined using TEM equipped with an energy dispersive X-ray (EDX) unit; thin foils and carbon extraction replicas.   Thin foils were sliced from bulk specimens as 3 mm diameter discs approximately 250 μm in thickness using a silicon carbide blade and cooling lubricant.   After slicing, the specimens were ground with silicon carbide paper to around 50 μm thickness.   Electropolishing was conducted using a twin jet electropolisher.   The solutions for electropolishing were 5 vol. % perchloric acid, 20 vol. % glycerol and 75 vol. % methanol.   The electropolishing was performed with the solution at 20 ^{o}C, the electrical potential difference being set at 50 V.

Carbon replica specimens were also prepared from each sample for TEM examination. By eliminating effects due to the steel matrix, the size and the chemical composition of the carbides may be measured more accurately. Single stage extraction replicas were prepared. The sample was polished mechanically by the same method as for optical microscopy, and chemically etched with 4 vol. % nital for few seconds. A carbon coating of 20 ~ 30 nm was deposited in a vacuum of 10^5 torr onto the etched surface. This film was then scored with a sharp blade to divide it into several smaller squares (about 1 mm^2). Electrolytic etching in a solution of 5 % hydrochloric acid in methanol at 7.5 V was used to remove the carbon film, which was then washed in methanol and floated off in distilled water. Each sample yielded approximately ten smaller squares of film which were mounted on copper grids and dried before examination in the TEM.

5.3   Results

5.3.1   Change of mechanical properties due to incomplete austenitization

As described in Chapter 4, tensile strength and reduction of area were reduced seriously in the case of the austenitization temperature of 830 ^{o}C. It was well known that austenitization behavior was related to the temperature and holding time. Especially, in the case of quenched and tempered steels, the mechanical property is mainly affected by the microstructural change during heat treatment and based on the tempered martensitic structure. If austenitization was not done completely, the microstructure would consist of martensite and ferrite+cementite. These microstructures could be caused the drop of mechanical property due to the soft ferrite and coarse cementite.
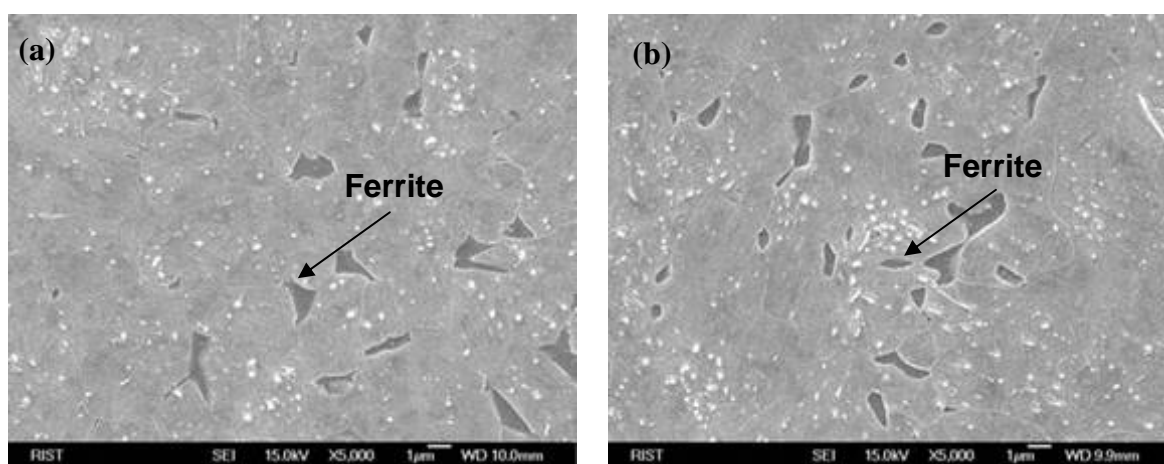

FIGURE 5.1.   SEM micrographs of oil-quenched steels, austenitized at 830 ^{o}C.   (a) S1 steel and (b) S3 steel.

In order to check the existence of ferrite after quenching, the microstructures of oil-quenched specimens were investigated. Fig. 5.1 shows the SEM micrographs of oil-quenched specimens of S1 and S3 steel austenitized at 830 ^{o}C. For S1 and S3 steels, the

second phase in martensitic structure existed along grain boundary and coarse cementite was retained to be undissolved during austenitization.   Fig. 5.2 shows the TEM micrographs and diffraction patterns of oil-quenched specimens of S1 and S3 steel austenitized at 830 $^{\circ}$C. The second phase in martensitic structure of S1 and S3 steels was confirmed to be the ferrite structure by TEM images and diffraction patterns.   Fig. 5.2 (b) shows the diffraction pattern of ferrite structure of S1 steel having zone axis [111].   Fig. 5.2 (d) shows the diffraction pattern of ferrite structure of S3 steel having a zone axis [011].
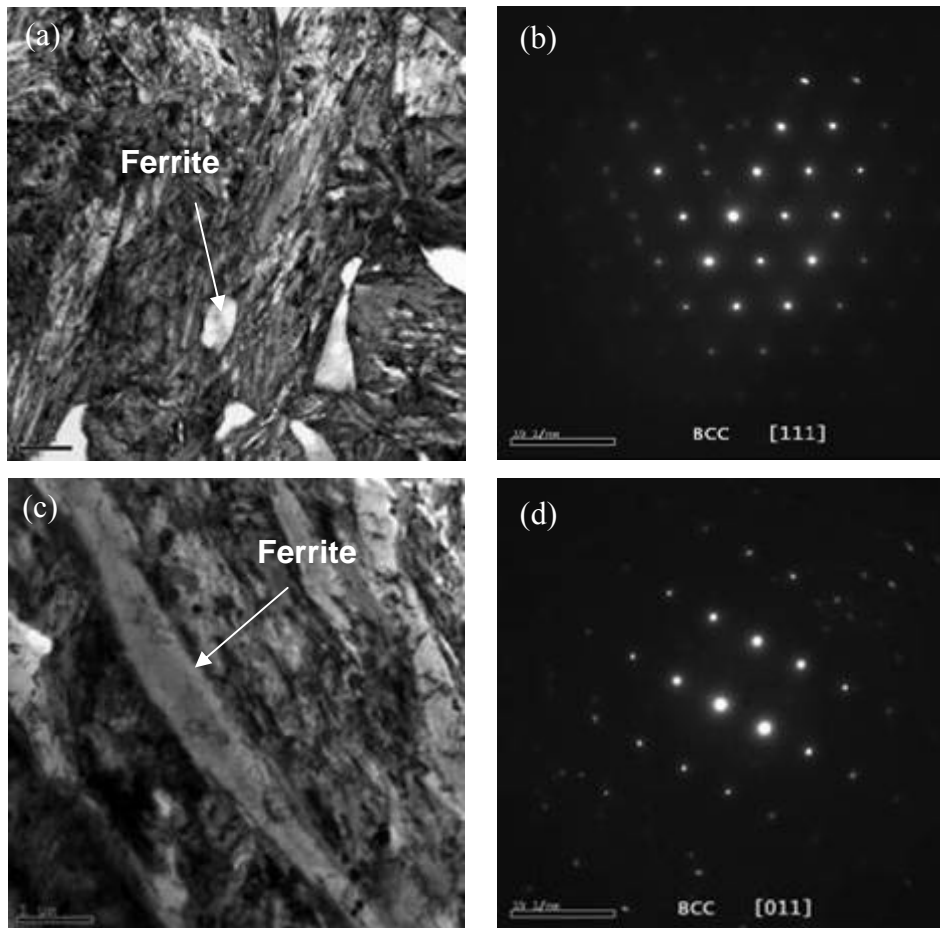
FIGURE 5.2.   TEM micrographs of oil-quenched S1 and S3 steels, austenitized at 830 $^{\circ}$C. (a) Bright field image, (b) Diffraction pattern of S1 steel and (c) Bright field image, (d) Diffraction pattern of S3 steel

As follows from SEM and TEM micrographs, the microstructure of S1 and S3 steels austenitized at 830 $^{\circ}$C consisted of martensite and ferrite, cementite regardless of tempering temperature.   The reason for the existence of ferrite in martensitic structure after quenching is caused by the incomplete austenitization due to the lower temperature of austenitization. The ferrite in martensitic structure was not investigated in the range of austenitization temperature from 880 $^{\circ}$C to 980 $^{\circ}$C.   The holding time of austenitization was set as 180 minutes for all conditions.

Therefore, the drop of tensile strength and reduction of area might be caused the existence

of ferrite by incomplete austenitization.   The ferrite existed along grain boundary and coarse cementite was retained in the grain and grain boundary.   These characteristics of microstructure were induced easily the crack formation and propagation along grain boundary.

5.3.2   Precipitation behavior

Alloy carbides play an important role in the development of spring steels.   It is well known that the addition of a certain substitutional alloying elements modify the tempering characteristics of martensite.   The precipitates in the proposed S1 and S3 steels were investigated as V_4C_3, and $Fe_{2.4}C$, cementite (Fe_3C).   The precipitation behavior in S1 and S3 steels was studied with changing the conditions of heat treatments.

5.3.2.1 V_4C_3 precipitation

TEM observations incorporated with EDX analyses provide an insight into the precipitation behavior as a function of tempering temperature.   Fig. 5.3 shows TEM images and chemical compositions of precipitates in carbon extraction replicas of as-rolled specimen of S1 and S3 steels.   Compositions of precipitates were estimated using energy dispersive X-ray spectroscopy on the carbon extraction replicas.   Fig, 5.3 illustrates that before austenitization treatment, V carbides already existed in as rolled specimens of S1 and S3 steels.   It is to be noted that the V carbides formed during hot rolling and cooling.
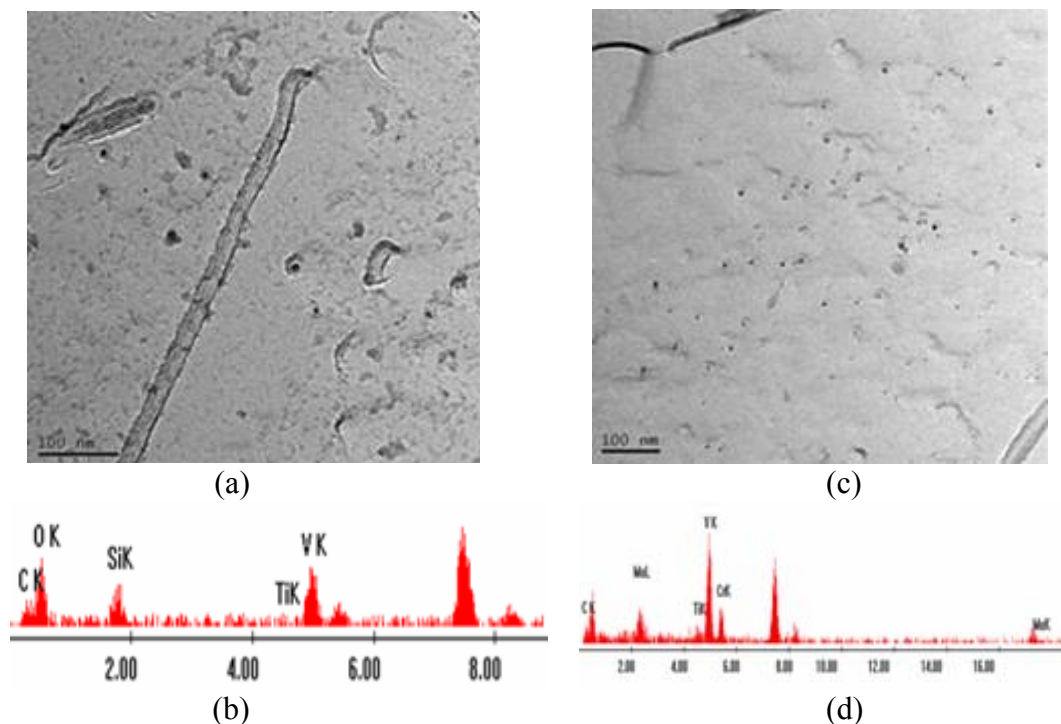

FIGURE 5.3.   TEM micrographs and EDX results of as-rolled specimens of S1 and S3 steel. (a) Replica image and (b) EDX analysis of S1 steel and (c) Replica image and (d) EDX analysis of S3 steel.

After austenitization, the V carbides in oil-quenched specimens of S1 and S3 steel were investigated.   Fig. 5.4 shows TEM images and diffraction pattern, chemical compositions of oil-quenched specimens of S1 steel.   The as-rolled specimens were oil-quenched after austenitizing for 180 seconds at 880 ^{o}C.   Fig. 5.4 illustrates that the V carbides also existed in oil-quenched microstructure and were examined as V_4C_3 having FCC structure of zone axis [110].   It indicates as shown in Fig. 5.4 (c) that the sphere shaped precipitates have a face centered cubic lattice with the same lattice parameter as V_4C_3 (4.2 Å) from diffraction patterns of extraction replicas.[104]   Compositions of precipitate were estimated using energy dispersive X-ray spectroscopy on the carbon extraction replicas, as shown in Fig. 5.4 (d).   The chemical composition of carbide consists of metallic elements (V, Ti) and carbon. It means that V_4C_3 carbide is replaced as $(V, Ti)_4C_3$ carbide by substituting Ti to V_4C_3 carbide. It is suggested that these $(V, Ti)_4C_3$ carbides were retained to be undissolved and / or formed during austenitization.
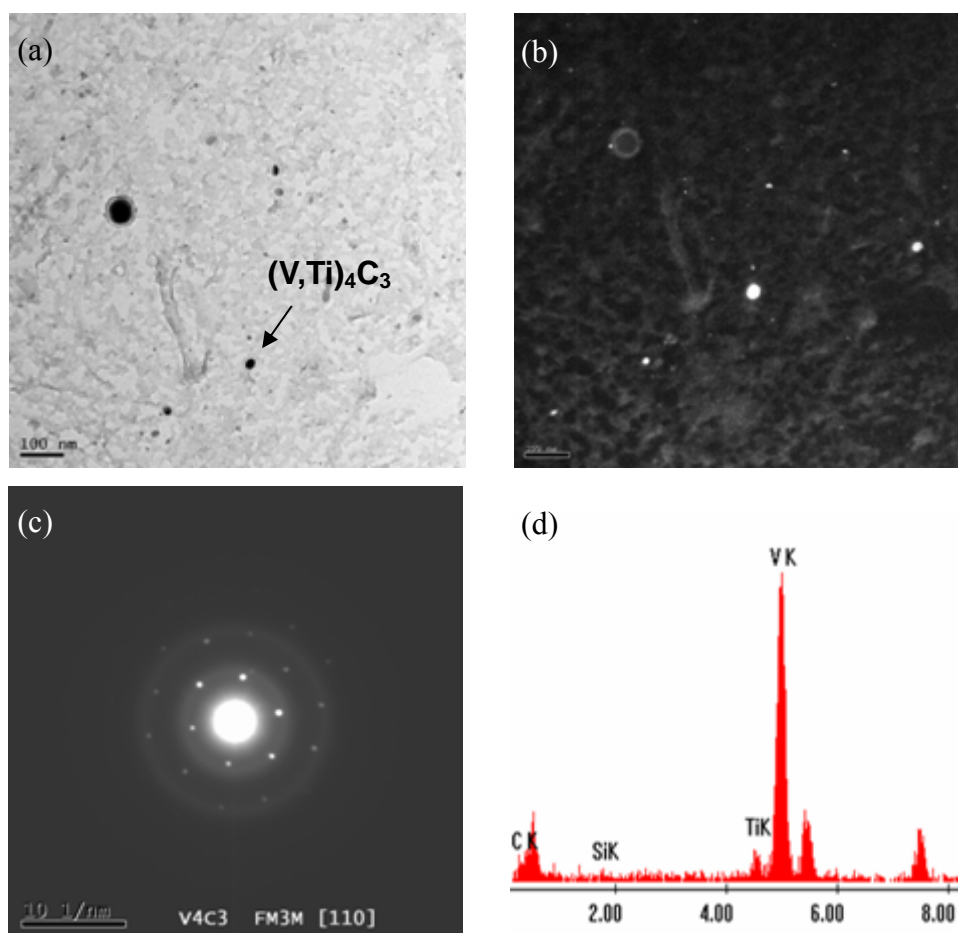

FIGURE 5.4.   TEM replica micrographs of $(V, Ti)_4C_3$ carbide in the oil-quenched S1 steels (austenitizing at 880 ^{o}C).   (a) bright filed image (b) dark filed image (c) diffraction pattern (d) EDX analysis.

The precipitation behavior of the V carbide in oil-quenched microstructure of S1 steel was investigated.   Fig. 5.5 shows the behavior of $(V, Ti)_4C_3$ precipitates of S1 steel as the austenitization temperature increased.   The fine precipitates were determined as $(V, Ti)_4C_3$

and coarse precipitates were cementite.   Fine $(V, Ti)_4C_3$ carbides were remained to be undissolved and /or formed newly at all temperatures of austenitization.
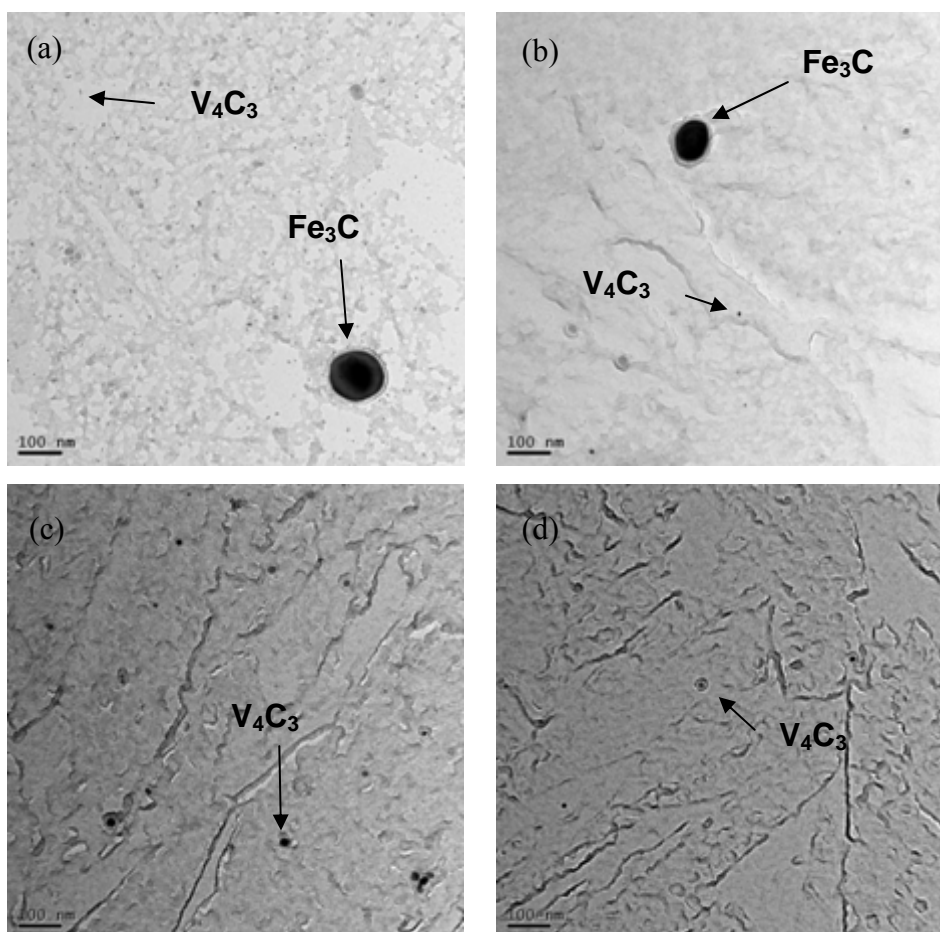

FIGURE 5.5.   TEM replica micrographs of V_4C_3 carbide in the oil-quenched specimens of S1 steel.   Austenitization temperature: (a) 830 ^{o}C, (b) 880 ^{o}C, (c) 930 ^{o}C, (d) 980 ^{o}C.

For S3 steel, the V carbides in oil-quenched microstructure were also investigated.   The as-rolled specimens were oil-quenched after austenitizing for 180 seconds at 880 ^{o}C. Fig. 5.6 shows TEM images and diffraction pattern, chemical compositions of oil-quenched specimens of S3 steel.   The V carbides in oil-quenched microstructure were V_4C_3 structure as shown in Fig. 5.6 (c).   These pictures were taken from the [211] orientation of the matrix.   Fig. 5.6 illustrates that the spherical shaped precipitates have a face centered cubic lattice with the same lattice parameter as V_4C_3 (4.2 Å) from diffraction patterns of extraction replicas, similar to that of S1 steel.

Compositions of precipitate were estimated using energy dispersive X-ray spectroscopy on the carbon extraction replicas, as shown in Fig. 5.6 (d).   It was found that chemical composition of carbide consists of metallic elements (V, Ti, Mo) and carbon.   It means that V_4C_3 carbide is replaced as $(V, Ti, Mo)_4C_3$ carbide by substituting Ti and Mo to V_4C_3 carbide. It is suggested that these $(V, Ti, Mo)_4C_3$ carbides were retained to be undissolved and / or formed during austenitization.
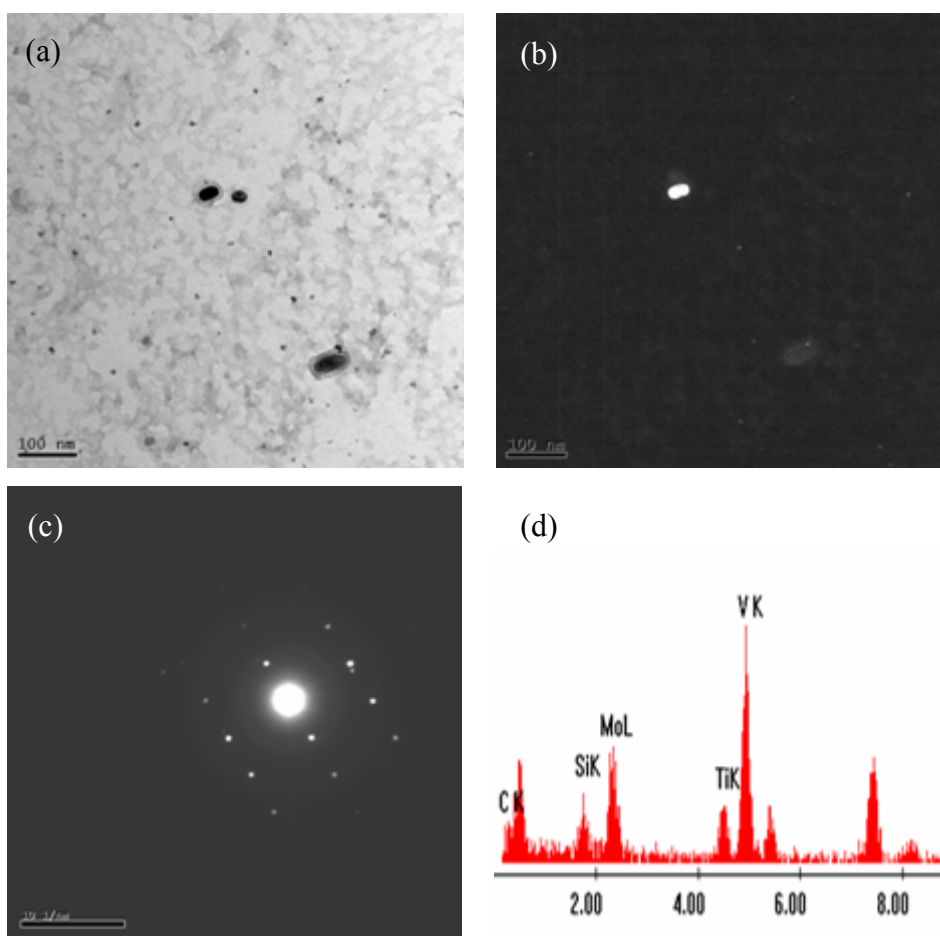
FIGURE 5.6.   TEM replica micrographs of (V, Ti, Mo)$_4$C$_3$ carbide in the oil-quenched S3 steels (austenitizing at 880 ^{o}C).   (a) Bright filed image (b) Dark filed image (c) Diffraction pattern (d) EDX analysis.

For austenitization temperatures from 830 ^{o}C to 980 ^{o}C, the precipitation behavior of the V carbide in oil-quenched microstructure of S3 steel was investigated.   Fig. 5.7 shows the behavior of (V, Ti)$_4$C$_3$ precipitates of S1 steel as the austenitization temperature increased. As shown in Fig. 5.7, fine precipitates of S3 steel were (V, Ti, Mo)$_4$C$_3$ and coarse precipitates were cementite.   Fine (V, Ti)$_4$C$_3$ carbides were remained to be undissolved and /or formed newly at all temperatures of austenitization.

The size distributions of (V, Ti)$_4$C$_3$ and (V, Ti, Mo)$_4$C$_3$ carbides in oil-quenched specimens of S1 and S3 steels austenitized at 880 ^{o}C were measured and compared as shown in Fig. 5.8. Mean diameter of (V, Ti)$_4$C$_3$ carbide of S1 steel was around 0.0075 um and that of (V, Ti, Mo)$_4$C$_3$ carbide of S3 steel was around 0.0073 um.   The size distributions of V carbides in S1 and S3 steel were similar.   It is suggested that the size distribution of V carbides of S1 and S3 steels are almost equal for the same temperature of austenitization.

Fig. 5.9 shows that the (V, Ti)$_4$C$_3$ carbide of S1 steel were distributed as fine precipitates in the microstructure tempered at 450 ^{o}C after austenitized at 880 ^{o}C.   As described above, the (V, Ti)$_4$C$_3$ carbides were already retained in oil-quenched specimens.   The (V, Ti)$_4$C$_3$ carbide

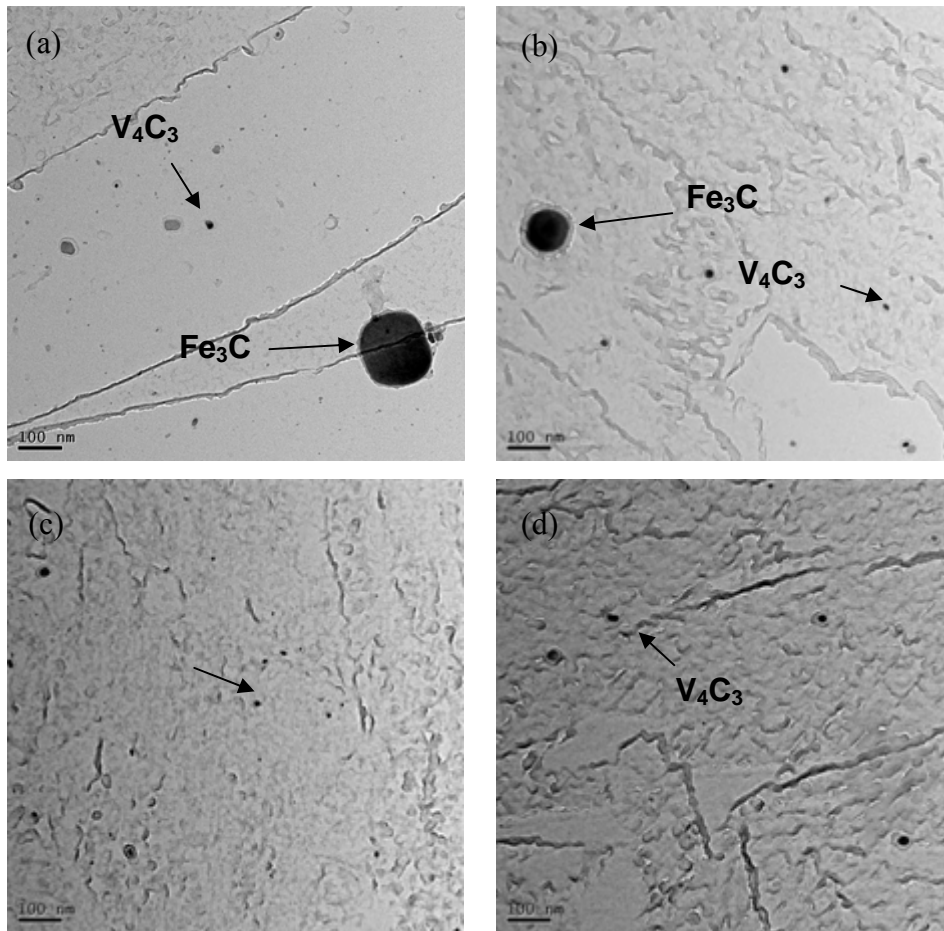in tempered structure was equal to that in oil-quenched specimens.   These pictures were

FIGURE 5.7.   TEM replica micrographs of V_4C_3 carbide of oil-quenched specimens of S3 steel, austenitized at (a) 830 ^{o}C, (b) 880 ^{o}C, (c) 930 ^{o}C, (d) 980 ^{o}C.
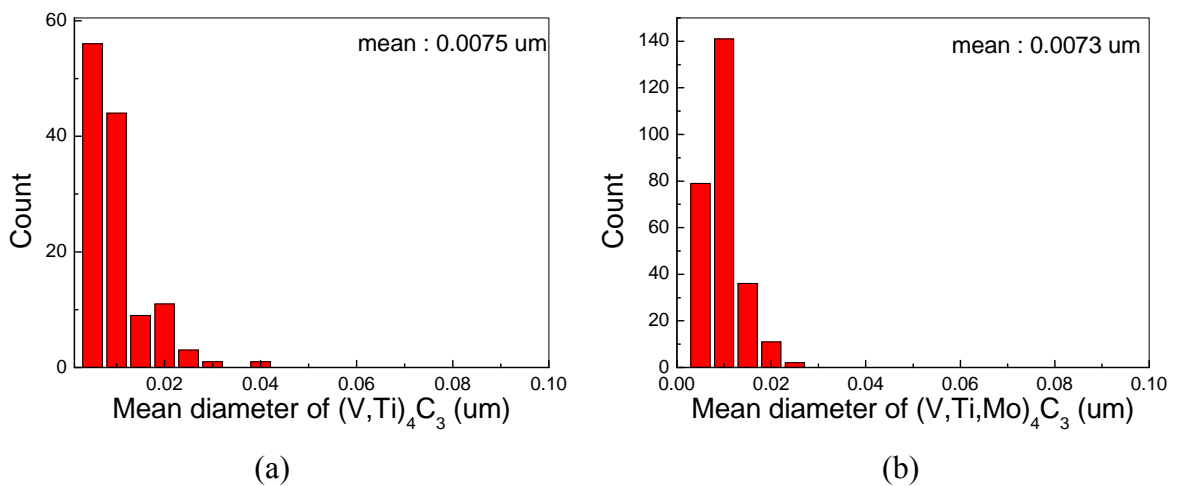

FIGURE 5.8.   Size distribution of V carbides in the oil-quenched specimens austenitized at 880 ^{o}C.   (a) $(V, Ti)_4C_3$ of S1 steel and (b) $(V, Ti, Mo)_4C_3$ of S3 steel.

taken from the [110] orientation of the matrix.   Diffraction patterns from extraction replicas confirmed that the sphere-shaped precipitates have a face centered cubic lattice with the same lattice parameter as V_4C_3 (4.2 Å).   It notes that the $(V, Ti)_4C_3$ carbide would grow continuously during tempering.
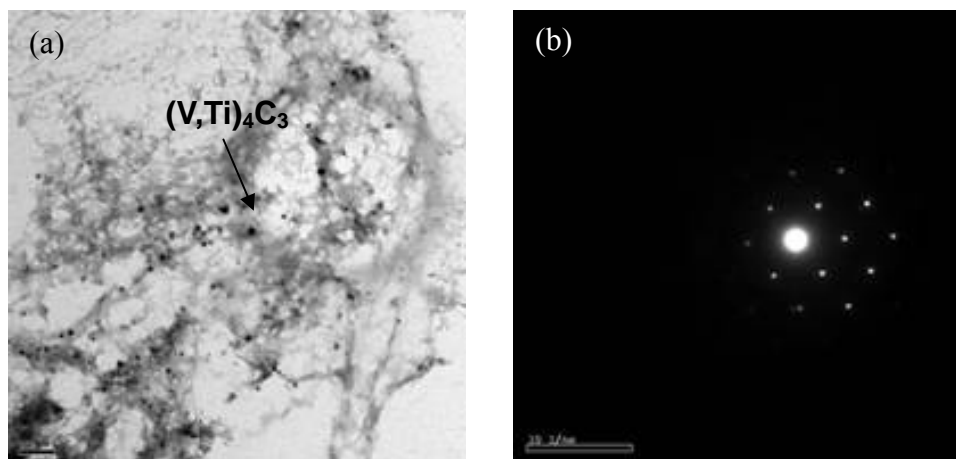

FIGURE 5.9.   TEM replica analysis of S1 steels tempered at 450 ^{o}C after austenitized at 880 ^{o}C.   (a) Bright filed image and (b) Diffraction pattern.

Fig. 5.10 shows that $(V, Ti)_4C_3$ carbides of S1 steel existed in the range of tempering temperature 350 ^{o}C ~ 450 ^{o}C, as results analyzed in Fig. 5.9.   In order to search the strengthening mechanism, the size distributions of   carbide were measured with increasing the tempering temperature.   Fig. 5.11 illustrates the size distribution of $(V, Ti)_4C_3$ carbide of S1 steel with increasing the tempering temperature.   Mean diameter of $(V, Ti)_4C_3$ were 0.0099 um, 0.01 um and 0.011 um at tempering temperatures of 350 ^{o}C, 400 ^{o}C and 450 ^{o}C, respectively.   The mean diameter and size distributions of $(V, Ti)_4C_3$ carbide were about equal regardless of tempering temperature.
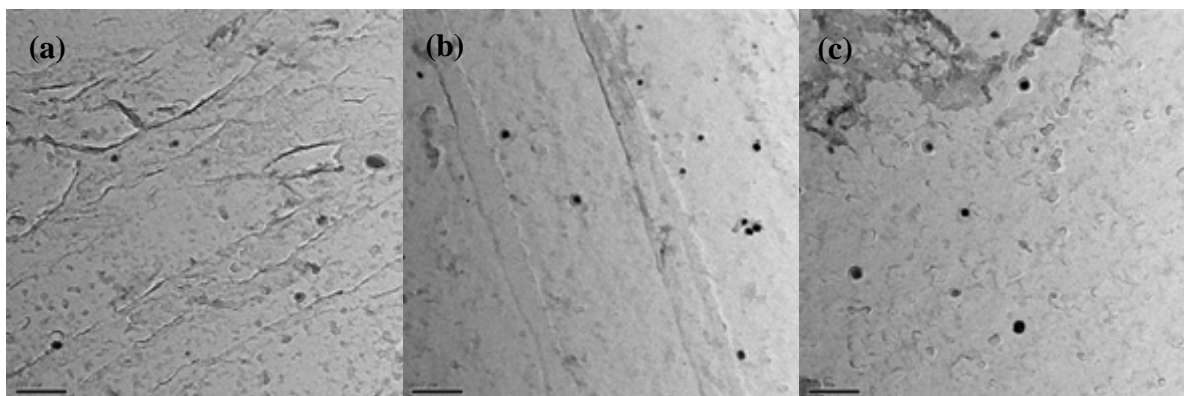

FIGURE 5.10.   TEM replica micrographs of V_4C_3 carbides in the tempered specimens austenitized at 880 ^{o}C.   Tempering temperature: (a) 350 ^{o}C, (b) 400 ^{o}C and (c) 450 ^{o}C.

Fig. 5.12 shows that the $(V, Ti, Mo)_4C_3$ carbide of S3 steel formed as fine precipitate in the

microstructure tempered at 450 ^{o}C after austenitized at 880 ^{o}C.   As described above, the (V, Ti, Mo)$_4$C$_3$ carbides already existed in oil-quenched specimens.   It is condirmed that the (V, Ti, Mo)$_4$C$_3$ carbide in tempered structure was equal to that in oil-quenched specimens.   These pictures were taken from the [110] orientation of the matrix as shown in Fig. 5.12 (b).   Diffraction patterns from extraction replicas confirmed that the sphere-shaped precipitates have a face centered cubic lattice with the same lattice parameter as V$_4$C$_3$ (4.2 Å).   The (V, Ti, Mo)$_4$C$_3$ carbide grows during tempering, similar to S1 steel.
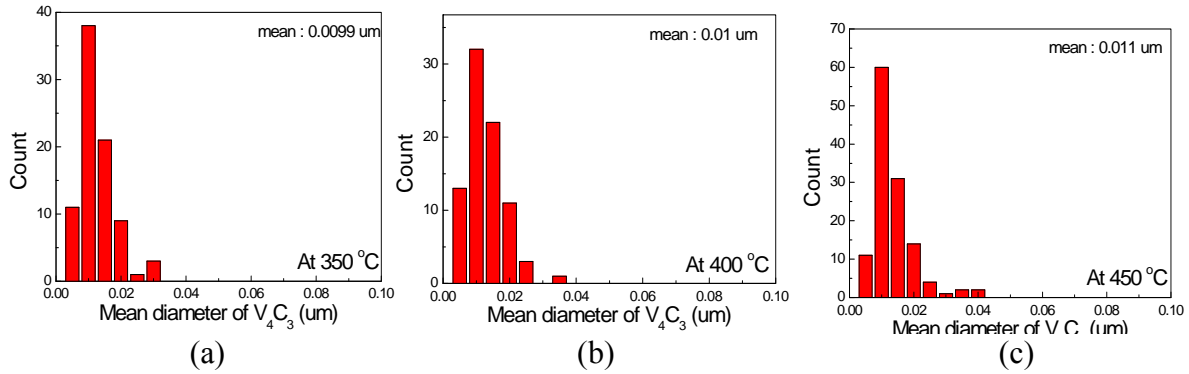

FIGURE 5.11.   Size distribution of (V, Ti)$_4$C$_3$ carbide of S1 steel with increasing the tempering temperature.   Tempering temperature: (a) 350 ^{o}C, (b) 400 ^{o}C and (c) 450 ^{o}C.
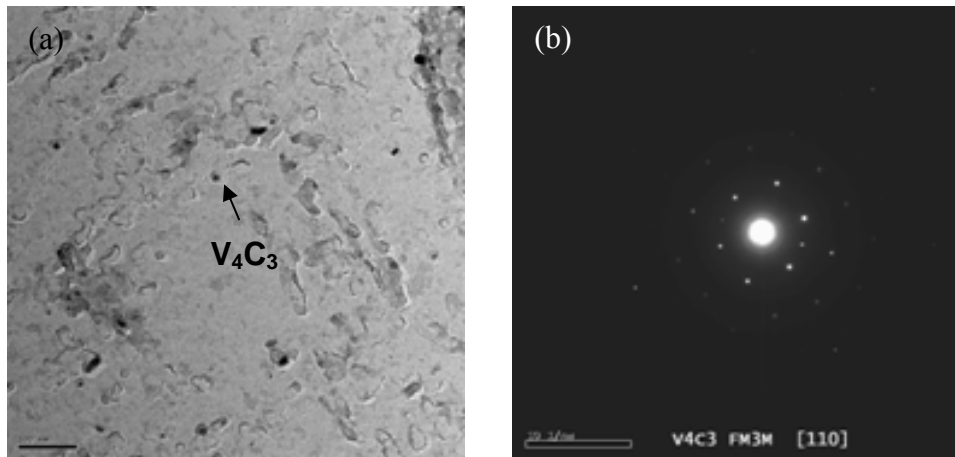

FIGURE 5.12.   TEM replica analysis of S3 steel tempered at 450 ^{o}C after austenitized at 880 ^{o}C.   (a) Bright filed image and (b) Diffraction pattern.

Fig. 5.13 shows that (V, Ti, Mo)$_4$C$_3$ carbides of S1 steel existed in the range of tempering temperature 350 ^{o}C ~ 450 ^{o}C, as results analyzed in Fig. 5.12.   In order to search the strengthening mechanism, the size distributions of (V, Ti, Mo)$_4$C$_3$ carbide were measured for increasing tempering temperature.   Fig. 5.14 illustrates the size distribution of (V, Ti, Mo)$_4$C$_3$ carbide of S1 steel with increasing the tempering temperature.   Mean diameter of (V, Ti, Mo)$_4$C$_3$ were 0.0092 um, 0.0091 um and 0.0057 um at tempering temperatures of 350 ^{o}C, 400 ^{o}C and 450 ^{o}C, respectively.   The mean diameter and size distribution of (V, Ti, Mo)$_4$C$_3$ carbide was almost equal regardless of tempering temperature.   However, the mean diameter
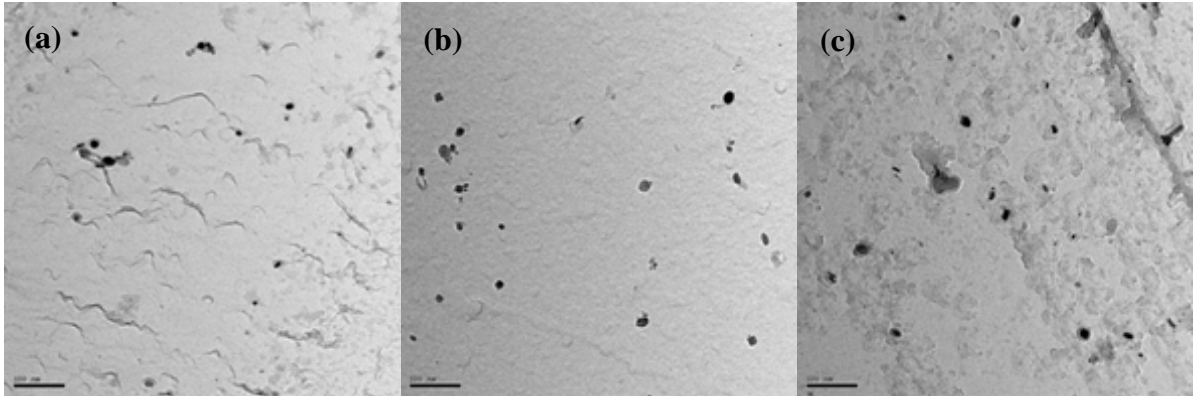
FIGURE 5.13.   TEM replica micrographs of (V, Ti, Mo)$_4$C$_3$ carbides in the tempered specimens austenitized at 880 ^{o}C.   Tempering temperature: (a) 350 ^{o}C, (b) 400 ^{o}C and (c) 450 ^{o}C.

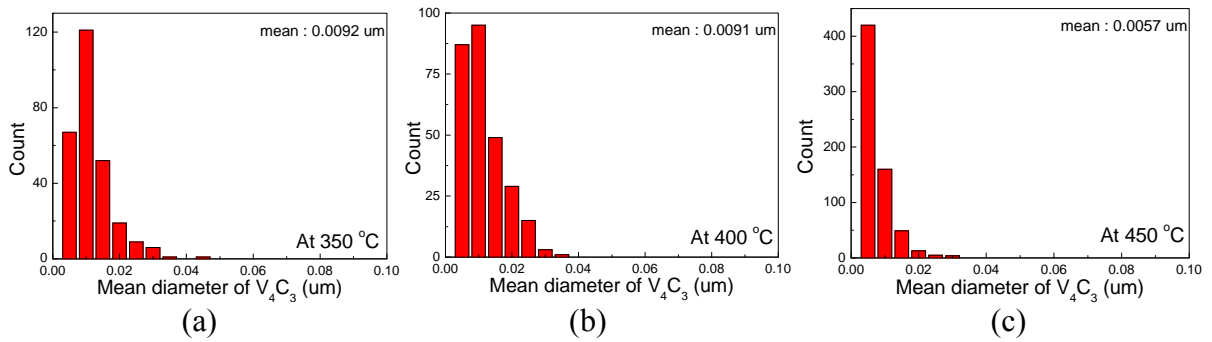FIGURE 5.14.   Size distribution of (V, Ti, Mo)$_4$C$_3$ carbide in the tempered specimens of S3 steel austenitized at 880 ^{o}C with increasing the tempering temperature. Tempering temperature: (a) 350 ^{o}C, (b) 400 ^{o}C and (c) 450 ^{o}C.
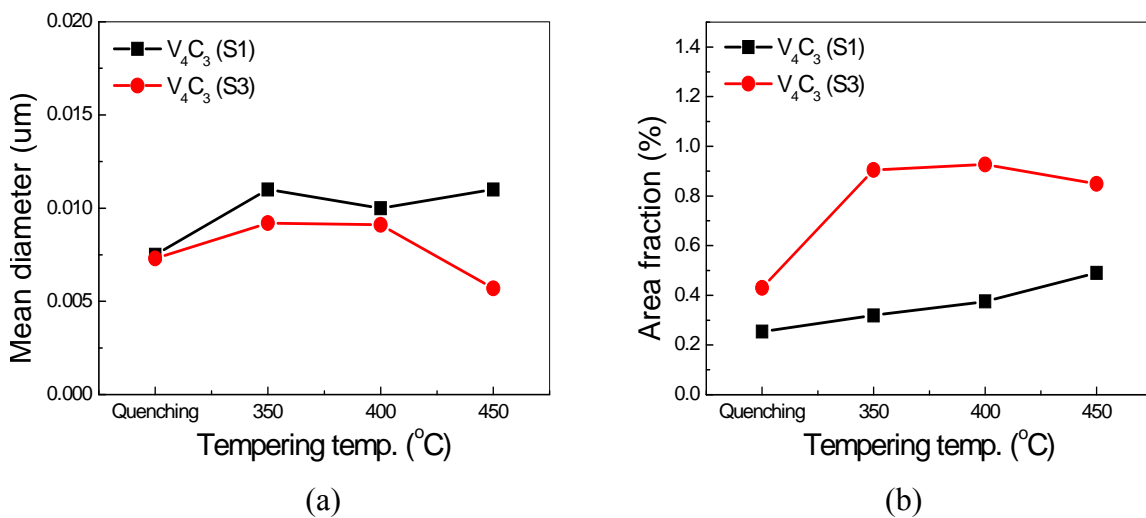

FIGURE 5.15.   Comparison of size distribution of V$_4$C$_3$-type carbide of S1 and S3 steels. Mean diameter and (b) Area fraction.

of (V, Ti, Mo)$_4$C$_3$ carbide tempered at 450 ^{o}C was smaller than that of specimens tempered at 350 ^{o}C and 400 ^{o}C.

Fig. 5.15 presents the comparison of size distribution of V$_4$C$_3$-type carbides of S1 and S3 steels from quenching state to tempering state.   Mean diameters of V$_4$C$_3$-type carbides of S1 and S3 steels were similar, but area fraction of (V, Ti, Mo)$_4$C$_3$ carbide of S3 steel was relatively higher than that of S1 steel.   Mean diameter and area fraction of V$_4$C$_3$ carbides of S1 and S3 steels almost did not change with tempering temperature.

For S3 steel, the area fraction of (V, Ti, Mo)$_4$C$_3$ carbide increased on moving from quenching state to tempering state.   This means that the (V, Ti, Mo)$_4$C$_3$ carbide of S3 steel may be continuously formed from fine pre-existing (V, Ti, Mo)$_4$C$_3$ particles in the oil-quenched microstructure.   In addition, the area fraction of (V, Ti)$_4$C$_3$ carbide of S1 steel have a tendency to increase a little on moving from quenching state to tempering state.   It is summarized that the V$_4$C$_3$-type carbide of S1 and S3 steels may be precipitated newly and / or grow continuously during tempering.

5.3.2.2 *Fe$_3$C precipitation*

Fig. 5.16 shows the TEM image and diffraction pattern, chemical compositions of coarse particles in the oil-quenched specimens of S1 steel.   The as-rolled specimens were oil-quenched after austenitizing for 180 seconds at 830 ^{o}C.   The coarse precipitates were determined as the hexagonal close-packed structure of cementite Fe$_3$C.   These pictures were taken from the [010] orientation of the matrix.   Chemical composition of cementite was estimated using energy dispersive X-ray spectroscopy on the carbon extraction replicas, as shown in Fig. 5.16 (c).   Composition of cementite consists of metallic elements (Fe, Mn, Cr) and carbon.   It means that Fe$_3$C is replaced as (Fe, Mn, Cr)$_3$C by substituting Mn and Cr to Fe$_3$C carbide.   The cementite did not dissolve completely during austenitization but spheroidized.
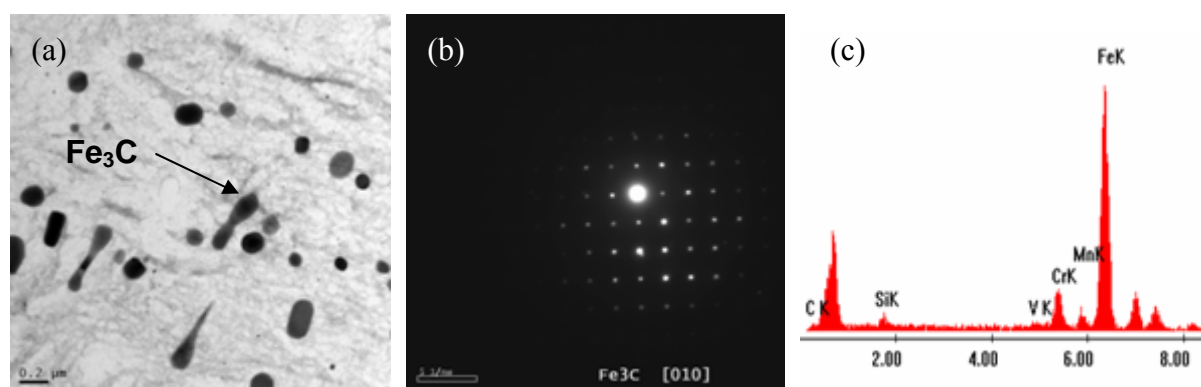

FIGURE 5.16.   TEM replica micrographs of cementite in the oil-quenched S1 steel austenitized at 830 ^{o}C.   (a) Bright field image, (b) Diffraction pattern and (c) EDX result.

When the austenitization temperature increases from 830 ^{o}C to 980 ^{o}C, the coarse cementite of S1 steel was dissolved to be a smaller size.   Fig. 5.17 shows that the cementite was retained as the coarse particle only at austenitization temperature 830 ^{o}C and almost dissolved
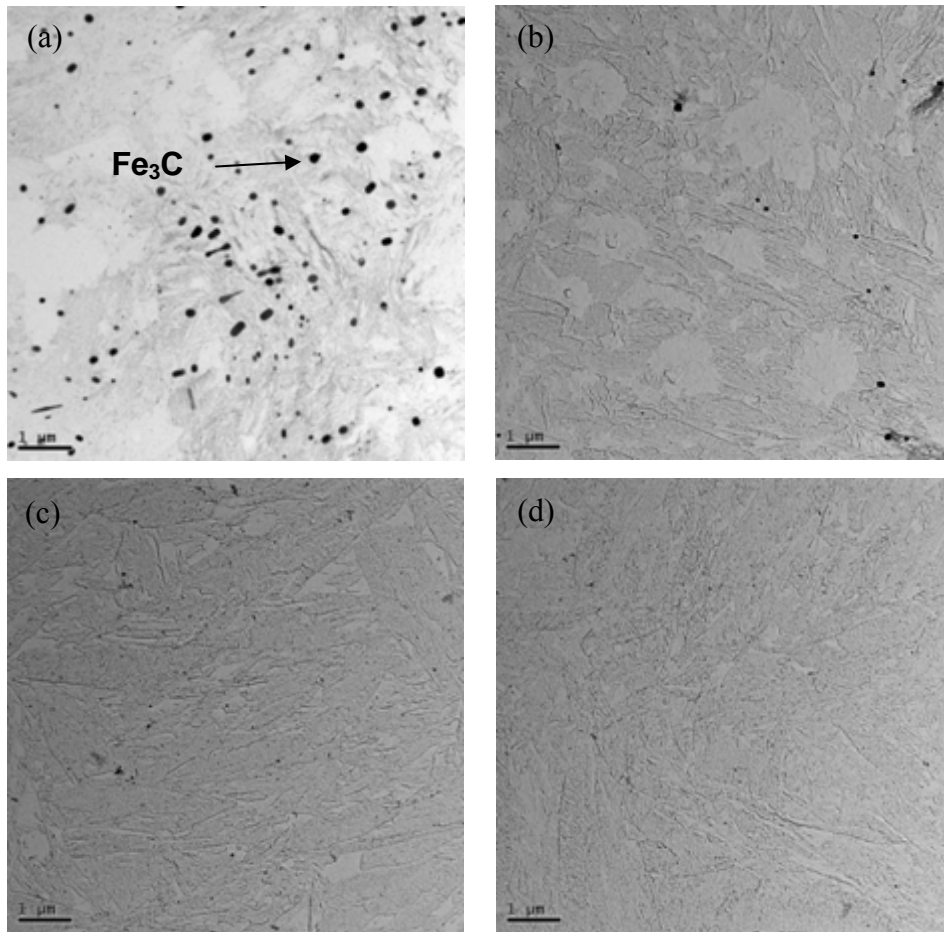
FIGURE 5.17.   TEM replica micrographs of cementite in the oil-quenched specimens of S1 steel.   Austenitization temperature: (a) 830 ^{o}C, (b) 880 ^{o}C, (c) 930 ^{o}C and (d) 980 ^{o}C.
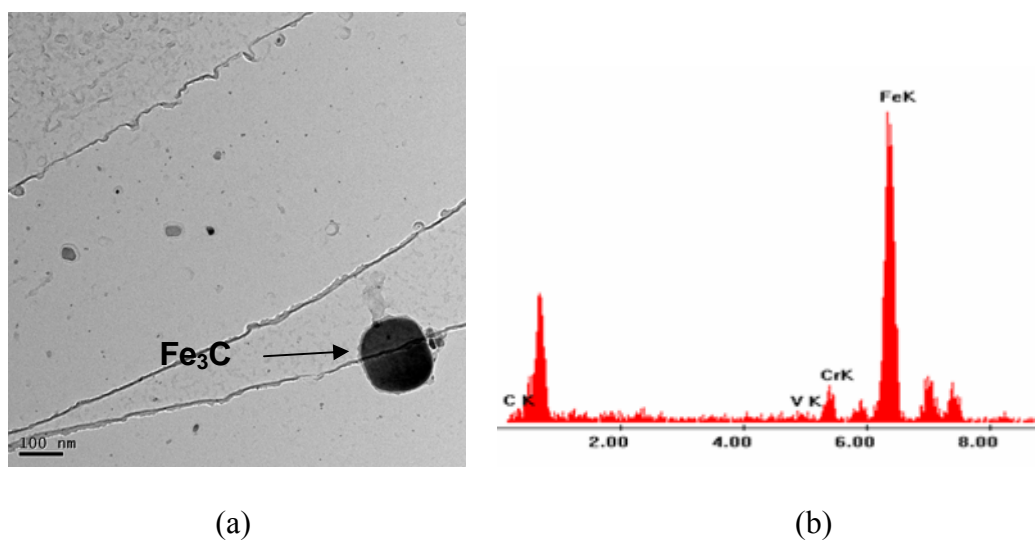

FIGURE 5.18.   TEM replica micrographs of cementite in the oil-quenched S3 steel austenitized at 830 ^{o}C.   (a) Bright field image and (b) EDX result.

as the fine particle at austenitization temperature from 880 $^{\circ}$C to 980 $^{\circ}$C.   The size and volume fraction of undissolved cementite increases with decreasing austenitization temperature.   As described above, the coarse cementite at 830 $^{\circ}$C was caused by incomplete austenitization.   Above the austenitization temperature of 880 $^{\circ}$C, austenitization was done completely and the cementite was almost dissolved.

Fig. 5.18 shows the TEM image and diffraction pattern, chemical compositions of coarse particles in the oil-quenched specimens of S3 steel.   The as-rolled specimens were oil-quenched after austenitizing for 180 seconds at 830 $^{\circ}$C.   The coarse precipitates were determined as the hexagonal close-packed structure of cementite Fe_3C.   These pictures were taken from the [010] orientation of the matrix.   Chemical compositions of cementite were estimated using energy dispersive X-ray spectroscopy on the carbon extraction replicas, as shown in Fig. 5.18 (b).   Composition of cementite consists of metallic elements (Fe, Mn, Cr) and carbon.   It means that Fe_3C is replaced as $(Fe, Mn, Cr)_3C$ by substituting Mn and Cr to Fe_3C carbide.   The cementite did not dissolve completely during austenitization but spheroidized.
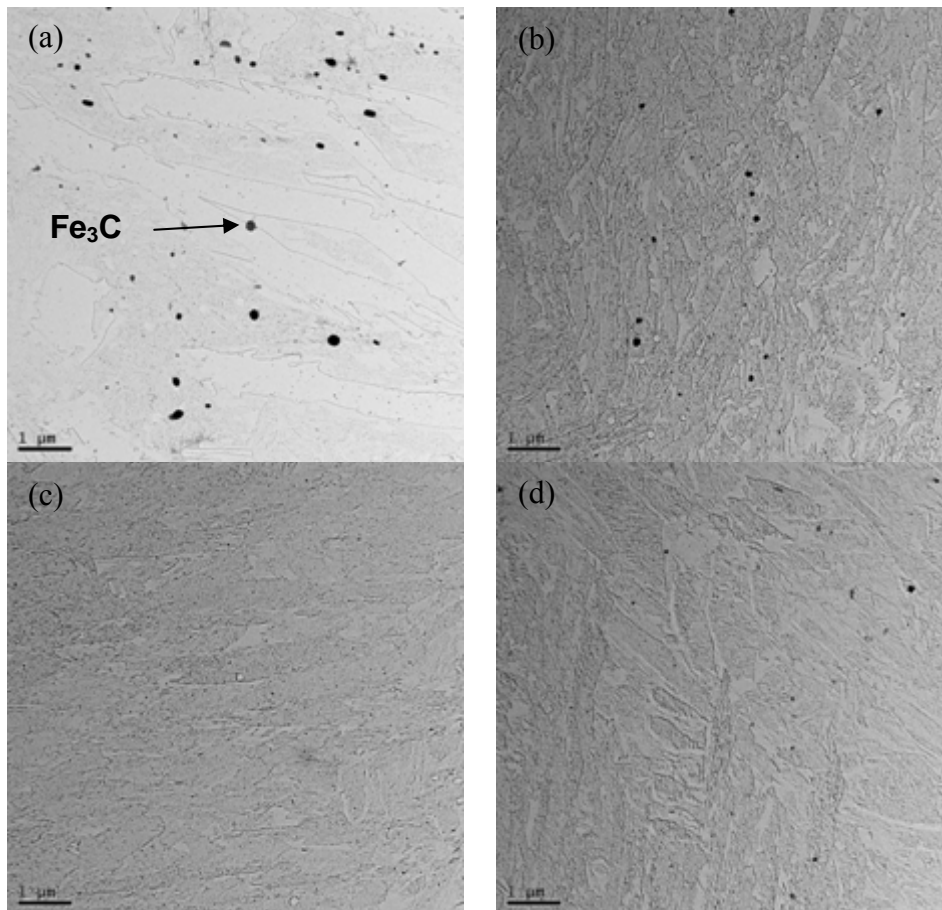

FIGURE 5.19.   TEM replica micrographs of cementite in the oil-quenched specimens of S3 steel.   Austenitization temperature: (a) 830 $^{\circ}$C, (b) 880 $^{\circ}$C, (c) 930 $^{\circ}$C and (d) 980 $^{\circ}$C.

Fig. 5.19 shows that when the austenitization temperature increases from 830 $^{\circ}$C to 980 $^{\circ}$C, the coarse cementite of S3 steel became fine.   The coarse cementite was retained only at

austenitization temperature of 830 $^{\circ}$C and almost dissolved as a few of fine particle at austenitization temperature from 880 $^{\circ}$C to 980 $^{\circ}$C.   The size and volume fraction of undissolved cementite increases with decreasing austenitization temperature.   As described above, the coarse cementite at 830 $^{\circ}$C was due to the incomplete austenitization.   Above the austenitization temperature of 880 $^{\circ}$C, austenitization was completed and the cementite was almost dissolved.

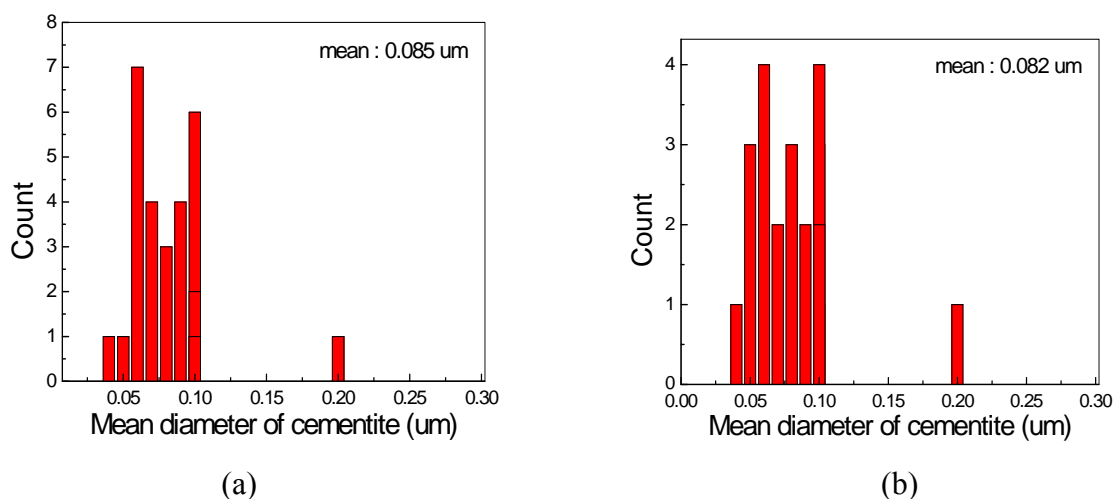(a)   (b)

FIGURE 5.20.   Size distribution of cementite in the oil-quenched specimens after austenitized at 880 $^{\circ}$C.   (a) S1 steel and (b) S3 steel.

The size distributions of undissolved cementite in oil-quenched specimens of S1 and S3 steels austenitized at 880 $^{\circ}$C were measured and compared in Fig. 5.20.   Mean diameter of undissolved cementite of S1 steel was around 0.0.085 um and that of undissolved cementite of S3 steel was around 0.082 um.   The size distributions of undissolved cementite in S1 and S3 steel were similar.   It is suggested that the size distribution of undissolved cementite in S1 and S3 steels were almost equal in the case of same temperature of austenitization.
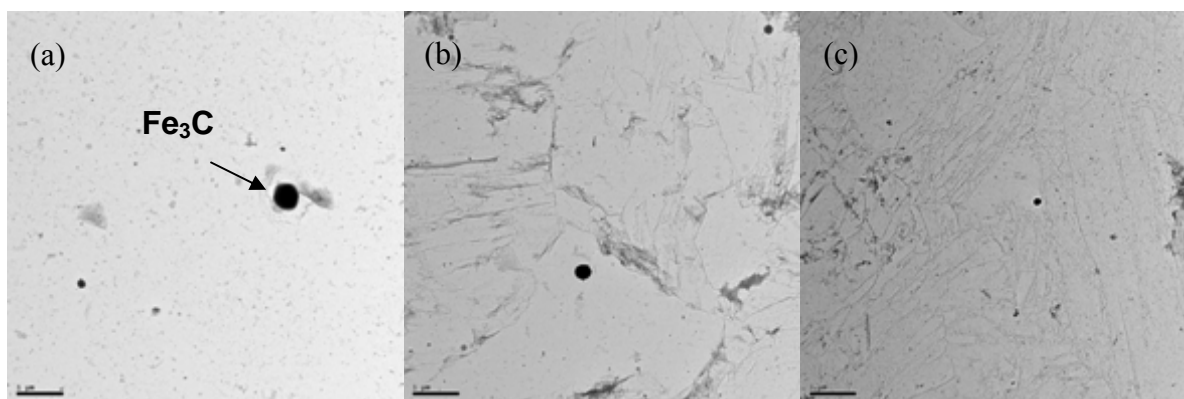

FIGURE 5.21.   TEM replica micrographs of coarse cementite in the tempered specimens of S1 steel austenitized at 880 $^{\circ}$C. Tempering temperature: (a) 350 $^{\circ}$C, (b) 400 $^{\circ}$C and (c) 450 $^{\circ}$C.

   The undissolved cementite will be grown continuously as the coarse particle during tempering.   As described above, the cementite was already retained in the oil-quenched specimens.   The coarse cementite in tempered structure was based on the undissolved cementite in oil-quenched structure.   Fig. 5.21 shows that the coarse cementite of S1 steel existed in the range of tempering temperature from 350 ^{o}C to 450 ^{o}C.   The size distributions of coarse cementite were measured with increasing the tempering temperature.   Fig. 5.22 illustrates the size distribution of coarse cementite of S1 steel with increasing the tempering temperature.   Mean diameters of coarse cementite were 0.192 um, 0.147 um and 0.141 um at tempering temperatures of 350 ^{o}C, 400 ^{o}C and 450 ^{o}C, respectively.   The mean diameter and size distribution of coarse cementite was almost similar regardless of tempering temperature.   However, the mean diameter of coarse cementite tempered at 450 ^{o}C was a little smaller than that of specimens tempered at 350 ^{o}C and 400 ^{o}C.
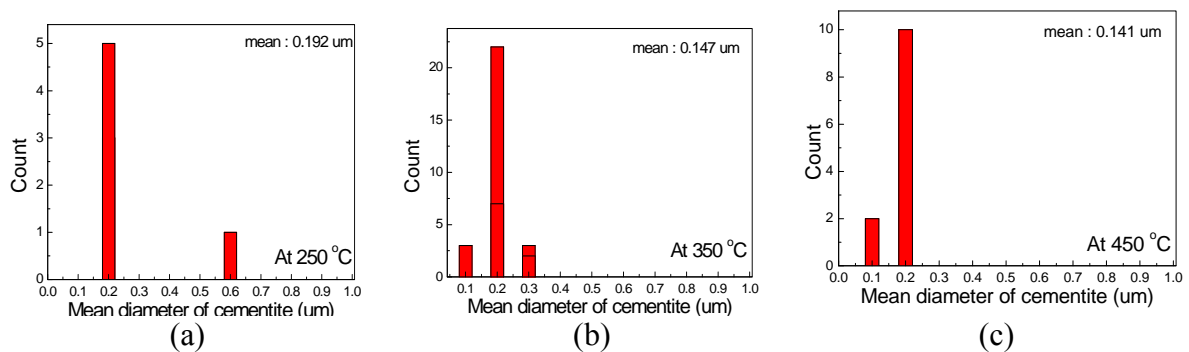

FIGURE 5.22.   Size distribution of coarse cementite in the tempered specimens of S1 steel. Tempering temperature: (a) 350 ^{o}C, (b) 400 ^{o}C and (c) 450 ^{o}C.
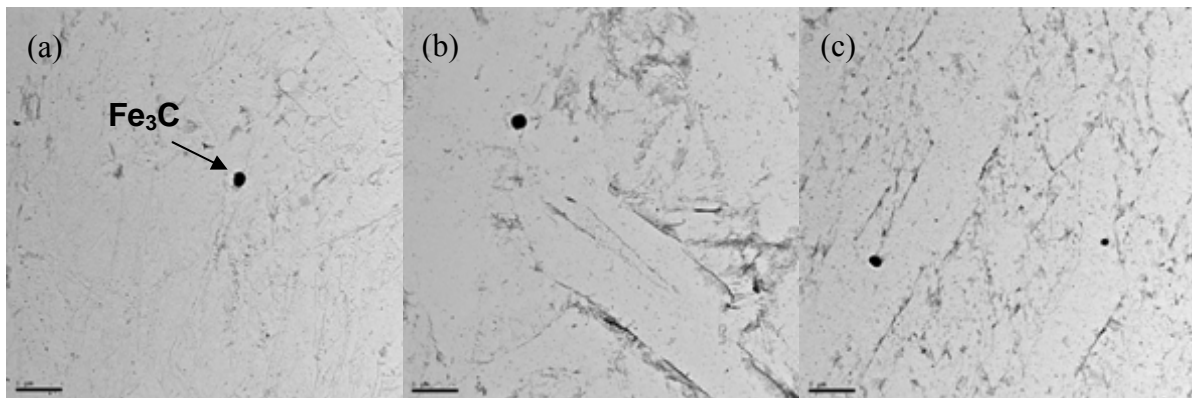

FIGURE 5.23.   TEM replica micrographs of coarse cementite in the tempered specimens of S3 steel austenitized at 880 ^{o}C. Tempering temperature: (a) 350 ^{o}C, (b) 400 ^{o}C and (c) 450 ^{o}C.

   Fig. 5.23 shows that the coarse cementite of S3 steel existed in the range of tempering temperatures from 350 ^{o}C to 450 ^{o}C.   The size distributions of coarse cementite were measured with increasing tempering temperature.   Fig. 5.24 illustrates the size distribution of coarse cementite of S3 steel with increasing the tempering temperature.   Mean diameters of

coarse cementite were 0.139 um, 0.205 um and 0.189 um at tempering temperatures of 350 $^{\circ}$C, 400 $^{\circ}$C and 450 $^{\circ}$C, respectively.   The mean diameter and size distribution of coarse cementite did not change with the tempering temperature.

 After tempering, the undissolved cementite of S1 and S3 steels was retained as coarse cementite.   The coarse cementite was observed for all tempering temperature of 350 ~ 450 $^{\circ}$C.   Fig. 5.25 shows the comparison of size distribution of cementite of S1 and S3 steels from quenching state to tempering state.   Mean diameters of coarse cementite of S1 steel were 0.192, 0.147 and 0.141 um in tempering temperature of 350, 400, and 450 $^{\circ}$C, respectively.   Mean diameters of coarse cementite of S3 steel were 0.139, 0.205 and 0.189 um in tempering temperature of 350, 400 and 450 $^{\circ}$C.   Area fraction of coarse cementite of S1 and S3 steels was almost not changed with increasing tempering temperature.   However, mean diameter of coarse cementite of S1 and S3 steel increased a little during tempering. This means that coarse cementite of S1 and S3 steels may grow during tempering.
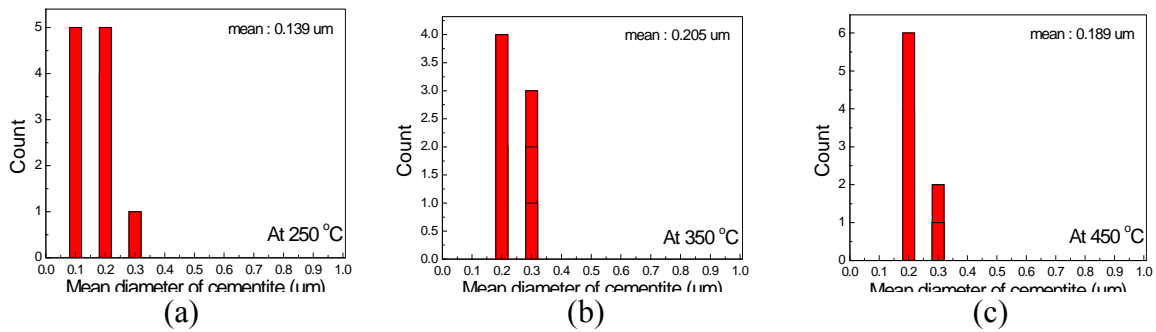

FIGURE 5.24.   Size distribution of coarse cementite in the tempered specimens of S3 steel. Tempering temperature: (a) 350 $^{\circ}$C, (b) 400 $^{\circ}$C and (c) 450 $^{\circ}$C.
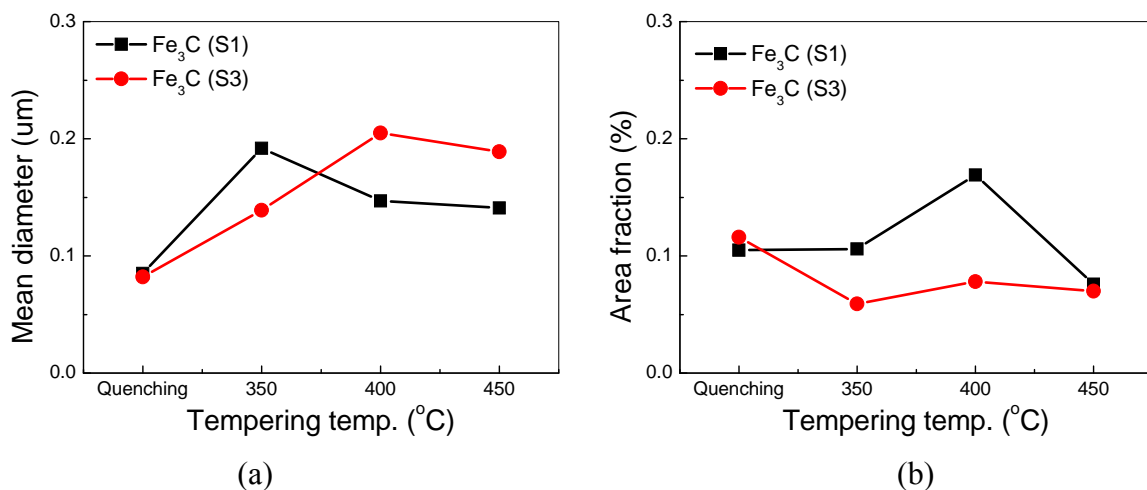

FIGURE 5.25.   Size comparison of coarse cementite of S1 and S3 steels with a tempering temperature.   (a) Mean diameter and (b) Area fraction.

5.3.2.3 $Fe_{2.4}C$ precipitation

Another important metallurgical factor that may influence the strength of high strength steels having fully martensitic structure is carbon segregation or ε-carbide precipitation during quenching.[105-108]   Ansell and Breinan [106] have investigated those effects of carbon segregation and ε-carbide precipitation on the strength of AISI 440A and 4340 steels.   They suggested that the beneficial effect on the strength on slowly-quenched steels is caused by a dispersion-strengthening effect due to carbon segregation to the structural imperfections in the austenite prior to austenitic transformation.   Redistribution of carbon in as-quenched martensite by (1) segregation to lattice defects, (2) transfer of a/b- to c-octahedral interstitials and (3) clustering.   These processes occur at about 0-80 ^{o}C, and (1)-step is accompanied by a slight volume decrease and a hardness increase.   The segregation of carbon to lattice defects (austenite, grain and phase boundaries) to form carbon clusters and metastable ε-carbides during quenching and tempering has a significant effect on the properties of martensitic steels. Several carbon redistribution processes (autotempering) are both thermodynamically and kinetically possible during cooling.   These processes include the segregation of carbon atoms to microstructural features (i.e., voids, dislocations, phase boundaries, or retained austenite), spinodal decomposition and ε-carbide precipitation.   In addition, carbon atoms
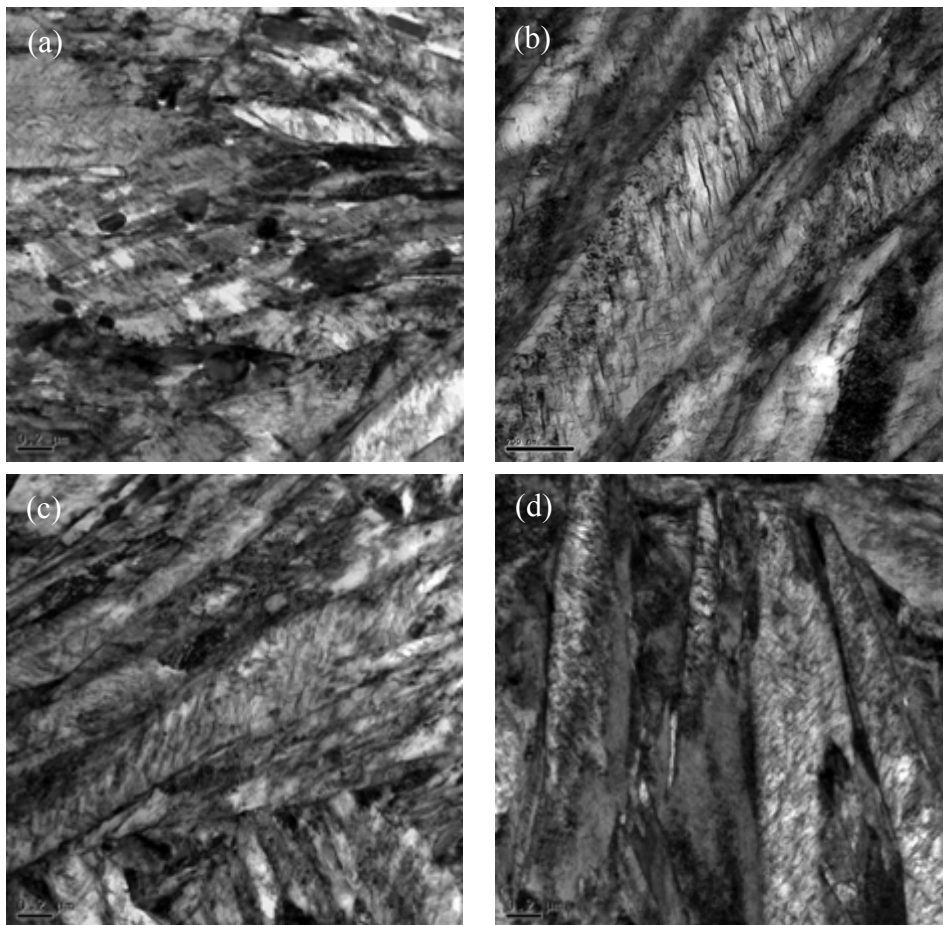

FIGURE 5.26.   TEM thin-foil micrographs of the oil-quenched specimens of S1 steel. Austenitization temperature: (a) 830 ^{o}C, (b) 880 ^{o}C, (c) 930 ^{o}C and (d) 980 ^{o}C.

can segregate to form coherent clusters that are randomly dispersed throughout a carbon depleted martensitic matrix.

Fig. 5.26 shows the TEM micrographs of martensitic structure of the oil quenched specimens of S1 steel.   When the austenitization temperature increased, the carbon clusters were formed in the lath, but ε-carbide was not observed just after oil quenching.   Fig. 5.27 shows the TEM micrographs of martensitic structure of the oil quenched specimens of S3 steel.   When the austenitization temperature increased, the carbon clusters were formed in the lath, but ε-carbide was not observed just after oil quenching, similar to S1 steel.   However, it is difficult to verify the ε-carbide after oil quenching, due to small size of carbide.
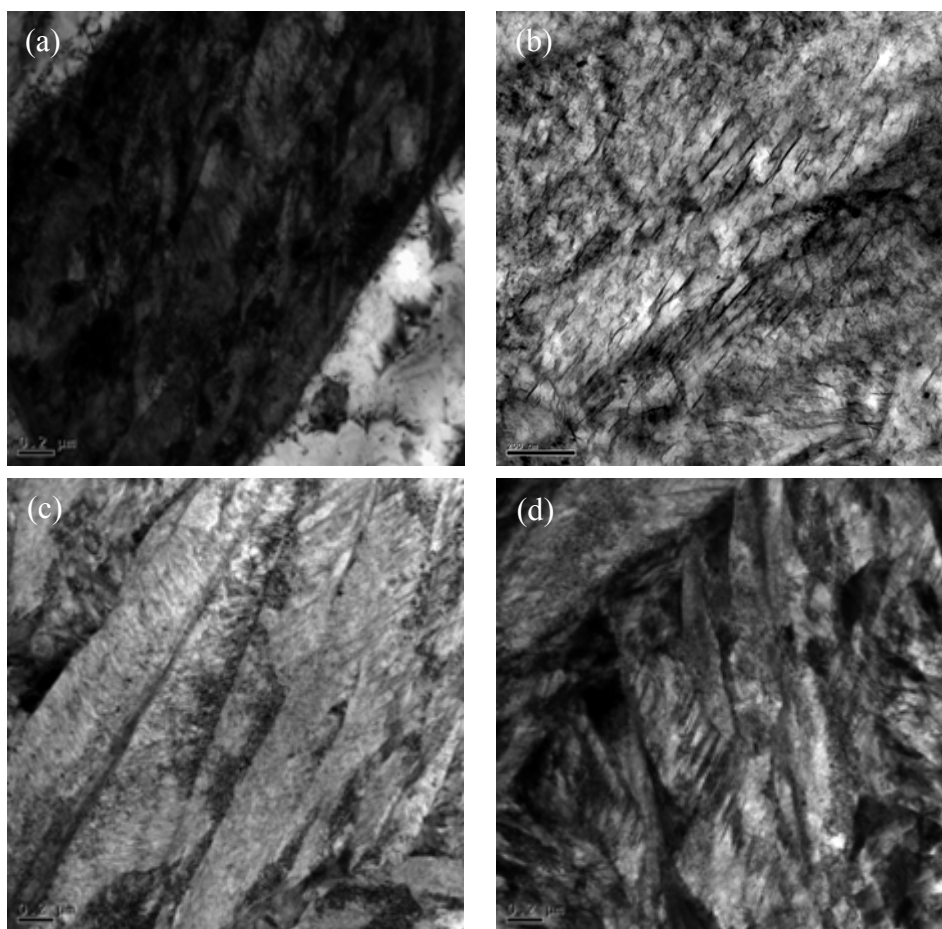

FIGURE 5.27. TEM thin-foil micrographs of the oil-quenched specimens of S3 steel. Austenitization temperature: (a) 830 ^{o}C, (b) 880 ^{o}C, (c) 930 ^{o}C and (d) 980 ^{o}C.

To confirm the ε-carbide precipitation during oil quenching, specimens of S1 and S3 steels were quenched by liquid nitrogen and oil.   The as-rolled specimens were austenitized for 180 seconds at 880 ^{o}C.   Fig. 5.28 shows the distribution of carbon clusters in the quenched microstructure of S1 and S3 steels, but ε-carbide was not detected.   Carbon clusters were investigated by TEM replica below 1 day after quenching in the liquid nitrogen, the oil, and more than 1 month after quenching by oil, respectively.   The distribution of carbon clusters like ε-carbide increases with decreasing cooling rate and increasing the holding time after oil

quenching. The ε-carbide was not formed just after oil quenching and only carbon clusters were formed.
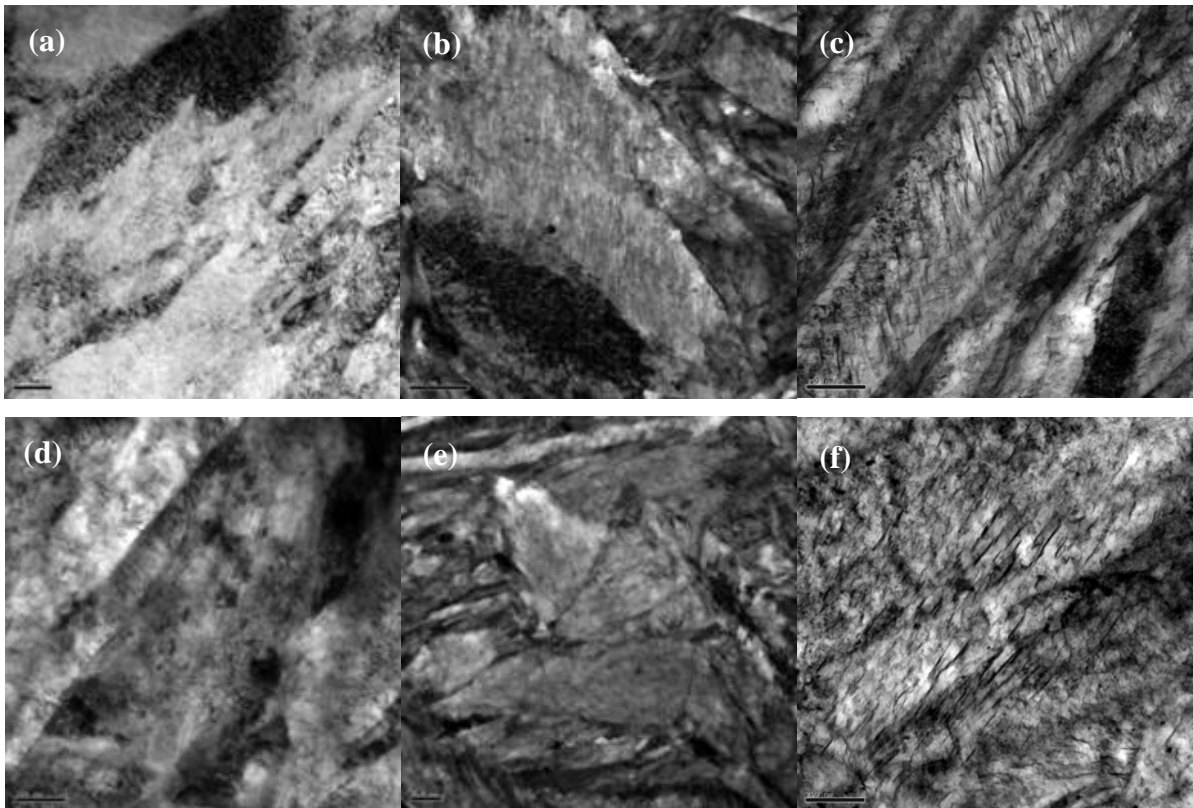
FIGURE 5.28. TEM thin-foil images of the quenched microstructure of S1 and S3 steels austenitized at 880 $^{\circ}$C. (a) S1 and (d) S3 steels held for below 1 day after quenching by liquid nitrogen. (b) S1 and (e) S3 steels held for more than 1 day after oil quenching. (c) S1 and (f) S3 steels held for more than 1 month after oil quenching.
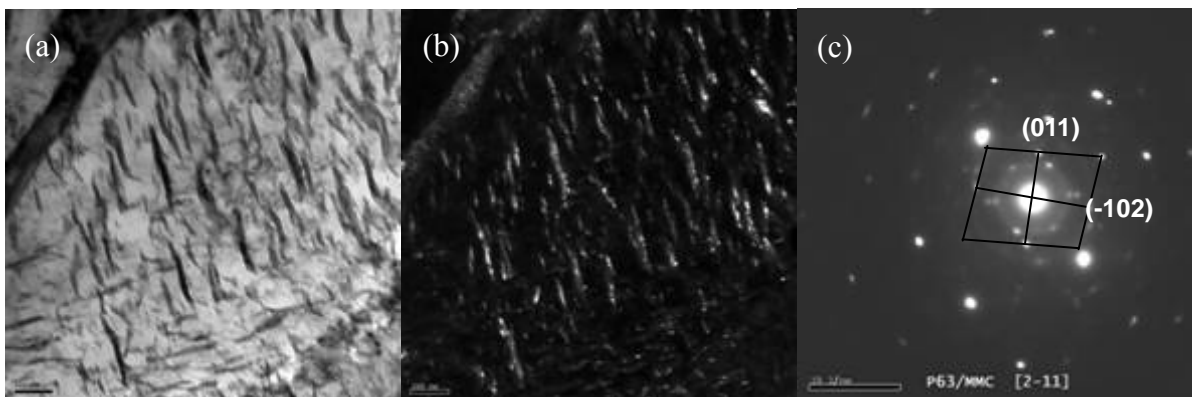
FIGURE 5.29. TEM replica micrographs of ε-cementite of S1 steels tempered at 350 $^{\circ}$C, austenitized at 880 $^{\circ}$C. (a) Bright filed image (b) Dark field image (c) Diffraction pattern.

Fig. 5.29 shows that the fine precipitates of tempered specimens of S1 steel were the

structure of ε-carbide.   In the first stage of tempering process, the carbon in martensite was precipitated to form the transition carbides designated ε-carbide.   This ε-carbide had a hexagonal crystal structure (a = 2.755 Å, c = 4.349 Å [109]) and a composition $Fe_{2.4}C$ [99], and formed as narrow plates or needles with a well-defined orientation relationship.

Fig. 5.30 shows that when the tempering temperature increased from 350 ^{o}C to 400 ^{o}C, ε-carbide in the tempered microstructure of S1 and S3 steels was formed in lath martensite.   At low temperatures (the very early stage of tempering), the quenched martensite was decomposed into the ε-carbide and a low carbon martensite via clustering of carbon atoms.[110-112]   In such a case, the characteristics of ε-carbide precipitates, i.e., inter-particle spacing and distribution, etc., would be improper for those precipitates to effectively hinder the movement of mobile dislocations during straining.
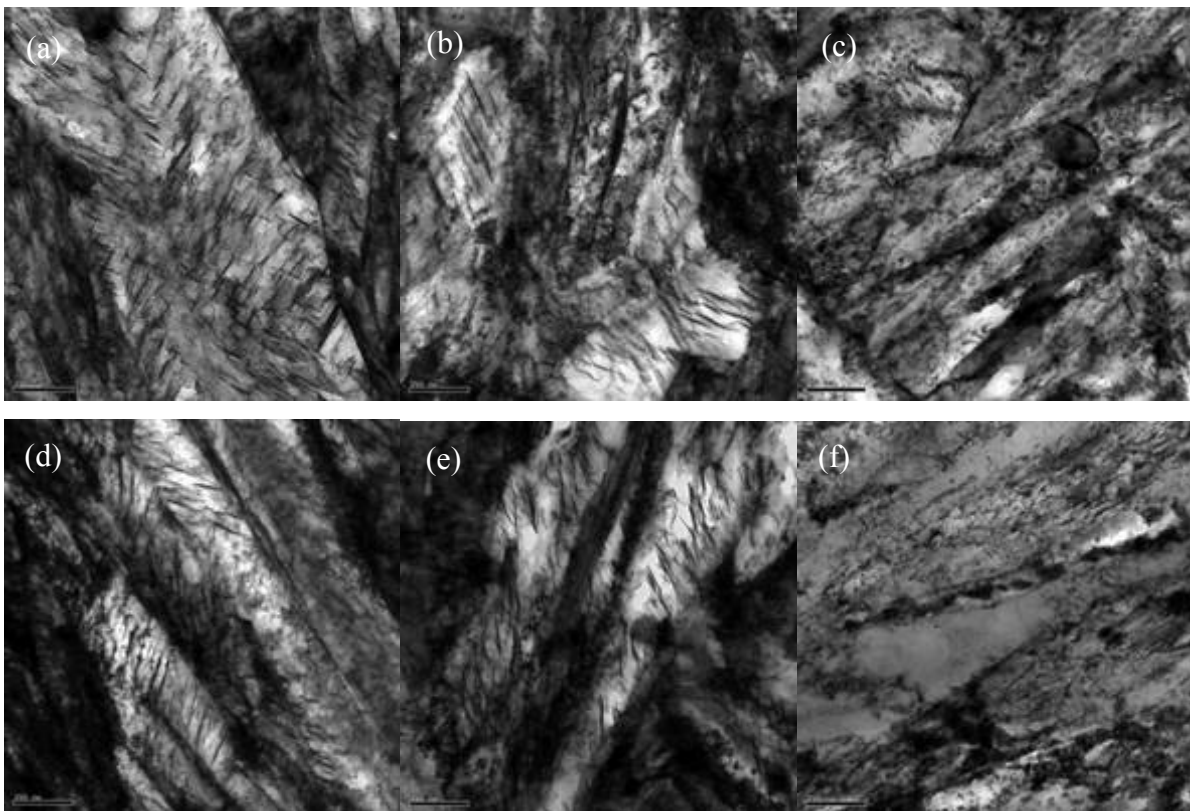
FIGURE 5.30.   TEM replica micrographs of cementite in the tempered specimens austenitized at 880 ^{o}C.   S1 steel tempered at (a) 350 ^{o}C, (b) 400 ^{o}C, (c) 450 ^{o}C and S3 steel tempered at (d) 350 ^{o}C, (e) 400 ^{o}C, (f) 450 ^{o}C.

When increasing the temperature from 400 ^{o}C to 450 ^{o}C, further precipitation of ε-carbide occurred due to the increased activity of supersaturated carbon in the matrix, and simultaneously the nucleation of cementite starts with the concurrent elimination of ε-carbide. Thus, a number of newly precipitated particles must be cementite particles, which are nucleated either at dislocations or at the interface of ε-carbide / ferrite matrix during the third stage of tempering.   At 450 ^{o}C tempering, spheroidal cementite particles became a main microstructural feature within the tempered martensite.   In the third stage of tempering

process, the segregated carbon and ε-carbides were changed into cementite and ferrite.   This occurred above about 450 °C and is accompanied by the decrease of strength and the increase of ductility (reduction of area).   Si and Cr stabilize ε-carbides so that the third stage occurs at a higher temperature (above 300 °C).   Si and Cr also retard the growth of cementite, and steels containing these elements resist softening up to 500 °C.[113]   The addition of carbide forming elements such as Mo, V and Nb, even in small amounts, gives a pronounced softening resistance.   These elements retard the climb of dislocations and keep the dislocation density high even if the steel is tempered above 500 °C.[114]   This resulting high dislocation density aids the precipitation of alloy carbides in the subsequent fourth stage.

5.3.3   Effects of austenite grain size and lath size
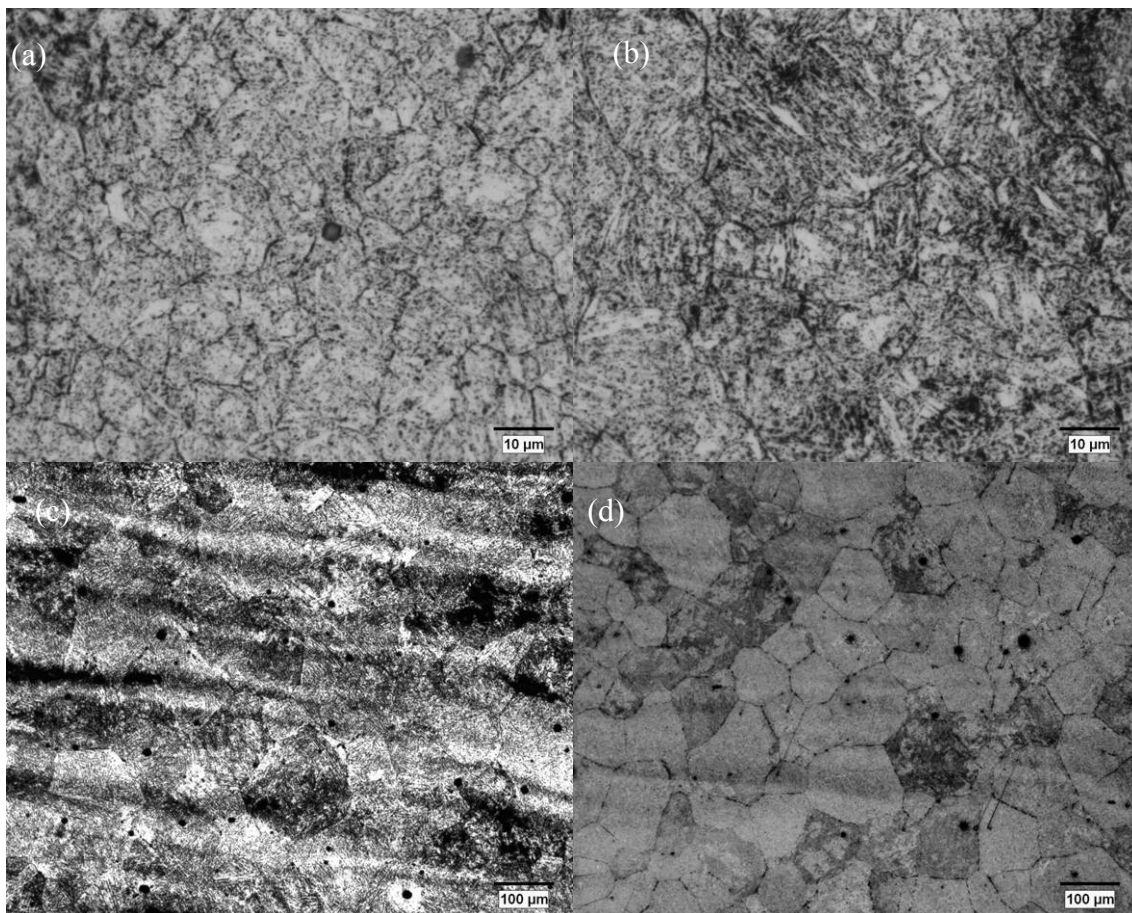
FIGURE 5.31.   Optical micrographs of the quenched specimens of S1 and S3 steels.   S1 steel austenitized at (a) 930 °C, (b) 980 °C and S3 steel austenitized at (c) 930 °C, (d) 980 °C.

Fig. 5.31 shows the optical micrographs of the oil-quenched microstructure of S1 and S3 steels.   The mean sizes of austenite grain of S1 and S3 steels austenitized at 930 °C were measured as 6.86 um and 77.87 um and those of S1 and S3 steels austenitized at 980 °C were 8.64 um and 64.11 um, respectively (Fig. 5.32).   The austenite grain sizes of S3 steel were totally larger than those of S1 steel.   The austenite grain size did not change with increasing

the austenitization temperature.   The difference of austenite grain size of S1 and S3 steels is by the addition of the alloying element (B, Mo).   Boron was added to S3 steel and then BN would be formed instead of AlN.   In general, AlN is used to suppress the growth of austenite grain during austenitization.   Therefore, the formation of BN instead of AlN may reduce the growth of austenite grain.
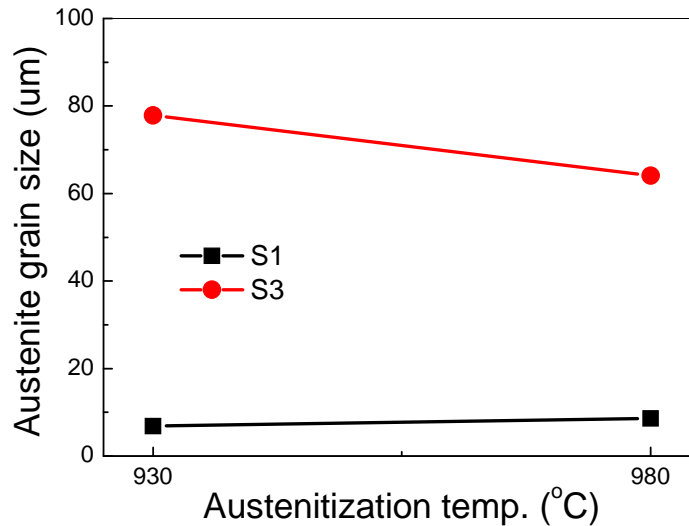
FIGURE 5.32.   Comparison of Austenite grain size of the quenched specimens of S1 and S3 steels.

The mean length and width of lath of S1 and S3 steels are compared in Fig. 5.33.   The size distributions of lath in martensite of S1 and S3 steels are presented in Fig. 5.34.   The length and width of lath structure were measured by using TEM images and Image analyzer. The length of lath increased a little with increasing the austenitization temperature and the width of lath did not change.   In conclusion, the size distribution of lath was not affected by the addition of alloying elements and austenitization temperature, austenite grain size.

(a)   (b)
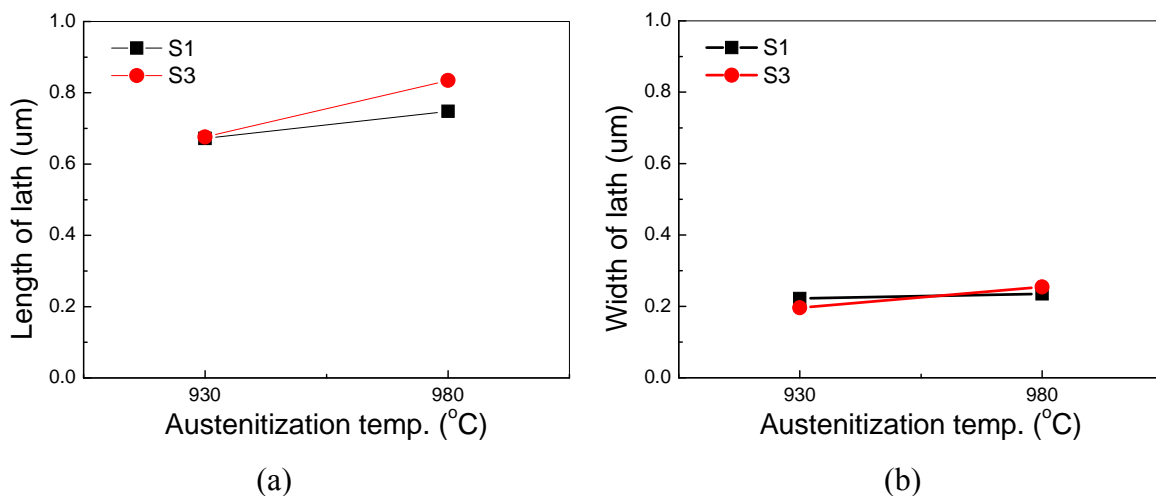
FIGURE 5.33.   Comparison of size distribution of lath microstructure of the quenched specimens of S1 and S3 steels.

FIGURE 5.34.   Size distribution of lath structure in the quenched specimens of S1 and S3 steels.   S1 steel: (a) and (b) austenitized at 930 $^{\circ}$C, and (c) and (d) austenitized at 980 $^{\circ}$C. S3 steel: (e) and (f) austenitized at 930 $^{\circ}$C, and (g) and (h) austenitized at 980 $^{\circ}$C.

5.4   Discussion

5.4.1   Incomplete austenitization at 830 ^{o}C

Tensile strength of samples austenitized at only 830 ^{o}C was lower than those austenitized at higher temperatures. When the samples were oil-quenched from 830 ^{o}C, microstructure consisted of martensite 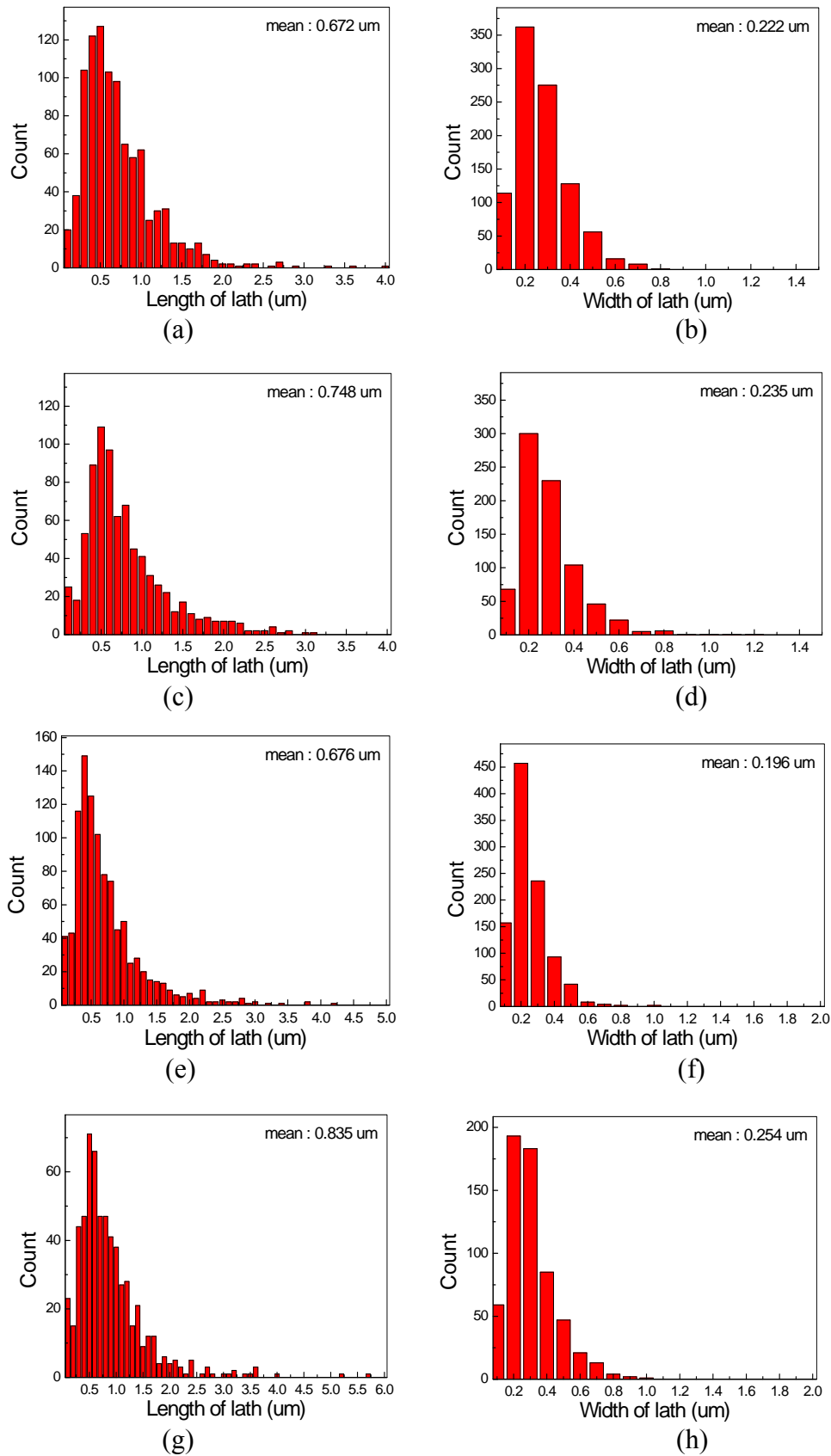and ferrite, undissolved coarse cementite as shown in Fig. 5.1.   Fig. 5.2 shows the existence of ferrite in the oil-quenched microstructure of S1 and S3 steels. The existence of ferrite and coarse cementite is due to insufficient time and temperature of austenitization.   The weak ferrite phase induced the decrease of tensile strength, and ferrite and undissolved cementite cause the decrease of reduction of area.   As shown in Fig. 5.1 and 5.2, the ferrite and coarse cementite existing along grain boundary may induce the easy propagation of crack.

5.4.2   Inter-particle distance of precipitates

For a random distribution of particles having volume fraction (f) and radius (r), the number of particles intercepted by 1 cm^2 of surface is $3f/(2\pi r^2)$.[115]   Therefore the average distance between particles assuming a simple cubic array is

$$d = \left(\frac{2\pi}{3f}\right)^{1/2} r \tag{1}$$

In addition, volume fraction (f) can be related to the area fraction (f_a) and given as

$$f = \left(f_a\right)^{3/2} \tag{2}$$

By the equations (1) and (2) described above, average distance between particles would be summarized as

$$d = \left(\frac{2\pi}{3(f_a)^{3/2}}\right)^{1/2} r \tag{3}$$

For V$_4$C$_3$ carbides, average inter-particle distance between V$_4$C$_3$ carbides was calculated and presented in Fig. 5.35 (a).   Fig. 5.35 (b) shows average inter-particle distance between coarse cementite of S1 and S3 steels.   The average inter-particle distances of V$_4$C$_3$ and coarse cementite are similar for all tempering temperature of 350 ^{o}C~ 450 ^{o}C.   The average inter-particle distances of ε-carbide of S1 and S3 steel were measured from the high resolution TEM images and presented in Fig. 5.35 (c).

For S1 steel, the average inter-particle distances between V$_4$C$_3$ precipitates were smaller than those of coarse cementite after tempering treatment.   When quenched from the austenitization temperature of 880 ^{o}C, the inter-particle distance of V$_4$C$_3$ precipitates was 0.48 um and the average inter-particle distance of coarse cementite was 9.5 um.   V$_4$C$_3$ precipitates were finer than the coarse cementite undissolved during austenitization.   With increasing the

tempering temperature, the inter-particle distance of V_4C_3 decreased from 0.59 um to 0.43 um. The V_4C_3-type carbide of S1 steel may be precipitated newly and / or grown continuously during tempering.   The inter-particle distance of coarse cementite was not changed relatively. The average inter-particle distance of cementite increased from 23.6 um to 22.3 um with increasing the tempering temperature.   It indicates that the coarse cementite of S1 steel may be grown continuously by dissolving the relative small cementite during tempering.   The inter-particle distances of ε-carbide were 42.8 nm and 42.3 nm at tempering temperatures of 350 °C and 400 °C respectively.   The precipitation behavior of ε-carbide was not affected by increasing the tempering temperature.

(a)

(b)

(c)
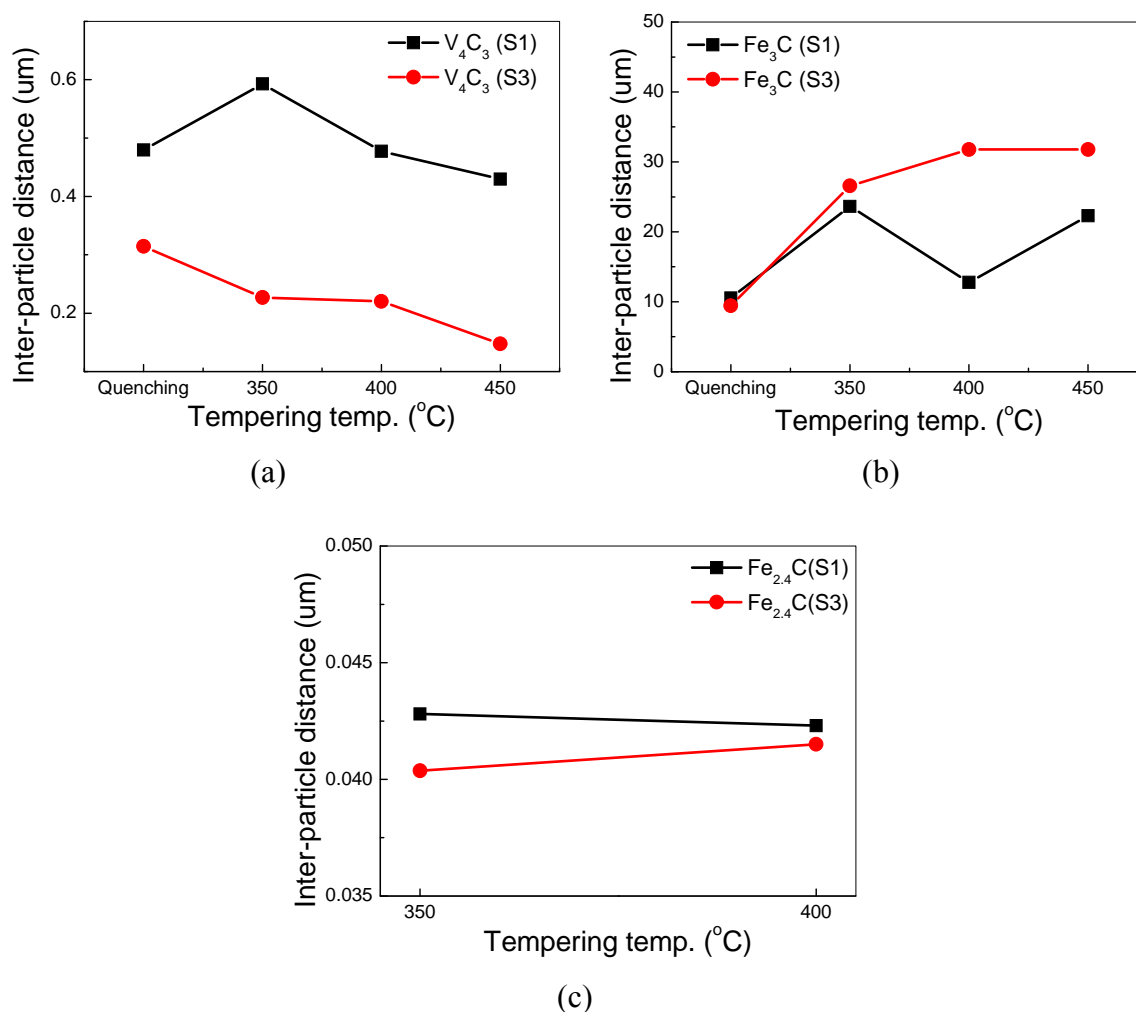
FIGURE 5.35.   Average inter-particle distance between precipitates of S1 and S3 steels with the tempering temperature.   (a) V_4C_3-type carbide, (b) coarse cementite and (c) ε-carbide.

In the case of S3 steel, the average inter-particle distance between V_4C_3 precipitates was 0.31 um and the average inter-particle distance of coarse cementite was 9.5 um. V_4C_3 precipitates were formed finer and closer than the coarse cementite undissolved during austenitization, similar to S1 steel. V_4C_3 carbide in the oil-quenched specimens was distributed more densely than the coarse cementite.

With increasing the tempering temperature, the inter-particle distance of V_4C_3 decreased from 0.23 um to 0.15 um.   The V_4C_3-type carbide of S3 steel may be precipitated newly and / or grown during tempering.   The inter-particle distance of coarse cementite changed smoothly.   The average inter-particle distance of coarse cementite increased from 26.6 um to 31.8 um with increasing the tempering temperature.   It indicates that the coarse cementite of S3 steel may grow continuously by dissolving the relative small cementite during tempering and the inter-particle distance increased.   The inter-particle distances of ε-carbide were 40.37 nm and 41.5 nm at tempering temperatures of 350 ^{o}C and 400 ^{o}C respectively.   The precipitation behavior of ε-carbide did change significantly when increasing the tempering temperature.

V_4C_3 carbides were formed continuously during tempering and the inter-particle distance had a tendency of decreasing with increasing the tempering temperature.   The coarse cementite grew during tempering and then the inter-particle distance increased with tempering temperature increased.   The average inter-particle distances of V_4C_3 carbide and coarse cementite of S1 and S3 steel were not changed largely with increasing tempering temperature. The inter-particle distance of V_4C_3 carbide of S1 was somewhat larger than that of S3 steel and the inter-particle distance of coarse cementite of S1 steel was a little smaller than S3 steel. Therefore, the tensile strength may not be related with the distribution of V_4C_3 carbide and coarse cementite because the V_4C_3 carbide and coarse cementite did not change with increasing the tempering temperature from 350 ^{o}C to 450 ^{o}C.   The ε-carbides of S1 and S3 steels were formed newly during tempering and precipitated as a number of a very fine particle among the other precipitates.   However, the inter-particle distance of ε-carbide did not change with the tempering temperature.

5.4.3   Transition from epsilon carbide to cementite during tempering

The precipitation behavior of ε-carbide was quite different from that of V_4C_3-type carbide. As shown in Fig. 5.30, ε-carbide was formed at tempering temperature of 350 ^{o}C and 400 ^{o}C, and at tempering temperature of 450 ^{o}C, ε-carbide was dissolved and simultaneously the nucleation of cementite starts with the concurrent elimination of ε-carbide.   Thus, a number of newly precipitated particles observed in Fig. 5.30 (c) and (f) were the fine cementite particles, which were nucleated either at dislocations or at the interface of ε-carbide/ferrite matrix during the third stage of tempering.   At tempering temperature of 450°C, the spheroidal cementite particles was the main microstructural feature within lath martensite.

5.4.4   Grain refinement

For S1 steel, the mean austenite grain size did not change significantly with increasing the austenitization temperature from 930 ^{o}C to 980 ^{o}C.   The refinement of austenite grain is a weak factor when the strengthening of S1 steel.   As shown in Fig. 5.32, the size of austenite grain of S3 steel also were not affected by increasing the austenitization temperature from 930 ^{o}C to 980 ^{o}C, similar to S1 steel.   However, the mean size of austenite grain of S3 steel was much bigger than that of S1 steel.   The mean sizes of austenite grain of S1 and S3 steels austenitized at 930 ^{o}C were measured as 6.86 um and 77.87 um and those of S1 and S3 steels austenitized at 980 ^{o}C were 8.64 um and 64.11 um, respectively (Fig. 5.32).   The tensile strengths of S1 and S3 steels were similar and then grain refinement may be weak factors on

the strengthening.   The reduction of area of S1 was a little larger than that of S3 steels and then may be affected by the grain refinement of austenite.   The difference of austenite grain size of S1 and S3 steels is by the addition of the alloying elements (B, Mo).   It was known that addition of Boron can be induced the abnormal grain growth of austenite of Boron added steel, due to replacing the formation of AlN by the formation of BN.   In addition, it was confirmed that as shown in Fig. 5.33, the size distributions of lath of S1 and S3 steels were not affected by the addition of alloying elements and austenitization temperature, austenite grain size.

5.4.5   *Analysis of strengthening mechanism*

Several factors described above were considered to explain the change of tensile strength of the proposed spring steels.   These strengthening factors were the austenitization behavior, precipitation behavior and the refinement of austenite grain and lath structure in martensite.   For austenitization behavior, the austenitization for S1 and S3 steels was not done completely for 180 seconds at 830 ^{o}C.   The incomplete austenitization caused the existence of ferrite and the insufficient dissolution of cementite in tempered martensitic structure.   The tensile strength was mainly induced by the weak phase of ferrite.   In order to suppress the drop of strength, the ferrite and cementite should be dissolved completely during austenitization.

In general, in order to increase the tensile strength of tempered martensitic structure, the precipitation strengthening has been used by adding the carbide-forming alloying elements.   For the proposed steels, V_4C_3-type carbide was mainly precipitated by adding the alloying elements of V, Ti and Mo.   The $(V, Ti)_4C_3$ carbide was main precipitates in S1 steel and $(V, Ti, Mo)_4C_3$ carbide was in S3 steel. V_4C_3-type carbide of S3 steel was precipitated a little finer and denser than that of S1 steel.   The addition of Mo of S3 steel may cause a fine precipitation of $(V, Ti, Mo)_4C_3$ carbide.   The size distribution of V_4C_3-type carbide was almost not changed with the tempering temperature.   The inter-particle distance of V_4C_3-type carbide decreased a little with increasing the tempering temperature. V_4C_3-type carbide may be contributed as a minor factor to increase the strength by precipitation strengthening.

The other precipitate of S1 and S3 steels was investigated as ε-carbide formed during tempering treatment.   The size distribution of ε-carbide was much finer and denser than that of V_4C_3-type carbide.   The increment of tensile strength may be based on the precipitation behavior of ε-carbide instead of V_4C_3-type carbide during tempering treatment.   At low temperatures (the very early stage of tempering), the primary martensite is decomposed into ε-carbide and a low carbon martensite via clustering of carbon atoms.[112,116,117]   When the tempering temperature changed from 400 ^{o}C to 450 ^{o}C, the rapid decrease of tensile strength can be explained by the transition from ε-carbide to cementite.   The ε-carbide was dissolved and simultaneously the nucleation of cementite starts with the concurrent elimination of ε-carbide.   The decrease of tensile strength may be caused the transition from ε-carbide to cementite with increasing the tempering temperature.   The main strengthening mechanism might be the precipitation behavior of ε-carbide during tempering.

Last, the grain refinement of austenite and lath in martensitic structure was examined to explain the change of tensile strength with the austenitization and tempering temperature.   Austenitic grain size has been observed to affect the strength of martensite in carbon steel.[2]   When the austenite grain size is reduced, a significant increase in strength is expected to occur.

The martensite laths may be related to the austenite grain size.   Since the first formed martensite plates grow clear across the individual grains, it is possible to reduce the martensite plate size by decreasing the prior austenite grain size.   As expected, the reduced martensite plate size does increase the strength and fortunately it is done so without loss in ductility.   Similar strengthening without loss in ductility is obtained by reducing prior austenite grain size in lath type martensites.[100]   However, the prior austenite grain size and the lath size of S1 and S3 steels was not changed with the austenitization temperature and the tempering temperature, respectively.   The prior austenite grain size of S1 steel was very smaller than that of S3 steel, but the difference of tensile strength of both steels could not be explained by the difference in prior austenite grain size.

5.4.6   Analysis of softening mechanism (Reduction of area)

Microstructural changes were investigated to explain the change of reduction of area with the austenitization and tempering temperature.   Similar to the strengthening mechanism, several factors were considered and followed as austenitization behavior, precipitation behavior and grain refinement of austenite and lath structure.   For austenitization behavior, the incomplete austenitization caused the existence of ferrite at grain boundary and the insufficient dissolution of cementite.   Even if the ferrite was weak phase, the boundary between tempered martensite and ferrite may be easy path of crack propagation and the undissolved coarse cementite was also helpful to the crack propagation. Therefore, at the austenitization temperature of 830 ^{o}C, the drop of reduction of area is due to the incomplete austenitization.

As described above, the precipitation behavior consisted of V_4C_3-type carbide and ε-carbide. V_4C_3-type carbide did not change with the tempering temperature and hence are not related to the reduction of area.   However, ε-carbide changed to the cementite with increasing the tempering temperature and cementite was spheroid and lager than ε-carbide. The increment of reduction of area could be explained the transition from ε-carbide to cementite.   Especially, the rapid increase of reduction of area at tempering temperature of 450 ^{o}C was due to increase of the fraction of cementite formation and ε-carbide dissolution.

Last, the grain refinement of austenite and lath in martensitic structure was examined to explain the change of reduction of area with the austenitization and tempering temperature. The prior austenite grain size and the lath size of S1 and S3 steels did not change with the austenitization and the tempering temperature.   This means that the prior austenite grain size and the lath size are not related to the reduction of area.   However, the prior austenite grain size of S1 steel was very smaller than that of S3 steel.   The large size of prior austenite grain of S3 steel may be more or less contributed to decrease the reduction of area and then the reduction of area was a little smaller than that of S1 steel.   It noted that the addition of Boron can be induced the abnormal grain growth of austenite, due to replacing the formation of AlN by the formation of BN.   In order to increase the reduction of area, the grain growth should be suppressed by using the fine particles such as carbide, nitride and carbonitride.

5.5 Conclusions

In the present investigation, the tensile strength and the reduction of area of the proposed spring steels have been studied.   As the austenitization and tempering temperatures changed, the microstructure and precipitation behavior was investigated.   The strengthening and softening mechanism was discussed to explain the mechanical properties and the microstructural change.

1.   The strengthening effect was investigated based on the behavior of austenitization, behavior of precipitation (V_4C_3, cementite and ε-carbide) and prior austenite grain size, lath size.   With increasing the tempering temperature, only ε-carbide changes to cementite and the other factors was almost not changed.   Therefore, the tensile strength and the reduction of area were related to the precipitation behavior of ε-carbide.

2.   In case of austenitization temperature 830 ^{o}C, ferrite existed in martensitic structure of S1 and S3 steels.   Existence of ferrite may be due to the incomplete austenitization at 830 ^{o}C. The drop of tensile strength and reduction of area may be caused the existence of ferrite in martensitic structure.

3.   ε-carbide contributes to the increase of tensile strength in the range of tempering temperature from 350 to 400 ^{o}C.   At low tempering temperature, ε-carbide precipitated from carbon clusters and a part of supersaturated carbon may be retained. With increasing the tempering temperature from 400 ^{o}C to 450 ^{o}C, ε-carbide dissolved and cementite was formed simultaneously.   As a result, the tensile strength decreased with increasing the tempering temperature, due to changing from ε-carbide to cementite.

4.   The increment of tensile strength may be mainly controlled by fine precipitates of ε-carbide.   At low tempering temperature, ε-carbide precipitated from carbon clusters and a part of supersaturated carbon may be retained.   These factors contribute to the increase of tensile strength.   With increasing the tempering temperature, ε-carbide dissolved and cementite is formed simultaneously.   A higher transformation temperature from ε-carbide to cementite may increase the tensile strength without losing the reduction of area at high tempering temperature.

5.   The grain refinement of austenite and lath structure could not explain the change of tensile strength and reduction of area with the austenitization and tempering temperature. However, the prior austenite grain size of S3 steel was quite large than that of S1 steel.   The large prior austenite grain size of S3 steel and / or the occurrence of undesirable precipitation reactions at the grain boundary may contribute to decrease the reduction of area.

5.	Microstructural studies to determine strengthening and softening mechanism

6
Embrittlement due to Fe$_{23}$(C, B)$_6$ precipitates

6.1 Introduction

Strength decreased and ductility increased continuously with increasing tempering temperature, as described at Chapter 4. In general, it is well known that ductility decreases as strength increases. In order to improve the formability and fatigue property of high strength steel, ductility (toughness, reduction of area, etc.) should be kept above a certain level.

However, in case of high strength steel with low ductility, embrittlement fracture frequently happens leading to a low fatigue life. Embrittlement implies a microstructural condition that creates lower toughness than expected for steel. For example, a generally valid rule for coupling mechanical properties and toughness states that the lower the hardness and strength, the higher are the ductility and toughness of a microstructure. However, embrittlement phenomena are exceptions to this rule, and tempered martensite embrittlement, for example, lowers ductility and toughness as hardness decreases within a certain range of tempering temperatures. Embrittlement fracture is thus one of the largest factors impeding the strengthening of steels.

In general, the relationship of strength and reduction of area is of major concern in the heat treatment and application of quench and tempered spring steels. Tempering is the heat treatment of hardened steels that has reduction of brittleness or increases the reduction of area as its major objective. It is the balance of strength and reduction of area required in service that determines the conditions of tempering for a given application.[2] Therefore, it is the aim

of the Chapter 6 to study the decrease in reduction of area and embrittlement phenomena with respect to the microstructural evolution during heat treatment.

6.1.1 Embrittlement during tempering

While cleavage fracture in steels is a common form of embrittlement, in many cases the embrittlement is intergranular, i.e. it takes place along the grain boundaries, usually the former austenitic boundaries.[74]   This behavior is encountered in as quenched steels, on tempering (temper embrittlement, tempered martensite embrittlement).   These forms of embrittlement are encountered at or around room temperature.   There are, however, other phenomena involving failure along grain boundaries which are essentially high temperature events, e.g. hot shortness during the hot working of steels and high temperature creep failure.

It is clear that no single mechanism will explain the various types of embrittlement, but the processes leading to Intergranular fracture all lead to reduced cohesion along the grain boundaries.   This can arise in different ways but the most relevant appear to be the segregation of solute atoms preferentially to grain boundaries and the distribution of second phase particles at grain boundaries.   These phenomena reduce the work of fracture either by lowering the grain boundary energy by segregation, or by reducing the plastic work term by having particles which provide crack nuclei more easily.

It has been shown that embrittlement of high-strength quenched and tempered martensitic steels occurs when thin carbide films form at the prior austenite grain boundaries (PAGB), that are enriched with impurities such as phosphorous [118-120].   The tempering temperature, where the embrittlement is observed, overlaps with the lower range of the third stage of tempering, in which cementite precipitation takes place.   Prior-austenite grain boundaries are preferential nucleation sites of carbide during tempering of quenched martensite. This grain boundary carbide has been discussed in connection with various types of embrittlement of quenched and tempered high-strength carbon steels, such as tempered martensite embrittlement [118,121,122] and hydrogen-induced fracture.[123,124]

The thin plate-like carbides can act as slip barriers and can initiate intergranular cracks at the already impurity weakened PAGB.   At tempering temperatures below 673K the diffusivity of impurity elements is relatively low. Banerji et al. [125] showed that enrichment of the PAGB occurs during the austenitization before quenching and not in the temperature range where tempered martensite embrittlement was observed.   It has been well recognized that cementite in the form of films precipitates at prior-austenite grain boundaries [126] and that these coarse cementite films cause failure along prior-austenite grain boundaries and degrade the fracture strength of steels [122].   In order to avoid or minimize the embrittlement, plate-like carbides should be fragmented or avoided at the PAGB, especially when impurity elements are present.   Refinement of the grain boundary cementite is thus one way to prevent brittle fracture.

High strength quench and tempered steels are susceptible to a number of different types of embrittlement.   It is well known that the embrittlement mechanisms are due to structural change introduced during processing and tempering.[2]   Examples of embrittlement are tempered martensite embrittlement and temper embrittlement.   Each of the embrittlement phenomena is then described in more detail in separate sections.   Tempered martensite

embrittlement (TME) occurs after tempering between 260 to 370 ^{o}C and temper embrittlement (TE) occurs after tempering in or cooling through the temperature range of 373 to 575 ^{o}C.

6.1.2 Tempered martensite embrittlement

Tempered martensite embrittlement (TME) may or may not be associated with impurity atom segregation to prior austenitic grain boundaries and may be associated with three different modes of fracture through the tempered martensite of specimens tempered between 260 to 370 ^{o}C. The common factor for TME appears to be the formation of cementite during tempering. The source of cementite that leads to brittle transgranular fracture is the decomposition of retained austenite in the second stage of tempering. This explanation for the cause of TME was first proposed by Thomas [127].

The intergranular mode of fracture associated with TME is quite common and has been related to phosphorous segregation to the austenite grain boundaries during austenitizing.[125,128,129] The phosphorous, therefore, is present at the grain boundaries in the as-quenched martensite and after tempering up to 200 ^{o}C, but only after tempering in the range where cementite forms in tempered martensite does TME fully develop. The latter observation indicates that an interaction between phosphorous and cementite is necessary for the intergranular mode of TME. Another type of transgranular fracture mode associated with TME is interlath cleavage induced by cracking parallel to the cementite formed by the transformation of the retained austenite. The cause of two types of transgranular fracture observed to accompany TME in certain steels may be related to interlath carbide thickness, the thinner carbides promoting interlath fracture and the thicker carbides promoting trans-lath cleavage.

6.1.3 Temper embrittlement

The cause of TE has been difficult to identify because there is no readily resolvable microstructural feature identifiable with the characteristic intergranular fracture of embrittled specimens. The only metallographic evidence of embrittlement has been the ability of certain etchants to reveal prior austenite grain boundaries containing segregated phosphorous.[130] Currently available surface analysis techniques, such as Auger Electron Spectroscopy (AES), have contributed greatly to the understanding of TE.

Two varieties of embrittlement serve to reduce ductility during tempering. The first has been called 250 ^{o}C embrittlement, 350 ^{o}C embrittlement, or one-step temper embrittlement. The one-step temper embrittlement occurs in high strength steels quenched, then tempered at a low temperature. It is a problem afflicting low alloy steels that have been quenched to martensite, then tempered in the range 250 ^{o}C - 350 ^{o}C. The hardness of the steel decreases continuously as the tempering temperature is raised, but the toughness passes through a minimum. When the steels are embrittled, the fracture becomes predominantly intergranular, along the prior austenite grain boundaries. The embrittlement is associated with the change in structure of carbides from ε-carbide to cementite. This embrittlement poses an awkward problem for the development to optimum strength and ductility, for often the strength desired can be obtained best by tempering near 250 ^{o}C - 350 ^{o}C.

Although the embrittlement is concurrent with the precipitation of ε-carbides and cementite, such precipitation is not in itself the cause of the loss of toughness. When P, Sb, Sn, As and N are absent from a steel, the embrittlement does not occur. Also, the problem can be avoided by adding sufficient Si to the steel to inhibit formation of cementite in the critical temperature range. The process may begin with segregation of P or N to grain boundaries in austenite, perhaps promoted by Mn. The segregation that occurs is slight.[119] Subsequent precipitation of cementite at the former austenite grain boundaries may increase the impurity segregation by rejecting solutes from the growing carbide particles. The likely combination is that impurity segregation weakens adhesion at the prior austenite grain boundaries and cracking of carbides initiates intergranular fracture.

The second variety of embrittlement is commonly called temper embrittlement or, less often, two-step temper embrittlement.[130,131] The two-step temper embrittlement occurs in alloy steels having much lower yield strengths because of tempering at high temperatures, 600 $^{\circ}$C ~ 700 $^{\circ}$C, followed by slow cooling through the range 600 $^{\circ}$C to 350 $^{\circ}$C, or having a service temperature in that range. The fracture in TE is intergranular, occurring on former austenite boundaries.

This chapter describes some of the interrelated chemical and microstructural causes associated with the decrease in reduction of area and embrittlement phenomena in carbon and low alloy steels and relates these causes to characteristic cleavage, or intergranular fracture surfaces. Special attention will be focused on the rule of $Fe_{23}(C, B)_6$.

6.2 Experimental methods

6.2.1 SEM metallography

Steel S3 specimens for optical microscopy observation were hot mounted in bakelite molding powder, ground with silicon carbide paper down 1200 grit and then polished with 6 and 1 um diamond pastes. The specimens were then etched with 3 vol. % natal (nitric acid in methanol) and picric acid. The etched specimens were gold-coated in vacuum atmosphere. SEM was performed using JEOL JSM-7000F field emission scanning electron microscope.

6.2.2 TEM metallography

TEM was performed using Philips transmission electron microscopes operated at 200 kV. Two types of specimens were examined using TEM equipped with an energy dispersive X-ray (EDX) unit; thin foils and carbon extraction replicas. Thin foils were sliced from bulk specimens as 3 mm diameter discs approximately 250 um in thickness using a silicon carbide blade and cooling lubricant. After slicing, the specimens were ground with silicon carbide paper to around 50 um thickness. Electropolishing was conducted using a twin jet electropolisher. The solutions for electropolishing were 5 vol. % perchloric acid, 20 vol. % glycerol and 75 vol. % methanol. The electropolishing was performed with the solution at 20 $^{\circ}$C, the electrical potential being set at 50 V.

Carbon replica specimens were also prepared from each sample for TEM examination. By eliminating effects due to the steel matrix, the size and the chemical composition of the

carbides may be measured more accurately. Single stage extraction replicas were prepared. The sample was polished mechanically by the same method as for optical microscopy, and chemically etched with 4 vol. % nital for few seconds. A carbon coating of 20 ~ 30 nm was deposited in a vacuum of 10^5 torr onto the etched surface. This film was then scored with a sharp blade to divide it into several smaller squares (about 1 mm^2). Electrolytic etching in a solution of 5 % hydrochloric acid in methanol at 7.5 V was used to remove the carbon film, which was then washed in methanol and floated off in distilled water. Each sample yielded approximately ten smaller squares of film which were mounted on copper grids and dried before examination in the TEM.

6.2.3 Atom probe analysis

To observe the $Fe_{23}(C, B)_6$ carbide, atomic probe (AP) analyses were conducted using a laser assisted 3-DAP (CAMECA, LAWATAP) in an analysis volume of 66 * 66 * 85 nm^3. The AP tips were prepared using dual beam FIB (Helius 600). Ga ion of 30 keV energy with beam current of 25 nA were used for imaging. Fig. 6.1 shows the sample procedures for AP. The AP analyses were carried out in the ultra-high vacuum ($\sim 1 \times 10^{-10}$ mbar) at tip temperature of 50 K under a pulse fraction of 15 % and a pulse repetition rate of 600 Hz. A typical mass spectrum as measured from a LAWATAP is shown in Fig. 6.2. All of the alloy atoms such as B, C, Cr, Mn, Ti, Ni and Fe were detected. Detected carbon peaks were found at mass-to-charge (m/n) ratios of 6 (C^{++}), 12(C^+ and C_2^{++}), 18(C_3^{++}), 24 (C_2^+ and C_4^{++}) and 36 (C_3^+). And boron peaks were also found at m/n ratio of 5 (B^{++}) and 11 (B^+). In addition, other alloy elements were indexed. It is assumed that H peaks came from the analysis chamber.
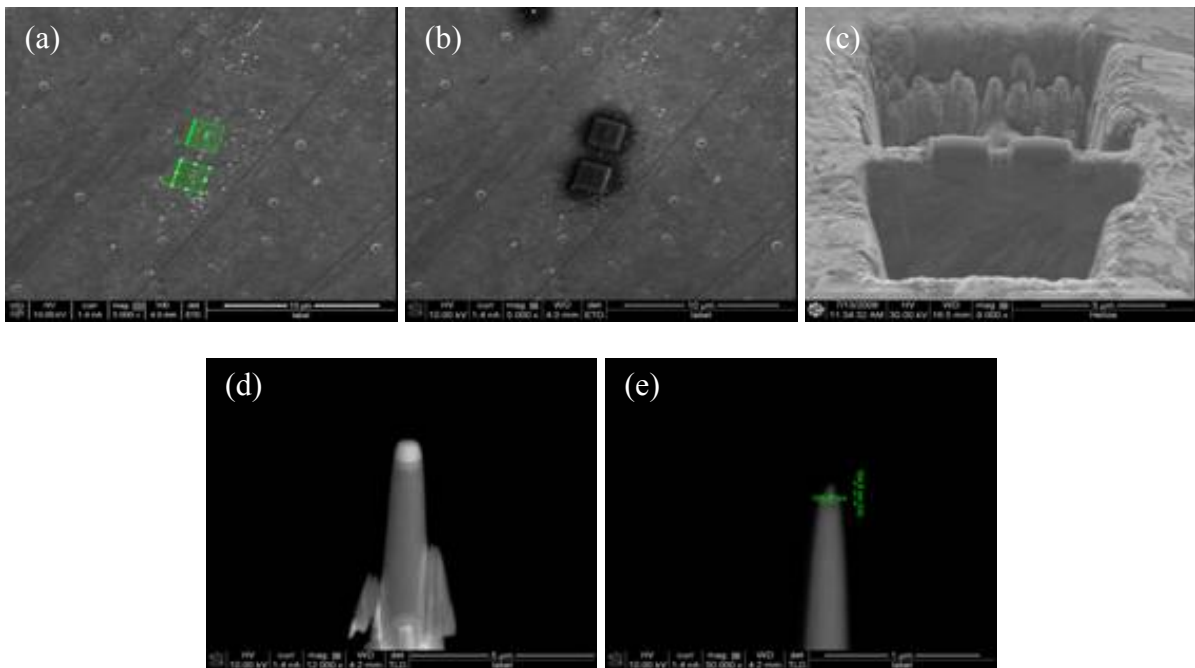

FIGURE 6.1. SEM images showing the procedures for AP sample preparation. (a) carbides, (b) Pt deposition, (c) trench milling, (d) annular milling and (e) final tip.
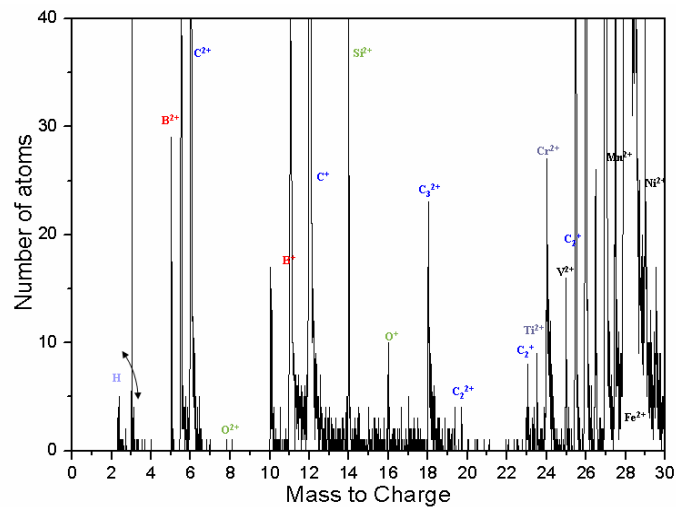
FIGURE 6.2. Mass spectrum of the steel wires obtained from laser pulsed atom probe. All of the atoms are detected.

6.3 Results

6.3.1 Effect of $Fe_{23}(C, B)_6$ carbide on intergranular fracture

Fig. 6.3 shows the fracture surfaces of tensile tested specimens of S1 and S3 steels. All specimens were austenitized at 880 ^{o}C and then tempered at 450 ^{o}C.   The fracture surface of S1 steel shows the ductile fracture with a high ductility (reduction of area RA = 43.5 %). However, S3 steel showed intergranular fracture leading to low ductility (reduction of area RA = 22.2 %) regardless of high tempering temperature. The crack propagation of S1 steel was conventional ductile fracture initiated at center of specimen, but the crack propagation of S3 steel was initiated from the surface and appeared like.   The longitudinal microstructure of surface crack of tensile tested specimens of S3 steel in Fig. 6.3 (c) is shown in Fig. 6.4. The crack was initiated and propagated along the carbides at grain boundaries. The crack also was initiated at the crack of carbides. The crack may initiate at the particle (inclusion, carbide) and propagate easily along prior austenite grain boundary by carbide formation.   These carbides can act as slip barriers and can initiate intergranular cracks at prior austenite grain boundary.   The reduction of area may be reduced significantly due to the intergranular fracture along austenite grain boundaries covered with these carbides.

6.3.2 $Fe_{23}(C, B)_6$ precipitation

In order to investigate the carbide caused the intergranular fracture, the precipitation behavior of carbide in tempered microstructure of S1 and S3 steels was compared and examined.   The microstructure of tempered specimens of S1 steel was investigated for austenitization temperatures of 880 ^{o}C and 930 ^{o}C, as shown in Fig. 6.5.   In case of austenization temperature 880 ^{o}C, the coarse cementite undissolved during austenization was retained after tempering.   The amount of undissolved coarse cementite decreased with increasing the austenitization temperature from 880 ^{o}C to 930 ^{o}C.
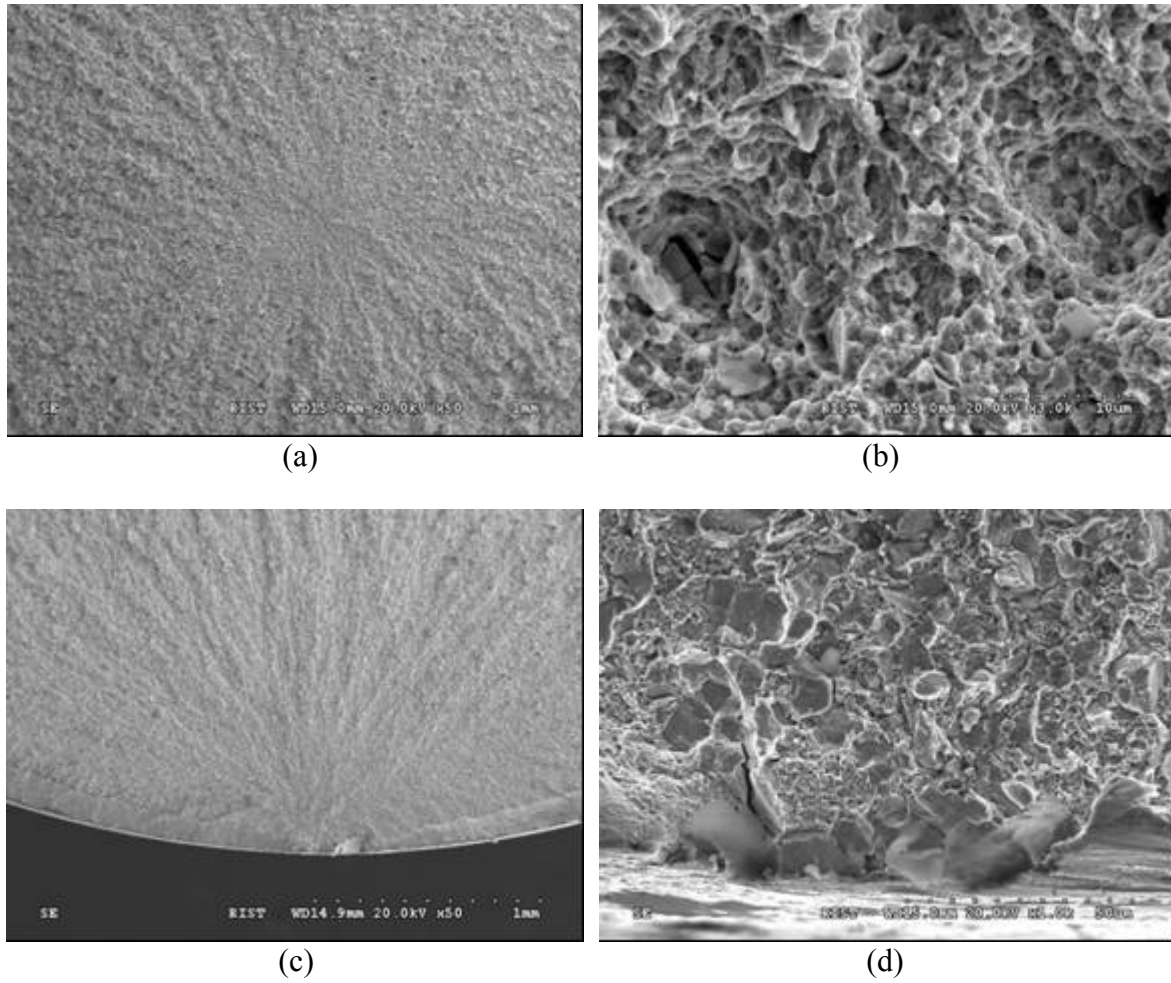
(a)

(b)

(c)

(d)

FIGURE 6.3. Fractographs of tensile tested specimens of S1 and S3 steel. All of specimens were austenitized at 880 ^{o}C and then tempered at 450 ^{o}C. (a), (b) of S1 steel and (c), (d) of S3 steel.
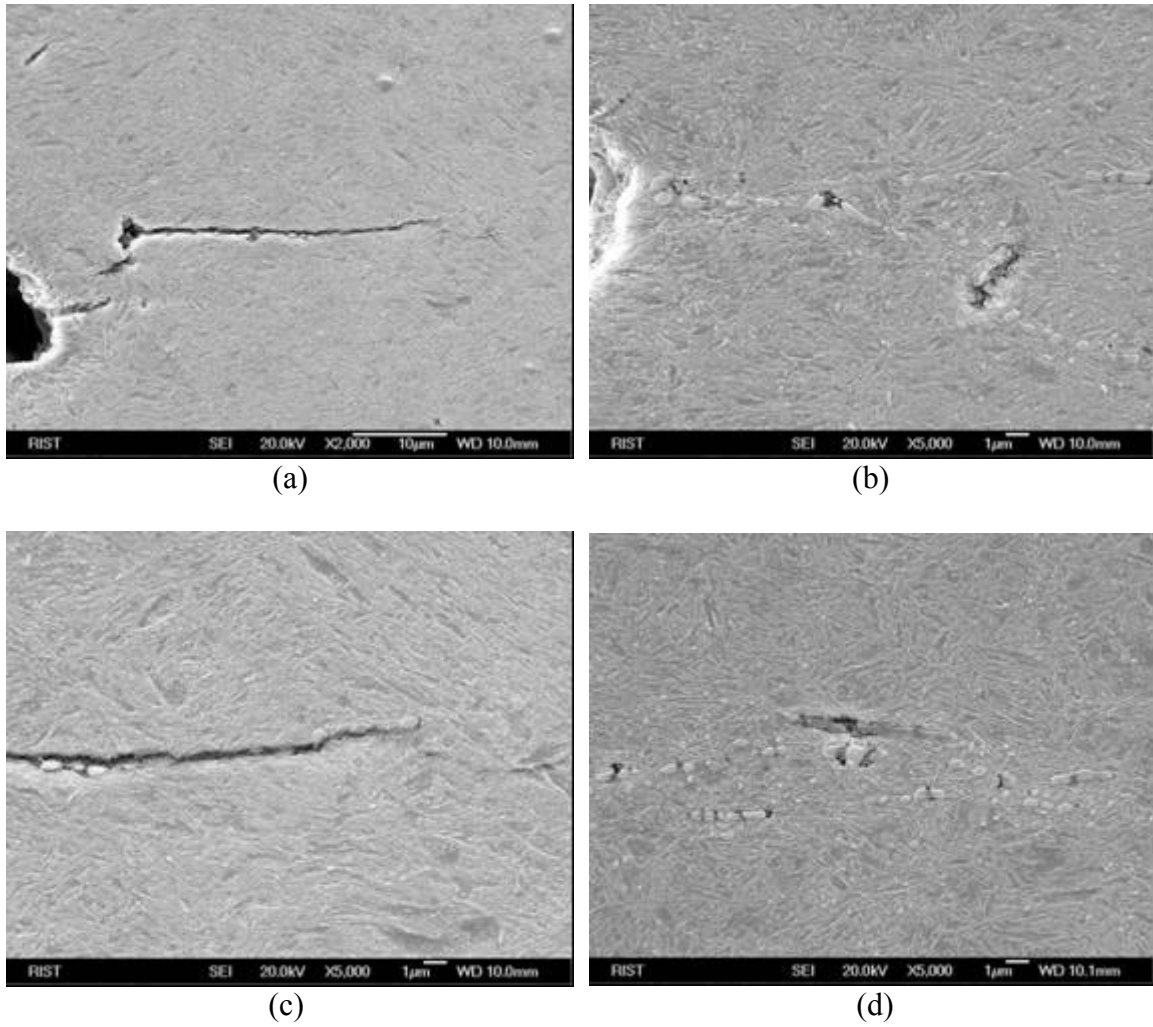
(a)

(b)

(c)

(d)

FIGURE 6.4. SEM micrographs of cross-sections of tensile tested specimens of S3 steel. (a), (b) tempered at 350 ^{o}C and (c), (d) at 450 ^{o}C.

The microstructure of tempered specimens of S1 steel consisted of tempered martensite and coarse cementite, but this carbide did not cause the intergranular fracture.

Fig. 6.6 shows that for S3 steel, the microstructure consists of tempered martensite and undissolved coarse cementite, similar to that of S1 steel. It indicates, however, that the carbides existed along prior austenite grain boundaries. Fig. 6.7 shows these carbides were examined as $Fe_{23}(C, B)_6$ carbide having the zone direction [112]. $Fe_{23}(C, B)_6$ carbide was retained at prior austenite grain boundary after tempering, regardless of tempering temperatures as shown in Fig. 6.6.

In addition, the chemical composition of $Fe_{23}(C, B)_6$ carbide was measured by using 3-DAP technique. Fig. 6.8 shows the 3-DAP elemental maps of alloy element in an analysis volume of 66 * 66 * 85 nm^3 in the side views. Each dot represents the location at which alloy atoms were detected. And the density of dots in the analyzed volume is proportional to the density of alloy atoms. It was found that all elements except Si co-existed. Fig. 6.9 represents the 2-dimensional composition profile showing the several alloy atoms such as C, B, Mn, Cr, V, Ti and Fe. The detection direction ($\rightarrow$) is listed in boron atom map in Fig. 6.8. Therefore, the carbides along prior austenite grain boundary is again confirmed as $Fe_{23}(C, B)_6$ carbide by using SEM, TEM and 3-DAP.

Fig. 6.10 shows the distribution and shape of $Fe_{23}(C, B)_6$ carbide at prior austenite grain boundary of S3 steel austenitized at 830 ^{o}C, 880 ^{o}C, 930 ^{o}C and 980 ^{o}C. It indicates that these $Fe_{23}(C, B)_6$ carbides were not dissolved completely during austenitization and existed at prior austenite grain boundary.

The microstructures of as-rolled specimens of S1 and S3 steels are shown in Fig. 6.11. The difference is the existence of carbide and ferrite along grain boundary in S3 steel. The microstructure of S3 steel was mainly pearlite and the carbides were existed along grain boundary, and ferrite was formed near the carbides at grain boundary. However, the microstructure of S1 steel was pearlitic structure, but carbide did not be formed at grain boundary. Fig, 6.12 shows the TEM results about the carbides along grain boundaries of S3 steel shown in Fig. 6.11. The carbides was investigated as $Fe_{23}(C, B)_6$ structure having lattice parameter 10.67 Å, and Fig. 6.12 (b) and (c) are the dark field image and diffraction pattern of carbide respectively [133,134]. The zone axis of carbide is [110] direction as shown in Fig. 6.12 (c). The phase near $Fe_{23}(C, B)_6$ carbide is ferrite having BCC (Body Centered Cubic) structure, and zone direction is [110] as shown in Fig. 6.5 (d) and (e).

The microstructure of as-rolled specimens of S3 steel consisted of pearlite, carbide and ferrite at grain boundary. As a result, $Fe_{23}(C, B)_6$ carbide and ferrite at grain boundary were formed in as-rolled state and still retained after tempering.

6.4 Discussion

The fracture surface of tensile tested specimen of S3 steel is intergranular brittle fracture with a low ductility (reduction of area, elongation etc.). Fig. 6.4 shows that the crack propagated easily along $Fe_{23}(C, B)_6$ carbide at prior austenite grain boundary. The $Fe_{23}(C, B)_6$ carbide can act as slip barriers and can initiate intergranular cracks at prior austenite grain boundary.
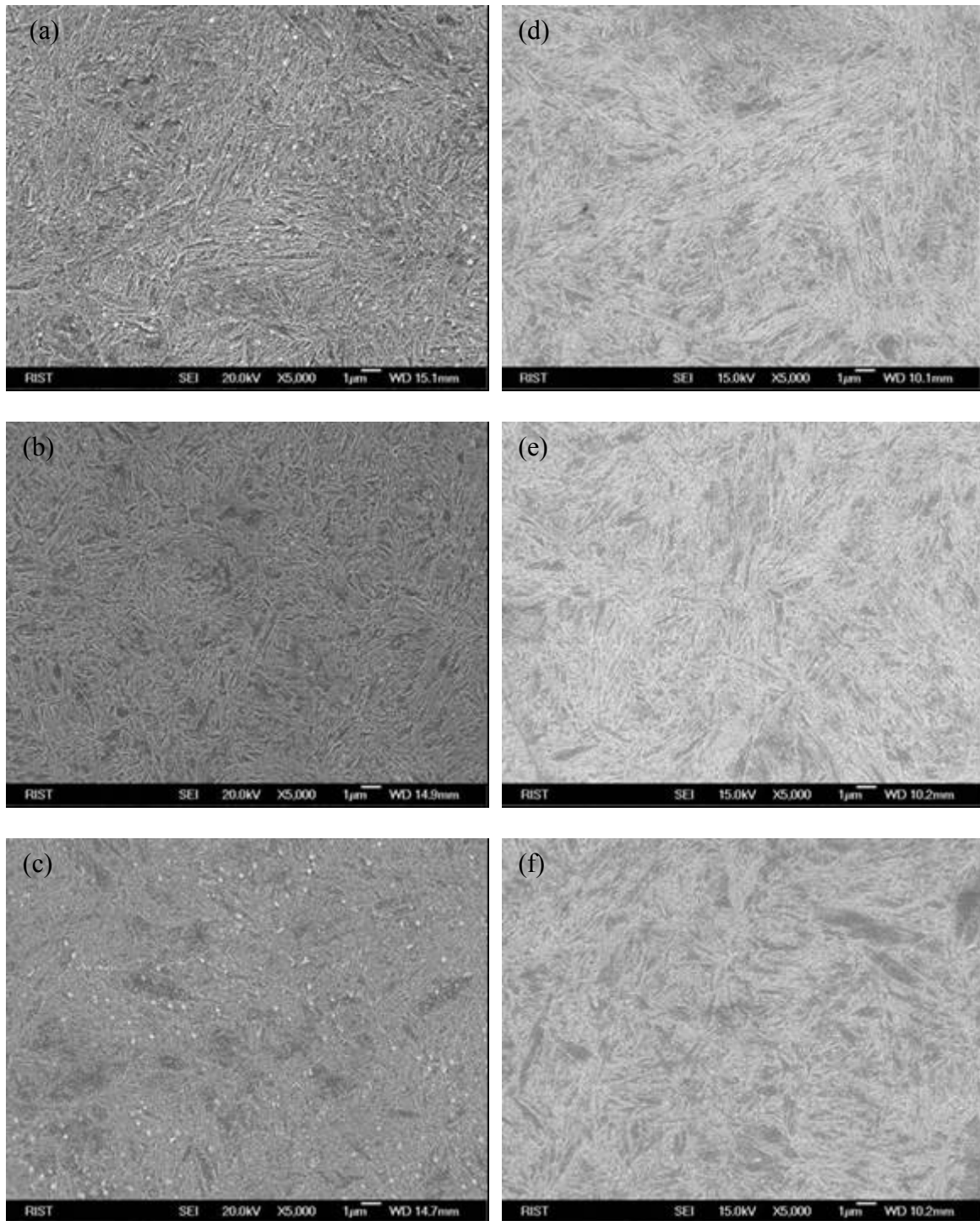
FIGURE 6.5 SEM micrographs of tempered specimens of S1 steel. Tempering temperature: (a) 350 $^{\circ}$C, (b) 400 $^{\circ}$C and (c) 450 $^{\circ}$C (austenitized at 880 $^{\circ}$C) and (d) 350 $^{\circ}$C, (e) 400 $^{\circ}$C and (f) 450 $^{\circ}$C (austenitized at 930 $^{\circ}$C)
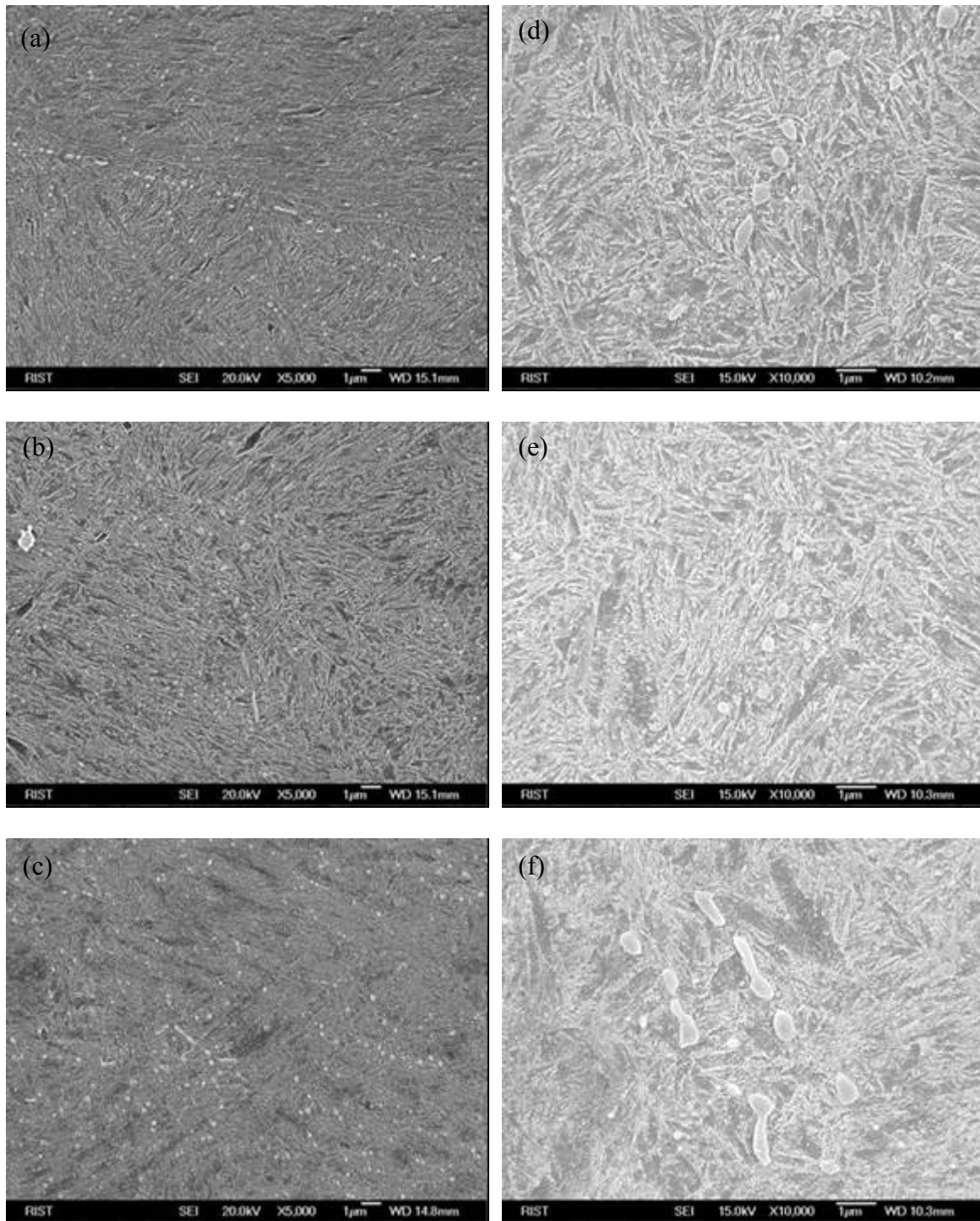
FIGURE 6.6. SEM micrographs of tempered specimens of S3 steel. Tempering temperature: (a) 350 ^{o}C, (b) 400 ^{o}C and (c) 450 ^{o}C (austenitized at 880 ^{o}C) and (d) 350 ^{o}C, (e) 400 ^{o}C and (f) 450 ^{o}C (austenitized at 930 ^{o}C)
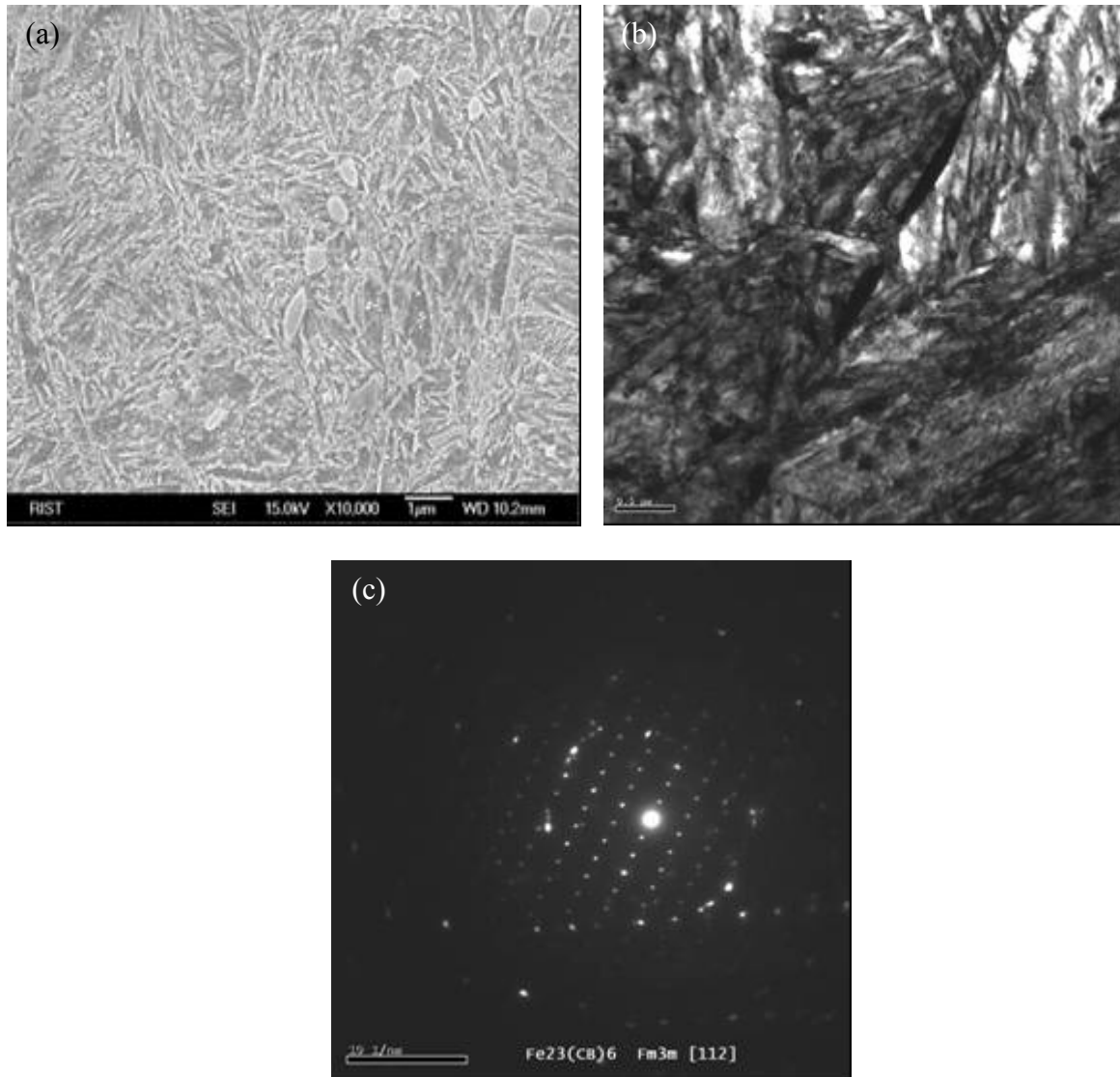
FIGURE 6.7. SEM, TEM micrographs and diffraction pattern of $Fe_{23}(C, B)_6$ carbide of S3 steel tempered at 350 °C (austenitized at 880 °C). (a) SEM image, TEM image and (b) diffraction pattern
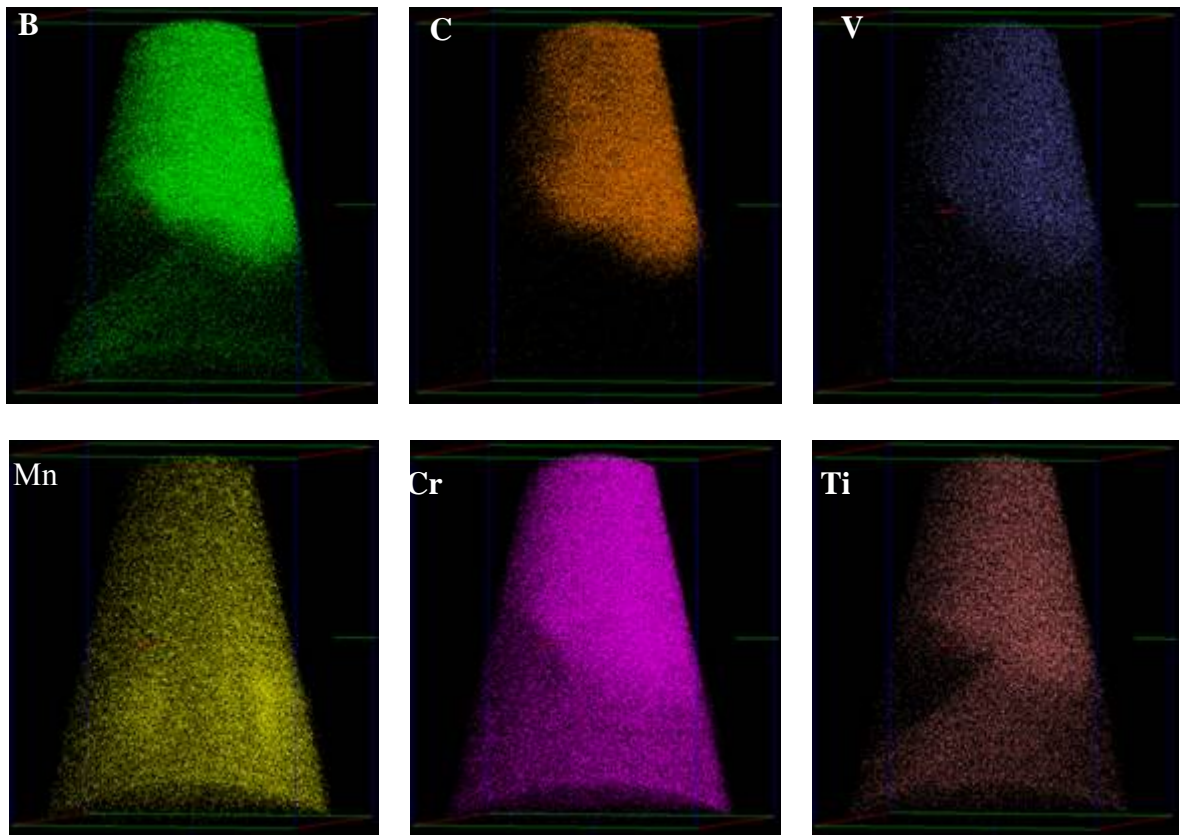
FIGURE 6.8. Dimensional atom map showing alloy element such as B (●), C (●), V (●), Mn (●), Cr (●) and Ti (●). It was found that all of alloy element except Si were co-existed.
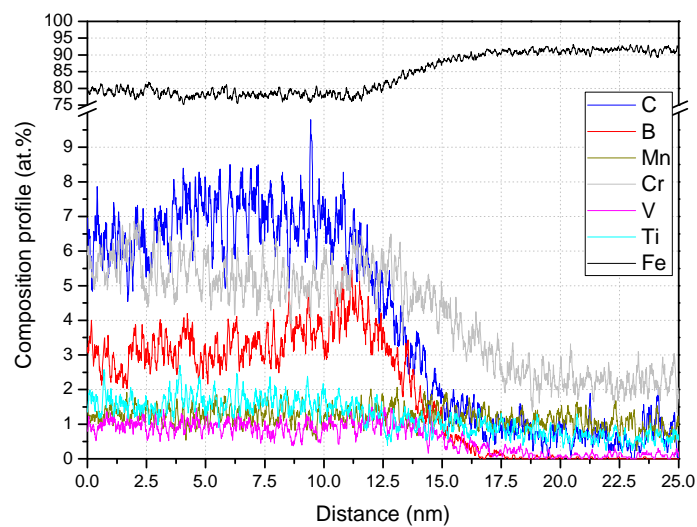

FIGURE 6.9. 2-dimensional composition profile showing the several alloy atoms such as C, B, Mn, Cr, V, Ti and Fe. The detection direction (→) is listed in carbon atom map in Fig. 6.8.
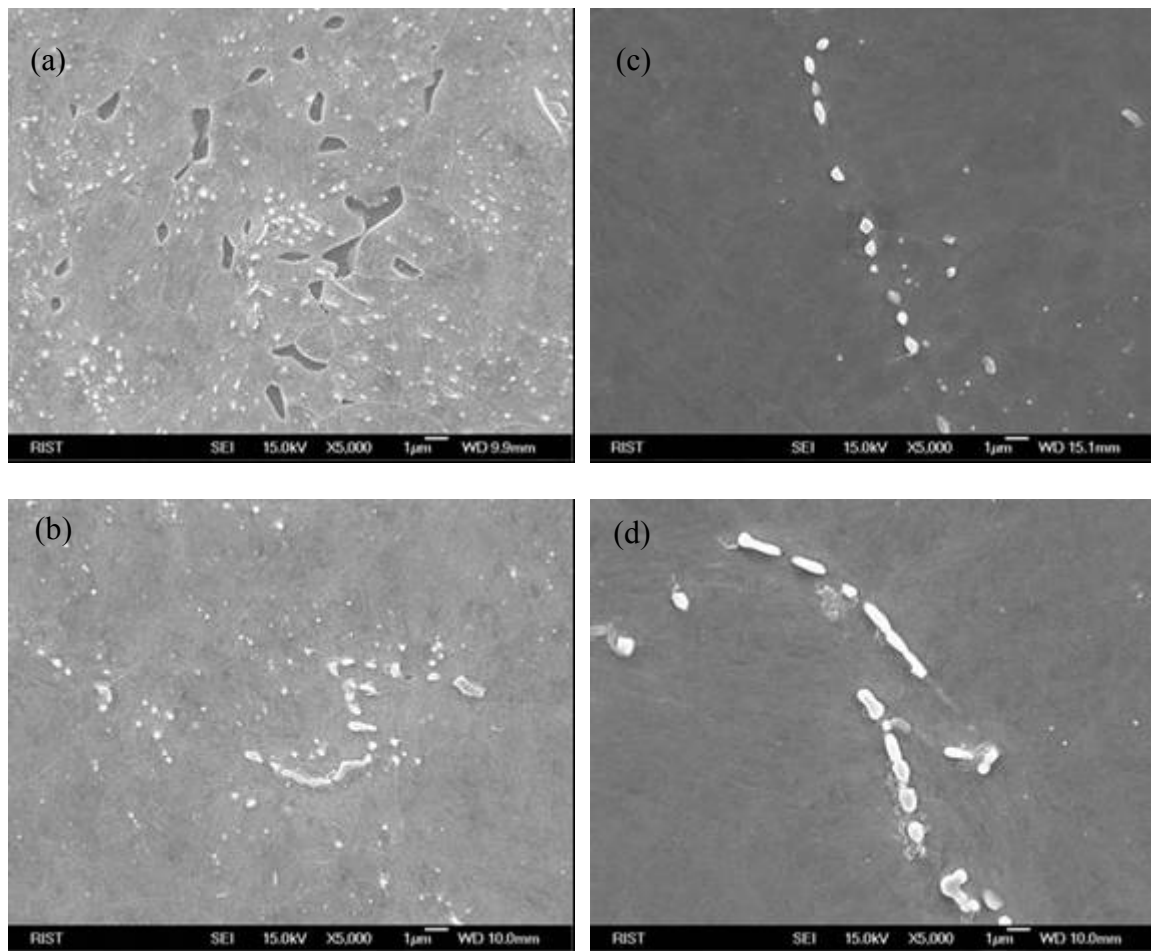
FIGURE 6.10. SEM micrographs of Fe$_{23}$(C, B)$_6$ carbide in the oil-quenched specimens of S3 steel austenitized at (a) 830 $^{\circ}$C, (b) 880 $^{\circ}$C, (c) 930 $^{\circ}$C and (d) 980 $^{\circ}$C.
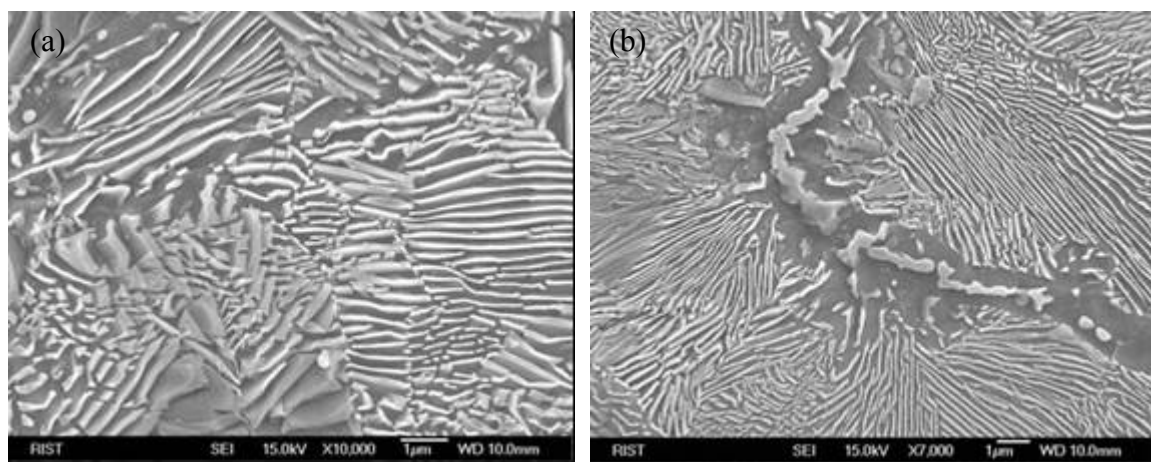

FIGURE 6.11. SEM micrographs of as-rolled specimens of S1 and S3 steels.   (a) S1 steel and (b) S3 steel
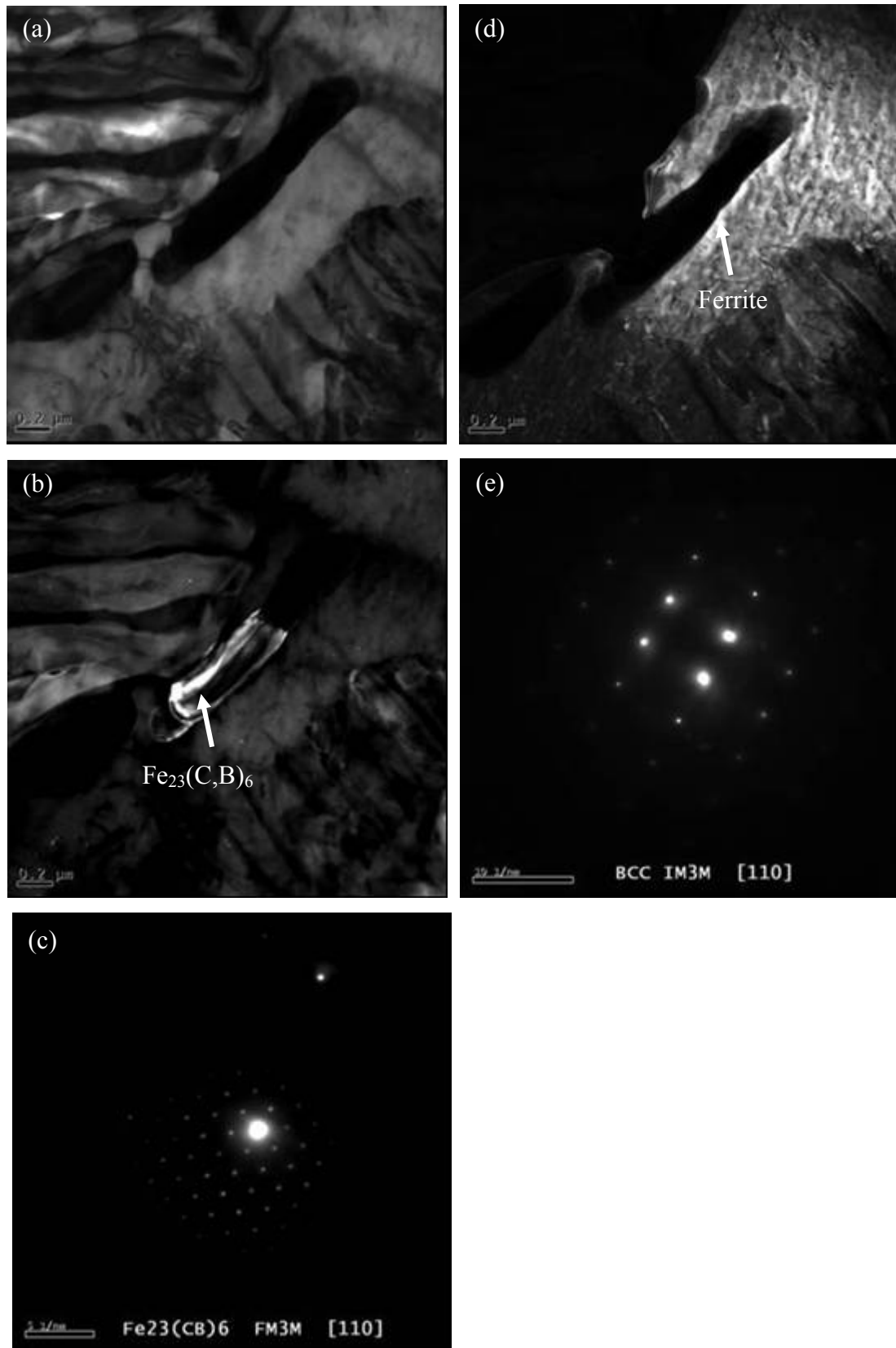
FIGURE 6.12. TEM micrographs and diffraction pattern of as-rolled specimens of S3 steel. (a) TEM image, (b) Fe$_{23}$(C,B)$_6$ image, (c) Diffraction pattern of Fe$_{23}$(C,B)$_6$, (d) Ferrite image and (e) Diffraction pattern of ferrite.

The formation of Fe$_{23}$(C, B)$_6$ carbide should be suppressed to avoid the intergranular fracture after quenching and tempering treatment. The precipitation behavior of Fe$_{23}$(C, B)$_6$ carbide in as-rolled state during cooling at a rate of 1.0 $^{\circ}$C/s was investigated (Fig. 6.13 (a)). Fig. 6.13 shows the SEM micrographs of microstructure of S3 steel during cooling. All of specimens were austenitized for 1800 seconds at 980 $^{\circ}$C. Fe$_{23}$(C, B)$_6$ carbide was absent after quenching from 980 $^{\circ}$C. When cooled from 980 $^{\circ}$C to 710 $^{\circ}$C, Fe$_{23}$(C, B)$_6$ carbide started to precipitate at prior austenite grain boundary. And ferrite formed at interface between Fe$_{23}$(C, B)$_6$ carbide and austenite, and pearlite appears simultaneously. Fe$_{23}$(C, B)$_6$ carbide formed first at prior austenite grain boundary and then the carbon depleted zone may be made near Fe$_{23}$(C, B)$_6$ carbide. Ferrite formed from carbon depleted zone near Fe$_{23}$(C, B)$_6$ carbide. After cooling to room temperature, the microstructure consisted of pearlite and, Fe$_{23}$(C, B)$_6$ carbide and ferrite at prior austenite grain boundary.

In order to analyze the dissolution behavior of Fe$_{23}$(C, B)$_6$ carbide and cementite during heating, the austenitization of S3 steels was simulated using the dilatometer. As-rolled specimens were heated to the desired temperatures 790 $^{\circ}$C ~ 930 $^{\circ}$C and directly quenched to room temperature.

Fig. 6.14 shows the austenitization behavior of S3 steel with increasing austenitization temperature. Pearlite dissolved completely above 850 $^{\circ}$C and a part of cementite was almost dissolved above 930 $^{\circ}$C. A part of coarse carbide along prior austenite grain boundary was retained during austenitization. The coarse carbide along grain boundary was Fe$_{23}$(C,B)$_6$ carbide as shown in Fig. 6.11 and 6.12. With increasing heating temperature, the Fe$_{23}$(C, B)$_6$ carbide dissolved but remained as coarse particles at prior austenite grain boundary. Fig. 6.15 shows the behavior of austenitization of S3 steel in the range 930 $^{\circ}$C ~ 1200 $^{\circ}$C. By using dilatometer, it was investigated the stability of Fe$_{23}$(C, B)$_6$ carbide during heating to 1200 $^{\circ}$C. The Fe$_{23}$(C, B)$_6$ carbide was stable and retained at prior austenite grain boundary after holding for 180 seconds at austenitization temperature from 930 $^{\circ}$C ~ 1200 $^{\circ}$C. Therefore, if Fe$_{23}$(C, B)$_6$ carbide was formed in as-rolled state, the stability of Fe$_{23}$(C, B)$_6$ carbide was very high at high temperature and Fe$_{23}$(C, B)$_6$ carbide did not dissolve completely under conventional conditions of spring heat treatment.

The fracture mechanism of intergranular fracture of S3 steel is schematically presented in Fig. 6.16. Fe$_{23}$(C, B)$_6$ carbide in as-rolled state was precipitated at prior austenite grain boundary during cooling. Ferrite was formed at carbon depleted zone near borocarbide. Finally the microstructure of as-rolled specimen of S3 steel consisted of pearlite and borocarbide and ferrite at prior austenite grain boundaries as shown in Fig. 6.16 (a).

The microstructure of as-rolled specimens transformed to austenite during austenitization. However, Fe$_{23}$(C, B)$_6$ carbides did not dissolve completely under general condition of spring heat treatments. These Fe$_{23}$(C, B)$_6$ carbides were still retained at prior austenite grain boundary after quenching and tempering. A part of Fe$_{23}$(C, B)$_6$ carbide was dissolved during austenitization and was segregated as free boron after quenching and tempering. The intergranular fracture of tensile tested specimens of S3 steel may be caused by the Fe$_{23}$(C, B)$_6$ carbide at prior austenite grain boundary. Crack initiates at the microcrack of surface or particles (inclusion, carbide, Fe$_{23}$(C, B)$_6$ carbide etc.) at prior austenite grain boundary and propagates easily along grain boundary by help of Fe$_{23}$(C, B)$_6$ carbide. The ductility (reduction of area, elongation etc.) may be reduced considerably because of intergranular fracture along prior austenite grain boundaries covered with Fe$_{23}$(C, B)$_6$ carbide.
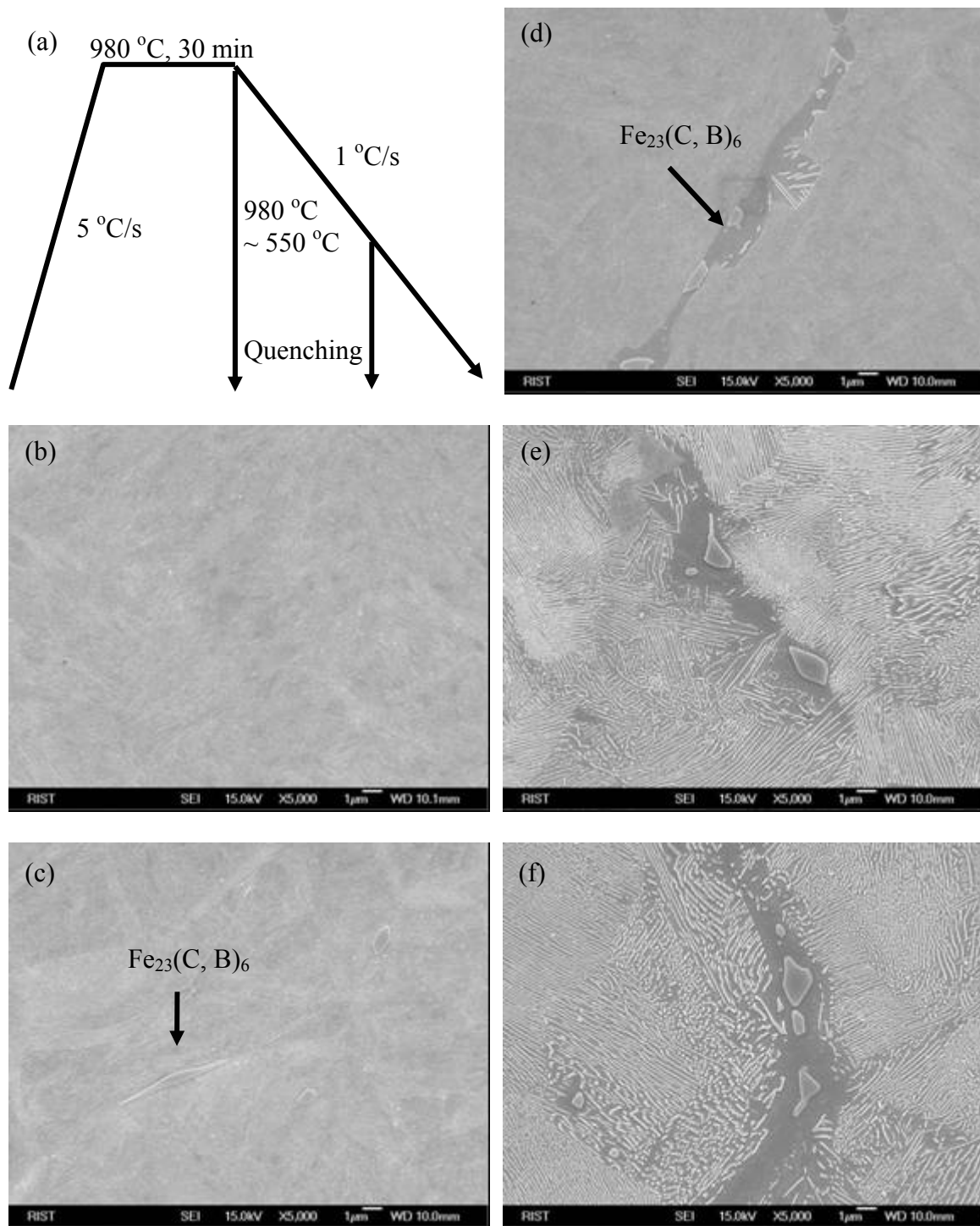
FIGURE 6.13.   SEM micrographs of microstructures of S3 steel during cooling.   (a) Schematic diagram of the cooing simulation by dilatometer. It was quenched at (b) 980 ^{o}C, (c) 710 ^{o}C, (d) 700 ^{o}C, (e) 690 ^{o}C and (f) 650 ^{o}C.
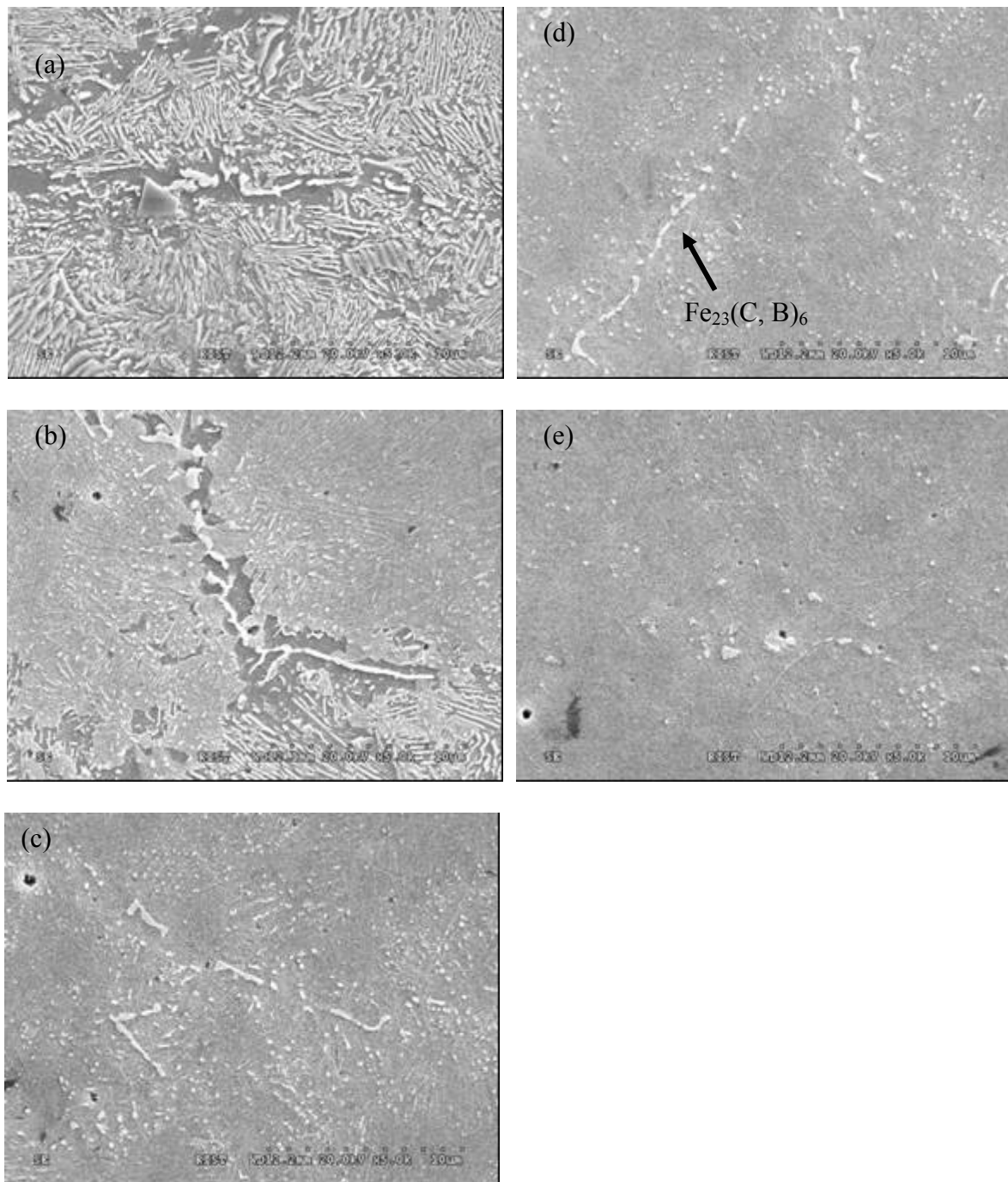
FIGURE 6.14. SEM micrographs of quenched specimens of S3 steel during heating. It was oil-quenched directly from (a) 790 ^{o}C, (b) 820 ^{o}C, (c) 850 ^{o}C, (d) 880 ^{o}C, (e) 930 ^{o}C.
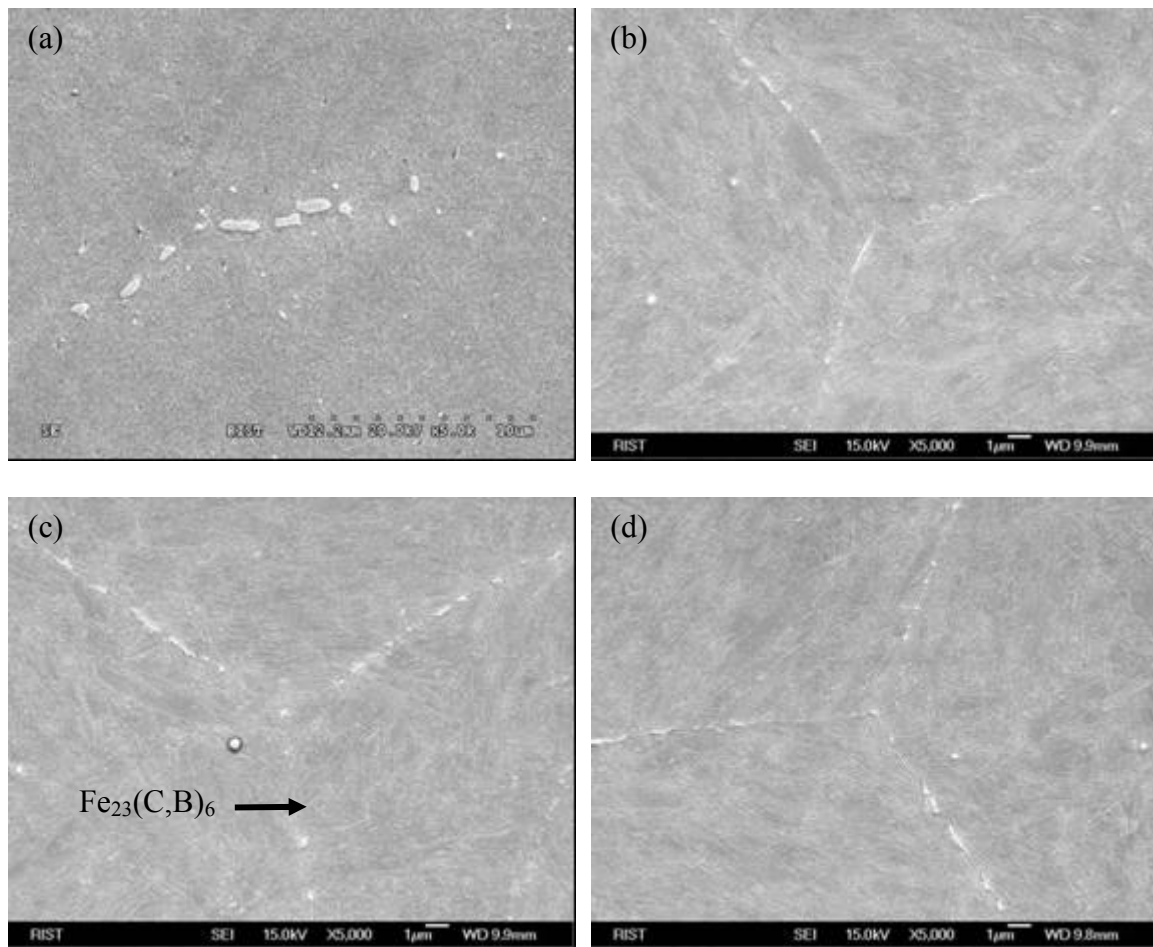
FIGURE 6.15. SEM micrographs of quenched specimens of S3 steel during heating. It was quenched after holding 180 sec. at (a) 930 ^{o}C, (b) 1000 ^{o}C, (c) 1100 ^{o}C and (d) 1200 ^{o}C.
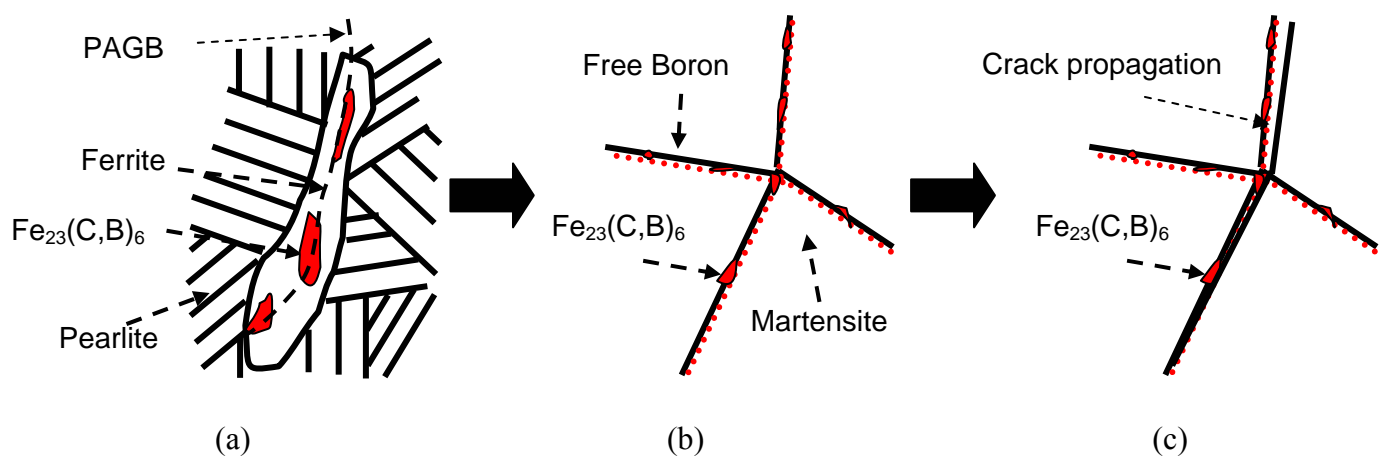
FIGURE. 6.16. Mechanism of $Fe_{23}(C, B)_6$ embrittlement. (a) as-rolled state, (b) tempered state and (c) cracking during deformation.

6.5 Conclusion

In the present investigation, embrittlement of a new high strength spring steel has been evaluated in relation to the microstructural study. The intergranular fracture of S3 steel is caused the borocarbide at prior austenite grain boundary. Crack initiates at the microcrack of surface or particles (inclusion, carbide, $Fe_{23}(C, B)_6$ carbide etc.) at prior austenite grain boundary and propagates easily along grain boundary by $Fe_{23}(C, B)_6$ carbide. The ductility (reduction of area, elongation etc.) may be reduced significantly because of intergranular fracture along prior austenite grain boundaries covered with $Fe_{23}(C, B)_6$ carbide.

7

Effect of step tempering on strength and reduction of area of spring steel

7.1 Introduction

Martensite in steels can be a very strong and in its virgin condition rather brittle. It is then necessary to modify its mechanical properties by heat treatment in the range 150 ^{o}C ~ 700 ^{o}C. This process is called tempering, in which the microstructure approaches equilibrium under the influence of thermal activation.[2,74] The general trend during the tempering of martensite therefore begins with the rejection of excess carbon to precipitate carbides but the substitutional solutes do not diffuse during this process. The end result of tempering is a dispersion of carbides in a ferritic matrix which bears little or more resemblance to the original martensite depending on the tempering temperature. Generally, the relationship of strength and ductility is of major concern in the heat treatment and application of quench and tempered steels. Both yield strength and tensile strength decrease continuously and elongation and reduction of area increase with increasing tempering temperature.

In addition to increasing the strength, certain alloying elements also help to retard the rate of softening during tempering. The most effective elements in this regard are strong carbide formers such as Cr, Mo and V.[135] Without these elements, iron-carbon alloys and low carbon steel soften rapidly with increasing tempering temperature.[2,74,135] This softening is largely due to the rapid coarsening of cementite with increasing tempering temperature, a process dependent on the diffusion of carbon and iron.[98,100] If present in a steel in sufficient quantity, however, the carbide forming elements not only retard softening but also form fine alloy carbides that produce a strength increase at higher tempering temperature.

7.1.1 Strengthening and softening mechanism

Several factors described above were considered to explain the change of tensile strength of the proposed spring steels.[2,74,135] These strengthening factors were the austenitization behavior, precipitation behavior and the refinement of austenite grain and lath structure in martensite. In general, in order to increase the tensile strength of tempered martensitic structure, the precipitation strengthening has been used by adding the carbide-forming alloying elements.[95,136] For the proposed steels, V_4C_3-type carbide was mainly precipitated by adding the alloying elements of V, Ti and Mo.[106] The $(V, Ti)_4C_3$ carbide was main precipitates in S1 steel and $(V, Ti, Mo)_4C_3$ carbide was in S3 steel. V_4C_3-type carbide of S3 steel was precipitated a little finer and denser than that of S1 steel. The addition of Mo of S3 steel may cause a fine precipitation of $(V, Ti, Mo)_4C_3$ carbide. The size distribution of V_4C_3-type carbide does not change with the tempering temperature. The inter-particle distance of V_4C_3-type carbide decreased a little with increasing the tempering temperature. It notes that V_4C_3-type carbide may be contributed as a minor factor to increase the strength by precipitation strengthening.

The other precipitate of S1 and S3 steels was investigated as ε-carbide formed during tempering treatment. The size distribution of ε-carbide was very finer and denser than that of V_4C_3-type carbide. The increment of tensile strength may be based on the precipitation behavior of ε-carbide instead of V_4C_3-type carbide during tempering treatment. At low temperatures (the very early stage of tempering), the primary martensite is decomposed into ε-carbide and a low carbon martensite via clustering of carbon atoms [74,100]. When the tempering temperature changed from 400 ^{o}C to 450 ^{o}C, the rapid decrease of tensile strength can be explained by the transition from ε-carbide to cementite. The ε-carbide was dissolved and simultaneously the nucleation of cementite starts with the concurrent elimination of ε-carbide. The decrease of tensile strength may be caused the transition from ε-carbide to cementite with increasing the tempering temperature. The main strengthening mechanism might be the precipitation behavior of ε-carbide during tempering.

For the softening, as described above, the precipitation behavior consisted of V_4C_3-type carbide and ε-carbide. V_4C_3-type carbide did not change with the tempering temperature and seems not related to the reduction of area. However, ε-carbide changed to the cementite with increasing the tempering temperature and cementite was spheroid and lager than ε-carbide. The increment of reduction of area could be explained by the transition from ε-carbide to cementite. Especially, the rapid increase of reduction of area at tempering temperature of 450 ^{o}C was due to increase of the fraction of cementite formation and ε-carbide dissolution. V_4C_3-type carbide may be contributing as a minor factor to increase the strength by precipitation strengthening. However, the main strengthening mechanism might be the precipitation behavior of ε-carbide during tempering.

7.1.2 Step tempering

Up to this point, tempering has been discussed with temperature as the major variable. The structural changes responsible for the property changes, however, are thermally activated and therefore dependent on both temperature and time. For instance, if a single mechanism of structural change is operating during a stage of tempering, the coarsening of cementite, a given strength may be obtained by tempering at a high temperature for a short time or by

tempering at a lower temperature for a longer time. Generally if time is not mentioned, as is the case for most of the preceding results, the total tempering time is 30 minutes.

In order to improve the mechanical properties, the new tempering treatment was developed which consisted of two step tempering processes. Fig. 7.1 shows the schematic diagram of conventional tempering [2,74,100] and step tempering treatment. Conventional tempering is under one temperature, but step tempering is stepwise process under two temperatures. Main reason for step tempering is to increase the number of ε-carbide and suppress the transition from ε-carbide to cementite. Furthermore, the step tempering will affect the width of the precipitate size distribution, as nucleation and growth are differently coupled.
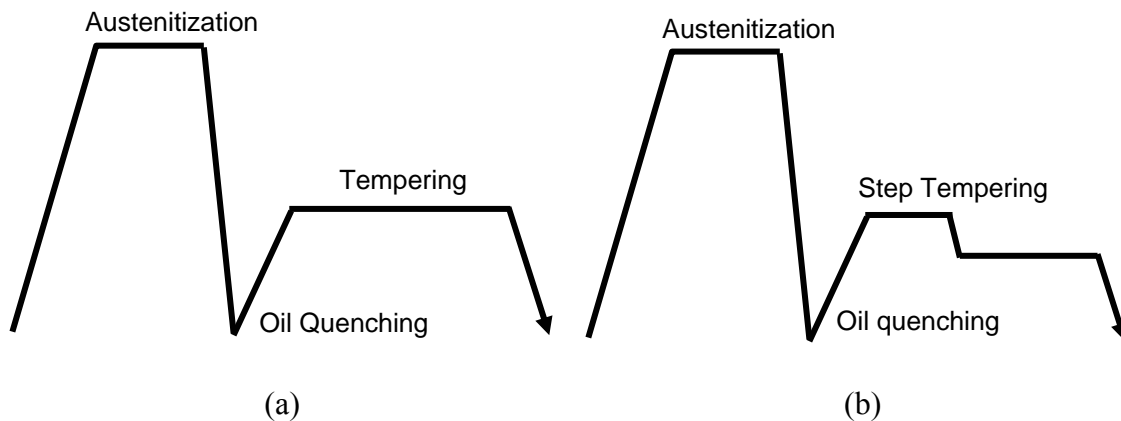

FIGURE 7.1. Schematic diagrams of conventional tempering and step tempering. (a) conventional tempering and (b) step tempering.

In step tempering, first tempering is under short time at higher temperature and second tempering is under comparative long time at lower temperature. It is assumed that in first tempering lots of ε-carbide is precipitated rapidly and in second tempering ε-carbide is suppressed to grow and transit to cementite. In this study, the step tempering process was applied to improve the mechanical properties of the proposed steels. The microstructure and mechanical property was investigated with changing the conditions of step tempering.

7.2 Experimental methods

7.2.1 Specimen preparation and heat treatment

The conventional spring steels of SAE9254 and POSHIS120D were used to make comparison to S1 and S3 steels and machined the cylindrical specimens as tensile test specimen. The chemical composition of SAE9254 is 0.55% C, 1.5% Si, 0.7% Mn, 0.7% Cr and those of POSHIS120D is 0.48% C, 2.1% Si, 0.65% Mn, 0.7% Cr, Fe (bal.) in weight %. The axis of tensile specimens was in the original rolling direction. All steels were found to become fully austenite at temperatures of 980 $^{\circ}$C for 3 min. They were subsequently quenched in oil at temperature of 50 $^{\circ}$C. Quenched specimens were tempered at temperature of 350, 400, 450 $^{\circ}$C for 30 minutes using a salt bath. Fig. 7.2 (a) shows the conventional tempering treatment.
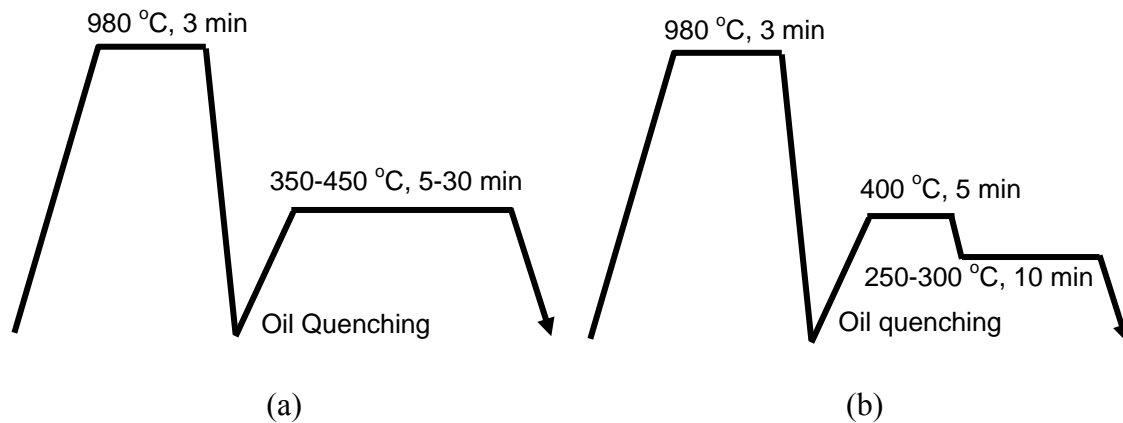
FIGURE 7.2.   Schematic diagrams of conventional tempering and step tempering.   (a) conventional tempering and (b) step tempering.

In step tempering experiments, all steels were found to become fully austenite at temperatures of 980 $^{\circ}$C for 3 min.   They were quenched in oil at temperature of 50 $^{\circ}$C.   Quenched specimens were first tempered at temperature of 400 $^{\circ}$C for 5 minutes and subsequently tempered at 250 and 300 $^{\circ}$C for 10 minutes using a salt bath.   The thermal history of step tempering is shown in Fig. 7.2 (b).

7.2.2 Mechanical and Fatigue tests

Tensile tests were conducted on samples with a gauge length of 25 mm, diameter 6.25 mm at a strain rate of 0.2 min^{-1}.   The Vickers hardness of the specimens was measured with a load of 10 kg applied for 10 seconds.   The surface hardness for each case was measured five times.   The coil springs were made of SAE9254 and POSHIS120D spring steels.   All springs were heated at 980 $^{\circ}$C for 3 minuets and then coiled to spring.   The coiled specimens were subsequently tempered as the conditions described above.   The fatigue test was done under the desired stress of 1100 ~ 1200 MPa.

7.2.3 SEM and TEM metallography

Specimens for optical microscopy observation were hot mounted in bakelite molding powder, ground with silicon carbide paper down 1200 grit and then polished with 6 and 1 μm diamond pastes.   The specimens were then etched with 3 vol. % natal (nitric acid in methanol) and picric acid.   The etched specimens were gold-coated in vacuum atmosphere.   SEM was performed using JEOL JSM-7000F field emission scanning electron microscope.   TEM was performed using Philips transmission electron microscopes operated at 200 kV.   Two types of specimens were examined using TEM equipped with an energy dispersive X-ray (EDX) unit; thin foils and carbon extraction replicas.   Thin foils were sliced from bulk specimens as 3 mm diameter discs approximately 250 μm in thickness using a silicon carbide blade and cooling lubricant.   After slicing, the specimens were ground with silicon carbide paper to around 50 μm thickness.   Electropolishing was conducted using a twin jet electropolisher.   The solutions for electropolishing were 5 vol. % perchloric acid, 20 vol. % glycerol and 75 vol. % methanol.

The electropolishing was performed with the solution at 20 ^{o}C, the electrical potential being set at 50 V.

7.3 Results and Discussions

7.3.1 Mechanical property

Tensile tests were carried out as a function of tempering temperature and time. The tensile strength (ultimate tensile strength) and the reduction of area of SAE9254 spring steel are shown in Fig. 7.3. These steels were austenitized at 980 ^{o}C and subsequently tempered at 350, 400 and 450 ^{o}C for 5 and 30 minutes. Tensile strength decreased with increasing tempering temperatures, but reduction of area increased as tempering temperature rose. As the tempering time increased from 5 to 30 minutes, the tensile strength decreased and the reduction of area increased.

(a)   (b)
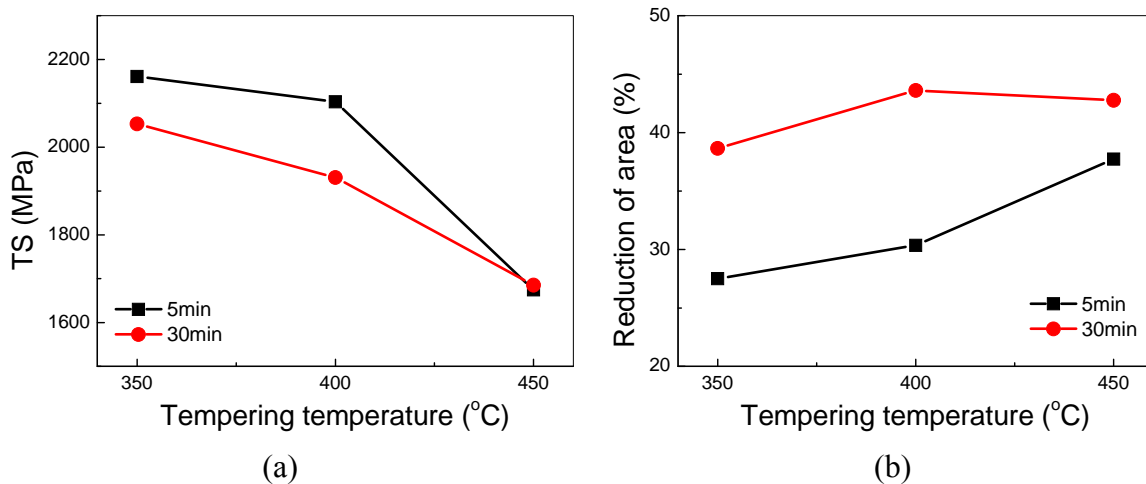
FIGURE 7.3. Mechanical properties of SAE9254 spring steel with tempering temperature and time. (a) Tensile strength and (b) Reduction of area

In order to improve the tensile strength and reduction of area, the tempering condition was redesigned as shown in Fig. 7.2 (b). It was known that as tempering time decreases the tensile strength increases on average more than 150 MPa. However, reduction of area decreases abruptly as tempering time reduces. As described at Chapter 6, the strengthening mechanism in tempering in spring steel is mainly precipitation of fine epsilon carbide ($Fe_{2.4}C$). Based on these results, tempering time was set to 5 minutes and second tempering treatment was added subsequently. Fig. 7.4 shows the mechanical properties of single tempered specimens and step tempered specimens of SAE9254 steel. All specimens were heated at 980 ^{o}C for 3minutes. The single tempered specimens were tempered at a given temperature for 5 minutes as shown in Fig. 7.3. The step tempered specimens were tempered firstly at a given temperature for 5 minutes and subsequently tempered at 250 ^{o}C and 300 ^{o}C for 10 minutes.

(a)   (b)
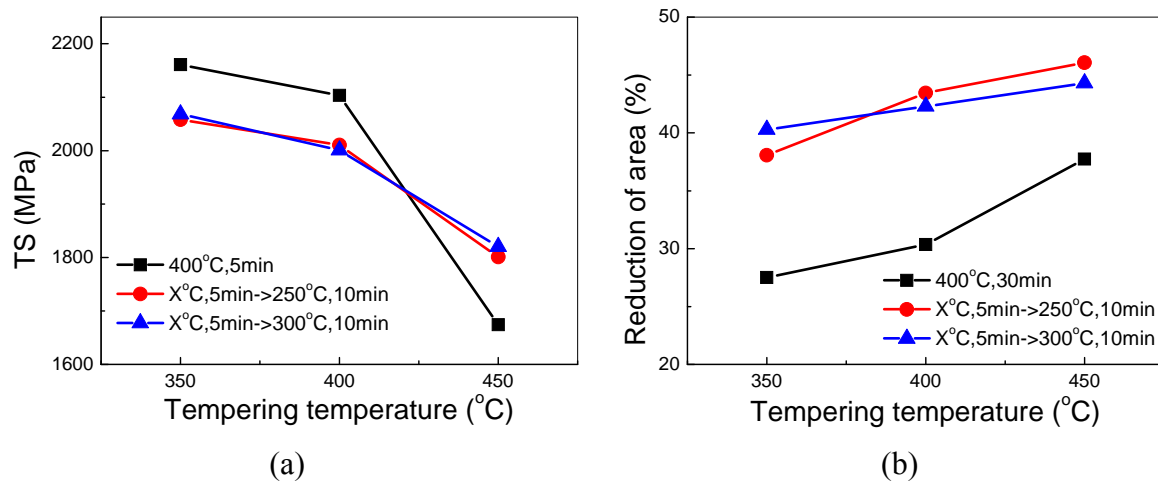
FIGURE 7.4.   Mechanical properties of single tempered specimens (5 min.) and step tempered specimens of SAE9254 spring steel. (a) Tensile strength and (b) Reduction of area

Tensile strength increases and reduction of area decreases as tempering temperature increases. Reduction of area in step tempered specimens is higher up to 40 % than that of specimens tempered for 5 minutes. Tensile strength in step tempered specimens is less than that of specimens tempered for 5 minutes. It indicates that even though time of first tempering treatment is short as 5 minutes, reduction of area is improved up to 40 % by subsequently second tempering treatment at 250 or 300 $^{\circ}$C for 10 minutes. The effect of second tempering temperature can not be distinguished.

(a)   (b)
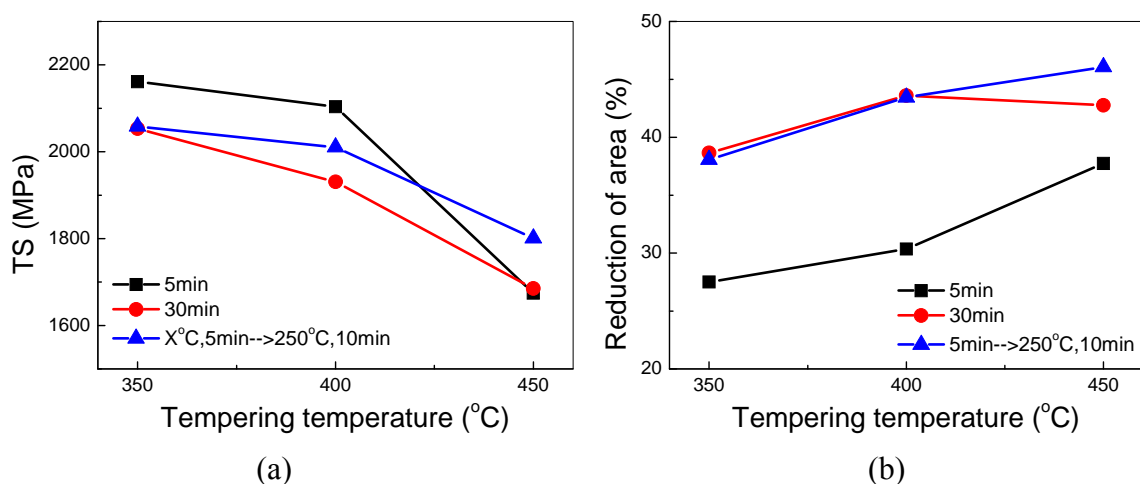
FIGURE 7.5. Mechanical properties of single tempered specimens for 5, 30 minutes and step tempered specimens of SAE9254 spring steel. (a) Tensile strength and (b) Reduction of area

Fig. 7.5 represents the mechanical properties of single tempered specimens for 5, 30 minutes and step tempered specimens of SAE9254 spring steel. For tensile strength, the single tempered specimens for 5 minutes had the highest value and the specimens tempered

for 30 minutes had the lowest value. For reduction of area, the step tempered specimens had the highest values and the single tempered specimens for 5 minutes had the lowest value near 30%. Also, the tensile strength of step tempered specimens increased as 50 MPa higher than that of single tempered specimens for 30 minutes. Step tempering can suppress the abrupt drop of tensile strength and improve largely the reduction of area.

Tensile strength and reduction of area of POSHIS120D spring steels are shown in Fig. 7.6. These steels were austenitized at 980 ^{o}C and subsequently tempered at 350, 400 and 450 ^{o}C for 5 and 30 minutes. Tensile strength decreased with increasing tempering temperatures, but reduction of area increased as tempering temperature rose. As the tempering time increased from 5 to 30 minutes, the tensile strength decreased and the reduction of area increased.
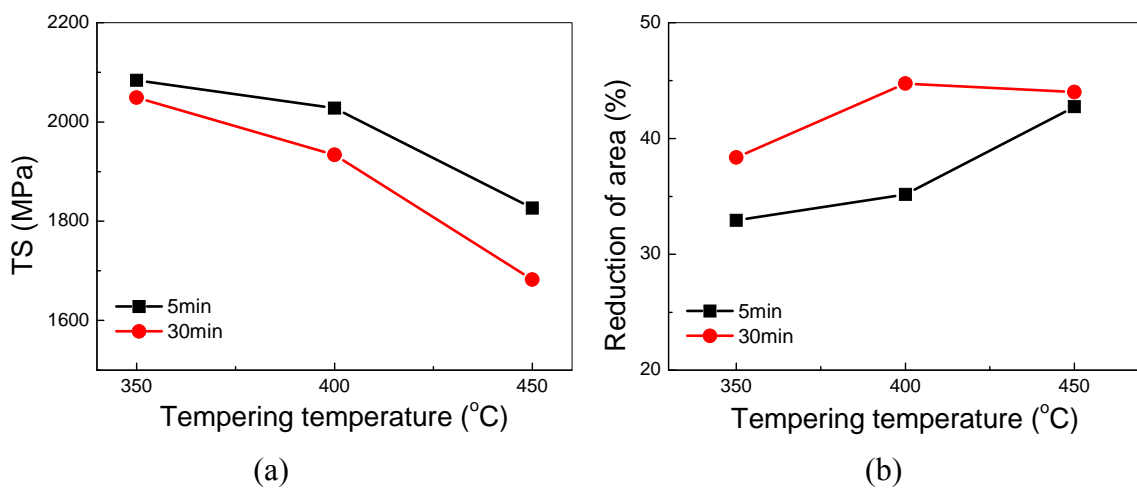
FIGURE 7.6. Mechanical properties of POSHIS120D spring steel with tempering temperature and time. (a) Tensile strength and (b) Reduction of area

Fig. 7.6 shows that as tempering time decreases the tensile strength increases by more than 100 MPa. However, reduction of area increases as tempering time reduces. As described at Chapter 6, the strengthening mechanism in tempering in spring steel is mainly precipitation of fine epsilon carbide ($Fe_{2.4}C$). Based on these results, the mechanical properties of step tempering and single tempering are compared in Fig. 7.7. Fig. 7.7 shows the mechanical properties of single tempered specimens and step tempered specimens of POSHIS120D steel. The conditions of step tempering in POSHIS120D were equal to those in SAE9254 steel.

Tensile strength increases and reduction of area decreases as tempering temperature increases. Reduction of area in step tempered specimens is higher up to 40 % than that of specimens tempered for 5 minutes. Tensile strength in step tempered specimens is a little less than that of specimens tempered for 5 minutes. It indicates that even though time of first tempering treatment is short as 5 minutes, reduction of area is improved up to 40 % by subsequently second tempering treatment at 250 or 300 ^{o}C for 10 minutes. The effect of second tempering temperature can not be distinguished on mechanical properties and is similar like SAE9254 steel. Especially, it was investigated that tensile strength of step tempered specimens was almost similar to that of single tempered specimens for 5 minutes.
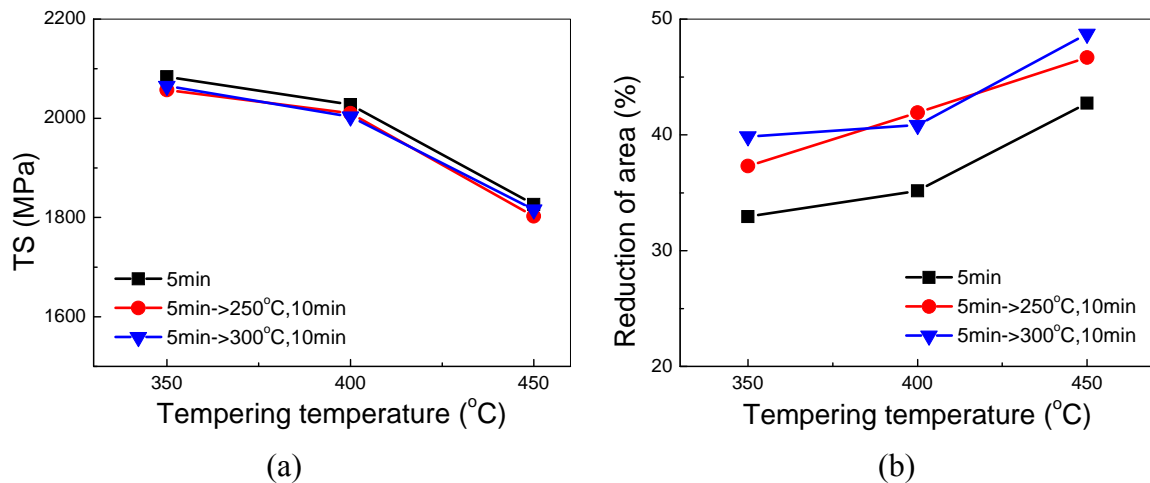
FIGURE 7.7.   Mechanical properties of single tempered specimens (5 min.) and step tempered specimens of POSHIS120D spring steel. (a) Tensile strength and (b) Reduction of area
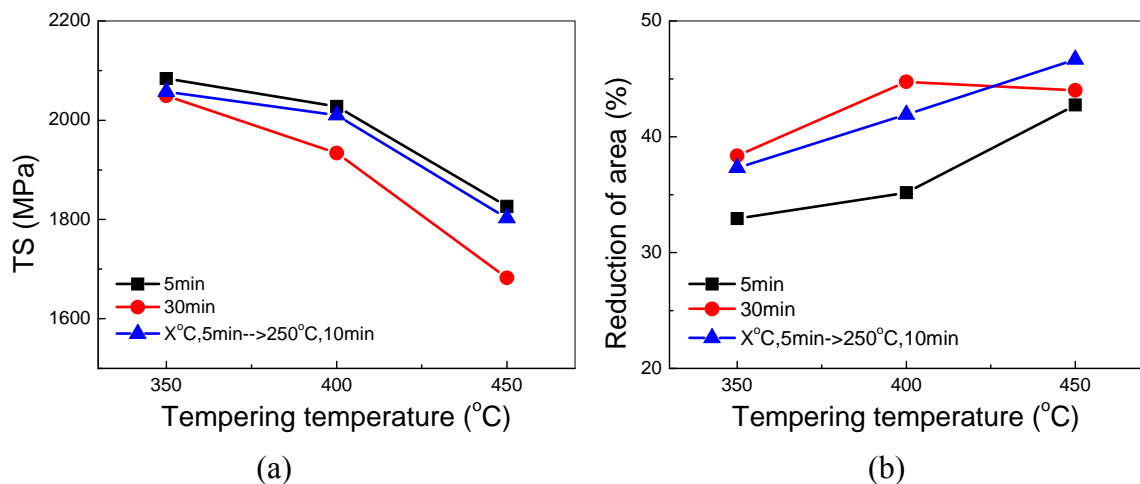
FIGURE 7.8. Mechanical properties of single tempered specimens for 5, 30 minutes and step tempered specimens of POSHIS120D spring steel. (a) Tensile strength and (b) Reduction of area

Fig. 7.8 shows the mechanical properties of single tempered specimens for 5, 30 minutes and step tempered specimens of POSHIS120D spring steel. Again, step tempering can suppress the abrupt drop of tensile strength and improve largely the reduction of area. In addition, the fatigue properties of conventional tempered spring and step tempered spring of SAE9254 and POSHIS120D steels were compared in Fig. 7.9. All specimens were heated at 980 ^{o}C for 3 minutes. The heated specimens were coiled as a shape of suspension spring for automobile and subsequently quenched in oil. The conventional spring was tempered at 400 ^{o}C for 30 minutes. On the other hand, the step tempered spring was tempered at 400 ^{o}C for 5 minutes and subsequently at 250 ^{o}C for 10 minutes. All springs were shot-peened and evaluated on fatigue life. The desired stress of fatigue test of spring was 1100 MPa for

SAE9254 and 1200 MPa for POSHIS120D steel as shown in Fig. 7.9. The fatigue life of conventional tempered spring and step tempered spring were almost equal. Therefore, by using step tempering treatment, the mechanical properties of conventional spring was improved and the fatigue life was not decreased even though tempering time is less than halve that of conventional tempering.
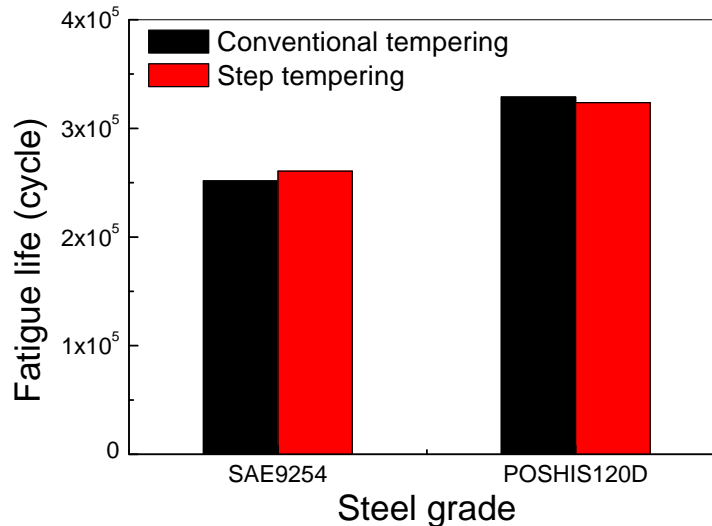
FIGURE 7.9. Fatigue properties of conventional tempered spring and step tempered spring of SAE9254 and POSHIS120D steel.

7.3.2 Microstructure

Fig. 7.10 shows the SEM micrographs of SAE9254 steel tempered for 5 and 30 minutes at 350, 400 and 450 $^{\circ}$C. The microstructures of SAE9254 were typically tempered martensite. Fig. 7.11 shows the SEM micrographs of POSHIS120D steel tempered for 5 and 30 minutes at 350, 400 and 450 $^{\circ}$C. The microstructure was typically tempered martensite and the difference of microstructures can not be distinguished with a tempering time like Fig. 7.10. However, as tempering time increased from 5 to 30 minutes, some spheroidized carbides were formed. After step tempering treatment, the microstructure of SAE9254 and POSHIS120D were typical tempered martensite as shown in Fig. 7.12. The difference of microstructure between single tempered specimen and step tempered specimen can not be distinguished. It is necessary to analyze in detail the microstructure by TEM instrument.

7.3.3 Precipitation behavior

Fig. 7.13 shows the TEM micrographs of SAE9254 tempered at 350, 400 and 450 $^{\circ}$C for 5 and 30 minutes. The epsilon carbide ($Fe_{2.4}C$) was investigated in tempered martensite as explained at Chapter 6. At tempering temperature of 450 $^{\circ}$C, microstructure consisted of fine $Fe_{2.4}C$ carbide and spheroidized cementite (Fe_3C), and fraction of spheroidized cementite increased with increasing tempering temperature from 5 to 30 minutes.
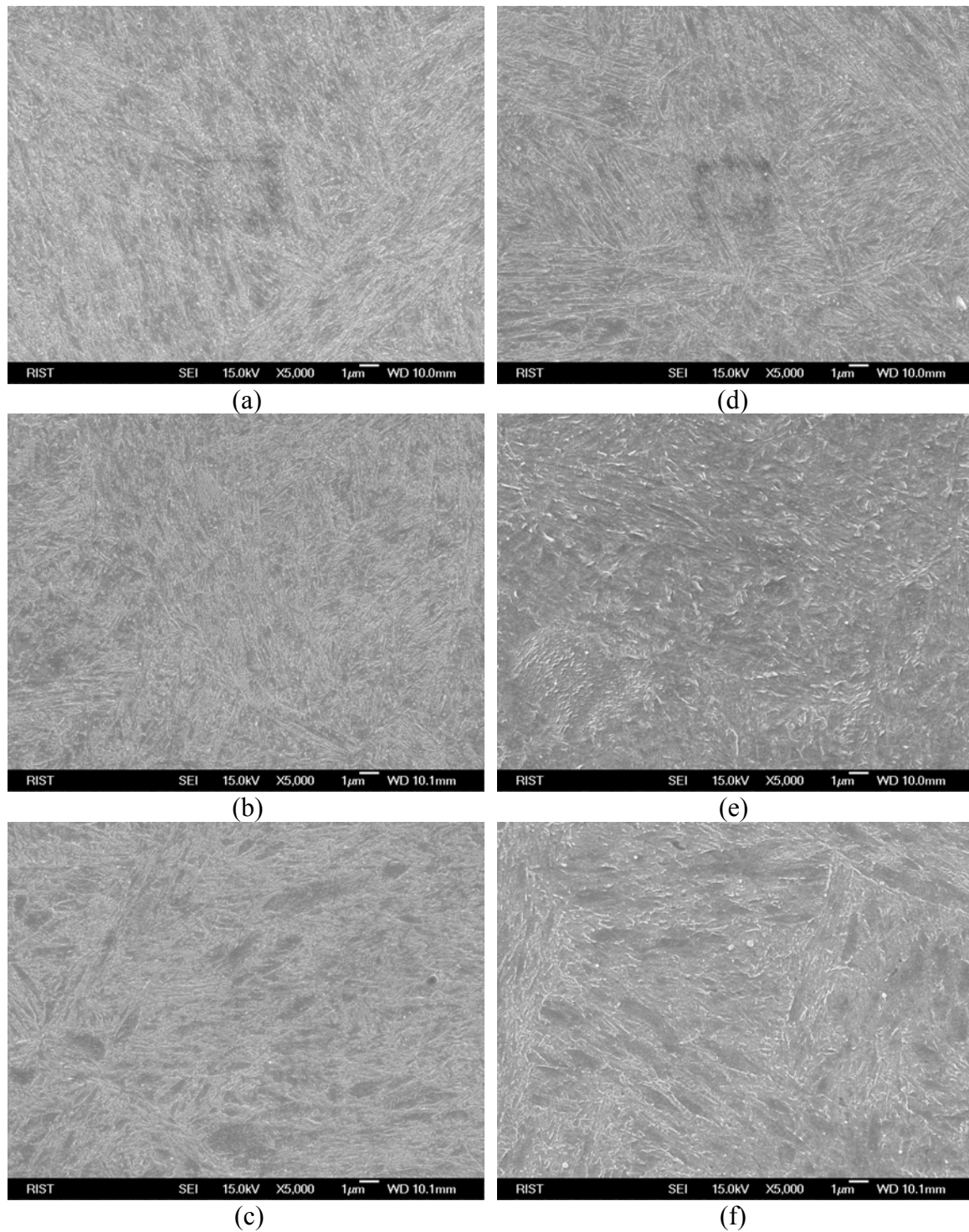
FIGURE 7.10. SEM micrographs of SAE9254 steel tempered for (a) 5 minutes and (d) 30 minutes at 350 $^{\circ}$C, (b) 5 minutes and (e) 30 minutes at 400 $^{\circ}$C and (c) 5 minutes and (f) 30 minutes at 450 $^{\circ}$C.
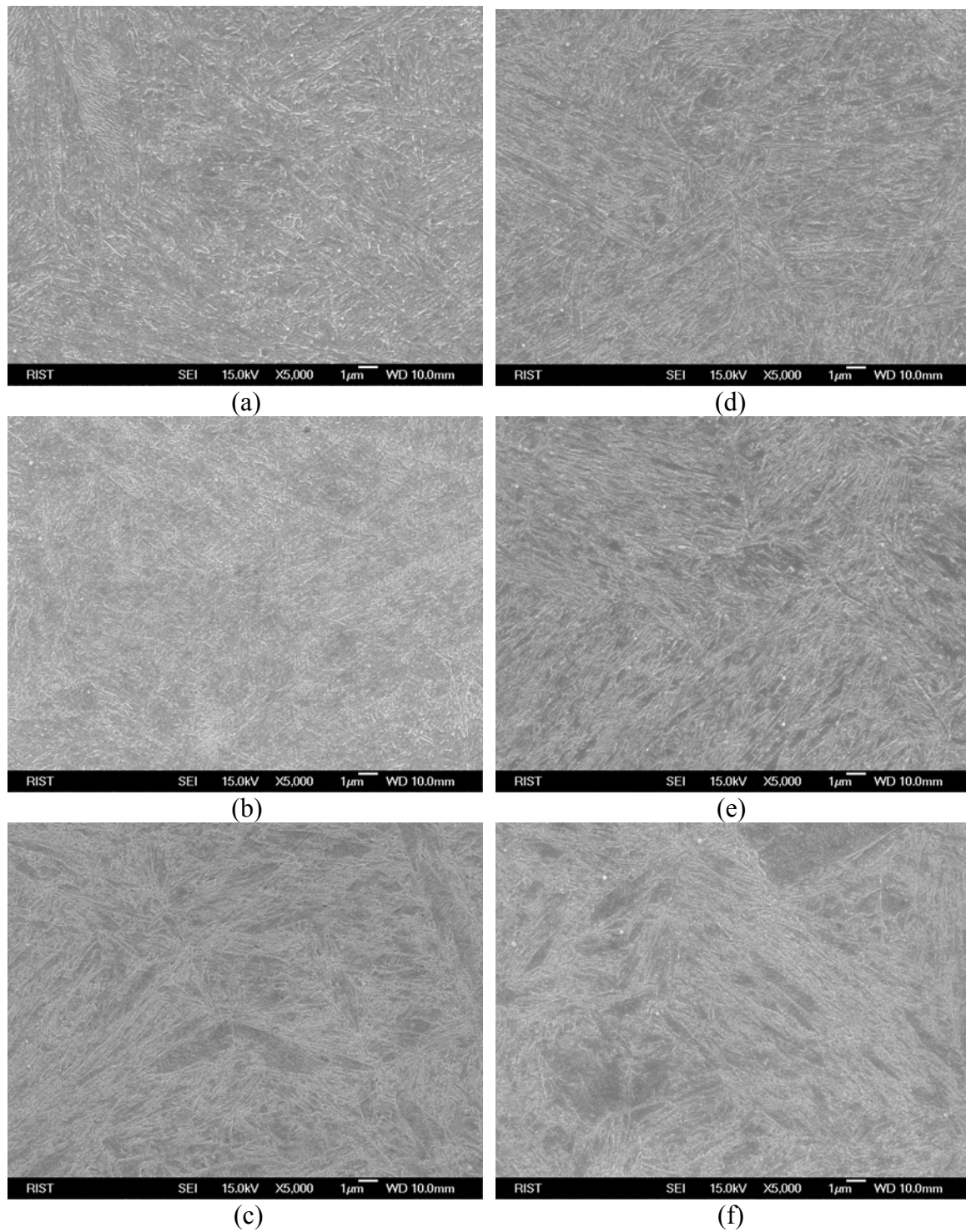
FIGURE 7.11. SEM micrographs of POSHIS120D steel tempered for (a) 5 minutes and (d) 30 minutes at 350 ^{o}C, (b) 5 minutes and (e) 30 minutes at 400 ^{o}C and (c) 5 minutes and (f) 30 minutes at 450 ^{o}C.

FIGURE 7.12.   SEM micrographs of spring steels tempered at 400 ^{o}C for 5 minutes and subsequently at 250 ^{o}C for 10 minutes. (a) SAE9254 and (b) POSHIS120D.

This was due to $Fe_{2.4}C$ changing to spheroidized cementite. It indicates that the decrease of tensile strength at 450 ^{o}C may be due to the changing from fine $Fe_{2.4}C$ to spheroidized cementite. At tempering temperature of 350 and 400 ^{o}C, $Fe_{2.4}C$ formed as fine carbide in the lath of martensite but a part of $Fe_{2.4}C$ changed to spheroidized cementite as tempering time increased from 5 to 30 minutes.

Fig. 7.14 shows the TEM micrographs of POSHIS120D tempered at 350, 400 and 450 ^{o}C for 5 and 30 minutes. The $Fe_{2.4}C$ carbide distribution in POSHIS120D was similar to that in SAE9254 steel. At a tempering temperature of 350 and 400 ^{o}C, $Fe_{2.4}C$ carbide formed in the lath of martensite and a part of $Fe_{2.4}C$ changed to spheroidized cementite as tempering time increased from 5 to 30 minutes. At tempering temperature of 450 ^{o}C, microstructure consisted of fine $Fe_{2.4}C$ carbide and spheroidized cementite (Fe_3C), and fraction of spheroidized cementite increas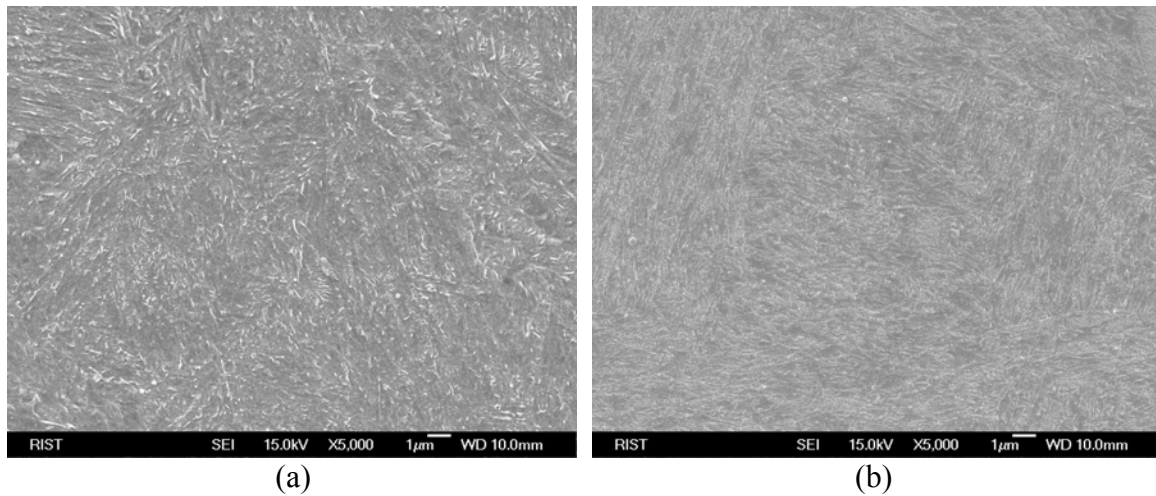ed with increasing tempering temperature from 5 to 30 minutes. It was due to changing from $Fe_{2.4}C$ to spheroidized cementite.

Fig. 7.15 shows the TEM micrographs of SAE9254 and POSHIS120D tempered at 400 ^{o}C for 5 minutes and subsequently at 250 ^{o}C for 10 minutes. It was investigated that fine $Fe_{2.4}C$ carbide was distributed in the lath of martensitic microstructure like single tempered microstructure. It was confirmed that the drop of tensile strength may be due to formation of spheroidized cementite from $Fe_{2.4}C$ with increasing tempering temperature.

7.3.4 Analysis of strengthening mechanism in step tempering

In order to improve the mechanical properties of conventional tempered spring, new process of tempering treatment was developed and called as step tempering. The commercial spring was conventionally processed by tempering for around 30 minutes. As shown in Figs. 7.5 and 7.8, tensile strength and reduction of area of step tempered specimen was higher than those of conventional specimens tempered for 30 minutes.
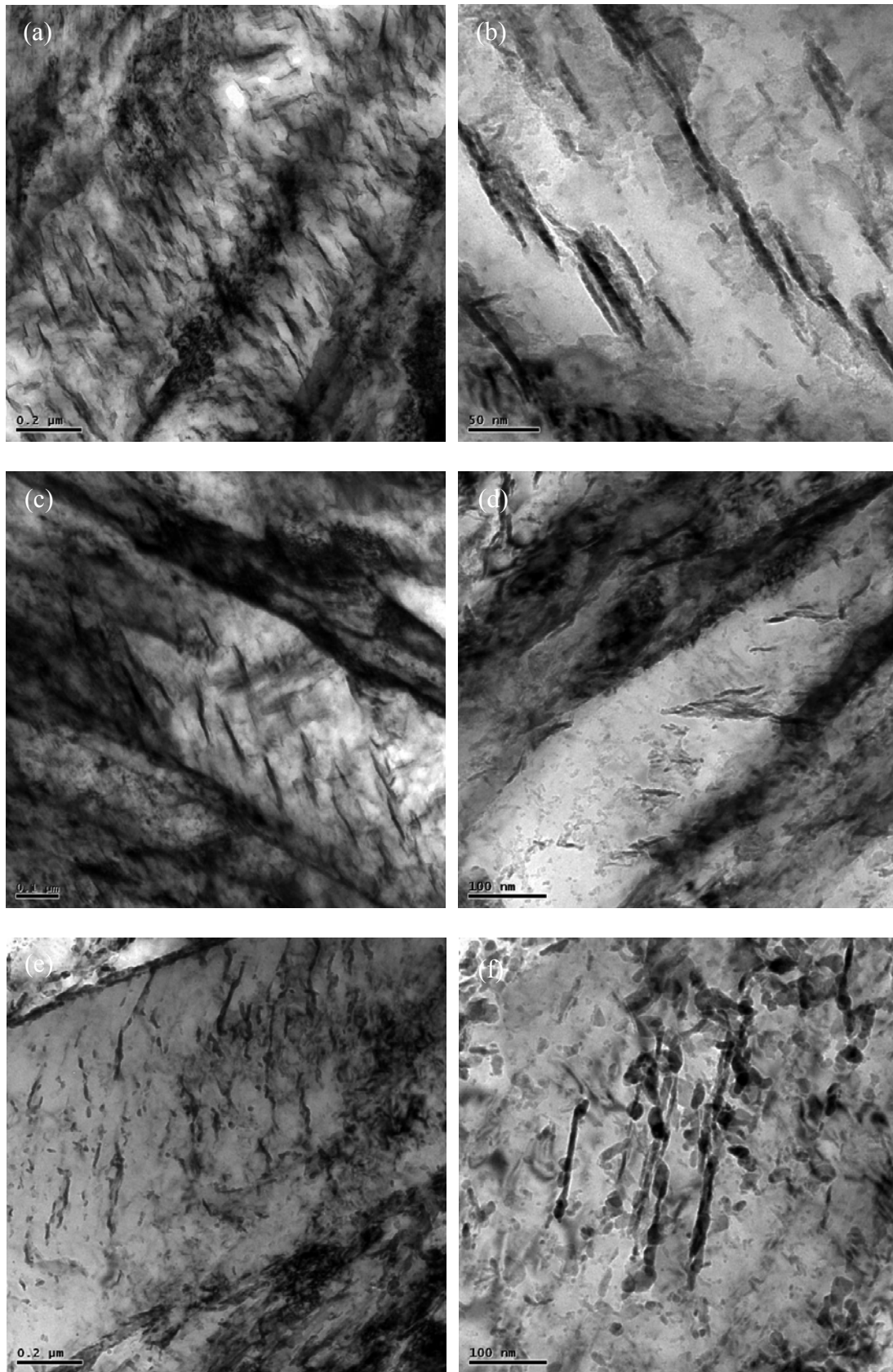
FIGURE 7.13. TEM micrographs of SAE9254 tempered for 5 minutes at (a) 350, (b) 400 and (c) 450 ^{o}C, and for 30 minutes at (d) 350, (e) 400 and (f) 450 ^{o}C.

FIGURE 7.14. TEM micrographs of POSHIS120D tempered for 5 minutes at (a) 350, (b) 400 and (c) 450 °C, and for 30 minutes at (d) 350, (e) 400 and (f) 450 °C.
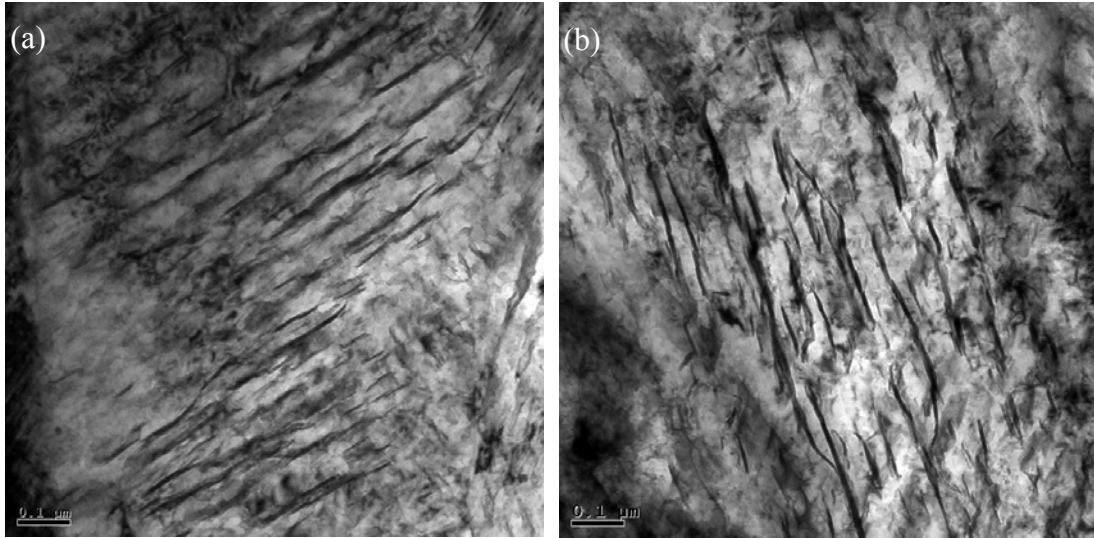
FIGURE 7.15. TEM micrographs of spring steels tempered at 400 $^{\circ}$C for 5 minutes and subsequently at 250 $^{\circ}$C for 10 minutes. (a) SAE9254 and (b) POSHIS120D.

Fig. 7.16 shows the inter-particle distance between $Fe_{2.4}C$ carbide of SAE9254 and POSHIS120D steels tempered at 400 $^{\circ}$C for 5 and 30 minutes, and tempered at 400 $^{\circ}$C for 5 minutes and subsequently at 250 $^{\circ}$C for 10 minutes (step tempering). For SAE9254 steel, the inter-particle distance of $Fe_{2.4}C$ carbide was respectively 0.0386, 0.0383 and 0.038 um, and the inter-particle distance of $Fe_{2.4}C$ carbide in POSHIS120D steel was respectively 0.0354, 0.0364 and 0.0358 um. The inter-particle distances were almost equal regardless of tempering conditions. It suggests that the precipitation density (inter-particle distance) of $Fe_{2.4}C$ carbide was not changed significantly even though tempering time increased.

FIGURE 7.16. Inter-particle distance between $Fe_{2.4}C$ carbide of SAE9254 and POSHIS120D steels tempered at 400 $^{\circ}$C for 5 and 30 minutes, and tempered at 400 $^{\circ}$C for 5 minutes and subsequently at 250 $^{\circ}$C for 10 minutes (step tempering).

Fig. 7.17 shows the distribution of hardness in cross-sectional area of spring steels tempered at 400 ^{o}C for 5 minutes and subsequently at 250 ^{o}C for 10 minutes, tempered at 400 ^{o}C for 5 minutes and for 30 minutes. The hardness of step tempered specimens was positioned between the specimens tempered for 5 and 30 minutes. The softening during tempering was related to the precipitation, growth of $Fe_{2.4}C$ carbide and transition from $Fe_{2.4}C$ to spheroidized cementite. The increase of reduction of area of specimens tempered from 30 minutes may be mainly related to the transition from $Fe_{2.4}C$ to spheroidized cementite and therefore hardness was the lowest among all specimens. However, the hardness of specimens tempered for 5 minutes was the highest and the reduction of area was the lowest among all specimens. It may be due to insufficient time of tempering. In order to improve the tensile strength and reduction of area, the new step tempering was developed and hardness was a little decreased. Therefore, tensile strength and reduction of area was improved more than those of conventional tempered specimens. It was due that the spheroidized cementite was not formed and second step of step tempering may be induced the softening. However, it was not easy to distinguish the change of fraction of $Fe_{2.4}C$ carbide between the specimens tempered for 5 minutes and step tempered specimens, due to very fine distribution of carbides.

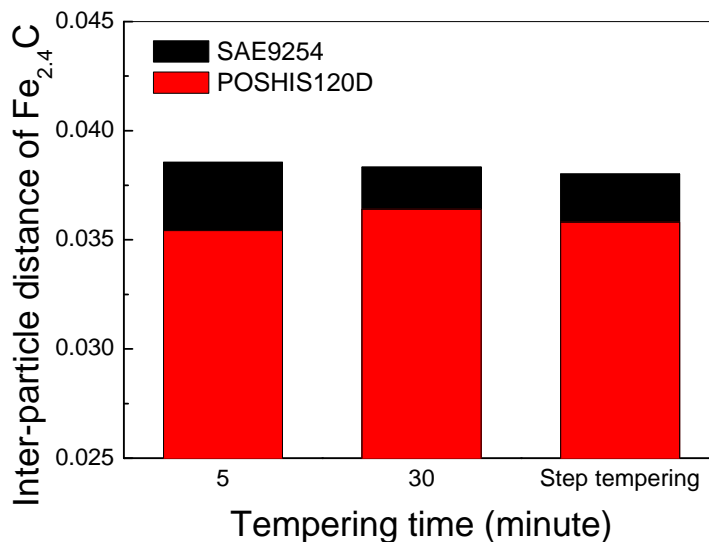FIGURE 7.17. Hardness distribution in cross-sectional area of spring steels tempered at 400 ^{o}C for 5 minutes and subsequently at 250 ^{o}C for 10 minutes (■), tempered at 400 ^{o}C for 5 minutes (●) and for 30 minutes (▲). (a) SAE9254 and (b) POSHIS120D.

7.4 Conclusion

In the present investigation, the tensile strength and the reduction of area of the step tempered spring steels have been studied. As the tempering conditions (time and step tempering) changed, the microstructure and precipitation behavior was investigated. The strengthening mechanism was discussed to explain the mechanical properties and the microstructural change. The mechanical properties of step tempered spring were improved more than the conventional tempered spring and the fatigue life was almost equal. The strengthening was based on the precipitation of fine $Fe_{2.4}C$ carbide and the suppression of transition from $Fe_{2.4}C$ carbide to spheroidized cementite. Then, second step of step tempering may be induced the softening and suppress the transition from $Fe_{2.4}C$ to cementite. However, it was not easy to distinguish the change of fraction of $Fe_{2.4}C$ carbide between the specimens

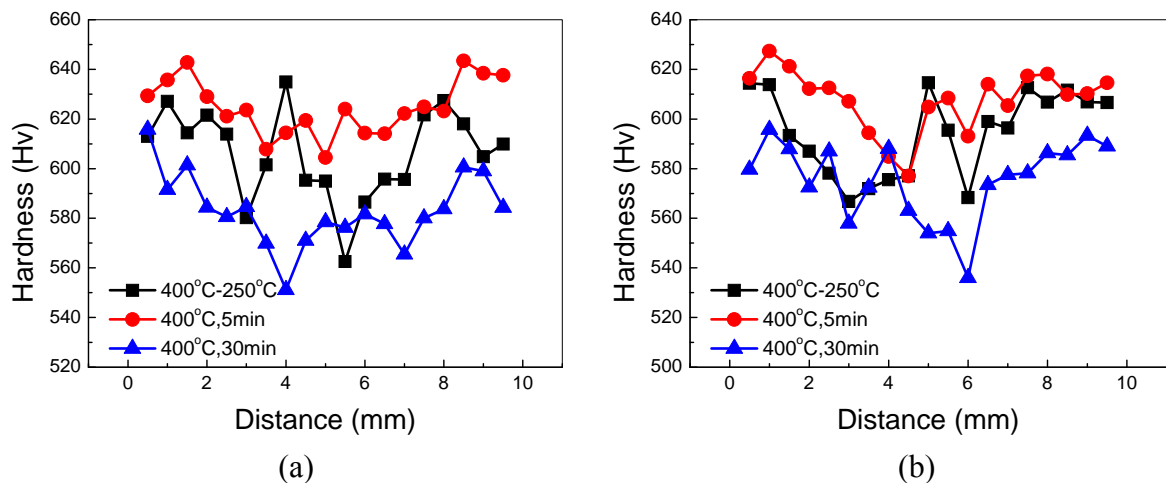tempered for 5 minutes and step tempered specimens, due to very fine distribution of carbides. In future, it is necessary to study the optimization of step tempering and the precipitation behavior in second step of step tempering in more detail.

8
Prediction of decarburized ferrite depth of spring steel with simultaneous oxidation during isothermal and non-isothermal heat treatment

8.1 Introduction

Decarburizing of steel surfaces sometimes occurs during hot rolling process or annealing process. Because the decarburized steel causes several problems, for example, lowering of strength and fatigue life, when the decarburized steel is used to manufacture parts such as springs or bearings, it is necessary to minimize the decarburizing depth. When already decarburized raw materials are processed into a coil spring without eliminating the decarburized layer, the final product of the coil springs will not be in an optimum metallurgical condition.[137]

Common hot rolling processes include several major steps, which are usually billet reheating, hot rolling, finish rolling, cooling and coiling. There are two important phenomena which always occur during these steps, i.e. oxidation and decarburization. These processes occur simultaneously in the reheating furnace, during hot rolling, roughing and finishing in air atmosphere, and during air cooling. Especially, the loss of carbon in the surface layers of the material is one of the oldest, most persistent problems in high carbon steel production. Since several material properties, such as the tensile strength, hardness, fatigue resistance and so on, depend primarily on the carbon content, decarburization can largely influence the material properties. As decarburization always occurs at the surface, all application in which

maximum stresses occur at the surface are highly affected. Poor material properties at the surface due to decarburization can thus lead to local failure on the surface and, consequently, failure of the entire component.

A decarburized layer is always softer than the base-material matrix. The effect of shot peening on a material that has a soft surface is not as good as that of a material that has a hard layer on the surface. In some cases, the microstructure even remains ferrite several hundred microns underneath the surface, while the rest of the matrix is tempered martensite, as required by the design. In this situation, the efficiency of the shot peening is greatly reduced.

The mechanism of shot peening [138] can be attributed to the formation of the compressive residual stresses in the surface layer of the material. The compressive residual stress usually decreases the tensile stress in the component by external forces and therefore increases the fatigue life of the material. Also, as compressive stresses are introduced into the surface and subsurface layers by shot peening, fatigue cracks do not easily initiate in (or propagate through) an area under compression and thus, improvements in fatigue strength are achieved. When the decarburized layer is present, this layer, which is softer, will be plastically deformed very easily. This soft layer locally has low ultimate tensile strength as well as low yield strength. As a result, this plastically deformed layer lacks the capability to generate desirable residual stresses that would provide proper strength and durability.

(a)	(b)
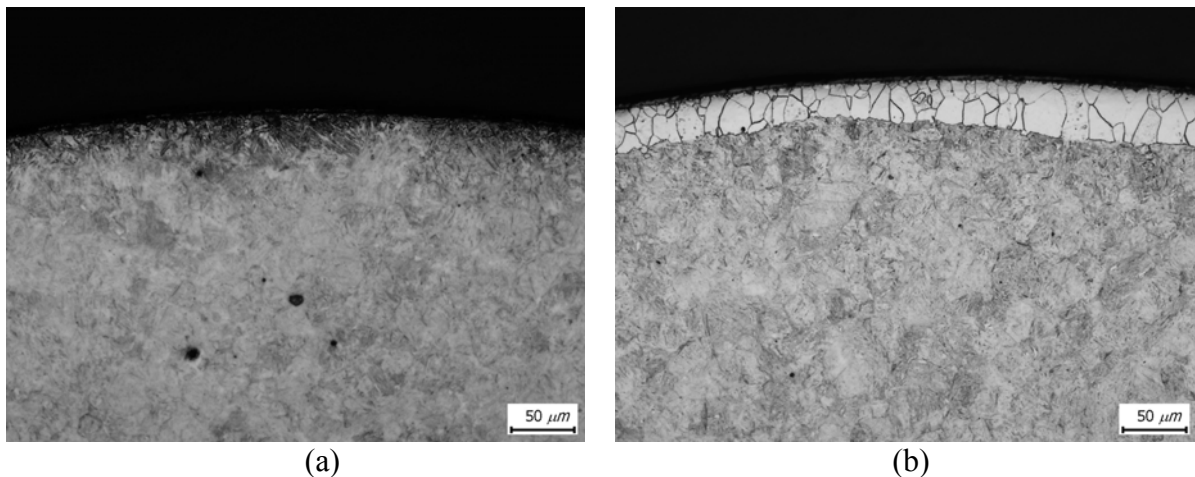
FIGURE 8.1. Optical micrographs of ferrite decarburization layer of as-quenched SAE 9254 spring steel after heating.   (a) non-existence of ferrite decarburization layer   and (b) decarburized ferrite layer.

A typical decarburized layer of SAE 9254 spring steel is shown in Fig. 8.1, where a layer of decarburized ferrite is created on the surface. The reason for the purely ferritic surface layer is that the carbon content is below the solid solubility of ferrite, which is known to be 0.022% for the binary Fe-C.

To avoid the surface decarburization, it is important to investigate the responsible physical mechanisms and to identify the main contributing factors to decarburization. If the main

causes for severe decarburization are known, methods can be developed to reduce the amount of decarburization during the steel production process. Normally, there are many factors, which might influence decarburization and oxidation, such as the type of atmosphere in the furnace, the thermal cycle during all production steps and the chemical composition of the materials. The metallurgical processes are complex and influenced by many factors, such as temperature, atmosphere, α/γ transformation, morphology of the surface, alloy composition and many more.[139-141] To understand the mutual interaction between oxidation and decarburization, computer simulation can be very helpful and assist in interpretation of complex and sometimes counter-intuitive results. Simulation is often cheaper and faster than experimental investigation, and in many cases, can provide not only trends but also quantitative information on the material behavior under laboratory as well as industrial condition. In this context, several models have been developed to investigate the decarburization process.[143-146]

Verhoeven suggested a model predicting the kinetics of ferrite and austenite layer formation in hypereutectoid Fe-C alloys by decarburization.[147] This model was applied to analyze the decarburization behavior of Damascus steel swords. However, Verhoeven's model was applied under the only decarburization condition of hypereutectoid steel having carbon composition lager than A_{cm} of Fe-C phase diagram, during isothermal heating without oxidation. Nomura et al. reported a model predicting the ferrite decarburizing depth of spring steel.[148] They used the approximation equation to predict the ferrite decarburizing depth assuming the no oxidation. Li et al. developed a simple integrated mode to describe simultaneous decarburization and oxidation kinetics.[149] The decarburization model was based on the vacancy exchange mechanism and random walk theory and be approximated by the mean square diffusion distance. However, the carbon concentration profile developing in the course of the decarburization process was not taken into account.

Our study focuses on the effect of the chemical composition of steel and heating condition on the ferrite decarburizing depth and the thickness of scale. In the present work, computer simulations have been used to investigate the influence of the chemical composition of the steel on the coupled growth of oxide layers and decarburization in steels based on phase transformation and diffusion calculation, and on the decarburization phenomenon during typical industrial conditions based on the finite differences approach. In this study, decarburization behavior of the Si-rich spring steel has been examined, theoretically and numerically based on the experimental data obtained on the Dilatometer and TGA. The objective of this research is to investigate the decarburization process during reheating and cooling for high silicon spring steel in ambient atmosphere and to identify the influence of thermal cycles on the decarburization behavior. Furthermore, the propriety of the simulation result was confirmed experimentally.

8.2 Mechanism of decarburization and oxidation

It is important to realize that, while these two concurring processes take place, the oxide scale growth usually consumes part of the decarburized metal and thus decreases the finally observed decarburized depth. It is assumed that the gas-solid decarburization reaction at the surface is rapid enough that the decarburization process is diffusion controlled throughout. In other words, the oxide layer is assumed not to affect the decarburization process as such. In

proposed model, nucleation is not considered early stage. Model describes the growth of the coupled layer consisting of an outer oxide layer and an inner depleted ferrite layer.

8.2.1 Oxidation

The oxidation of steel at high temperature is a very common phenomenon. The kinetics of oxidation and the stability of the oxidation products are strongly dependent on the type of oxide forming element and, consequently, of the steel composition. Basically, in the oxidizing atmosphere of the furnace, a scale of iron oxide forms and grows. At the scale-metal interface, carbon interacts with the scale to form carbon monoxide by the reaction shown in Fig. 8.2. This reaction can only proceed if the carbon monoxide reaction product can escape through the scale. In general, porous scales are produced, particularly under industrial conditions, and removal of carbon monoxide is not a problem.

Atmosphere	**Scale**	**Steel**

CO via crack

CO

$Fe^{2+} + 2e^-$

C

CO gas transport out through scale via pores and cracks

Carbon diffuses via lattice and grain boundaries to metal-scale interface

CO via pore and crack

CO ← C

CO

$Fe^{2+} + 2e^-$

$2Fe + O_2 = 2FeO$
$6FeO + O_2 = 2Fe_3O_4$
$4Fe_3O_4 + O_2 = 6Fe_2O_3$
$Fe + H_2O = FeO + H_2$

Fe^{2+} and e^- diffuse out over lattice defects

$C_{Fe} + 1/2O_2 = CO$
$C_{Fe} + H_2O = CO + H_2$
$C_{Fe} + FeO = Fe + CO$
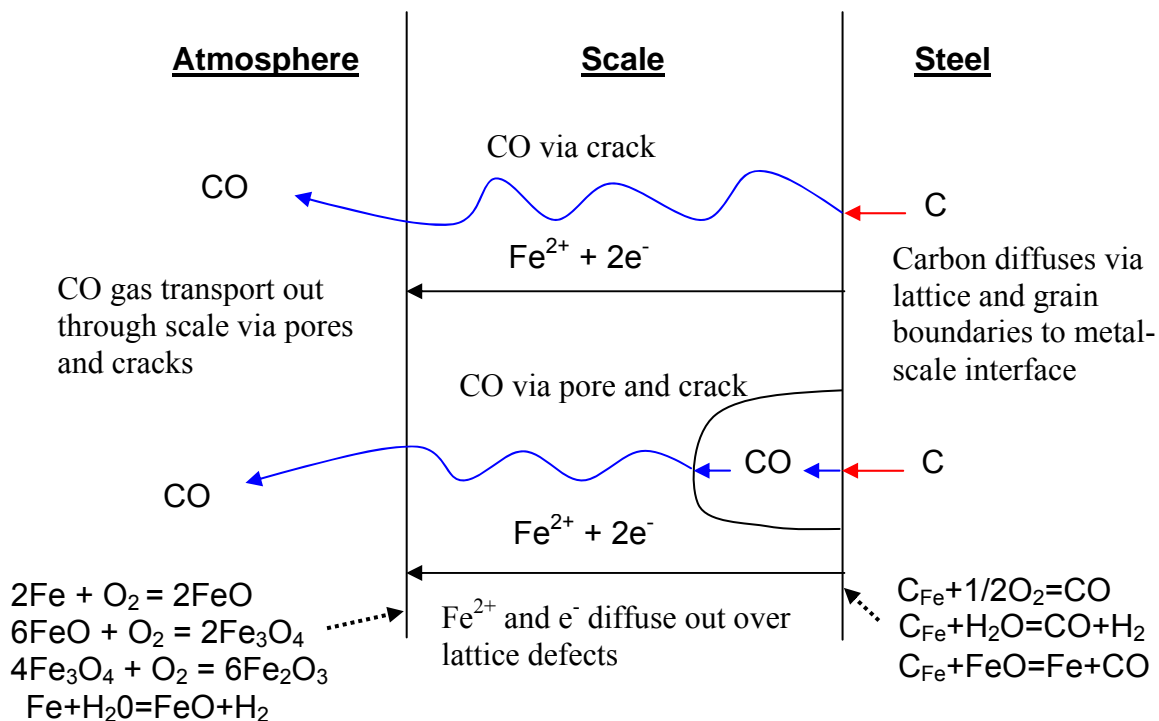
FIGURE 8.2.   Mechanisms of decarburization of plain carbon steel with simultaneous scaling.[151]

At low temperatures ($\approx$ 500 ^{o}C), the alloys form layered scales consisting of Fe_3O_4 and Fe_2O_3. The oxidation of Fe-C alloys containing 0.1, 0.5 and 1.0 wt.% C at 500 ^{o}C in 1 atm oxygen has been studied by Caplan et al.[152] It was found that the oxide scales grew thicker over pearlite colonies than over single phase ferrite for annealed alloys as the result of a finer grained Fe_3O_4 layer forming over the pearlite. Cold worked alloys oxidized substantially faster than annealed alloys. No carburization or decarburization was observed for any of the alloys. This was postulated to result from C diffusing out through the inner portion of Fe_3O_4

layer and being oxidized to CO which escaped through channels and pores in the outer part of the Fe_3O_4 and Fe_2O_3 layer.

In air at temperatures higher than 500 ^oC, the scale developed comprises an extremely thin outermost hematite layer, a thin intermediate magnetite layer, and a thick inner wüstite layer.[167] This proportion of oxide phases reflects the fact that the diffusion coefficient of iron in wüstite is much greater than in magnetite and that the diffusion of oxygen and iron through the hematite layer is extremely slow. Oxidation at high temperatures, typical of reheating conditions during steel processing, can lead to substantial decarburization. This can have a large effect on the properties of components. The tensile strength of a heat-treated steel depends primarily on the carbon content. The maximum stress on a component in bending occurs at the surface. Clearly, if excessive failure of steel component under reversing bending stresses is to be avoided, the specified carbon content must be maintained within the surface layers of the component.

8.2.2 Decarburization

Decarburization is a loss of carbon atoms from the surface of the work pieces, thereby producing a surface with lower carbon content than at some other distance beneath the surface. The mechanisms by which the decarburization of steels occurs are well understood.[150] The phenomenon of decarburization usually takes place at temperatures above about 700 °C, with the following reaction.[137]

$$C_{Fe} + \frac{1}{2}O_2 = CO$$
$$C_{Fe} + H_2O = CO + H_2 \qquad\qquad (1)$$
$$C_{Fe} + FeO = Fe + CO$$

When the reaction goes from the left to right, decarburization occurs as shown in Fig. 8.2. Analysis of the phenomena taking place during decarburization of steel leads to the conclusion that the kinetics of the process depends fundamentally on four reaction rates, associated with; (i) diffusion of carbon atoms from the bulk to the steel surface; (ii) gas adsorption (water vapor and hydrogen) on the steel surface; (iii) oxidation of carbon; and (iv) formation of iron oxides.[168] It is important to note that all these processes are thermally activated and should be accelerated by an increase in temperature.

8.3 Mathematical Model

8.3.1 Oxidation model

In general, the mechanism which is responsible for this physico-chemical transformation can be divided in two stages, according to the oxidation rate (e.g. the mass change of the oxides formed with regard to the exposure time in the aggressive environment): an initial stage, where the rate of oxidation is linear and a subsequent stage, where the rate of oxidation follows a parabolic low.[153] The linear behavior lasts for a short period of time up to the formation of a thin oxide layer. The actual rate observed in this stage depends on the

oxidizing species. It is also controlled either by the rate of chemical reactions taking place at the scale–gas interface or by the rate of transport of the oxidizing species through the gaseous phase to the reaction surface. The former is usually interpreted in terms of adsorption rate of the oxidizing species on the scale surface and the incorporation of atomic oxygen into the oxide layer.

When the scale reaches a certain thickness, as found by Pettit and Wagner [154], the oxidation mechanism changes and the oxidation rate starts being controlled by the diffusion of ionic species through the oxide layer (and not through the gaseous phase). As a result, the growth rate of the scale is a parabolic function of the exposure time. Wagner [155] assumed that parabolic oxidation is strictly driven by the diffusion of metal ions and vacancies through the scale and that the chemical equilibrium at the metal–oxide and oxide–gas interfaces is maintained during the course of oxidation. Studies on the self-diffusion coefficient of iron in iron oxides [156,157] have shown that the growth of iron oxides is driven by cationic diffusion of iron ions, in accordance with the Wagner's postulations.

The oxidation behavior of metals and alloys have been elucidated in many texts [158,159] as mentioned above; however a brief summary of the kinetic equations involved and the procedure for determining oxidation kinetics used in this study are given below. The weight gain (typically normalized with surface area and given as mg/cm^2) as a function of time can follow a linear, parabolic, logarithmic or cubic relationship and such behavior has been compiled for various metals and alloys. In general, the rate law for oxidation kinetics can be given by

$$\frac{W}{A} = Kt^n \tag{2}$$

where (W/A) is the weight gain per unit area at time t, K is the rate constant, n is the time exponent of the rate law. The rate constant, K(T), is the temperature dependent rate constant (a constant value for isothermal experiments) and follows an Arrhenius relation given by

$$K = K_0 \exp\left(-\frac{\Delta E_\alpha}{RT}\right) \tag{3}$$

where K_o is the pre-exponential factor, R is the gas constant (8.314 $Jmol^{-1}K^{-1}$), T is the absolute temperature (K) and ΔE_α is the activation energy.   The activation energy is determined from the slope of ln(K) versus 1/T plot.

In numerous experiments [160] the growth of oxide layers on steel substrates has been investigated. Depending on the type of atmosphere and the amount of continuous oxygen support, linear or parabolic growth laws have been observed. The initial stages of oxidation usually obey the linear growth rate law, because oxide growth is controlled either by the rate of chemical reaction at the metal surface, or by the rate of adsorption of the oxidizing species on the scale surface and the incorporation of atomic oxygen into the forming layer. When the oxide layer reaches a certain thickness, the mechanism of oxidation becomes controlled by the diffusion of ionic species through the oxide layer, leading to a parabolic growth rate. As the oxide scale grows onto a ferrite layer, the carbon level in the underlying tempered martensite does not affect the oxidation rate.

8.3.2 Decarburization-oxidation model

8.3.2.1 Model for isothermal heat treatments

The basic governing equation of the diffusion of interstitial carbon in the iron matrix is known as Fick's second law.[161]

$$\frac{\partial C}{\partial t} = \frac{\partial}{\partial x}\left(D\frac{\partial C}{\partial x}\right)$$

(4)

where D is the diffusion coefficient, and C is the concentration. The derivators t and x are time and position, respectively. When the diffusion coefficient is assumed constant and independent of the composition, Eq. (4) can be simplified to

$$\frac{\partial C}{\partial t} = D\left(\frac{\partial^2 C}{\partial x^2}\right)$$

(5)

Generally, the diffusion coefficient, D, is known to be temperature dependent, as expressed in

$$D = D_0 \exp\left(-\frac{Q}{RT}\right)$$

(6)

where D_0 is the temperature-independent pre-exponential, Q is the activation energy, R is the gas constant, and T is the absolute temperature. Eq. (5) has a physical meaning when the boundary condition is specified. The composition profiles of carbon in both the ferrite and the austenite phases can be determined by solving Fick's second law of diffusion in each phase as Eq. (5). Eq. (5) assumes that the carbon diffusion coefficients are constant for a given temperature throughout the ferrite phase and the austenite phase. Because the composition variation in the ferrite phase is very small, this is probably an excellent assumption in that phase. In the austenite phase, however, experiments have shown [162,163] that D varies significantly with composition. Kidson [164] has shown that because the boundary conditions of the present case allow the Matano-Boltzmann transformation to be applied to Eq. (5), the two interfaces must be linear functions of the square root of time.

For carbon steels, the decarburization behavior is divided into three regions as shown in Fig. 8.3.   In temperature region (a) above A_3 (C = 0.0 wt.%), ferrite is not stable thermodynamically and can not be formed during decarburization. For this condition the concentration profiles of carbon changes as a function of time and temperature of heating. In temperature region (b) below A_3 (C = 0.0 wt.%) and above A_3 (C = C_0, initial carbon composition), profiles of carbon concentration drop to 0.0 wt.% at surface and ferrite starts to form and grows during decarburization. Finally, in temperature region (c) below A_3 (C = C_0) austenite transforms to ferrite+austenite or ferrite+cementite and decarburizing ferrite forms at surface during decarburization. The decarburization-oxidation model should be developed for the three temperature regions due to the difference in decarburization behavior.
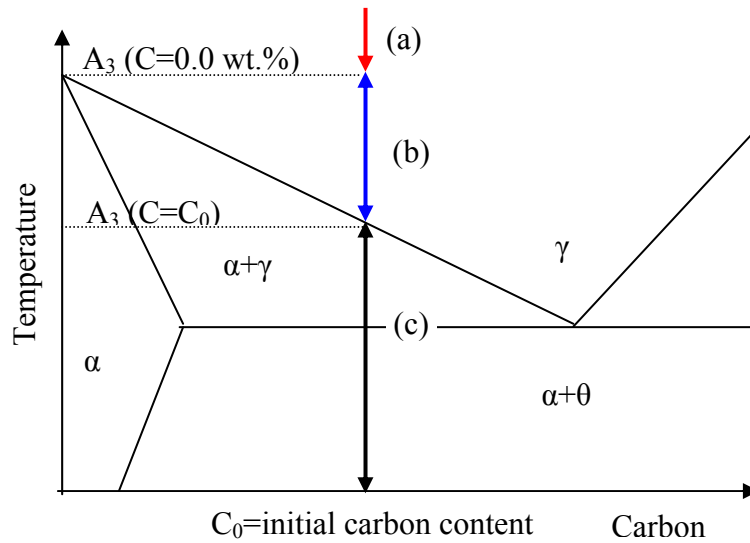
FIGURE 8.3. Fe-C phase diagram and three regions of decarburization.

FIGURE 8.4. Schematic diagram of decarburization-oxidation behavior and phase diagram of region (a).   The relationship between the equilibrium diagram, the diffusion annealing temperature and the diffusion zone interface concentrations for a two phase system.

   In temperature region (a), ferrite decarburizing layer is not formed and profiles of carbon concentration changes with a function of time and distance during decarburization. Fig. 8.4 shows the schematic pictures of carbon concentration profiles and Fe-C phase diagram during decarburization.   Solving the diffusion equation in temperature region (a), the carbon concentration can be calculated as Eq. (7). It is assumed that the carbon concentration is zero at the surface ($x = X_s$) and the initial carbon composition before decarburization is C_0.

$$C_\gamma(x,t) = a_\gamma + b_\gamma \cdot erf\left(\frac{x}{2\sqrt{D_\gamma t}}\right)$$

(7)

$$a_\gamma = C_0 - \frac{C_0 - C_S}{1 - erf\left(\dfrac{X_S}{2\sqrt{D_\gamma t}}\right)}, \qquad b_\gamma = \frac{C_0 - C_S}{1 - erf\left(\dfrac{X_S}{2\sqrt{D_\gamma t}}\right)}$$

In temperature region (b), when decarburization occurs, a discontinuous concentration profile of carbon is observed as shown in Fig. 8.5. The discontinuous concentration profile is caused by the continuity of chemical potential of carbon in ferrite and austenite.[165]
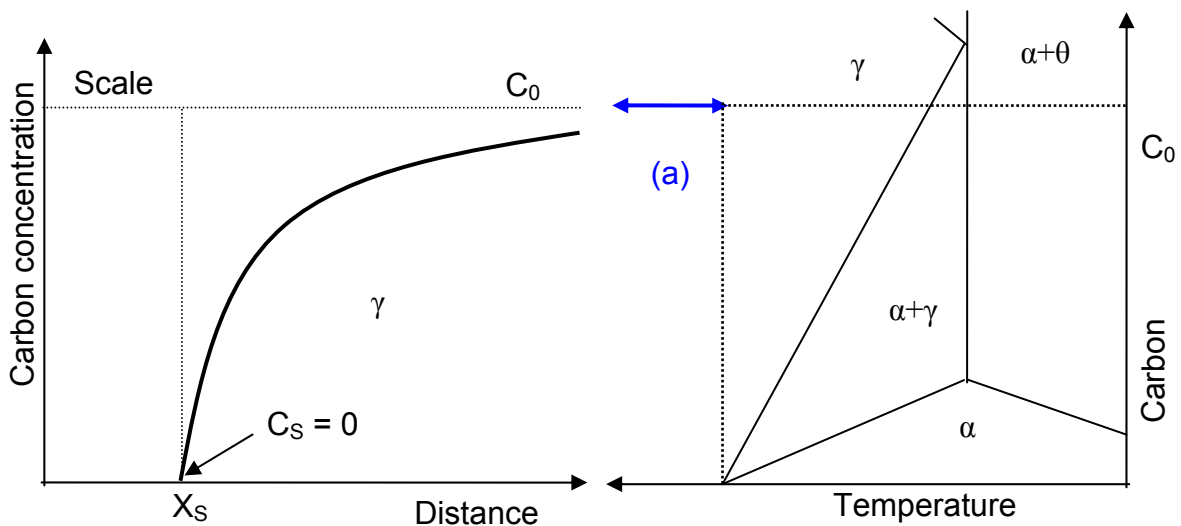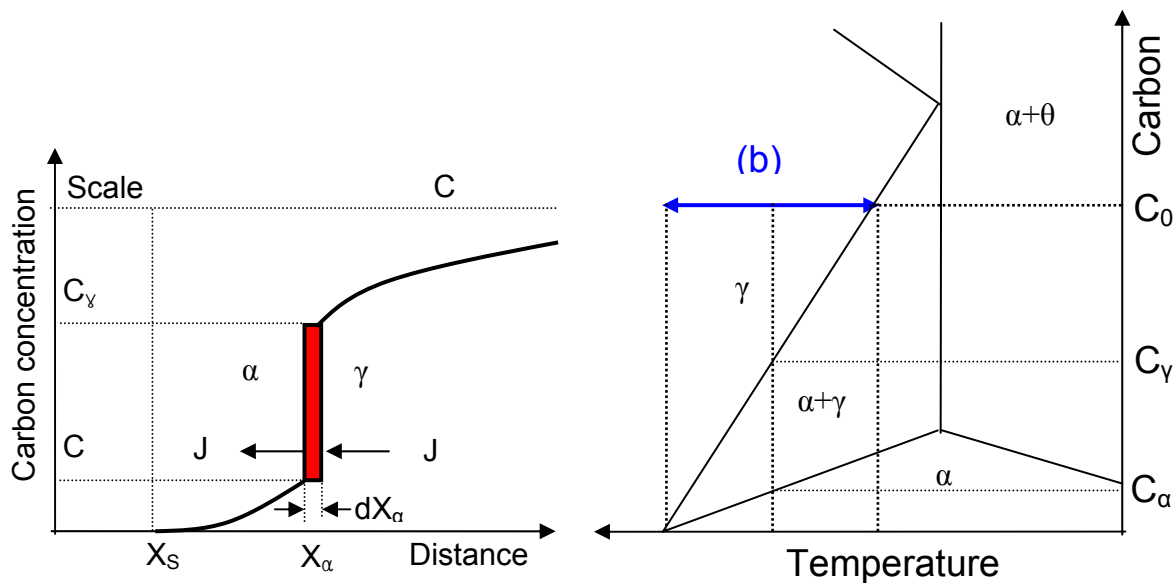

FIGURE 8.5. Schematic diagram of decarburization-oxidation behavior and phase diagram of region (b). The relationship between the equilibrium diagram, the diffusion annealing temperature and the diffusion zone interface concentrations for a two phase system.

Fick's first law of diffusion simply states that the flow of material (J) across unit area in unit time is proportional to the concentration gradient. The proportionality factor D is the diffusion coefficient (or, more strictly, the interdiffusion coefficient, if we refer our distance measurements to the Matano-Interface). Let us consider the application of Eq. (8) to a diffusion couple made up of two pure metals which have limited solubility in the primary phases, and no intermediate phases.

$$J = -D\frac{\partial C}{\partial x} \tag{8}$$

Fig. 8.5 shows the c-x curve and corresponding equilibrium diagram. It is assumed that the concentrations at the interface are constant and equal to the equilibrium values (Kirkaldy).[166]

The carbon concentration in ferrite decarburizing layer is then calculated according to Eq. (9). At the interface of ferrite decarburized layer and austenite matrix, the carbon

concentration of ferrite is C_α as shown in Fig. 8.5. The carbon concentration of ferrite is zero at the interface of scale and steel.

$$C_\alpha(x,t) = a_\alpha + b_\alpha \cdot erf\left(\frac{x}{2\sqrt{D_\alpha t}}\right) \tag{9}$$

$$a_\alpha = C_\alpha - \frac{C_\alpha - C_S}{erf\left(\frac{X_\alpha}{2\sqrt{D_\alpha t}}\right) - erf\left(\frac{X_S}{2\sqrt{D_\alpha t}}\right)} erf\left(\frac{X_\alpha}{2\sqrt{D_\alpha t}}\right),$$

$$b_\alpha = \frac{C_\alpha - C_S}{erf\left(\frac{X_\alpha}{2\sqrt{D_\alpha t}}\right) - erf\left(\frac{X_S}{2\sqrt{D_\alpha t}}\right)}$$

The carbon concentration in austenite is calculated as Eq. (10). The carbon concentration of austenite is C_γ in Fig. 8.5. The carbon concentration at interface of ferrite and austenite is calculated using the software of ThermoCalc. Before decarburization, the carbon concentration is the initial composition.

$$C_\gamma(x,t) = a_\gamma + b_\gamma \cdot erf\left(\frac{x}{2\sqrt{D_\gamma t}}\right) \tag{10}$$

$$a_\gamma = \frac{C_\gamma - C_0 erf\left(\frac{X_\alpha}{2\sqrt{D_\gamma t}}\right)}{1 - erf\left(\frac{X_\alpha}{2\sqrt{D_\gamma t}}\right)}, \qquad b_\gamma = \frac{C_\gamma - C_0}{erf\left(\frac{X_\alpha}{2\sqrt{D_\gamma t}}\right) - 1}$$

If we consider the flux of material from right to left, the rate of advance of the interface at X_α is given by

$$(C_\gamma - C_\alpha)\frac{dX_\alpha}{dt} = J_\gamma - J_\alpha \tag{11}$$

The flux from the ferrite phase at the interface must supply the surplus quantity ($C_\gamma - C_\alpha$)dX_α per unit time in order to advance the ferrite phase into the austenite phase region. Substituting for J from (11), we have

$$\frac{dX_\alpha}{dt} = \frac{1}{(C_\gamma - C_\alpha)}\left[D_\alpha\left(\frac{\partial C}{\partial x}\right)_\alpha - D_\gamma\left(\frac{\partial C}{\partial x}\right)_\gamma\right] \tag{12}$$

Now the system considered fulfils the conditions required for the application of the Boltzmann theorem [164]; thus the concentration C(x, t) may be expressed as a function of a single parameter $\lambda = x/\sqrt{t}$, and we may write

$$K = \frac{\partial C}{\partial \lambda} = \sqrt{t}\frac{\partial C}{\partial x} = \sqrt{t}\left[\frac{b}{\sqrt{\pi Dt}}\exp\left(-\left(\frac{x}{2\sqrt{Dt}}\right)^2\right)\right] \tag{13}$$

If, as has been assumed, the concentrations remain constant at the interface, then the value of the parameter A, in terms of which c is expressed, must be constant. But $dc/d\lambda$ is again a function of λ alone, and hence it also is constant at the interface. Thus Eq. (13) may be rewritten as

$$\frac{dX_\alpha}{dt} = \frac{(D_\alpha K_\alpha - D_\gamma K_\gamma)}{(C_\gamma - C_\alpha)}\frac{1}{\sqrt{t}} \tag{14}$$

Integrating Eq. (14),

$$X_\alpha - X_S = 2\frac{(D_\alpha K_\alpha - D_\gamma K_\gamma)}{(C_\gamma - C_\alpha)}\sqrt{t} \tag{15}$$

$$K_\alpha = \frac{C_\alpha}{\sqrt{\pi D_\alpha}\left[erf\left(\frac{X_\alpha}{2\sqrt{D_\alpha t}}\right) - erf\left(\frac{X_S}{2\sqrt{D_\alpha t}}\right)\right]}\exp\left(-\left(\frac{X_\alpha}{2\sqrt{D_\alpha t}}\right)^2\right)$$

$$K_\gamma = \frac{C_\gamma - C_0}{\sqrt{\pi D_\gamma}\left(erf\left(\frac{X_\alpha}{2\sqrt{D_\gamma t}}\right) - 1\right)}\exp\left(-\left(\frac{X_\alpha}{2\sqrt{D_\gamma t}}\right)^2\right)$$

Eq. (15) exhibits the experimentally observed parabolic time dependence of the interface movement.

In temperature region (c), when decarburization occurs, a discontinuous concentration profile of carbon is observed as shown in Fig. 8.6. The discontinuous concentration profile is caused by the continuity of chemical potential of carbon in ferrite and austenite + ferrite. Austenite phase starts to transform ferrite phase at temperature more than A1 and ferrite + cementite at temperature less than A1. The carbon concentration in ferrite decarburizing layer is calculated as Eq. (16). At interface of ferrite decarburized layer and austenite matrix, the carbon concentration of ferrite is C_α as in Fig. 8.6. The carbon concentration of ferrite is zero at the interface of scale and steel.

$$C_\alpha(x,t) = a_\alpha + b_\alpha \cdot erf\left(\frac{x}{2\sqrt{D_\alpha t}}\right) \tag{16}$$

$$a_\alpha = C_\alpha - \frac{C_\alpha - C_S}{erf\left(\frac{X_\alpha}{2\sqrt{D_\alpha t}}\right) - erf\left(\frac{X_S}{2\sqrt{D_\alpha t}}\right)} erf\left(\frac{X_\alpha}{2\sqrt{D_\alpha t}}\right),$$

$$b_\alpha = \frac{C_\alpha - C_S}{erf\left(\frac{X_\alpha}{2\sqrt{D_\alpha t}}\right) - erf\left(\frac{X_S}{2\sqrt{D_\alpha t}}\right)}$$

FIGURE 8.6. Schematic diagram of decarburization-oxidation behavior and phase diagram of region (c).   The relationship between the equilibrium diagram, the diffusion annealing temperature and the diffusion zone interface concentrations for a two phase system.

The carbon concentration in austenite + ferrite is calculated as Eq. (17).   The carbon concentration of austenite + ferrite phase is initial carbon concentration (C_0) and ferrite and austenite transformed from austenite (no decarburization) are stable as shown in Fig. 8.6. Austenite and ferrite are stable phases and the chemical potential of both phases is equal.   It indicates that the flux in austenite + ferrite phase is zero.

$$C_\gamma(x,t) = C_0 = (1-f)_\gamma C_\alpha + f_\gamma C_\gamma \tag{17}$$

The rate of advance of the interface at X_α is given by

$$(C_0 - C_\alpha)\frac{dX_\alpha}{dt} = J_\alpha \tag{18}$$

The flux from the decarburized ferrite phase at the interface must supply the surplus quantity ($C_0 - C_\alpha$)dX_α per unit time in order to advance the decarburized ferrite into the austenite+ferrite phase region.

$$\frac{dX_\alpha}{dt} = \frac{1}{(C_0 - C_\alpha)} \left[D_\alpha \left(\frac{\partial C}{\partial x} \right)_\alpha \right] \tag{19}$$

Integrating Eq. (19), the thickness of ferrite decarburized layer is given by

$$X_\alpha - Xs = 2 \frac{D_\alpha K_\alpha}{(C_0 - C_\alpha)} \sqrt{t} \tag{20}$$

$$K_\alpha = \frac{C_\alpha}{\sqrt{\pi D_\alpha} \left[erf\left(\frac{X_\alpha}{2\sqrt{D_\alpha t}} \right) - erf\left(\frac{X_S}{2\sqrt{D_\alpha t}} \right) \right]} \exp\left(-\left(\frac{X_\alpha}{2\sqrt{D_\alpha t}} \right)^2 \right)$$

Fig. 8.7 shows the algorithm for computing the decarburization-oxidation model during isothermal heating.
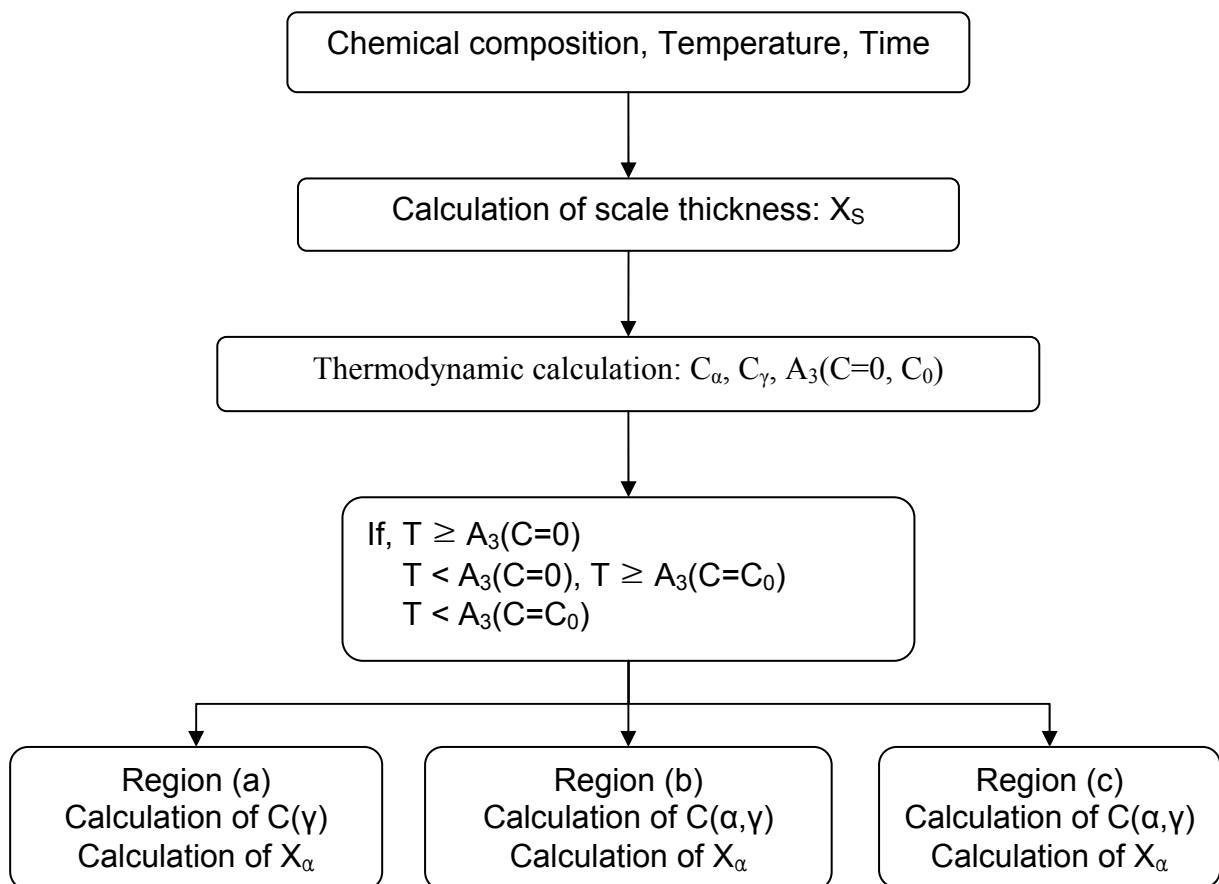

FIGURE 8.7.   Algorithm for computing the decarburization-oxidation model in isothermal heating.

Based on this algorithm the depth of decarburized ferrite with simultaneous oxidation is calculated from Eqs. (15) and (20) in the temperature region (b) and (c) in Fig. 8.3. In the temperature region (b), the decarburized depth, Xα can be obtained when Eq. (21) equal to zero and then equation is mathematically solved by Newton-Raphson method.   In the temperature region (c), the decarburized depth in Eq. (22) is calculated via the same method as in the temperature region (b).

$$X_\alpha - X_S - 2\frac{\left(D_\alpha K_\alpha - D_\gamma K_\gamma\right)}{\left(C_\gamma - C_\alpha\right)}\sqrt{t} = 0 \tag{21}$$

$$X_\alpha - Xs - 2\frac{D_\alpha K_\alpha}{\left(C_0 - C_\alpha\right)}\sqrt{t} = 0 \tag{22}$$

8.3.2.2 Model for a non-isothermal heat treatments

Under non-isothermal conditions, the depth of decarburized ferrite is straightforwardly obtained by stepwise calculation as shown in Fig. 8.8. This method is used to calculate the depth of scale and decarburized ferrite during cooling, based on the model of isothermal heat treatment.   Fig. 8.8 shows the stepwise method calculating the decarburization-oxidation behavior in non-isothermal heat treatment.
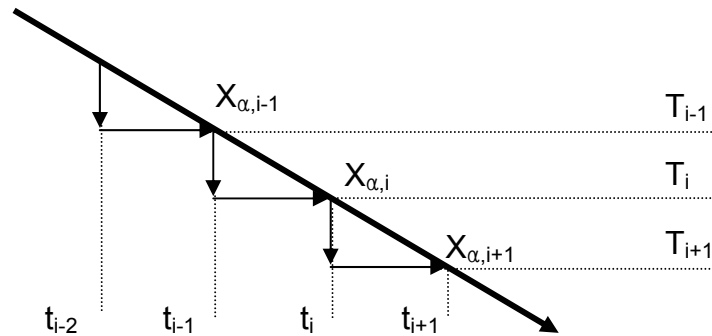
FIGURE 8.8.   Stepwise method calculating the decarburization-oxidation behavior in non-isothermal heat treatment.

First, the start time (t_{i-1}) at temperature T_i is computed from the previous value (X_{i-1}) at temperature T_{i-1} as Eq. (23).

$$t_{i-1} = f^{-1}\left(X_{i-1}\right) \tag{23}$$

where f is a function of the depth of scale growth and decarburization, t is time and X is the depth of scale or the depth of decarburized ferrite. After a given interval of time (Δt), the changed value (ΔX_i) at temperature T_i is calculated by

$$\Delta X_i = f\left(t_{i-1} + \Delta t\right) - f\left(t_{i-1}\right) \tag{24}$$

Finally, the depth at temperature T_i is given by

$$X_i = X_{i-1} + \Delta X_i \qquad\qquad (25)$$

Fig. 8.9 shows the algorithm for computing the decarburization-oxidation model in non-isothermal heat treatment. The cooling profile is divided into discrete isothermal steps and each decarburized depth is solved at the discrete temperature. This may be possible using a suitable computer program.
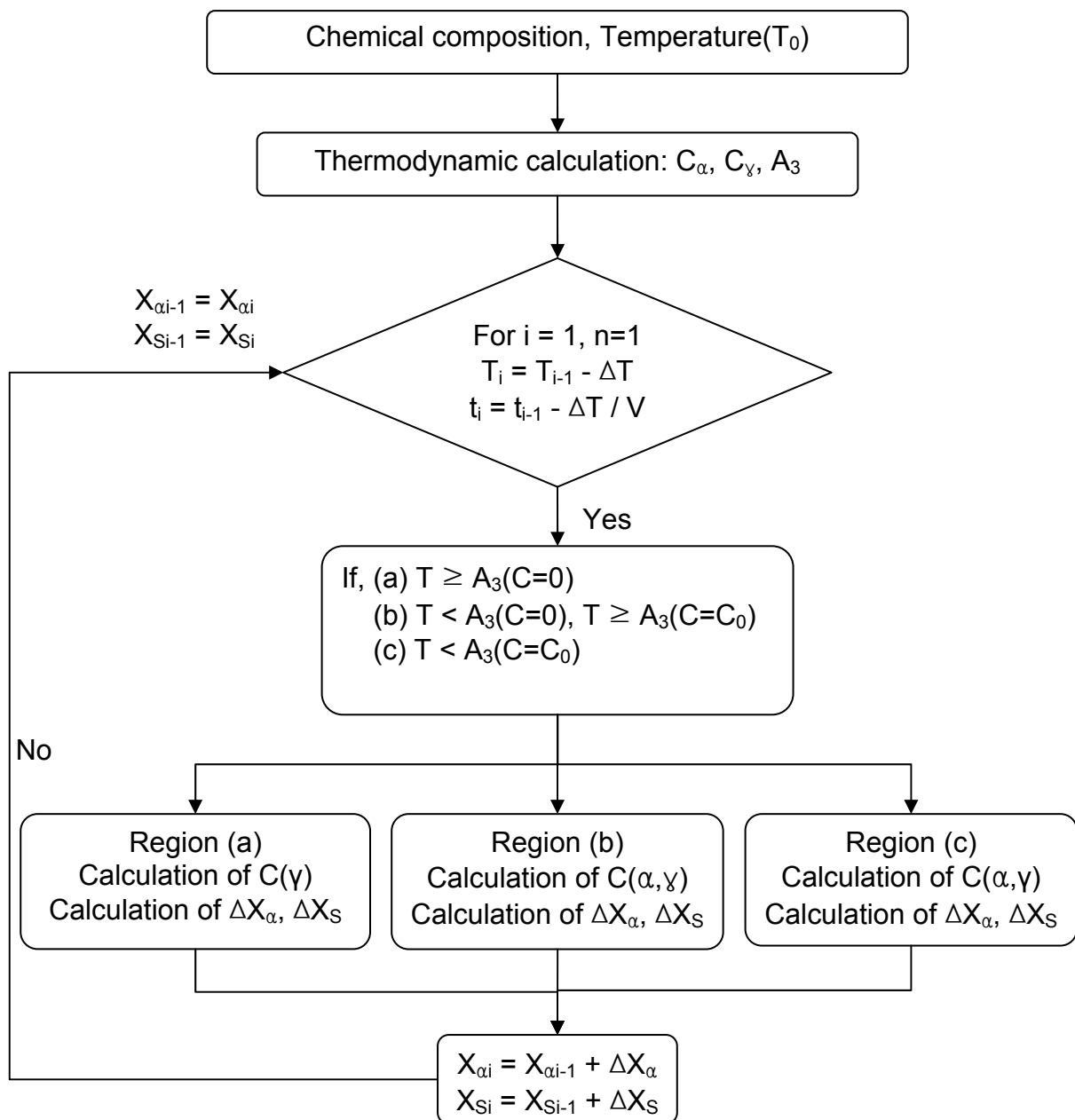

FIGURE 8.9.   Algorithm for computing the decarburization-oxidation model in non-isothermal heating.

8.4 Experiment methods

8.4.1 Specimen preparation

The steel composition used in the study corresponds to the steel grade SAE9254 spring steel used for the step tempering experiments. Its average chemical composition is 0.55% C, 1.5% Si, 0.7% Mn, 0.7% Cr, Fe (bal.) in weight %. It is reported that the high silicon content offers some degree of oxidation resistance.

8.4.2 Analysis of scale growth by TGA

In order to obtain accurate oxide scale growth rates, isothermal oxidation experiments have been performed under 1 atm of air and over the temperature range from 550 ^{o}C to 1050 ^{o}C. Oxidation experiments were conducted using a thermal gravimetric analyzed (TGA). All the specimens were ground with SiC paper to a grid of 1000, cleaned in acetone and then dried in air before TGA tests. The weight change during the period of oxidation was monitored continuously.

8.4.3 Analysis of decarburization by Dilatometer simulator

In the first experiment, decarburization during isothermal heating has been investigated by Dilatometer simulator operating in air. The specimens were heated at 950 ^{o}C for 30 second and cooled rapidly to different temperatures between 750 ^{o}C and 1050 ^{o}C, held for 10 to 300 second. After such heat treatment, all specimens were quenched to room temperature and the decarburized ferrite depth below the surface was measured. In the second experiment, the influence of the cooling rate on decarburization in air has been investigated. The specimens were heated to 1050 ^{o}C at 50 ^{o}C/s and held for 60 second. Subsequently, the specimens were cooled down to room temperature at cooling rate of 0.1, 1.0 and 5.0 ^{o}C/s respectively by Dilatometer simulator. Fig. 8.10 represents the schematic pictures of decarburization experiment.
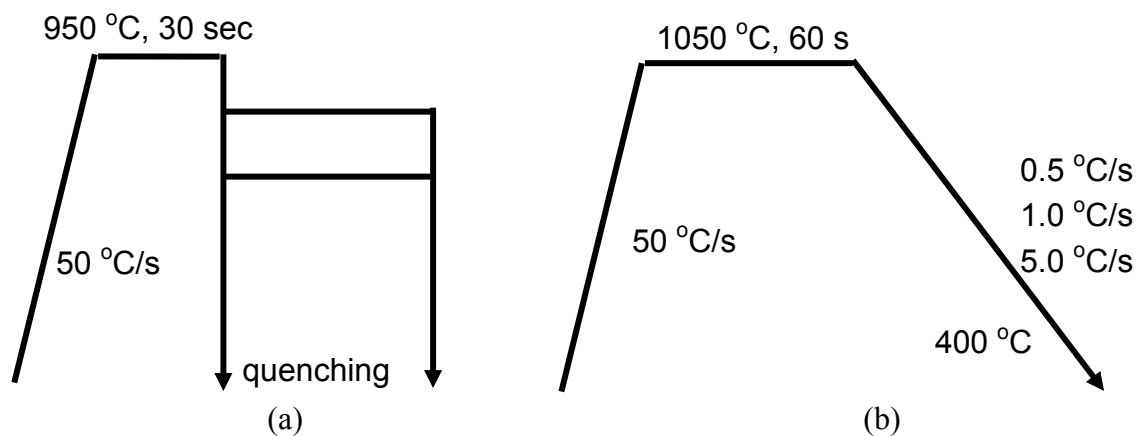

FIGURE. 8.10. Schematic diagram of (a) isothermal decarburization-oxidation experiments and (b) non-isothermal decarburization-oxidation experiments by Dilatometer simulator.

8.4.4 Optical and SEM metallography

Specimens for optical microscopy observation were hot mounted in bakelite molding powder, ground with silicon carbide paper down 1200 grit and then polished with 6 and 1 μm diamond pastes. The specimens wee then etched with 5 vol. % natal (nitric acid in methanol). The optical microstructures were observed using an Olympus microscope.   The etched specimens were gold-coated in vacuum atmosphere. SEM was performed using JEOL JSM-7000F field emission scanning electron microscope.

8.5 Results and Discussion

8.5.1 Scale growth

The oxidation studies were carried out on SAE9254 steels at different holding temperatures for 1 hr. The plot of weight gain versus time is given in Fig. 8.11. As seen from Fig. 8.11 oxidation rates are seen to increase with temperature. Oxidation kinetics at all temperatures shows a period of fast and linear oxidation.
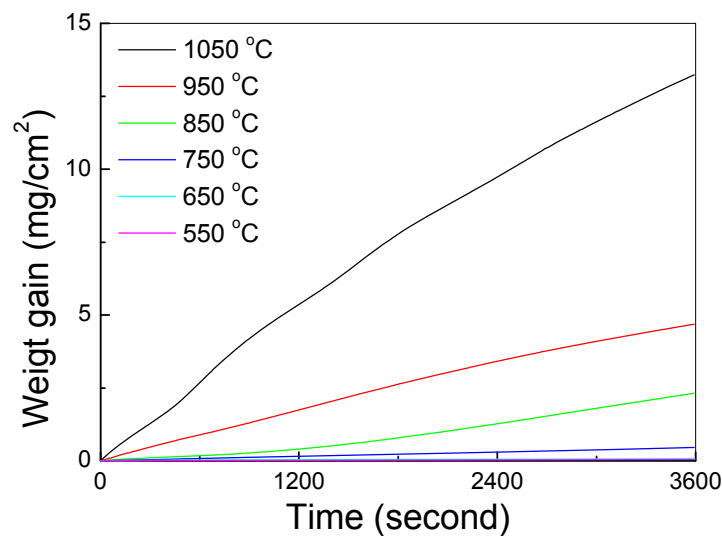
FIGURE 8.11. Weight gain per unit area (mg/cm^2) of SAE9254 steel as a function of time during oxidation obtained in the temperature range of 550 ^{o}C ~ 1050 ∘C.

The fit of the linear regression for all the curves was found to lie between 0.99 and 1.0. Therefore, for the purpose of determining activation energy the index of rate (n) is assumed to be 1.0 for SAE9254. The rate constants determined were then used in a plot of ln(K) versus 1/T (Fig. 8.12) and the activation energy was calculated as 16.2 kJ/mol. In high carbon steel of 0.85 %C, 0.85 %Mn, and 0.18 %Si, activation energy of rate constant for the oxidation was obtained as 21.7 kJ/mol.[151] The depth of scale can be calculated from dividing the weight gain per unit area by the density of scale. Scale was assumed to be FeO. The equation of scale growth with time is given by

$$d = K \cdot t$$

$$K = 1.481 \cdot \exp\left(\frac{-16181.64}{T}\right) \tag{26}$$

where d is depth of scale, [mm], and K is rate constant, [mm/s] and t is time, [s].
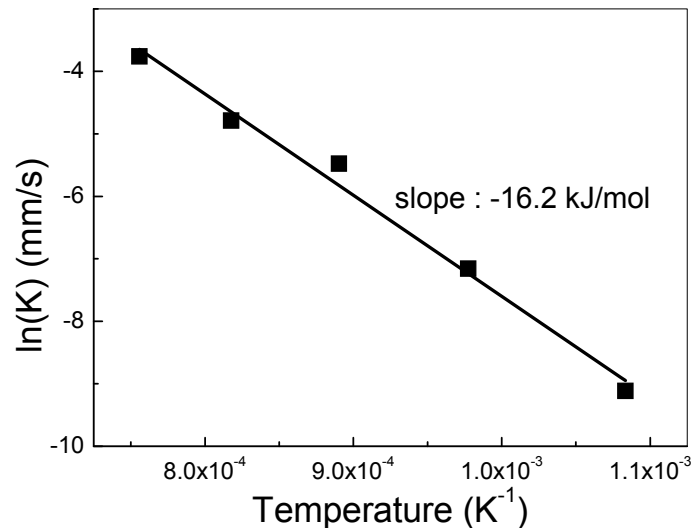
FIGURE 8.12. Dependence of the linear rate constant of oxidation of the temperature.

8.5.2 Decarburization behavior in isothermal heating

Fig. 8.13 shows the optical micrographs of the microstructures formed during the isothermal heating. The specimens underwent an oxidation and decarburization treatment at different temperatures between 750 $^{\circ}$C and 950 $^{\circ}$C. It can be clearly observed that the depth of the decarburized region increases with increasing heating temperatures.

At the highest temperature of 900 $^{\circ}$C, the decarburized ferrite layer on the surface appears to be discontinuous. At the heating temperature of 850°C, an apparently thick decarburized layer has formed on the surface. Moreover, the treatments at the lower temperatures of 800 and 750°C produce large, almost columnar ferrite grains with an extension of around 40 μm. The scale which forms on the outer surface of the specimens increases with increasing temperature. Based on the experimental results of Fig. 8.13 and the database of Dictra, the diffusivity of SAE9254 was determined as function of the temperature. The carbon diffusivities for ferrite and austenite are given by

$$Log(D_\alpha) = 0.667E6 * 10^{-5.08872 - \frac{4947.305}{T}}, \qquad \text{in ferrite region} \tag{27}$$

$$Log(D_\gamma) = 3.0E6 * 10^{-4.61805 - \frac{7493.08}{T}}, \qquad \text{in austenite region} \tag{28}$$

FIGURE 8.13.   Optical micrographs of decarburized surface of SAE9254 heated at the temperature of 900 ^{o}C for (a) 60 s, (b) 120 s, (c) 180 s and (d) 300 s.

FIGURE 8.14.   Optical micrographs of decarburized surface of SAE9254 heated at the temperature of 850 ^{o}C for (a) 60 s, (b) 120 s, (c) 180 s and (d) 300 s.

FIGURE 8.15.   Optical micrographs of decarburized surface of SAE9254 heated at the temperature of 800 ^{o}C for (a) 60 s, (b) 120 s, (c) 180 s and (d) 300 s.

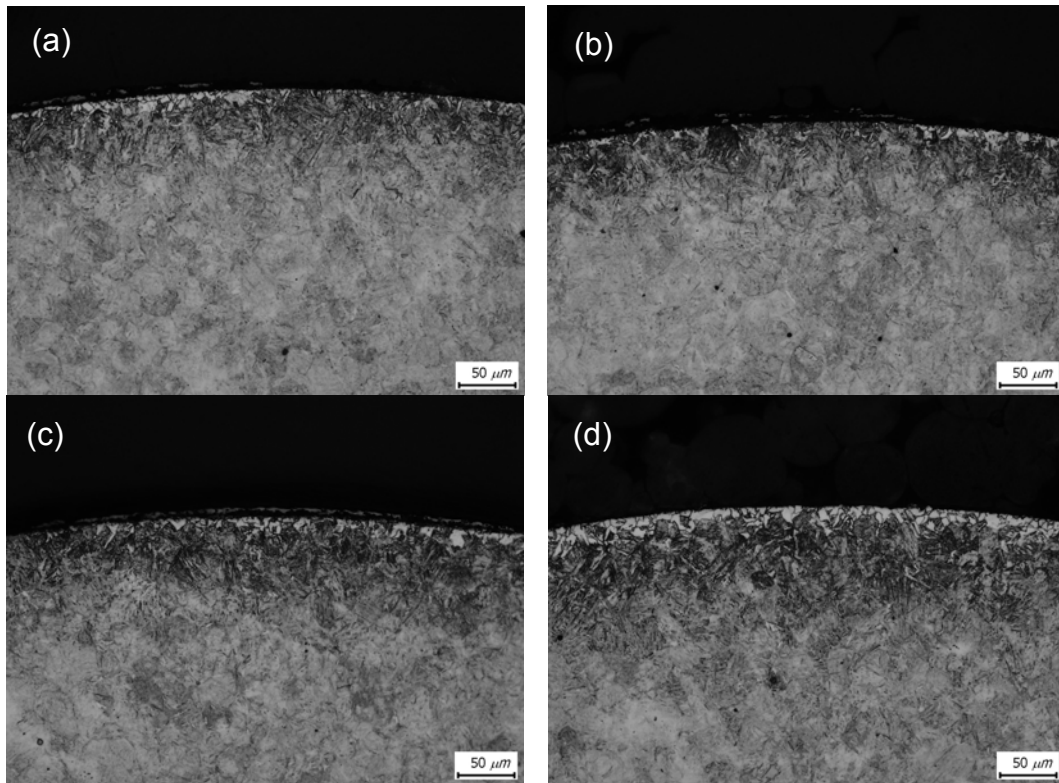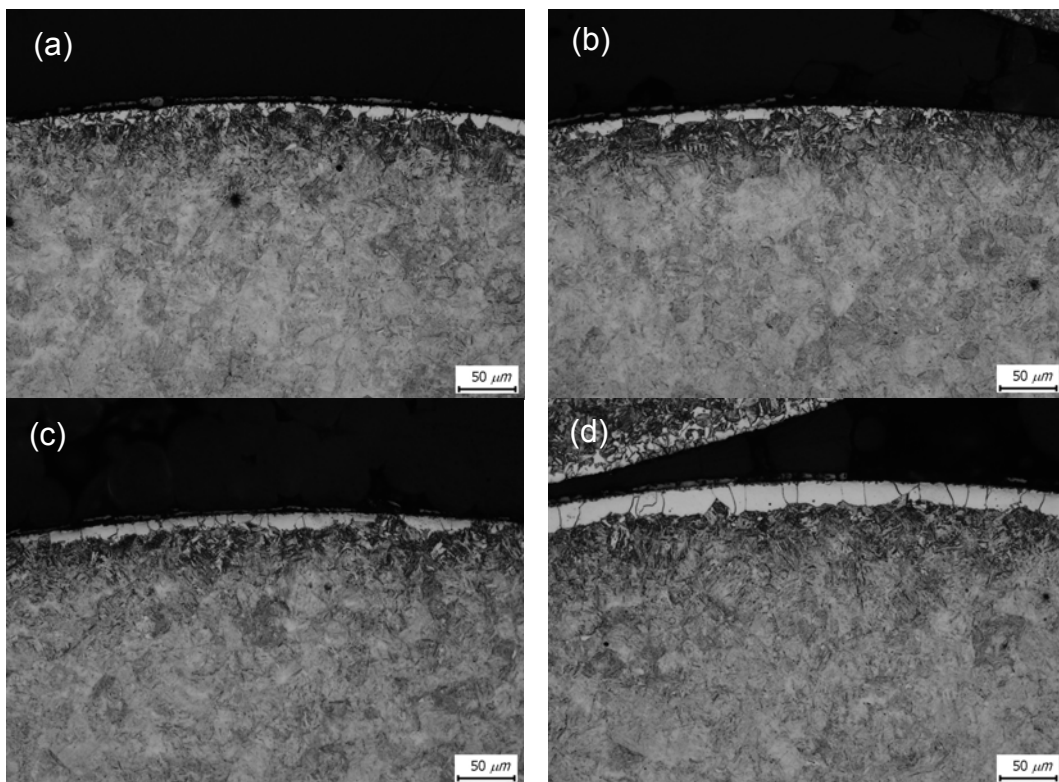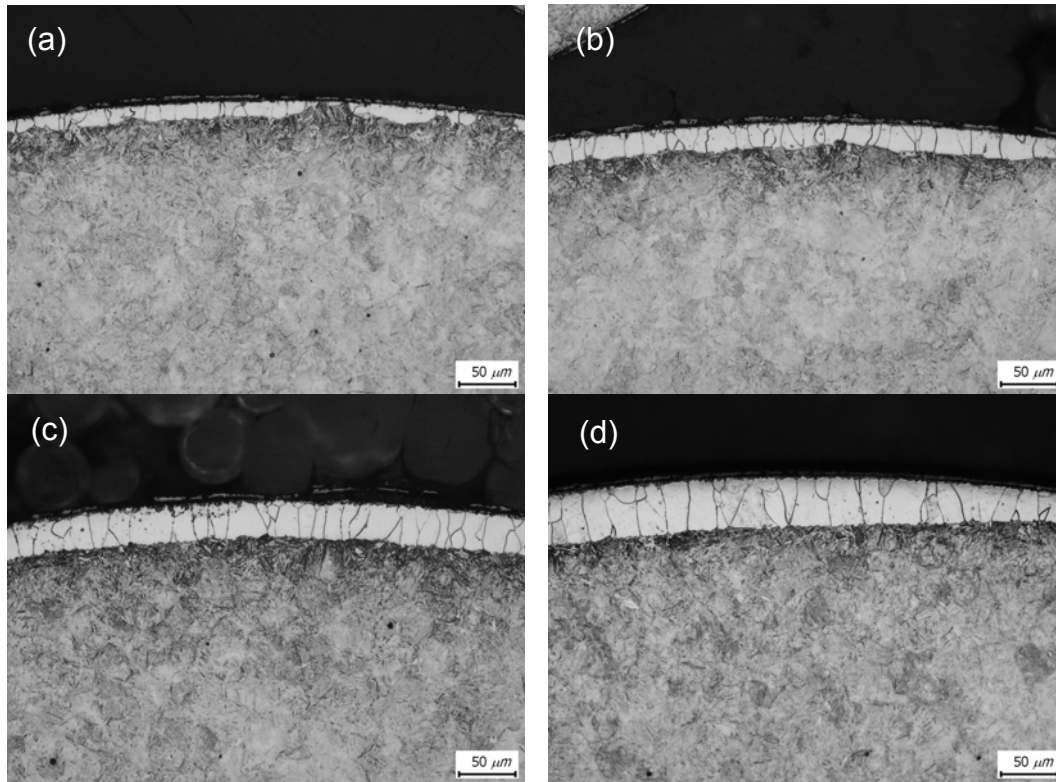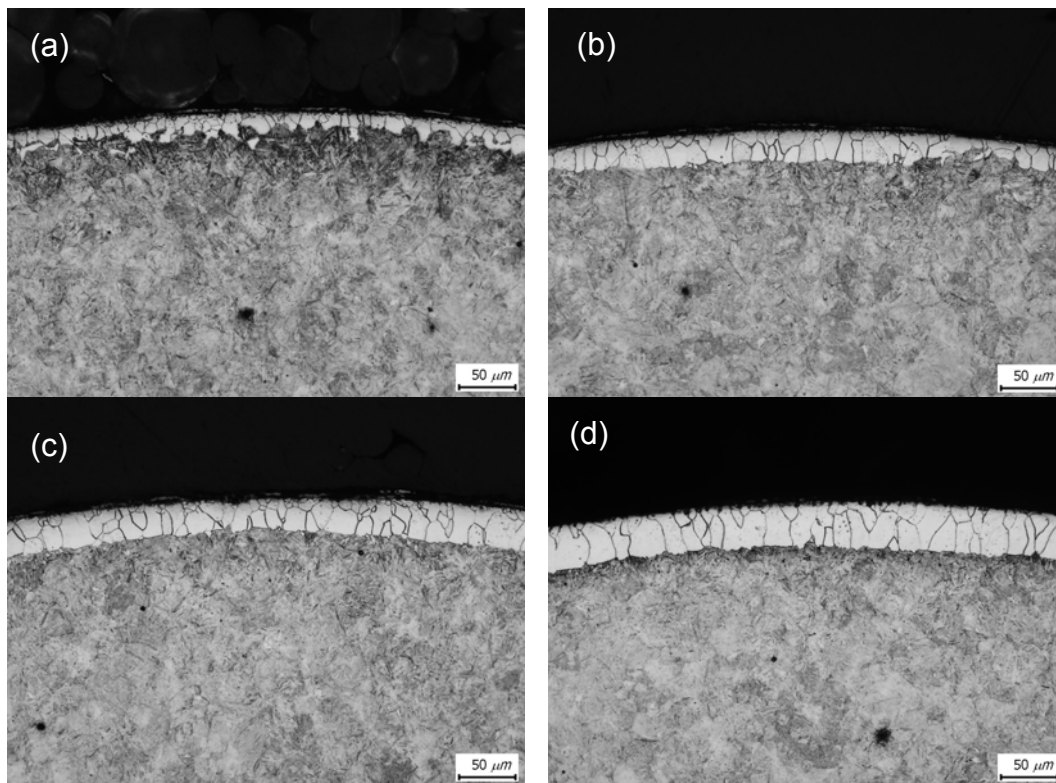FIGURE 8.16.   Optical micrographs of decarburized surface of SAE9254 heated at the temperature of 750 ^{o}C for (a) 60 s, (b) 120 s, (c) 180 s and (d) 300 s.

Fig. 8.17 shows the decarburized ferrite depth for isothermal heating at 750 °C to 900 °C. It can be noticed that the decarburized depth grows continuously with time, while decreasing the temperature from 900 °C to 750 °C leads to increasing growth rates. The decarburization rate is strongly influenced by the carbon diffusion coefficient. The explanation of this phenomenon is that the carbon diffusion coefficient in ferrite is much higher than that in austenite.

The simulated results of decarburization-oxidation model were compared to the measurements of decarburized ferrite depth in Fig. 8.17. As described above, the ferrite decarburizing depth by calculations basically coincided with that by experiments. The values of the decarburization depth are slightly smaller or larger for simulations compared to experimental results. Oxide formation decreased the decarburized depth by transforming parts of the surface decarburized layer into oxide and, also, by protecting the bulk metal from rapid loss of carbon by sealing against the outer atmosphere.

FIGURE 8.17. Decarburized ferrite depths of experimental and predicted results of SAE9254 during heating obtained at 750 °C ~ 900 °C.

8.5.3 Decarburization behavior in non-isothermal heat treatment

Fig. 8.18 shows the optical micrographs of the surface of specimens formed during cooling. The specimens were heated at 1050 °C and cooled in air to room temperature The cooling rates were 0.1, 1.0 and 5.0 °C/s respectively. The decarburized ferrite depth increases with decreasing the cooling rate. At cooling rate of 5.0 °C/s, microstructure was martensite and at less than 5.0 °C/s the microstructure consisted of pearlite and ferrite at grain boundary.

Fig. 8.19 shows the decarburized ferrite depths of the surface of microstructure shown in Fig. 8.18. The decarburized ferrite depths were measured to be about 67.8 um at cooling rate of 0.5 °C/s, 45.6 um at cooling rate of 1.0 °C/s and 18.9 um at cooling rate of 5.0 °C/s respectively. On the other hand, the decarburized ferrite depth calculated by the proposed

model became about the same value under the same conditions of the experiment.   The measured and predicted values of decarburized ferrite depth were compared as a function of cooling rate in Fig. 8.19.   As described above, the decarburized ferrite depth by calculation coincided with that by experiments, and it is considered that the decarburized ferrite depth can be calculated considering the chemical composition of SAE9254 and oxidation in air using the proposed model.
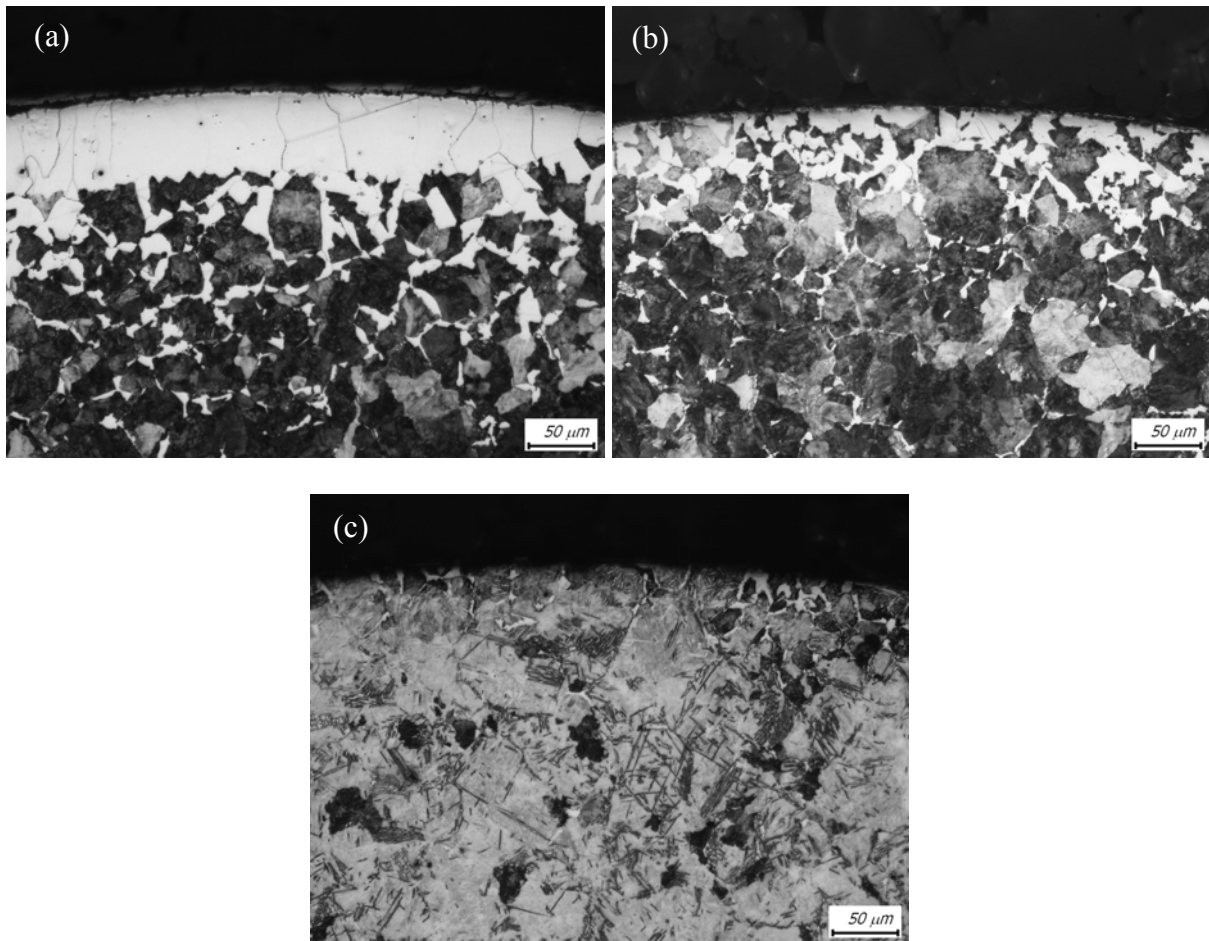
FIGURE 8.18. Optical micrographs of decarburized surface of SAE9254 cooled as rates of (a) 0.1, (b) 1.0 and (c) 5.0 ^{o}C/s.

From this fact, it is considered that the decarburized ferrite depth can be calculated considering heating condition (heating, cooling) using the model described above. It is also possible to calculate the decarburized ferrite depth considering the effects of chemical composition, decarburization and oxidation simultaneously in isothermal and non-isothermal heat treatments. Numerical simulations have in all cases proved to be useful in determining trends in materials behavior during thermal treatment. Moreover, quantitative information on the oxidation and decarburization characteristics has been obtained and were found to be in good agreement with the experiments.
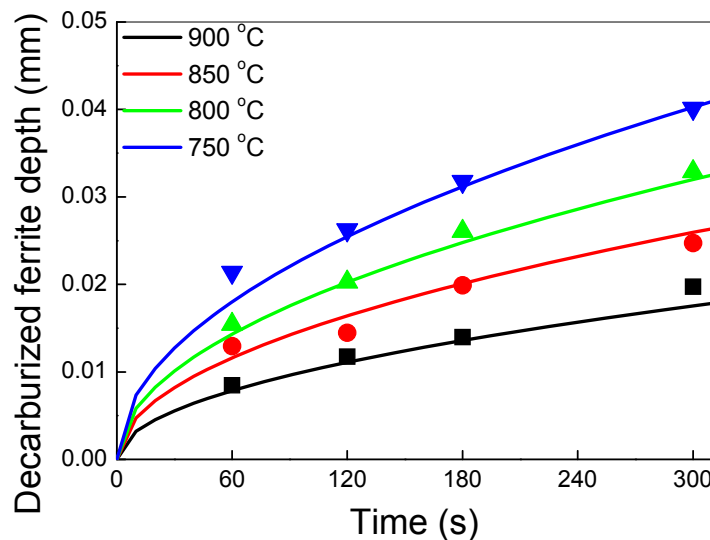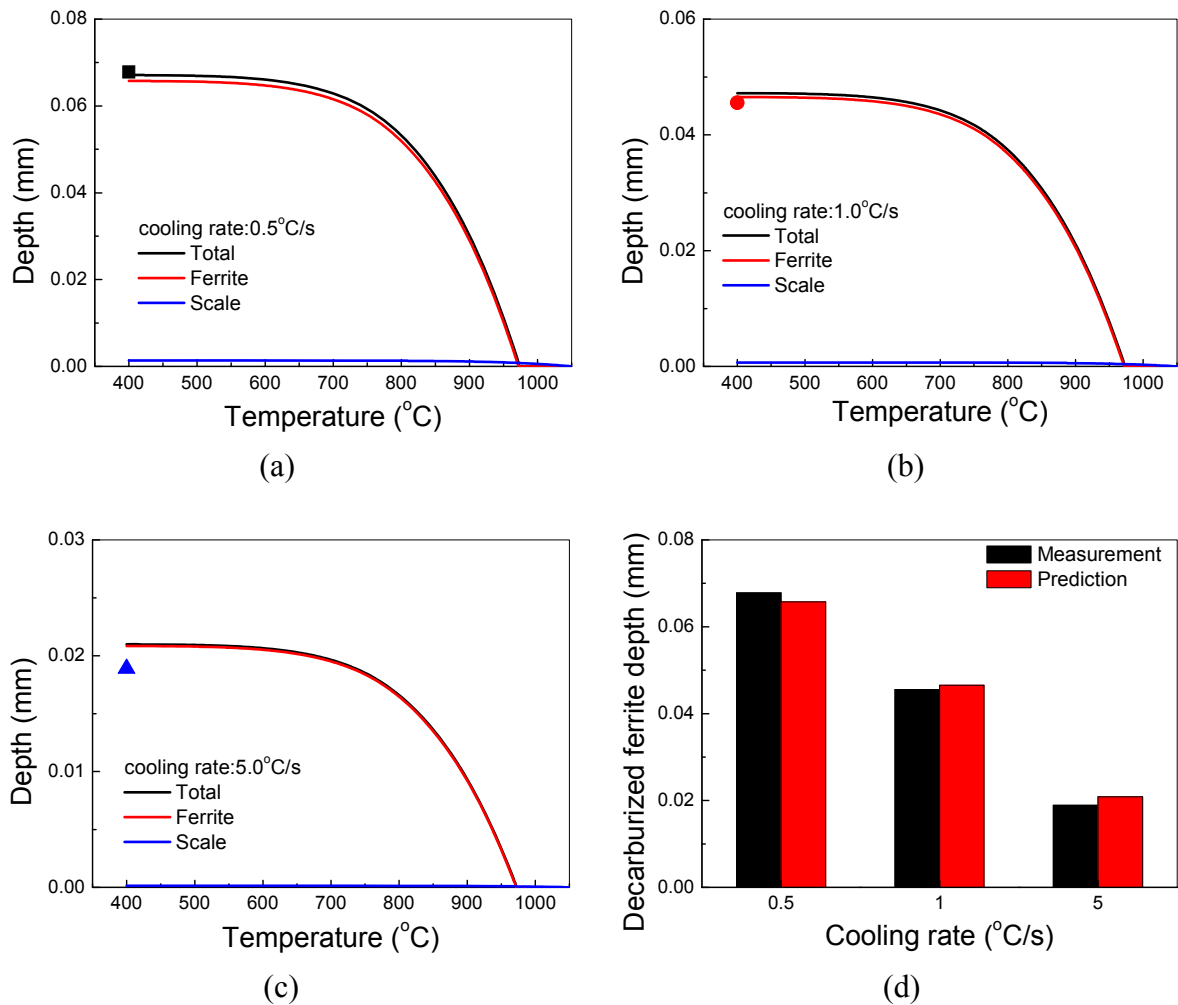
FIGURE 8.19. Decarburized ferrite depths of experimental and predicted results of SAE9254 during heating obtained at 750 °C ~ 900 °C. The cooling rates are (a) 0.5 °C/s, (b) 1.0 °C/s, and 5.0 °C/s, and the decarburized ferrite depths are compared in (d).

8.6 Conclusions

A numerical model for decarburized ferrite depth considering the effects of chemical composition of steel and heating condition was constructed and its propriety was confirmed by comparing with the experimental results. Experiments and simulations have shown that heating conditions and cooling rates have a large affect on oxidation, as well as on decarburization. The model shows good agreement with experimental results, and can be used to optimize the thermal cycle during steel production. The following conclusions were obtained.

1. The analysis of the oxidation weight gain curves of SAE9254 show that there are linear relation between oxidation and time. The rate constants determined show that the activation energy is 16.2 kJ/mol. Activation energy was calculated assuming an average time exponent of the rate law of 1.0.

2. The calculated decarburized ferrite depth taking into account the chemical composition of steel was almost the same as that by experiments under constant temperature conditions. The model is applicable to the calculation of the ferrite decarburizing depth considering the decarburization and oxidation during isothermal and non-isothermal heat treatments.

3. Oxidation and surface decarburization occur simultaneously during the production process of spring steels. A new model has been developed which includes effects of both phenomena. A mathematical solution is presented here for the diffusion control of this decarburization process and it is shown that the decarburized depth is a fairly strong function of the temperature and time at which the decarburization is carried out.

4. Numerical simulations have in all cases proved to be useful in determining trends in materials behavior during thermal treatment. Moreover, quantitative information on the oxidation and decarburization characteristics has been obtained in good agreement with the experiments.

Summary

Weight reduction in automobile industry is important so as to reduce the amount of fuel consumption, which can be achieved in part by improving the design strength of suspension coil springs. However, the increment in strength should not degrade other spring properties such as formability and fatigue. For spring steels, the emphasis in materials research has been focused on increasing the strength while maintaining good ductility, toughness and fatigue properties. The purpose of this study is to design the spring steel with the tensile strength 2350 MPa and reduction of area more than 25 % for the desired strength 1400 MPa grade spring.

In Chapter 1 the history of developing the spring steels is introduced and the necessity of higher strength spring steel is described in detail. As an attempt to satisfy such demands, it is desired to develop springs with an increased tensile stress specification. However, if presently available spring steels are used under a high stress conditions, problems related to durability, low fatigue life and sagging will exist.

For achieving the target mechanical properties it is essential to control the alloy composition and to find appropriate heat treatments routes to optimize the desired multiphase structures for high carbon steels. To this aim a new method to analyze the phase transformation during cooling from the austenitic state was developed in Chapter 2. The proposed model takes into account the austenite-ferrite, austenite-pearlite reactions and their interaction and can estimate the phase transformation information from the dilatation curve. If the volume fractions of phases can be quantitatively related to the dilatation data, the dilatometric technique may be efficiently applicable to the investigation of the phase transformation kinetics. The proposed model is essentially based on the carbon enrichment of the austenite and the difference in unit volume of the phases. The self consistent model has been applied to the determination of the phase transformation kinetics from the dilatation

curves and verified by comparing the model results to experimental results of hypoeutectoid steels.   Excellent agreement between the calculation and the experimental results is observed.

A significant step in thermo-mechanical processing of steels is reaustenitization.   Since reaustenitization usually affects the grain size, grain size distribution and alloying element concentration homogeneity, the prior austenite microstructure has a great impact on the kinetics of further phase transformations, and in turn on the mechanical properties of components in subsequent cooling processes, such as quenching and tempering.   The experimental observation of reaustenitization kinetics and morphology developments is difficult because austenite formed during heating is subsequently destroyed due to the transformation during cooling.   To this aim a new method to determine the phase transformation during heating was developed in Chapter 3.   In order to study the kinetics of austenite formation, the simplifying assumption was adopted stating that austenite (γ) nucleates at the lamellar Fe_3C/α interface, creating two new interfaces, Fe_3C/γ and γ/α.   The proposed model is based on the ferrite-austenite and cementite-austenite boundary reaction under local equilibrium conditions.   Excellent agreement between the calculation and the experimental results is observed.

The aim of Chapter 4 is to develop a spring steel with a tensile strength higher than 2350 MPa and a reduction of area more than 25 %.   In order to develop such a new high strength steel, the 5 steel grades have been studied.   The chemical composition was based on the high C-Si steel with additions of Mo, B or Nb.   Microstructures were examined to explain the characteristics of mechanical properties with austenitization and tempering temperature.   The tensile properties of experimental steels S1 and S3 reached the desired values.   Therefore, further examinations focused on these two steel grades.

In Chapter 5 the strengthening and softening mechanisms in spring steels are discussed to explain the mechanical properties and the microstructural changes.   The strengthening effect was investigated taking into account the austenite conditions, V_4C_3, cementite and ε-carbide precipitation and the martensite lath size.   The increment of tensile strength may be mainly controlled by fine precipitates of ε-carbide.   At low tempering temperatures, ε-carbide precipitated from carbon clusters and a part of supersaturated carbon may be retained.   These factors contribute to the increase of tensile strength.   With increasing the tempering temperature, ε-carbide dissolves and cementite is formed simultaneously.   A delayed transformation from ε-carbide to cementite may increase the tensile strength without losing the reduction of area at high tempering temperature.   The large prior austenite grain size of S3 steel and/or unwanted borocarbides at grain boundary may contribute to decrease the reduction of area.

Chapter 6 describes some of the interrelated chemical and microstructural causes associated with a decrease in reduction of area and embrittlement phenomena in high carbon steels and relates these causes to characteristic cleavage, or intergranular fracture surfaces.   The intergranular fracture of S3 steel is caused by the presence of borocarbides at prior austenite grain boundary.   Micro cracks initiate at particles (inclusion, carbide, $Fe_{23}(C, B)_6$ carbide etc.) at prior austenite grain boundary and propagates easily along grain boundary by $Fe_{23}(C, B)_6$ carbide.   The ductility (reduction of area) may be reduced significantly because of intergranular fracture along prior austenite grain boundaries covered with $Fe_{23}(C, B)_6$ carbide.

In order to improve the mechanical properties, a new tempering treatment was developed

which consisted of a two step tempering processes.   Main reason of step tempering is to increase the number of ε-carbide and suppress the transition from ε-carbide to cementite. The mechanical properties of step tempered spring were improved beyond those of the conventional tempered spring and the fatigue life was almost equal.   The strengthening was based on the precipitation of fine $Fe_{2.4}C$ carbide and the suppression of transition from $Fe_{2.4}C$ carbide to spheroidized cementite.   Further work on the details of the microstructural changes in two step tempering is desirable.

It is necessary to minimize the decarburizing depth, especially for wire and rod steels in order to presence good fatigue properties in spring steels.   Chapter 8 described the effect of the chemical composition of steel and heating condition on the ferrite decarburizing depth and the thickness of scale.   The objective is to investigate the decarburization process during reheating and cooling for high silicon spring steel in ambient atmosphere and to identify the influence of thermal cycles on the decarburization behavior.   A numerical model of decarburized ferrite depth considering the effects of chemical composition of steel and heating condition is developed which includes effects of decarburization and oxidation.   The model shows good agreement with experimental results, and can be used to optimize the thermal cycle during steel production.

The combined results of this thesis lead to new and improved high strength spring steels with applications in the field of automobile industry and elsewhere.   Numerical simulations have in all cases proved to be useful in determining trends in material behavior during thermal treatment.

166   Summary

Samenvatting

Er is een belangrijk maatschappelijk belang in het terugbrengen van het benzineverbruik van personen- en vrachtwagens. De verlaging van het gewicht van hun veersystemen door gebruik te maken van verenstaal met hogere treksterkte kan hier een kleine maar niet onbelangrijke bijdrage aan leveren. Deze hogere treksterkte moet echter niet ten koste gaan van andere mechanische eigenschappen. Het materiaalkundige onderzoek aan nieuwe generaties verenstaal richt zich op een verhoging van de treksterkte met behoud van vervormbaarheid, taaiheid en vermoeiingssterkte. Het doel van het onderzoek beschreven in dit proefschrift is de ontwikkeling van een verenstaal met een sterkte hoger dan 2350 MPa en een insnoering bij breuk van meer dan 25% om te komen tot een veer met een ontwerpspanning van 1400 MPa of hoger.

Hoofdstuk 1 beschrijft de geschiedenis van de ontwikkeling van verenstaal, zijn samenstelling en zijn warmtebehandeling. Een verdere ontwikkeling van de eigenschappen is nodig in verband met de gewenste gewichtsreductie in een uiteindelijk toepassing. Indien veren, gemaakt uit de nu bestaande kwaliteiten verenstaal, op het gewenste nieuwe en hogere spanningsniveau belast worden, treden er problemen op in de levensduur alsmede in de vormvastheid. Hoofdstuk 1 geeft tevens een overzicht van de samenhang van de diverse deelonderzoeken in dit proefschrift.

Om voor een gegeven staalsamenstelling de gewenste mechanische eigenschappen te bereiken is het nodig om de gewenste microstructuur via een geoptimaliseerde warmtebehandeling te verkrijgen. Hoofdstuk 2 beschrijft een nieuwe methode om het verloop van de fasetransformatie tijdens afkoelen vanaf de austenietfase uit het dilatatiesignaal te bepalen. De voorgestelde methode houdt rekening met de austeniet-ferriet- en de austeniet-perliet reactie en hun onderlinge interactie. In het model worden de effecten van de koolstofverrijking van de austeniet op de transformatie in rekening gebracht. De nieuwe

zelfconsistente methode is toegepast op de fasetransformaties van hypo-eutectoidische hoog-koolstof staalsoorten tijdens rustige afkoeling. Een uitstekende overeenkomst tussen de gemeten en berekende resultaten werd verkregen.

Een andere belangrijke stap in de warmtebehandeling van verenstaal is de austeniteerstap. De austeniteerstap bepaalt de austenietkorrelgrootte en homogeniteit van de verdeling van legeringselementen in de matrix, welke beide een grote invloed hebben op de uiteindelijke eigenschappen na afkoelen of afschrikken. De bepaling van de ontwikkeling van de austeniet tijdens de austeniteerstap is echter moeilijk omdat de austeniet verloren gaat bij iedere noodzakelijke afkoeling van het materiaal. Het doel van het onderzoek als beschreven in hoofdstuk 3 is de ontwikkeling van een model om de transformatiekinetiek tijdens opwarmen uit het dilatatiesignaal te bepalen. In het model wordt verondersteld dat de austeniet kiemt op het ferriet-cementietgrensvlak en daarbij twee nieuwe grensvlakken creëert. De verdere groei van de austeniet zou plaatsvinden onder lokaal-evenwichtscondities aan beide grensvlakken. Een uitstekende overeenkomst tussen berekende en experimentele resultaten werd verkregen.

Het doel van hoofdstuk 4 is de ontwikkeling van een verenstaal met een treksterkte hoger dan 2350 MPa en een insnoering bij breuk groter dan 25%. Hiertoe zijn 5 experimentele staalsoorten met een nieuwe samenstelling onderzocht. De samenstelling is gebaseerd op een gangbaar hoog koolstof- en siliciumgehalte met toevoeging van Mo, B en Nb. De microstructuren van deze staalsoorten in hun afgeschrokken en ontlaten toestand zijn voor diverse austeniteercondities onderzocht en gerelateerd aan de mechanische eigenschappen. De mechanische eigenschappen van de experimentele staalsoorten S1 en S3 voldeden aan de gestelde doelen. Het verdere microstructurele onderzoek in dit proefschrift werd dan ook op deze twee staalsoorten geconcentreerd.

Hoofdstuk 5 beschrijft de relevante verstevigings- en ontstevigingsmechanismes in verenstaal en de veranderingen in mechanische eigenschappen als gevolg van de microstructurele veranderingen tijdens de ontlaatstap. De versteviging is in beginsel een functie van de microstructuur van de austeniet, het optreden van precipitatiereacties (V4C3, cementiet en   -carbides) en de microstructuur van de martensiet. Voor de onderzochte staalsoorten wordt de uiteindelijk te realiseren treksterkte toegeschreven aan de vorming van   -carbides. Deze   -carbides ontstaan   bij lage ontlaattemperaturen uit koolstofclusters en de   martensiet   matrix   blijft   enigszins   oververzadigd   in   koolstof.   Bij   hogere ontlaattemperaturen lossen de   -carbides op en worden cementiet precipitaten gevormd. Een vertraging in de vorming van cementiet precipitaten uit   -carbides kan leiden tot hogere sterktes met behoud van de insnoering bij breuk op hogere ontlaattemperaturen. De grotere austeniet korrelgrootte, dan wel het optreden van ongewenste uitscheidingen op de korrelgrens wordt verantwoordelijk geacht voor de lagere insnoering bij breuk voor staalsoort S3.

Hoofdstuk 6 beschrijf de aan elkaar gerelateerde chemische en microstructurele processen welke kunnen leiden tot een afname van de insnoering bij breuk en verbrossing van koolstofstaal en koppelt die aan het optreden van splijtbreuk langs de korrelgrenzen. Het inter-granulaire breukgedrag van staal S3 kon worden toegeschreven aan de aanwezigheid van boorhoudende carbides op de voormalige austeniet korrelgrenzen. Microscheuren ontstaan rond deeltjes (insluitsels, carbides, in het bijzonder Fe23(C,B)6) langs de voormalige austeniet korrelgrenzen en breiden zich makkelijk langs de korrelgrens uit dankzij de

aanwezigheid van de Fe23(C,B)6 carbides. Dit breukgedrag leidt tot een belangrijke afname in de insnoering bij breuk en verlies van taaiheid.

Een nieuwe twee-traps ontlaatbehandeling is ontworpen om de gewenste mechanische eigenschappen, een combinatie van een hoge sterkte en een grote insnoering, te verkrijgen. Doel van de procesaanpassing is het verhogen van het aantal   -carbides en het uitstellen van de vorming van cementiet-precipitaten. De nieuwe behandeling en de resulterende eigenschappen voor 2 staalsoorten zijn beschreven in hoofdstuk 7. De combinatie van trekstrekte en insnoering bij breuk na deze twee-traps ontlaatbehandeling was beter dan die verkregen door een ontlaatbehandeling op één temperatuur, terwijl de vermoeiingssterkte vrijwel behouden bleef. De verbetering werd toegeschreven aan een fijne verdeling van carbides en een vertraagde vorming van bolvormige cementiet. Verder onderzoek naar de microstructurele veranderingen tijdens een twee-traps warmtebehandeling is wenselijk.

Om een goed vermoeiingsgedrag in verenstaalconstructies te verkrijgen is het noodzakelijk om de dikte van de oxide- en ontkolingslaag aan het oppervlak na een warmtebehandeling zo klein mogelijk te houden. Hoofdstuk 8 beschrijft het effect van staalsamenstelling en thermische condities op de dikte van de oxidelaag en de ontkoolde ferrietlaag aan het oppervlak. Doel van het onderzoek is een beter begrip van de ontkoling tijdens alle stappen van het austeniteerproces van staalsoorten met een hoog siliciumgehalte. Een numeriek model voor de ontkoling als functie van de staalsamenstelling en de austeniteercondities is ontwikkeld waarmee de laagdiktes tijdens oxidatieve ontkoling berekend kan worden. Het model geeft een goede voorspelling van de waargenomen laagdiktes als functie van de austeniteercondities en kon gebruikt worden om de warmtebehandeling tijdens productie te optimaliseren.

Het totaal aan resultaten zoals beschreven in dit proefschrift heeft geleid tot de ontwikkeling van een verenstaal met nieuwe samenstelling en procesvoering en met aantrekkelijke eigenschappen voor toepassing in de automobiel-industrie en daarbuiten. Het onderzoek bevestigde tevens het belang van numerieke simulaties voor de nauwkeurige bepaling van het materiaalgedrag tijdens de diverse warmtebehandelingen.

요약

자동차 산업에서 차체 경량화가 연비향상 측면에 있어서 매우 중요한 요인이다. 이에 대해 현가 스프링강의 설계응력을 향상시킴에 따라 부분적으로 연비향상 및 경량화가 가능해질 수 있다. 그러나, 강도가 증가할수록 스프링의 다른 요구특성들, 스프링 성형성 및 피로수명 등이 저하될 수 있으므로 조심해야 한다. 피로수명 및 영구변형저항성 등을 개선시키기 위해서, 높은 값의 강도 및 단면감소율을 갖는 새로운 스프링강이 개발될 필요가 있다. 현재의 산업적 환경에 대응하는 새로운 고강도 현가스프링강 소재에 대한 연구가 활발히 진행중이다. 고강도 스프링강에 있어서 기존에 사용되는 저강도 스프링강의 피로특성, 연성 및 인성등이 동등 유지되면서 강도를 증가시키는 것이 중요한 연구분야였다. 본 연구의 목적은 현가스프링에 있어서 고객사 요구에 따라 설계응력 1400 MPa 를 만족시킬 수 있는 단면감소율이 25 % 이상, 평균인장강도 2350 MPa 를 갖는 스프링강을 개발하는 것이다. 이에 대해 오스테나이트화 및 템퍼링조건에 따른 미세조직변화 및 기계적 성질을 조사하였다.

제 1장에서는 스프링강의 개발역사가 소개되며 고강도 스프링강의 개발필요성이 상세하게 설명되어 있다. 최근에, 자동차 경량화를 위해서 가벼운 현가스프링강 개발에 대한 요구가 급증되고 있다. 이러한 요구를 만족시키기 위해서 고강도 스프링 개발에 대한 연구가 진행되고 있다. 그러나, 현재 상용화되어 있는 스프링강은 고응력 조건하에서 사용하게 되면 내구성 관련문제, 낮은 피로특성 및 영구변형저항성이 발생될 것이다: 따라서 스프링의 높이는

낮아질 것이고 자동차의 높이는 감소하게 되어 안정성에 대한 심각한 문제를 야기할 것이다.

개발하고자 하는 고강도 스프링강의 요구물성을 만족시키기 위해서는 합금성분의 조정 및 최적 미세조직을 얻기 위한 열처리조건 설계가 기본적 연구방향이 될 것이다. 이 목적을 달성하기 위하여 열처리 냉각중 오스테나이트로 부터의 상변태거동을 해석할 수 있는 방법이 제 2장에 설명되어 있다. 새로이 제안된 모델은 dialtation 곡선으로부터 오스테나이트-페라이트, 오스테나이트-펄라이트의 상변태거동을 해석할 수 있다. 상들의 부피분율이 정량적으로 dilatation 데이터와 관련이 있다면, dilatometric 방법은 상변태 거동조사에 매우 효과적인 방법이 될 것이다. 해석모델은 상변태시 탄소의 재분포에 따른 오스테나이트내 탄소농화 및 상들의 단위부피차이를 기반으로 개발되었다. self consistent model 이 dilatation 곡선으로부터 상변태거동을 해석할시 적용되어 보다 정확도를 높였으며 아공석강에 대한 상변태실험으로 모델결과와 실험결과를 비교 검증하였다. 계산결과와 실험결과가 아주 잘 일치함을 확인하였다.

강의 가공열처리에서 중요한 단계는 재오스테나아트화이다. 재오스테나이트화 거동은 오스테나이트 입자크기, 분포 및 합금원소농도의 균질화에 영향을 미치므로 가열중 생성된 austenite microstructure 가 상변태거동 및 결국에는 냉각조건에 (quenching and tempering) 따라 기계적 물성에도 아주 큰 영향을 갖게 되는 것이다. 그러나, 가열중 재오스테나이트화의 거동 및 조직에 대한 실험적 관찰 및 조사등이 매우 힘들다. 이는 가열중 생성된 오스테나이트가 냉각중에 상변태로 사라지고 마르텐사이트로 변태되기 때문이다. 이를 해결하기 위하여 가열중 펄라이트 → 오스테나이트 상변태거동을 해석할 수 있는 모델을 제 3장에서 개발 및 설명하였다. 가열중 오스테나이트 조직생성에 대해서 오스테나이트가 페라이트-시멘타이트 계면에서 핵생성되어 새로운 시멘타이트-오스테나이트 및 오스테나이트-페라이트 계면이 새로이 생기게 됨을 알 수 있었다. 고전적으로 이해왔던 가열중 오스테나이트화는 냉각중 공석반응과 동일한 상변태 반응으로 여겨져왔던 것이 아님을 확인할 수 있었다. 제안된 모델은 이를 기반으로 개발되었으며 새로이 생기는 상간 경계면에서 local equilibrium 조건하에서 페라이트 + 시멘타이트 → 오스테나이트 상변태가 있다고 가정하였다. 이 또한 실험을 통한 결과와 계산된 결과가 아주 잘 일치함을 확인할 수 있었다.

제 4장의 목적은 단면감소율 25% 이상, 평균인장강도 2350 MPa 를 갖는 스프링강을 개발하는 것이다. 이들 물성을 갖는 스프링강 개발목적으로 5가지 후보 강종을 연구하였다. 합금성분은 고 C- Si 강을 기본으로 하여 Mo, B, Nb 등을 첨가시켜 변화를 꾀했다. 열처리조건(quenching and tempering,..) 변화에 따른 기계적 특성 및 미세조직 변화를 조사하였다. 후보강종중 S1 및 S3 강이 고객사 요구물성치를 만족시키는 것을 확인하였다.

제 5장에서는 이들 후보강종에 대한 강화 및 연화기구를 제시하였고 기계적

물성 및 미세조직 변화를 설명하였다.   강화기구는 오스테나이트화 거동, 석출거동 (V_4C_3, cementite and ε-carbide) 및 prior austenite grain size, lath size 등을 기반으로 조사되었다.   인장강도의 증가는 입실론 탄화물의 미세석출에 기인하는 것을 확인하였다.   저온 템퍼링온도에서는 입실론 탄화물이 탄소 clusters 에서 석출되며 일부 과포화된 탄소가 마르텐사이트내에 존재하게 된다.   템퍼링온도가 증가할수록, 입실론 탄화물은 재고용되고 시멘타이트가 동시에 석출되기 시작한다.   입실론 탄화물에서 시멘타이트로의 천이온도를 증가시키면 단면감소율 감소없이 인장강도를 증가시킬 수 있다.   S3 강의 prior austenite grain size 는 비교적 크게 관찰되었고 이로 인해 단면감소율이 다소 감소하는 경향을 보였으며 S1 강은 변화가 작은 것을 확인하였다. 단면감소율을 증가시키기 위해서는 미세 석출물을 이용하여 오스테나이트 입자크기를 미세화할 필요가 있었다.

템퍼링온도가 증가할수록 강도는 감소하고 연성은 계속적으로 증가한다. 성형성 및 피로특성을 개선하기 위해서는 연성(단면감소율)은 임계값 이상으로 유지되어야 한다.   제 6장은 단면감소율 감소 및 취성 현상과 관련된 성분 및 미세조직 특성을 설명하고 벽계파괴 또는 입내파괴에 대한 원인을 규명하였다. S3 강의 입내취성파괴원인은 prior austenite grain boundary 에 존재하는 borocarbide 때문이었다.   크랙은 표면 또는 오스테나이트 입계에 존재하는 particles 에서 시작되어 $Fe_{23}(C, B)_6$ carbide 에 의해 입계를 따라 쉽게 전파되어 간다.   단면감소율은 오스테나이트 입계에 존재하는 $Fe_{23}(C, B)_6$ 탄화물에 의해 심각하게 감소하는 것을 알 수 있었다.

제 7장에서는 기계적 성질을 개선하기 위하여 새로운 템퍼링 방법이 개발되었고 이는 2단의 tempering 으로 구성되어 있다.   통상은 템퍼링은 한 온도에하에서 이루어지마 step tempering 은 2 온도하에서 계단식으로 행해진다.   주요 실시목적은 입실론 탄화물의 생성수를 증가시키고 시멘타이트로의 천이를 억제하고자 하는 것이다.   Step tempering 된 스프링강의 기계적 물성은 일반 템퍼링된 강보다 향상되었으며 피로수명은 거의 동일하였다.   2번째 step tempering 단계는 마르텐사이트의 연화 및 시멘타이트로의 천이를 억제하는 위한 것이다.   향후 step tempering 의 최적조건을 찾기위해서는 계속적인 연구가 필요할 것이다.

강에서 탈탄은 강도 및 피로수명 저감을 야기하므로 스프링강에서 탈탄억제는 반드시 필요하다.   제 8장에서는 탈탄 및 산화에 의한 스케일생성에 대한 합금성분 및 열처리조건의 영향을 분석하였다.   이 장의 목적은 가열 및 냉각중 고 Si 스프링강의 공기중 탈탄거동을 조사하는 것이다.   합금성분 및 열처리조건을 고려한 페라이트 탈탄두께에 대한 계산모델을 개발하였고 탈탄 및 산화거동을 동시에 고려하였다.   계산된 모델결과를 실험을 통하여 검증하였고 탈탄억제에 대한 최적 패턴도 제시 및 비교하였다.

결론적으로, 본 논문은 새로운 초고강도 스프링강개발(인장강도 2350 MPa, 단면감소율 25 %이상)을 위하여 열처리중 dilatation 곡선으로부터 상변태해석모델을 개발하였다.   또한 강화기구를 설명하였으며 취성파괴, 단면감소율

감소에 대한 Borocarbide 역할도 규명하였다. 마지막으로, 피로수명 저감을 억제하기 위하여 탈탄 및 산화기구를 해석 모델을 개발하였다. 페라이트 탈탄두께는 열처리조건을 최적화함에 따라 최소화될 수 있음을 확인하였다. 이들 결과를 토대로 자동차용 현가스프링강의 고강도화 및 기타 요구물성을 개선할 수 있으며 그에 따른 자동차 경량화, 연비향상을 도모할 수 있다.

Bibliography

[1]   A.R. Marder and J.I. Goldstein, *Phase transformations in ferrous alloy*, ASM, Philadelphia, 1984.

[2]   Gorge Krauss, *Principles of Heat Treatment of Steel*, ASM, Metals Park, Ohio, USA, 1980.

[3]   R.W.K. Honeycombe, *Steels: Microstructure and Properties*, Edward Arnold Ltd., 1981.

[4]   Joseph Edward Shigley and Charles R. Mischke, *Mechanical Engineering Design*, 4th ed. McGraw-Hill Inc., 1989.

[5]   G.R.Speich, *Trans. Met. Soc. AIME*, 245:2553, 1969.

[6]   A.G. Alten and P. Payson, *Trans. ASM*, 45:498, 1953.

[7]   J. Gordine and I. Codd, *J. Iron Steel Inst.*, 207(1):461, 1969.

[8]   W. Stevens and A.G. Haynes, *JISI*, 183:349, 1956.

[9]   C.J. Altstetter, Morris Cohen and B.L. Averbach, *Trans*, 55:287, 1962.

[10]   W.S. Owen: *Trans. ASM*, 46:812, 1954.

[11]   W.F. Smith, *Structure and properties of engineering alloys*, McGraw-Hill, 1981.

[12]   Spring, 2nd ed., *JSSE*, 1970.

[13]   Heat treatment of Steel, *JSSE*, 1985.

[14]   *ASM Handbook*, ASM International, 1990.

[15]   S.T. Furr, *J. of Basic Eng. ASME*, 94:223, 1972.

[16]   S. Choi and J.S. Lee, Development of high strength spring steel, *POSCO Technical Report*, .2006.

[17]   D.L. Lee and H.C. Choi, Effect of Si and C on the mechanical property of SAE9254, *POSCO Technical Report*, 1999.

[18]   K.C. Kim, J.S. Lee and H. C. Choi, Effect of microstructure on the high temp. mechanical property of engine valve spring steel, *POSCO Technical Report*, 2004.

[19]   M. Saito et al., *Heat treatment*, 27(1):23, 1987.

[20]   T. Lund and R. Lyrberg, *OVAKO Steel Technical Report*, 1:3, 1988.

[21]   Spring, *JSSE*, 37:89, 1992.

[22]   F. Borik, V.A. Biss and V.E. Smith, *SAE paper No.790409*, SAE Congress, 1979.

[23]   H.J. Tata, E.R. Driscoll and J.J. Kary, *SAE paper No.800480*, SAE Congress, 1980.

[24]   M. Takahashi and H.K.D.H. Bhadeshia, *Journal of Materials Science Letters*, 8:477, 1989.

[25]   M. Onink, F.D. Tichelaar, C.M. Brakman, E.J. Mittemeijer and S. van der Zwaag, *Z. Metallkd.*, 87:24, 1996.

[26]   C. Qiu and S. van der Zwaag, *Steel Res.*, 68:32, 1997.

[27]   C. Garcı´a de Andre´s, F.G. Caballero, C. Capdevila and H.K.D.H. Bhadeshia, *Scripta Mater.*, 39:791, 1998.

[28]   T.A. Kop, J. Sietsma and S. van der Zwaag, *Journal of Materials Science*, 36:519, 2001

[29]   J.Z. Zhao, C. Mesplont and B.C. De Cooman, *ISIJ International*, 41:492, 2001.

[30]   A. van der Ven and L. Delaey, *Progress in Materials Science*, 40:181, 1996.

[31]   T. Tanaka, H.I. Aaronson and M. Enomoto, *Metall. Trans. A*, 26A:535, 1995.

[32]   T. Senuma, M. Suehiro and H. Yada, *ISIJ International*, 32:423, 1992.

[33]   S. Choi, Mater. *Sci. & Eng. A*, 363:72, 2003.

[34]   N. Ridley, H. Stuart and L. Zwell, *Trans. AIME*, 245:1834, 1969.

[35]   D.J. Dyson and B. Holmes, *JISI*, 208:469, 1970

[36]   M. Onink, C.M. Brakman, F.D. Tichelaar, E.J. Mittemeijer and S. van der Zwaag, *Scr. Metall. Mater.*, 29:1011, 1993.

[37]   C. Atkinson, T. Akbay and R.C. Reed, *Acta. Metall. Mater.*, 43:2013, 1995.

[38]   International Trends in Welding Science & Technology, Eds. S.A. David and J.M. Vitek, *ASM international*, Materials Park, Ohio, USA, 1993.

[39]   Proceedings, *Modeling of Casting, Welding and Advanced Solidification Processes*, Eds. M. Rappaz, M.R. Özgü and K.W. Mahin, *TMS*, Warrendale, Penn., 1991.

[40]   A.I. Katsamas, *Surface & Coatings Technology*, 201:6414, 2007.

[41]   C.R. Brooks, *Principles of the Austenitization of Steels*, Elsevier Applied Science, London 1992.

[42]   G.A. Roberts and R.F. Mehl, *Trans. ASM*, 31:613, 1943.

[43]   R.R. Judd and H.W. Paxton, *Trans. Metall. Soc. A.I.M.E.*, 242:206, 1968).

[44]   C.I. Garcia and A.J. Deardo, *Met. Trans.*, 12A:521, 1981.

[45]   G.R. Speich and A. Szirmae, *Trans. TMS of AIME*, 245:1063, 1969.

[46]   M. Hillert, K. Nilsson and L.E. Törndahl, *J. Iron Steel Inst.*, 209:49, 1971.

[47]   N.C. Low and D.V. Edmonds, *Metall. Trans.*, 11A:33, 1980.

[48]   G.R. Speich, V.A. Demarest and R.L. Miller, *Metall. Trans. A*, 12A:1419, 1981.

[49]   A. Hultgren, *Trans. Am. Soc. Steel Treating*, 16:227, 1929.

[50]   C. Garcı´a de Andre´s, F.G. Caballero and C. Capdevila, *Scripta Mater.*, 38:1835, 1998.

[51]   F.G. Caballero, C. Capdevila and C. Garcı´a de Andre´s, *Scripta Mater.*, 42:1159, 2000.

[52]   F.G. Caballero, C. Capdevila and C. Garcı´a de Andre´s, *Metrall. & Mater. Trans. A*, 32A:1283, 2001.

[53]   A. Jacot and M. Rappaz, *Acta Mater.*, 45:575, 1997.

[54]   A. Jacot and M. Rappaz and R.C. Reed, *Acta Mater.*, 46:3949, 1998.

[55]   A. Jacot and M. Rappaz, *Acta Mater.*, 47:1645, 1999.

[56]   R.C. Reed, T. Akbay, Z. Shena, J.M. Robinson and J.H. Root, *Mater. Sci. & Eng. A*, 256:152, 1998.

[57] F.L.G. Oliveira, M.S. Andrade and A.B. Cota, *Materials Characterization*, 58:256, 2007.

[58] R. Mancini and C. Budde, *Acta Matell. Mater.*, 47:2907, 1999.

[59] R.C. Dykhuizen, C.V. Robino and G.A. Knorovsky, *Metall. & Mater. Trans. B*, 30B:107, 1999.

[60] B.J. Yang, L. Chuzhoy and M.L. Johnson, *Computational Materials Science*, 41:186, 2007.

[61] E.Ohmura, K. Inoue and Y. Takamachi, *JSME Int. J.*, 34:421, 1991.

[62] S. Choi and S.W. Lee, *POSCO Internal Report*, Pohang, 2008.

[63] N. Yoshihara and S. Nagamatsu, *Kobe Steel Engineering Reports*, 59(1):54-58, 2009.

[64] L. Godfrey, *Metals Handbook*, 10th Ed., ASM International,1:302-326, 1990.

[65] D. Schreiber and I. Wiesenecker-Frieg, *A Handbook for Materials Research and Engineering*, Ed. by Verein Deutscher EisenHuttenleute, Springer Verlag and Verlag Stahleisen, Berlin and Dusseldorf, 2:468-477, 1993.

[66] H. Dziemballa and L. Manke, *Future for Automotive Industry*, Ed. by I. von Hagen and H.-J. Wieland, Verlag Stahleisen GmbH, Dusseldorf, :341-348, 2005.

[67] H. Berns, G. Siekmann and I. Wiesenecker, *Draht*, 35(5):247-252, 1984.

[68] T. Iikubo and Y. Ito, *Denki Seiko* (Electr. Furn. Steel), 57:33, 1986.

[69] W.J. Nam and H.C. Choi, *Wire J. Int.*, 29:94, 1996.

[70] W.E. Heitmann, T.G. Oakwood and H.J. Dziemballa, *Proc. Of Microalloying 1995*, Pittsburgh, PA, The Iron and Steel Society, Warrendale, PA, :395, 1995.

[71] N. Ridley, S. Maropoulos and J.D.H. Paul, *Mater. Sci. Tech.*, 10:239, 1994.

[72] T. Yamamoto, R. Kobayashi, T. Ozone and M. Kurimoto, *J. Heat. Treat.*, 3:220, 1984.

[73] T. Nakano, T. Sakayuki, M. Wakita and A. Sugimoto, *JSAE Review*, 22:337-342, 2001.

[74] H.K.D.H. Bhadeshia and R. Honeycombe, *Steel*, 3rd ed., Elsevier, 2006.

[75] S.J. Matas and R.F. Hehemann, *Trans. TMS AIME*, 221:179–185, 1961.

[76] R. Entin, *Decomposition of austenite by diffusional processes*, Ed. V. F. Zacky and H. I. Aaronson, 295–211, New York, Interscience, 1962.

[77] J. Deliry, Memor. *Sci. Rev. Met.*, 62:527–550, 1965.

[78]   J. Pomey, Memor. *Sci. Rev. Met.*, 63: 507–532, 1966.

[79]   R.F. Hehemann, *Phase transformations*, Ed. H.I. Aaronson and V.F. Zackay, 397–432, Metals Park, OH, ASM, 1970.

[80]   R. Le-Houillier, G. Begin and A. Dube, *Metall. Trans.*, 2:2645–2653, 1971.

[81]   H.K. D. H. Bhadeshia and D. V. Edmonds, *Met. Sci.*, 17:420–425, 1983.

[82]   B.J. P. Sandvik, *Metall. Trans. A*, 13A: 777–787, 1982

[83]   B.J. P. Sandvik, *Metall. Trans. A*, 13A:789–800, 1982.

[84]   S.J. Barnard and G.D.W. Smith and A.J. Garratt-Reed and J. van der Sande, *Solid Solid Phase Transformations*, TMS AIME , Materials Park, Ohio, 881-885, 1981.

[85]   S.S. Babu and K. Hono and T. Sakuri, Metall. *Mater. Trans. A*, 25:499-508, 1994.

[86]   G. Miyamoto, J.C. Oh, K. Hono, T. Furuhara, T. Maki, *Acta Mater.*, 55:5027-5038, 2007.

[87]   A.A. Barabi, F. Li, P. Romano, D. Ponge and D. Raabe, *Mater. Sci. Eng. A*, 463:138-146, 2007.

[88]   M. Ayada, M. Yuga, N. Tsuji, Y. Saito and A. Yoneguti, *ISIJ Int.*, 38:1022-1031, 1998.

[89]   J.W. Morris Jr., Z. Guo, C.R. Krenn and Y.-H. Kim, *ISIJ Int.*, 41:599-611, 2001.

[90]   H. Ohtani, F. Terasaki and T. Kunitake, *Trans. ISIJ*, 12:118-127, 1972.

[91]   A. Peters, R. Kaspar, J. Janovec and O. Pawelski, *Steel Res. Int.*, 67:291-297, 1996.

[92]   M. Wettlaufer, R. Kaspar, *Steel Res.*, 71:357-361, 2000.

[93]   M. Wettlaufer, R. Kaspar, *Steel Res.*, 71:362-365, 2000.

[94]   K.J. Irvine, F.B. Pickering and J. Garston, *J. Iron Steel Inst.*, 196:66, 1960.

[95]   R. G. Baker and J. Nutting, *ISI Special Report*, 64:1-10, 1959.

[96]   E. Tekin and P.M. Kelly, *J. Iron and Steel Inst.*, 203:715-720, 1965.

[97]   M. Cohen, The strengthening of Steel, *Trans TMS-AIME*, 224:638-657, 1962.

[98]   P.G. Winchell and M.Cohen, The Strength of Martensite, *Trans. ASM*, 55:347-361, 1962

[99]   K. H. Jack: *J. Iron and Steel Inst.*, 169:26–36, 1951.

[100]   J.D. Verhoeven, *Fundamentals of Physical Metallurgy*, John Wiley & Sons, Canada, 1975.

[101]   R.A. Grange, C.R. Hribal and L.F. Porter, Hardness of tempered martensite in carbon and low-alloy steels, *Met. Trans. S*, 8A:1775-1785, 1977.

[102]   A.G. Allen and P. Payson, The effect of silicon on the tempering of martensite, *Trans. ASM*, 45:498-532, 1953.

[103]   W. Crafts and J.L. Lamont, Effects of alloys in steel as resistance to tempering, *Trans. AIME*, 172:222-243, 1947.

[104]   S. Yamasaki and H.K.D.H. Bhadeshia, *Mater. Sci. Tech.*, 19:1335-1343, 2003.

[105]   D.H. Sherman, S.M. Cross, S. Kim, F. Grandjean, G.J. Long and M.K. Miller, *Metall. Mater. Trans. A*, 38A:1698-1711, 2007.

[106]   G.S. Ansell and E.M. Breinan, *Trans. ASM*, 58:110-113, 1965.

[107]   Y. Tomita and K. Okabayashi, *Metall. Trans.*, 18A:115-121, 1987.

[108]   T. Thors, M. Mangard, S. Larsson and B. Hildenwall, Scand. *J. Metall.*, 27:171-179, 1998.

[109]   L.J.E. Hofer, E.M. Cohn and W.C.Peebles: *J. Amer. Chem. Soc.*, 71:189–195, 1949.

[110]   G.R. Speich and K.A. Taylor, Martensite, Ed. by G.B. Olson and W.S. Owen, *ASM International*, 1992.

[111]   L. Cheng, C.M. Brakman, B.M. Korevaar and E.J. Mittemeijer, *Metall. Trans.*, 19A:2415-2426, 1988.

[112]   A.M. Sherman, G.T. Eldis and M. Cohen, *Metall. Trans.*, 14A:995-1005, 1983.

[113]   A. K. Seal and R.W.K. Honeycombe, *J. Iron and Steel Inst.*, 188:343–350, 1958.

[114]   M. Tanino and K. Aoki, *Trans. Iron and Steel Inst. Japan*, 8:337–345, 1968.

[115]   D..McLean, *Grain boundaries in Metals*, Oxford Univ. Pr., Oxford, 1957.

[116]   H.K.D.H. Bhadeshia, M. Lord and L.-E. Svensson, *Trans. JWRI*, 32:91-96, 2003.

[117]   T. Sakuma, N. Watanabe and T. Nishizawa, *Trans. JIM*, 21:159, 1980.

[118]   R.M. Horn and R.O. Ritchie, *Metall. Trans. A*, 9A:1039–1053, 1978.

[119]   C.L. Briant and S.K. Banerji, *Metall. Trans. A*, 10A:123–126, 1979.

[120]   C.L. Briant and S.K. Banerji, *Metall. Trans. A*, 10A:1729-1737, 1979.

[121]   N. Bandyopadhyay and C.J. MacMahon Jr., *Metall. Trans. A*, 14A:1313, 1983.

[122]   G. Krauss and C.J. McMahon Jr., *Martensite, ASM International*, Eds. G.B. Olson and W.S. Owen, New York, 295, 1992.

[123]   C.J. McMahon Jr., Hydrogen Effects in Metals, Eds. I.M. Bernstein and A.W. Thompson, *TMS-AIME*, New York, 219, 1981.

[124]   F. Nakasato, F. Terasaki, *Tetsu to Hagane*, 61:856, 1975.

[125]   S.K. Banerji, C.J. McHaon Jr. and H.C. Feng, Intergranular Fracture in 4330-type Steels, *Met. Trans. A*, 9A:237-247, 1978.

[126]   B.S. Lement, B.L. Averbach and M. Cohen, *Trans. ASM,* 47:291, 1955.

[127]   G. Thomas, *Metall. Trans. A*, 9A:439-450, 1978.

[128]   B.J. Schultz and C.J. McHaon Jr., *STP-499, ASTM*, 104, 1972.

[129]   H. Ohtani and C.J. Mchaon Jr., Modes of Fracture in Temper Embrittled Steels, *Acta Metallurgica,* 23:377-386, 1975.

[130]   I. Olefjord, Temper Embrittlement, Review 231, *Inter. Met. Rev.*, 23:149-163, 1978.

[131]   C.J. McMahon Jr. and L. Marchut, *J. Vac. Sci. Technol.*, 15:450, 1978.

[132]   G. Krauss, *Steels*, 1st ed. *ASM International*, 2005.

[133]   P. Rogl, J.C. Schuster and H. Nowotony, *Boron in Steel*, Eds. S.K. Banerji and J.E. Morral, *TMS-AIME*, 1980.

[134]   Ph. Maitrepierre, J. Rofes-Vernis and D. Thivellier, Structure-Properties Relationships in Boron Steels, *Boron in Steel*, Ed. by S.K. Banerji and J.E. Morral, The Metallurgical Society of AIME, New York, 1080.

[135]   Edgar C. Bain and Harold W. Paxton, *Alloying Elements in Steel*, 2nd ed., American Society for Metals, Metals Park, Ohio, USA, 1966.

[136]   E. Tekin and P.M. Kelly, *J. Iron and Steel Inst.*, 203:715-720, 1965.

[137]   Y. Prawoto, N. Sato, I. Otani, and M. Ikeda, *Journal of Materials Engineering and Performance*, 13(5):627-636, 2004.

[138]   S. Tekeli, *Mater. Lett.*, 57:604, 2002.

[139]   J. Gegner, *Z. Metallkd.*, 94:30-35, 2003.

[140]   J. Kucera, P. Braz and K. Adamaszek, *Acta Techn.*, 45:45-64, 2000.

[141]   J. Kucera and K. Adamaszek, *Acta Techn.*, 46:51-60, 2001.

[142]   N. Birks and W. Jackson, *J. Iron Steel Inst.*, 201:81, 1970.

[143]   A. Phillion, H. S. Zurob, C. R. Hutchinson, H. Guo, D. V. Malakhov, J. Nakano, G. R. Purdy, *Metall. Trans. A*, 35A:1237-1242, 2004.

[144]   B. Millon, J. Ruzickova and K. Stransky, *Kovove Mater.*, 27(4):492-503, 1989.

[145]   C. R. Oldani, *Scripta Mater.*, 35(11):1253-1257, 1996.

[146]   P. Marini and G. Abbruzzese, *J. Magn. Magn. Mat.*, 26:15-21, 1982.

[147]   J.D. Verhoeven, *Materials Characterization*, 25:221-239, 1990.

[148]   M. Nomura, H. Morimoto and M. Toyama, *ISIJ International*, 40(6):619–623, 2000.

[149]   D. Li, D. Anghelina, D. Burzic, W. Krieger and E. Kozeschnik*, Steel Research Int.*, 80(4):304-310, 2009.

[150]   W. Sachs and C.W. Tuck, *ISI Publication 111*, London, The Iron and Steel Institute, 1, 1968.

[151]   N. Birks, G.H. Meier and F.S. Pettit, *Introduction to the High-Temperature Oxidation of Metals*, Cambridge University Press, Cambridge, 2006.

[152]   D. Caplan, G.I. Sproule, R.J. Hussey and M.J. Graham, *Oxid. Met.*, 12:67, 1968.

[153]   N. Birks, G.H. Meier, *Introduction to High Temperature Oxidation of Metals*, Edward Arnold, London, 1983.

[154]   F.S. Pettit, J.B.Wagner Jr., *Acta Metall.*, 12:35-40, 1964.

[155]   C.Wagner, *Z. Phys. Chem. B21*, 25, 1933.

[156]   L. Himmel, R.F. Mehl, C.E. Birchenall, *J. Met. Trans. AIME*, 827-843, 1953.

[157]   M.H. Davies, M.T. Simnad, C.E. Birchenall, *J. Met. Trans. AIME*, 889-896, 1951.

[158]   A.S. Khanna, *High Temperature Oxidation and Corrosion*, ASM International, OH, 2002.

[159]   O. Kubaschewski, B.E. Hopkins, *Oxidation of Metals and Alloys*, second ed., Academic Press Inc., New York, 1962.

[160]   H.T. Abuluwefa, R.I.L. Guthrie and F. Ajersch, Metall. *Mater. Trans. A*, 28:1633-1641, 1997.

[161]   W.F. Smith, *Foundations of Materials Science and Engineering*, Irwin/McGraw-Hill, New York, 1993.

[162]   C. Wells, W. Batz, and R.F. Mehl, *Diffusion coefficient of carbon in austenite*, Trans. AIME, 188:553-560, 1950.

[163]   R.P. Smith, *Acta Met.*, 1:578-587, 1953.

[164]   G.V. Kidson, *J. Nucl. Mat.*, 3:21-29, 1961.

[165]   W. Jost, *Diffusion in Solids*, Liquids and Gases, Academic Press Inc., New York, 69, 1960.

[166]   J.S. Kirkaldy, *Can. Jour. Phys*. 36:917, 1958.

[167]   R.Y. Chen and W.Y.D. Yuen, *Oxidation of Metals*, 59:433-468, 2003.

[168] K.M. Marra, E.A. Alvarenga and V.T.L. Buono, *ISIJ International*, 44(3):618-622, 2004.

Acknowledgments

It was my pleasure to thank the many people who made this thesis possible.

I am heartily thankful to my promoter Professor dr. ir. Sybrand van der Zwaag, whose encouragement, guidance and support from the initial to the final level enabled me to develop an understanding of the subject. With his enthusiasm, his inspiration, and his great efforts to explain things clearly and simply, he helped to make metallurgical fun for me. Throughout my thesis-writing period, he provided encouragement, sound advice, good teaching, good company, and lots of good ideas. I would have been lost without him.

Another important partner of this thesis is Dr. Pedro E.J. Rivera Díaz del Castillo in Department of Materials Science and Metallurgy, University of Cambridge. Dr. Pedro Rivera was always very kind and provided all necessary supports. I appreciate his assistance and guidance in writing thesis.

I would like to express my deep and sincere gratitude to my supervisor, Professor Youngseog Lee in Mechanical Engineering, Chung-Ang University. His logical way of thinking has been of great value for me. His understanding, encouraging and personal guidance have provided a good basis for the present thesis. I wish to thank for revising the English of my manuscript.

I warmly thank Dr. KiHo Rhee for his valuable revising and friendly help. His extensive discussions around my work and interesting explorations in operations have been very helpful for this study. I wish to thank for revising the English of my manuscript.

I am grateful to Dr. Sang-Yoon Lee for helping me the experimental supports when I was in TU Delft. I must also acknowledge Dr. Yo-Sep Yang for his help for analyzing the 3D Atom

probe in this study.   I am grateful to Dr. Duk-Lak Lee for supporting me the collaboration research to TU Delft.

I also wish to thank Dr. Mingxin Huang and Dr. Wei Xu for their kindness and help when I was in TU Delft.   Mrs. Laura is thanked for cordial help in secretarial work in TU Delft. Our research group has been the most international group and I was always proud to be a part of this group.   Here I would like to thank all the (ex-) members of the group for providing such a great atmosphere.   Thanks Suresh, Theo, Alwin, Steven, Arek, Doty, Geeta, Maruti, Mazhar, Rahul, Chris, Pim, Meijie and all FAM members.

My special gratitude is due to my parents, parent in law for their loving support.   I would also like to thank my family for the support they provided me through my entire life and in particular, I must acknowledge my wife and daughters, Inkyung, Dahee, Dayeong and Dain, without whose love and encouragement, I would not have finished this thesis.

Lastly, I offer my regards and blessings to all of those who supported me in any respect during the completion of the thesis.

Curriculum Vitae

Sangwoo Choi

born on 4 December 1969
in Gwangju, KOREA

March 1988 - Feb. 1993
Bachelor of Science Department of Materials Science and Engineering, KAIST (Korea Advanced Institute of Science & Technology), Daejeon, KOREA

March 1993 - Feb. 1995
Master of Science in Department of Electronic Materials Engineering, KAIST (Korea Advanced Institute of Science & Technology), Daejeon, KOREA.   Thesis under supervision of Professor Dang Moon Wee: "Microstructure and creep behavior of a rapidly solidified Al-Fe-V-Si-Ti-W alloy"

March 1995 - Present
Principal researcher, Wire Rod Research Group, Technical Research Laboratories, POSCO, KOREA

Aug. 2007 - Aug. 2008
Visiting researcher, Fundamentals of Advanced Materials, Faculty of Aerospace Engineering, Delft University of Technology, Delft, The Netherlands

List of Publications

Journal

- Y. Lee, **Sangwoo Choi**, H. Kim and W.Y. Choo, "An experimental study of the mean effective strain in rod (or bar) rolling process", *Metals and Materials*, 6(6):525-513, 2000.

- Y. Lee, **Sangwoo Choi** and Y.H. Kim, "Mathematical model and experimental validation of surface profile of a workpiece in round-oval-round pass sequence", *J. Materials and Processing Technology*, 108:87-96, 2000.

- Y. Lee and **Sangwoo Choi**, "New approach for the prediction of stress free surface profile of work piece in rod rolling", *ISIJ International*, 40(6):624-626, 2000.

- **Sangwoo Choi**, Y. Lee and S. Lee, "A study of influence of strain path change on the microstructure and mechanical properties of low carbon steel using plate and bar rolling", *Metals and Materials International*, 7(2):115-121, 2001.

- Y. Lee, S.I. Kim, **Sangwoo Choi**, B.L. Jang and W.Y. Choo, "Mathematical model to simulate thermo-mechanical controlled processing in rod (or bar) rolling", *Metals and Materials International*, 7(6):519-530, 2001.

- S.-J. Yoo, **Sangwoo Choi**, S.-K. Han, B.-J. Jung, B.-H. Song and C.-N. Park, "The effects of V, Al and N on the fatigue life of a carbonitrided bearings", *Bearing Steel Technology*, ASTM STP 1419, J.M. Beswick, Ed. *ASTM International*, pp. 297-300, 2002.

- **Sangwoo Choi**, Y. Lee and P.D. Hodgson, "A comparative study of microstructures and mechanical properties obtained by bar and plate rolling", *J. Materials and Processing Technology*, 124:329-336, 2002.

- Y. Lee, **Sangwoo Choi** and P.D. Hodgson, "Analytical model of pass-by-pass strain in rod (or bar) rolling and its application to prediction of austenite grain size", *Materials Science and Engineering A*, 336:177-189, 2002.

- **Sangwoo Choi** and Y. Lee, "A new approach to predicting partial recrystallization in the multi-pass hot rolling process", *Metals and Materials International*, 8:15-23, 2002.

- Y. Lee, **Sangwoo Choi** and P.D. Hodgson, "Integrated model for thermo-mechanical controlled process in rod (or bar) rolling", *J. Materials and Processing Technology*, 125-126:678-688, 2002.

- **Sangwoo Choi**, Y. Lee, P.D. Hodgson and J.S. Woo, " Feasibility study of partial recrystallization in multi-pass hot deformation process and application to calculation of mean flow stress", *J. Materials and Processing Technology*, 125-126:63-71, 2002.

- **Sangwoo Choi**, "Models for estimation of transformation kinetics from the dilatation data during a cooling of hypoeutectoid steels", *Materials Science and Engineering A*, 363:73-81, 2003.

Conference

- S.K. Cho and **Sangwoo Choi**, "Effect of wire rod size and its packing density on the tensile strength deviation of high carbon steel wire rod in the stelmor process", Wire Association International 67th Annual Convention: 1997 Conference Proceeding (USA), pp. 36-42, 1997.

- S.J. Yoo, J.K. Park, **Sangwoo Choi** and D.L. Lee, "Improvement of ball bearing fatigue life by reducing segregation and proeutectoid cementite", Wire Association International 69th Annual Convention: 1999 Conference Proceeding (USA), pp. 217-224, 1999.

- **Sangwoo Choi**, Y. Lee, P.D. Hodgson and J.S. Woo, "Feasibility study of partial recrystallization in multi-pass hot deformation process and application to calculation of mean flow stress", The 9th International Conference on Metal Forming (UK), pp. 63-71, 2002.

- Y. Lee, **Sangwoo Choi** and P.D. Hodgson, "Integrated model for thermo-mechanical controlled process in rod (or bar) rolling", The 9th International Conference on Metal Forming (UK), pp. 678-688, 2002.

- **Sangwoo Choi** and C.S. Lee, "New approach for extracting proeutectoid ferrite and pearlite transformation kinetics from dilatation curve of hypoeutectoid steels and its verification", The 2003 Korea-Japan symposium of phase transformations : Current issues of phase transformations (KOREA), 2003.